UNIVERSIDAD Ð LA LAGUNA
Departamento de Astrofísica

Universidad de La Laguna

The Lockman–SpReSO project. Optical properties of far-infrared selected galaxies.

Memoria que presenta
D. **Mauro González Otero**
para optar al grado de
Doctor por la Universidad de La Laguna.

INSTITUTO Ð ASTROFISICA Ð CANARIAS
mayo de 2024

Examination date: June, 2024
Thesis supervisor: Dr. Jordi Cepa
Dra. Carmen P. Padilla-Torres

ISBN: xx-xxx-xxxx-x
Depósito legal: TF-xxxx/2024

Some of the material included in this document has been already published in the journal *Astronomy & Astrophysics*.

Some of the figures included in this document have been already published in the journal *Astronomy & Astrophysics*.

A meus pais,
a Mara e a Jenni,
que non me falten nunca

Agradecimientos

En primer lugar, me gustaría agradecer a mis directores de tesis por permitirme conocer la astrofísica desde dentro, un sueño realmente cumplido. Jordi, gracias por tus sabios consejos y por la confianza depositada en mí, espero haber estado a la altura. La libertad que me has dado para investigar por mi cuenta, con mis aciertos y mis errores, estando siempre atento por si se descarrilaba la cosa, me ha hecho evolucionar, crecer en mil aspectos. Carmen, gracias por estar siempre dispuesta a echarme una mano con los datos, sin importar el que, el momento o la hora. Tus comentarios siempre positivos, tus ánimos, así como tus consejos sobre la tesis, o sobre la vida, han ayudado a que esté aquí hoy.

En este punto quiero agradecerles a todos y cada uno de los compañeros del grupo sus consejos, sus comentarios y ayuda, todos han aportado su granito de arena para que esta tesis saliese adelante. Si este texto solo tratase de lo profesional, se acabaría aquí, pero va mucho más allá. En lo personal, y pese a la distancia, ha sido fantástico. Las "reuniones" de los viernes a medio día y su posterior adaptación a telecervezas, las reuniones gastro-científico-culturales, ... solo me apena no haber podido disfrutar de más reuniones de esas. En mi memoria están muchos momentos estupendos pero, sin duda, siempre recordaré ese karaoke en La Palma.

Me gustaría agradecer también a los amigos que me han acompañado en esta aventura. A los del grupo de café del IAC, "madrugar" para compartir esos ratos mereció la pena: Alberto, David, Javi, Jorge, Mateo y Salva; esos momentos de charla, risas, debates y quejas sobre cualquier tema imaginable fueron buena parte del combustible necesario para sacar esta tesis adelante. Quiero agradecer también a los de Santiago, aunque no sean de allí: Carlos, Sara, Alberto y María, a pesar de la distancia habéis sido un gran apoyo.

Quero agradecer a toda a miña familia o seu apoio durante esta etapa. A meus abuelos, tíos e primos, aínda que non tivera a paciencia pa explicar repetidas veces o que facía, moitas gracias por facerme saber que podo contar con vós para o que sexa. Mamá, Papá, miles de gracias! sen a vosa paciencia infinita, sen o voso apoio incondicional, sen os vosos consellos, sen o voso sacrificio, sen a vosa compresión e

sen o voso amor, isto non sería posible. Á repunante de Mara, esa irmá que é capaz de poñerme tolo, tirarme do xenio e discutir en cinco minutos, pero facerme rir en moito menos, gracias! Sen ti, a vida sería máis aburrida, máis triste.

Por último, quiero agradecerle desde lo más profundo de mi ser a la persona que más paciencia y tiempo ha gastado conmigo durante estos años. Jenni, muchas gracias por tener toda la paciencia del mundo conmigo y por aguantarme, sé que no te lo he puesto fácil. Gracias por estar ahí siempre, cuando todo iba bien y, sobre todo, cuando todo se torció. Gracias a ti salimos adelante. Gracias por tu cariño, por tu amor, por tu sonrisa, por tu alegría, por tus planes, por tus ideas, por tu locura, ... ¡gracias por TODO!

Mauro González Otero
La Laguna, 17 de mayo de 2024

Acknowledgments

This work has been supported by the project Evolution of Galaxies, of references PRE2018-086047, AYA2017-88007-C3-1-P, AYA2017-88007-C3-2-P, AYA2018-RTI-096188-BI00, PID2019-107408GB-C41, PID2019-106027GB-C41, PID2021-122544NB-C41, and PID2022-136598NB-C33, within the *Programa estatal de fomento de la investigación científica y técnica de excelencia del Plan Estatal de Investigación Científica y Técnica y de Innovación (2013-2016)* of the Spanish Ministry of Science and Innovation/State Agency of Research MCIN/AEI/ 10.13039/5011000-11033 and by 'ERDF A way of making Europe'. Based on observations made with the Gran Telescopio Canarias (GTC), installed in the Spanish Observatorio del Roque de los Muchachos of the Instituto de Astrofísica de Canarias, on the island of La Palma, with the Willian Herschel Telescope (WHT) at Roque de los Muchachos Observatory on the island of La Palma and on observations at Kitt Peak National Observatory, NSF's National Optical-Infrared Astronomy Research Laboratory, which is operated by the Association of Universities for Research in Astronomy (AURA) under a cooperative agreement with the National Science Foundation. This research made use of observations made with GALEX, LBT, Subaru, SLOAN, CFHT, UKIRT, *Spitzer*, *Herschel*, and JCMT telescopes. This research has made use of the NASA/IPAC Extragalactic Database (NED), which is funded by the National Aeronautics and Space Administration and operated by the California Institute of Technology. This work made use of the IAC Supercomputing facilities[1]. This work made use of the Wright (2006) cosmological calculator. Data analysis was performed using IRAF (Tody, 1986), DS9 (Smithsonian Astrophysical Observatory, 2000), TOPCAT (Taylor, 2011), and ALADIN (Bonnarel et al., 2000) software. Data analysis also was performed using Python[2] programming language and the following modules: LMFIT (Newville et al., 2014), pandas (The pandas development Team, 2024), NUMPY (Harris et al., 2020), SciPy (Virtanen et al., 2020), Matplotlib (Hunter, 2007), Seaborn (Waskom et al., 2017), and Astropy (Astropy Collaboration et al., 2013).

[1] https://research.iac.es/sieinvens/SINFIN/Main/supercomputing.php
[2] https://www.python.org

Resumen

Históricamente, los mapas celestes han sido la principal fuente de datos astronómicos, utilizados para explorar y comprender el Universo. Este trabajo está dedicado al estudio de uno de ellos, Lockman–SpReSO, un seguimiento espectroscópico óptico cartográfico de fuentes seleccionadas por su emisión infrarroja, a partir de observaciones previas con el *Telescopio Espacial Herschel*. Las observaciones del cartografiado se llevaron a cabo utilizando el intrumento OSIRIS instalado al Gran Telescopio de Canarias.

En particular, el trabajo de investigación desarrollado en esta tesis se ha centrado en determinar las propiedades ópticas de las galaxias infrarrojas. Para ello se han obtenido medidas como la tasa de formación estelar (SFR, por sus siglas en inglés), la metalicidad del gas, la extinción del polvo interestelar, la masa estelar (M_*) y la luminosidad infrarroja total ($L_{\rm TIR}$). Estas propiedades se han comparado con las obtenidas para muestras de galaxias no seleccionadas por su emisión infrarroja para comprobar posibles similitudes o diferencias entre ambos casos.

Durante esta tesis, se ha llevado a cabo la reducción completa desde cero de los datos de Lockman–SpReSO. Esto supuso un proceso complejo y delicado que requirió múltiples iteraciones y de el diseño de procedimientos específicos, como el realizado para la sustracción de la emisión del cielo en los espectros. A su vez, se elaboró el catálogo al completo del cartografiado, incluyendo toda la información disponible sobre los objetos del proyecto en la bibliografía. La siguiente etapa del proceso consistió en el análisis de los espectros, con el objetivo de detectar y medir las líneas espectrales y determinar el desplazamiento al rojo espectroscópico de los objetos. Además, a partir del desplazamiento al rojo y de todos los datos fotométricos recopilados en el catálogo, se realizaron ajustes a las distribuciones de energía espectral, de los que se derivaron parámetros como la M_* o la $L_{\rm TIR}$.

Posteriormente, se seleccionó una muestra de galaxias con formación estelar (SFGs, por sus siglas en inglés) a partir del los objetos del catálogo de Lockman-SpReSO. Además, se analizaron en detalle las líneas espectrales medidas para corregir la extinción producida por el polvo interestelar y se utilizaron para determinar la SFR

y la metalicidad de las SFG. En este punto, la investigación se centró en el análisis de las relaciones globales mostradas por las SFGs. Por un lado, se estudió la secuencia principal de las SFGs, donde se analizó conjuntamente la M_* y la SFR. Esto mostró que las SFGs del catálogo poblaban la región de galaxias con intensos estallidos de formación estelar. También se estudió la relación entre la M_* y la metalicidad de las galaxias. Esto demostró que la muestra de SFGs seleccionada por la emisión infrarroja tendía a presentar metalicidades más bajas de lo esperado a partir de su M_* y desplazamiento al rojo. Por último, se analizó la relación en el espacio tridimensional formado por la M_*, la SFR y la metalicidad. Se comprobó que las SFG están bien representadas por las calibraciones existentes de esta relación tridimensional, apoyando así la idea de la universalidad de la relación.

Además, la tesis aborda el estudio de los flujos de material observados en una pequeña fracción de los objetos del catálogo. Este material puede ser expulsado de la galaxia por eventos como estallidos de formación estelar, muertes estelares por supernovas o núcleos galácticos activos, o puede ser capturado por la galaxia debido a su potencial gravitatorio. El análisis de las líneas de absorción en el rango ultravioleta, como la líneas de Mg II y Fe II, permite investigar las correlaciones entre la velocidad del viento y la anchura equivalente de las líneas con las propiedades de la galaxia anfitriona, incluyendo la M_*, la SFR y la tasa específica de formación estelar.

Abstract

Historically, celestial maps have been the main source of astronomical data used to explore and understand the Universe. This work is dedicated to the study of one of them, Lockman–SpReSO, an optical spectroscopic follow-up of sources selected for their infrared emission, obtained from previous observations with the *Herschel Space Telescope*. The observations of the survey were carried out with the OSIRIS instrument at the Gran Telescopio de Canarias.

In particular, our research has focused on determining the optical properties of infrared galaxies. This has involved obtaining measurements such as the star formation rate (SFR), the gas metallicity, the interstellar dust extinction, the stellar mass (M_*), and the total infrared luminosity ($L_{\rm TIR}$). These properties have been compared with those shown by samples of galaxies not selected as infrared galaxies to check for possible similarities or differences between the two cases.

In this thesis, the complete reduction of the Lockman–SpReSO data from scratch has been carried out. This involved a complex and delicate process that required multiple iterations and the design of specific procedures, such as the subtraction of the sky emission from the spectra. In addition, the complete catalogue of the survey was elaborated, including all the information available in the bibliography of the objects of the survey. The subsequent stage of the process involved the analysis of the spectra, with the objective of detecting and measuring the spectral lines and determining the spectroscopic redshift of the objects. Furthermore, using the redshift and all the photometric data collated, fits were made to the spectral energy distributions, from which parameters such as the M_* or the $L_{\rm TIR}$ were derived.

Subsequently, a sample of star-forming galaxies (SFGs) was selected from the Lockman-SpReSO catalogue. In addition, the measured spectral lines were analysed in detail to correct for dust extinction and used for the determination of the SFR and metallicity of the SFGs. At this point, the investigation focused on the analysis of the global relations that the SFGs showed. On the one hand, the main sequence of the SFGs was studied, where the M_* and SFR were analysed together. This showed that the SFGs in the catalogue populated the region of galaxies with intense bursts of star

formation. Also, the relationship between the M_* and the metallicity of the galaxies was studied. This showed that the infrared-selected SFGs sample tended to have lower metallicities than expected from their M_* and redshift. Finally, the relationship in the three-dimensional space formed by the M_*, the SFR and the metallicity was analysed. It was found that the SFGs are well represented by the existing calibrations of this three-dimensional relationship, thereby supporting the idea of the universality of the relation.

In addition, the thesis addresses the study of the flux of material observed in a small fraction of the objects in the catalogue. This material may be ejected from the galaxy by events such as burst of star formation, supernova explosions, or active galactic nuclei, or it may be captured by the galaxy due to its gravitational potential. The analysis of absorption lines in the ultraviolet range, such as Mg II and Fe II, allows the investigation of the correlations between wind velocity and equivalent width of the lines with host galaxy properties, including M_*, SFR and the specific star formation rate.

Contents

1

Introduction

"I checked it very thoroughly," said the computer,"and that quite definitely is the answer. I think the problem, to be quite honest with you, is that you've never actually known what the question is."
The Hitchhiker's Guide to the Galaxy - Douglas Adams (1979)

This chapter provides a concise overview of the historical development about extra-galactic astronomy and galaxy surveys, along with a discussion of the analysis of spectral lines to derive galaxy properties. Furthermore, the chapter covers objects with infrared (IR) emission and their properties. Finally, the Lockman-SpReSO project is introduced, and the thesis objectives, motivation, and overview are summarised.

1.1 Introduction to extra-galactic astronomy and surveys

Extra-galactic astrophysics is a captivating field of astronomy that explores the universe beyond our galaxy, the Milky Way. It aims to investigate the properties, formation, and evolution of galaxies in the cosmos. Galaxies are the fundamental building blocks of the universe's large-scale structure, and studying them is crucial to understanding the cosmos. They act as the basic units on the vast cosmic canvas.

During the 17th century, the invention of the telescope was an important step in the knowledge of the universe because it allowed us to surpass the limits imposed by our own eye and reach beyond our own galaxy. A century later, Charles Messier created his emblematic catalogue of celestial objects, in the second half of the 18th century, which is *The Catalogue des Nébuleuses et des Amas d'Étoiles* (Messier, 1781). Approximately one hundred objects constituted the initial and tangible benchmark

for ascension to the systematic exploration of celestial objects and the universe. The Messier's catalogue consisted of deep sky objects in which galaxies can be found, but also star clusters, planetary nebulae, and supernova remnants.

A few decades after, William Herschel and his sister, Caroline Herschel, created a new catalogue, which included thousands of deep sky objects (Herschel, 1786). Their labour laid the first and modest, but the absolute establisher of a more profound knowledge about the deep sky. Son of William Herschel, John Herschel, expanded this catalogue with the addition of several thousand more deep sky objects, which considerably enriched the knowledge about the night sky (Herschel, 1864). This catalogue was used by John Ludwig and Emil Dreyer as a basis for *New General Catalogue* described in Dreyer (1888), and which is still widely used worldwide by astronomers on which galaxies, star clusters, nebulae, and other celestial objects can be found.

Astronomers have been looking at the stars up in the sky for hundreds of years, never having recorded the images of the stars. Though, thanks to the discovery of the photographic plates in the 19th century, astronomers began recording the images of the skies in permanent forms. This made it easier to compare new images with previous ones, detect changes, make long exposures, measure stellar motions, and record transient events such as supernovae, asteroids, and comets. This technology is a significant breakthrough in accurately and permanently documenting the cosmos, transforming the way astronomers study and understand the universe. The plates allow covering greater and larger areas of the sky, which provide more objects to be identified. The *Henry Draper catalogue* made use of the plates for star classification, which Annie Jump Cannon and Edward C. Pickering compiled with the help of the Harvard College observatory telescope. The first publication of the catalogue was in 1890 (Pickering, 1890) and it was expanded from 1918 to 1924 (Cannon and Pickering, 1918, 1924) to finally comprise 225 300 stars and provide their spectrum type and luminosity.

One of the most famous contributions to astronomy was the Edwin Hubble's work at the Mount Wilson Observatory, using the 2.5-metre Hooker telescope to capture photographic plates. The results were compiled in Hubble (1936). By observing Cepheid variable stars in the Andromeda spiral and others nebulae, he was able to calculate distances and prove that this nebulae were actually distant galaxies (Hubble, 1925a,b). These result were of great importance to the astronomical community at the time, as it put an end to the "Great Debate" between Harlow Shapley and Heber Doust Curtis that took place in 1920. In that debate, Shapley was arguing that the spiral nebulae and star clusters observed in the sky were relatively small and part of our own galaxy. This view would have reduced the entire universe to our galaxy. Curtis, however, espoused an opposing viewpoint, contending that the spiral nebulae were, in fact, distant galaxies that were larger than the size proposed by

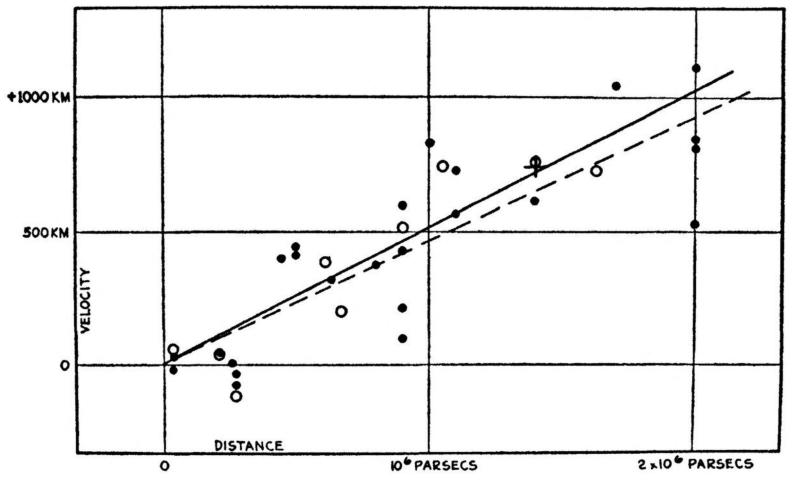

FIGURE 1.1— Diagramn from Hubble (1929) showing the radial velocity of galaxies as a function of their distance, measured from involved stars and mean luminosities of nebulae in a cluster. This constant relationship between the two properties is known as the Hubble-Lemaître law and was the first evidence for the known expansion of the universe.

Shapley. It is also pertinent to note that the initial models of the Universe proposed by Einstein (1917) and de Sitter (1917) were developed without the knowledge of the extra-galactic nature of spiral nebulae and, of course, the accelerated expansion of the Universe. This would subsequently lead Einstein to introduce the well-known cosmological constant (Λ) into the field equations of the General Theory of Relativity (GTR). Few years later, Einstein and de Sitter (1932) published the first expanding cosmological model devoid of a cosmological constant based on the GTR.

The work of Hubble at the Mount Wilson was also significant in detecting the redshift of galaxies, finding a clear relation between the radial velocity and the distance of the galaxies getting an observational probe about the expansion of the Universe (Figure 1.1), previously theoretically predicted by Lemaître (1927) on basis of the GTR and also experimentally using the radial velocities obtained by Stromberg (1925) and the distances obtained by Hubble (1926). Moreover, a morphological classification system for galaxies was developed by Hubble. It remains in use and is commonly referred to as Hubble's tuning fork and it was developed after an exhaustive examination of photographic plates. The great investigation that Hubble done in the astrophysics field revolutionised the understanding of the cosmos at the time.

The *Palomar Observatory Sky Survey I* (POSS-I) was a pioneering astronomical project carried out at the Palomar Observatory in California. First conceived in the 1950s and completed in the 1990s with *Palomar Observatory Sky Survey II* (POSS-II), it used photographic plates to essentially survey the entire visible sky in the northern hemisphere. The main goal of the project was to construct a catalog of

stars, galaxies, nebulae, and other celestial bodies. It mainly used the Samuel Oschin 1.2-metre telescope equipped with a wide-field camera. It obtained approximately 2000 photographic plates in each version of the project.

Digitisation and Charge-Couple Device (CCD) detector are a crucial technical development in observational astronomy. These were introduced in the 1960s. Initially invented for use in photography and television, this semiconductor component soon came to be invaluable in astronomy as it has the property of turning light into electric signals which readily can be processed and stored. They were much more sensitive to the light and also offered a linear response compared to the older technology of photographic plates. With the help of this device, more accurate and detailed images of the fainter objects in the night sky were possible. The mass use of CCDs in observational astronomy opened a new epoch of scientific developments and breakthroughs. The advent of enhanced image processing and data analysis tools made possible the automation of observatories and the completion of large digital databases of astronomical objects. The process is synchronized with the rise in computation power, a significant factor for analyzing the huge amount of data that is being gathered. The *Two-degree Field Galaxy Redshift Survey* (2dFGRS) was a redshift survey conducted using the 3.9-meter Anglo-Australian Telescope between 1997 and 2002 (Colless et al., 2001). The survey observed approximately 250 000 objects, resulting in the first density map of the optical Universe to a depth of approximately $z \sim 0.2$. This map illustrates the large-scale structure of the Universe. Another notable example is the *Sloan Digital Sky Survey* (SDSS), which has become one of the most popular surveys. It developed an all-sky survey with the use of a 2.5-m telescope at the Apache point Observatory in New Mexico(York et al., 2000). The Sloan Digital Sky Survey (SDSS) has been characterized by unmatched amount of astronomical data. With its images of hundreds of millions of galaxies, stars and other celestial objects, it also offers the spectra of millions of these. Moreover, this project was able to obtain three dimensional maps of the distribution of the nearby galaxies in the universe which led to the valuable information about the clustering galaxy evolution of over the cosmic time. The Data Release 18 (Almeida et al., 2023) has been recently released, making it one the most detailed projects in modern astronomy currently.

Around the same time as the aforementioned events, observations in other electromagnetic ranges began to explore the cosmos. Systematic study of the IR range began in the 1950s, using detectors sensitive to IR radiation at Mount Wilson Observatory. These initial efforts uncovered stars and star-forming regions that were not visible in visible light due to cosmic dust opacity. The *Two Micron All-Sky Survey* (2MASS, Skrutskie et al., 2006) is one of the most comprehensive works in the near-IR (NIR) range. It was conducted between 1997 and 2001 with the main objective of mapping the sky using two 1.3-metre telescopes, one located in each hemisphere. The survey produced the most complete catalogue of celestial objects in the NIR, including stars,

galaxies, nebulae, and other objects. It is estimated to have catalogued around 300 million individual sources across the sky, representing a significant advance in understanding the distribution and nature of celestial objects. Radio astronomy emerged by accident in 1932, when Karl Jansky, while investigating interference in radio communications, identified mysterious signals from outer space. His discovery, together with the first radio telescope built by Grote Reber in 1937, laid the foundations for future research in the field. This radio telescope was nine metres long and marked the beginning of the observation of the universe through radio waves. It was not long before interferometry began to be used for astronomical observations. By using two or more radio telescopes, astronomers were able to obtain unprecedented angular resolutions, giving rise to the radio-source object catalogues. An example of these is the numbered series of catalogues that make up the *Cambridge Radio Surveys* (Ryle et al., 1950). The third edition of this catalogue, the *Third Cambridge Catalogue* (3C, Edge et al., 1959), is famous for being the catalogue in which the first quasar, known as 3C273, was identified. In time, large interferometers such as the VLA, NOEMA or ALMA would revolutionise the field of radio astronomy.

Observations of the universe in the more energetic regions of the spectrum, such as ultraviolet (UV), X-rays or gamma rays, which are difficult to analyse from ground-based telescopes, flourished during the Cold War and the Space Race. The chance of mounting instruments on satellites in the near-Earth orbit allows for a broad spectrum of opportunities not only in energetic bands, but also both in optical and IR ones, since the atmosphere contribution is eliminated. The *Infrared Astronomical Satellite* (IRAS) space telescope, dedicated to the IR astronomy, launched in 1983 was the first observatory to map the entire sky for sources of far-IR (FIR) heat sources and found thousands of previously unknown stars, galaxies and solar system objects. The *Hubble Space Telescope* (HST), which was launched in 1990 and is still in operation, is one of the most important devices in the history of the optical and near-UV (NUV) astronomy. It has provided images of unprecedented clarity of the distant universe, allowing astronomers to study star formation, the evolution of galaxies and the structure of the cosmos as a whole. In recent times, more contemporary telescopes, such as *James Webb Space Telescope* (JWST) and *Euclid*, have been placed in orbit at the L2 Lagrange point. Their observations are now reaching us, extending our understanding of the cosmos to unprecedented depths. These observations are set to revolutionise astrophysics in the coming years.

From the brief history of extra-galactic astronomy and the object surveys we have reviewed, it is clear that there is a wide variety of approaches. There are surveys that scan the whole sky in a particular spectral range, such as the SDSS or 2MASS. There are also surveys that focus on small regions of the sky in order to reach greater depths. Two notable examples are the *Hubble Ultra Deep Field* project (Beckwith et al., 2006) and the OTELO project (Bongiovanni et al., 2019). Moreover, the surveys are able

to be conducted from the Earth's surface or from space, and can be photometric or spectroscopic. Some do not involve any selection criteria, while others are carried out to observe particular kinds of objects. Besides, they can cover different wavelengths or not depending on science goals. These extensive studies have helped us to obtain the information about the formation and distribution of galaxies in the Universe. A more profound historical review on the evolution of extra-galactic astronomy along with surveys can be found in Smith (2008, 2009) and Djorgovski et al. (2013), among others.

In order to understand the properties and the evolution of these distant galaxies, the knowledge of the spectra observed is very important. The spectral lines embedded in these spectra are a rich source of knowledge, furnishing the information about the chemical composition, temperature, velocity as well as the other physical parameters of the galaxies.

In the next section, we explore how these spectral lines lead us to the secrets hidden in starlight, and how their meticulous analysis allows us to unravel the mysteries of our vast universe.

1.2 Spectral lines, the cosmic fingerprints

In this section we explore how these spectral lines, like cosmic fingerprints, give us crucial information about the physics, chemical composition and dynamical processes in distant galaxies.

Spectral lines are produced by the atoms and molecules found in galaxies. When a photon is absorbed or emitted by an atom, it occurs at specific frequencies that are determined by the electronic transitions within its structure[1]. This results in each chemical element having its own unique set of spectral lines. By analysing the spectral lines of a galaxy's spectrum, we can deduce fundamental properties of the galaxy (Cepa, 2008). This section discusses the applications of the study of spectral lines that will be useful throughout this thesis.

1.2.1 Galaxy classification

Spectral line ratios are frequently used to classify galaxies, with the BPT diagram (Baldwin et al., 1981) being one of the most popular methods. This diagram utilises the ratio of intense lines generated from different excitation mechanisms, typically [N II] λ6584/Hα against [O III] λ5007/Hβ, to distinguish between star-forming galaxies (SFGs), composite galaxies, and narrow-line active galactic nuclei (AGNs).

The [N II] λ6584 line is a forbidden line that is produced by low-density gas, while the Hα line is produced by ionized hydrogen, which is a sign of ongoing

[1]This work focuses solely on the examination of spectral lines generated by electron transitions.

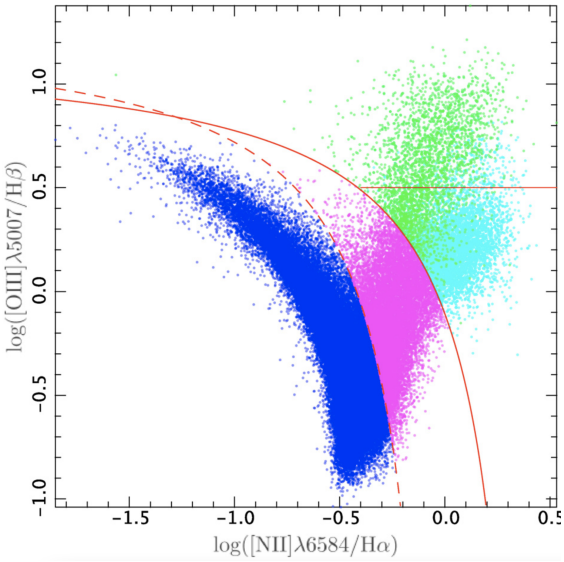

FIGURE 1.2— The BPT diagram from Lamareille (2010). It displays 90,000 objects, with SFGs represented in blue, composite galaxies in magenta, LINERs in cyan, and Seyfert 2 in green. The red lines indicate various criteria for galaxy classification, with the dashed red line representing the criteria of Kauffmann et al. (2003), the red line representing the criteria of Kewley et al. (2001), and the horizontal line representing the criteria of Veilleux and Osterbrock (1987).

star formation. The ratio between these two lines can tell us whether the gas in a galaxy is being ionized by stars or by some other mechanism, such as an AGN. Meanwhile, the ionization parameter, which is a measure of the ionizing flux per unit volume, is higher in AGN-dominated galaxies compared to star-forming galaxies. The [O III] λ5007/Hβ ratio is sensitive to the ionization parameter, and it increases with increasing ionization parameter.

Figure 1.2 displays an example from Lamareille (2010) where they use 90 000 objects from the SDSS survey where the power of spectral lines in object classification and the significance of galaxy surveys in enabling this work through object statistics is highlighted.

Other line ratios have been studied, for example replacing the [N II] λ6584 flux in the BPT diagram by the doublet [S II] $\lambda\lambda$6717, 31 flux. Additionally, the use of bluer line ratios, such as [O II]/Hβ (Lamareille et al., 2004), has been studied because the Hα, [N II], and [S II] lines are out of the optical range at redshifts $z \gtrsim 0.4$. Furthermore, various calibrations have been developed to define the regions occupied by each type of objects in the different versions of the BPT diagram (Veilleux and Osterbrock, 1987; Kewley et al., 2001, 2013; Kauffmann et al., 2003; Lamareille et al., 2004; Lamareille, 2010; Stasińska et al., 2006, among others).

Sometimes multiple spectral lines are not available in the spectra. Therefore,

alternative methods based on the use of only two spectral lines have been developed. Cid Fernandes et al. (2010) postulated the use of the [N II] λ6584/Hα ratio against the Hα equivalent width (EW) at rest-frame to discriminate between SFGs and AGNs.

1.2.2 Attenuation by interstellar dust

Comprehending the spectral line is quite frequently difficult because of the extinction effects attributed to the existence of interstellar dust inside galaxies. The extinction phenomena happen when the light is absorbed and scattered by the dust particles in the interstellar medium, and the reddened light appears in the spectra. The reddening effect could be systematic since it leads to errors in the measured emission lines, thereby the physical properties of a galaxy like start-formation rates (SFRs) and metallicity are not properly determined. Hence, the correction for dust extinction effect is a mandatory task.

To produce the accurate correction of extinction, one of the most useful methods is to study the ratios of the Balmer series lines. The line ratios can be derived theoretically from quantum physics. The values are then compared to the ratios observed at spectral lines to determine how high the extinction is. Therefore, when using the ratio Hα/Hβ, we can parameterise the colour excess $E(B-V)$, which represents the variation of the colour $B-V$ due to extinction, as:

$$E(B-V) = \frac{2.5}{k(\lambda_{\mathrm{H}\beta}) - k(\lambda_{\mathrm{H}\alpha})} \log\left(\frac{(\mathrm{H}\alpha/\mathrm{H}\beta)_{\mathrm{obs}}}{(\mathrm{H}\alpha/\mathrm{H}\beta)_{\mathrm{th}}}\right), \tag{1.1}$$

where $k(\lambda_{\mathrm{H}\beta})$ and $k(\lambda_{\mathrm{H}\alpha})$ are the values of the reddening curve evaluated at Hβ and Hα wavelengths, respectively. In this thesis we have adopted the reddening curve established by Calzetti et al. (2000). $(\mathrm{H}\alpha/\mathrm{H}\beta)_{\mathrm{obs}}$ is the observed Balmer decrement, and $(\mathrm{H}\alpha/\mathrm{H}\beta)_{\mathrm{th}}$ is the quantum-physical value of the Balmer decrement in the case of non-extinction. The standard case adopted in the study of SFGs is the recombination Case B described by Osterbrock (1989), where $(\mathrm{H}\alpha/\mathrm{H}\beta)_{\mathrm{th}} = 2.86$ is defined for an electron temperature $T = 10^4$ K and an electron density $n_e = 10^2$ cm^{-3}. Other ratios of Balmer lines are also used using the same reasoning, for example the Hβ/Hγ ratio, that in the same conditions, the quantum theory predicts a value of $(\mathrm{H}\beta/\mathrm{H}\gamma)_{\mathrm{th}} = 2.13$. These ratio allows to correct objects that are at higher redshifts using optical spectroscopy.

Finally, to correct for dust extinction the flux of the spectral lines, the most common method is to use the empirical relationships established by Calzetti et al. (1994), who established that the intrinsic flux (F_{int}) at a given wavelength (λ) can be obtained as follows

$$F_{\mathrm{int}}(\lambda) = F(\lambda)\, 10^{0.4\,A(\lambda)} = F(\lambda)\, 10^{0.4\,k(\lambda)\,E(B-V)}, \tag{1.2}$$

where $F(\lambda)$ is the observed flux at that wavelength, $A(\lambda)$ is the extinction at that wavelength, $k(\lambda)$ is the reddening curve evaluated at that wavelength.

1.2.3 Chemical abundances and metallicities

The study of spectral emission lines enables us to determine the gas-phase metallicity of the galaxies. Typically, metallicity is calibrated based on the abundance of oxygen relative to hydrogen, expressed as $12 + \log(\mathrm{O/H})$.

The most reliable technique involves calculating the electron temperature (T_e) of the ionised gas from auroral lines such as [O III] λ4363 or [N II] λ5755. However, these lines are challenging to observe due to their weak signal, requiring high signal-to-noise (S/N) ratios for detection.

To overcome this difficulty, methods based on empirical calibrations of the T_e were developed. These calibrations were made by fitting direct measurements of the T_e and ratios of intense lines in the H II regions of galaxies. The commonly used ratios in this context are optical line ratios, such as [N II] λ6584/Hα and ([O II]/Hβ)/([N II]/Hα) as described in Pettini and Pagel (2004). Pilyugin and Grebel (2016) demonstrated the usefulness of more complex relationships with dependencies on multiple lines. They calibrated metallicity by using combinations of line ratios, which allowed them to separate the two branches observed in metallicity. The upper branch is thus defined as $\log(N_2) < -0.6$, where $N_2 =$ [N II] $\lambda\lambda$6548, 84/Hβ. The metallicity equation is:

$$\begin{aligned} 12 + \log(\mathrm{O/H}) = {} & 8.589 + 0.022 \log(R_3/R_2) + 0.399 \log(N_2) \\ & + (-0.137 + 0.164 \log(R_3/R_2) + 0.589 \log(N_2)) \log(R_2)\,. \end{aligned} \quad (1.3)$$

The lower branch definition is $\log(N_2) > -0.6$ and the metallicity equation is:

$$\begin{aligned} 12 + \log(\mathrm{O/H}) = {} & 7.932 + 0.944 \log(R_3/R_2) + 0.695 \log(N_2) \\ & + (0.970 - 0.291 \log(R_3/R_2) + 0.19 \log(N_2)) \log R_2. \end{aligned} \quad (1.4)$$

Where, in both equations, the coefficients are $R_2 =$ [O II] $\lambda\lambda$3727, 29/Hβ and $R_3 =$ [O III] $\lambda\lambda$4959, 5007/Hβ.

On the other hand, some methods rely on theoretical models of photoionisation of H II regions to obtain metallicity measurements from ratios of spectral lines. Obtaining the T_e directly in highly metallic H II regions can be challenging due to the weakness of auroral lines. However, this difficulty is solved by theoretical models because they do not require measurements of the T_e, unlike models based on empirical calibrations. For instance, Tremonti et al. (2004) developed models that combined SSPs models from Bruzual and Charlot (2003) with photoionisation models from CLOUDY (Ferland et al., 1998). The metallicity parameterisation was based on the R_{23} calibrator, where

$R_{23} = ([\mathrm{O\,II}]\,\lambda\lambda 3727, 29 + [\mathrm{O\,III}]\,\lambda\lambda 4959, 5007)\,/\mathrm{H}\beta$, which is calculated using the following equation:

$$12 + \log(\mathrm{O/H}) = 9.185 - 0.313\,x - 0.264\,x^2 - 0.321\,x^3 \tag{1.5}$$

where $x = \log(R_{23})$ and is valid only for the upper branch of the double-valued R_{23}-abundance relation. Kobulnicky and Kewley (2004) also used the R_{23} calibrator and developed an iterative method to recursively determine the ionisation parameter and metallicity. Dopita et al. (2016) obtained a metallicity calibration using redder lines in the optical spectra [N II] λ5684, Hα and the [S II] $\lambda\lambda$6717, 31 doublet, also based on theoretical models of photoionisation. The use of lines with similar wavelengths in this calibration obviates the need for extinction correction. For more information on metallicity and its calibrators, please refer to the work of Kewley and Ellison (2008).

1.2.4 Star formation rate determinations

Another important property of galaxies that can be inferred from emission lines is the star formation rate (SFR). The most common method is to assume that the flux of the spectral lines (and also flux in photometric bands) is produced directly by high-mass stars.

The Hα line is commonly used to trace the SFR. Different calibrations exist to derive the SFR from this spectral line, with the most widely used being the one developed by Kennicutt (1983, 1998), Kennicutt et al. (1994), and Kennicutt and Evans (2012). This line is intense in the optical range and enables the analysis of time scales up to 10 Myrs (Kennicutt and Evans, 2012) and it is insensitive to the gas metallicity. However, for objects at redshift $z > 0.5$, the line is redshifted out of the optical range.

The Balmer series offers alternative orders that can be used with the same calibrations, assuming Case B of recombination from Osterbrock (1989). However, these lines are weaker and more susceptible to extinction and underlying stellar absorption. Other spectral lines, such as [O II] $\lambda\lambda$3726, 29 or [O III] λ5007, have also been calibrated for determining the SFR with acceptable results (Figueira et al., 2022). However, these lines are subject to extinction, particularly the [O II] line, and are also strongly dependent on the metallicity of the gas and the ionisation parameter.

As we have seen, SFR calibrations use various tracers, including photometric bands in the UV range and total IR luminosity (L_{TIR}). The former directly analyses the continuum emitted by high-mass stars, while the latter indirectly traces their emission by absorbing their UV emission and re-emitting it in the IR range. These tracers analyse longer timescales up to 100 or 200 Myr (Kennicutt and Evans, 2012). Table 1.1 shows the SFR calibrations for different tracers obtained from the works of Kennicutt and Evans (2012) and Figueira et al. (2022).

TABLE 1.1— SFR calibrations using spectral lines and photometric bands. Adapted from Kennicutt and Evans (2012) and Figueira et al. (2022).

$$\log[\mathrm{SFR}_{\mathrm{band}}(M_\odot\ \mathrm{yr}^{-1})] = A \times \log\,[L_{\mathrm{band}}(\mathrm{units})] - \log C_{\mathrm{band}}$$

Band	Age Range (Myr)	L_{band} units	A	$\log C_{\mathrm{band}}$
FUV[a]	0-10-100	erg s^{-1}	1	43.35
NUV[a]	0-10-200	erg s^{-1}	1	43.17
[O II] λ3727[b]	0-10	erg s^{-1}	0.96	39.69
Hβ[b]	0-3-10	erg s^{-1}	0.94	38.34
[O III] λ5007[b]	0-10	erg s^{-1}	0.89	35.94
Hα[a]	0-3-10	erg s^{-1}	1	41.27
24 μm[a]	0-5-100	erg s^{-1}	1	42.69
L_{TIR}[a]	0-5-100	erg s^{-1}	1	43.41
1.4 GHz[a]	0-100	erg s^{-1} Hz^{-1}	1	28.20

[a] Calibrations obtained from Kennicutt and Evans (2012).
[b] Calibrations obtained from Figueira et al. (2022).

1.3 Global relations of the properties of galaxies and its evolution

The analysis of parameters obtained from the study of spectral lines in galaxies spectrum, such as $E(B-V)$, SFRs, and metallicities, provides valuable information about their chemical composition and evolution. Therefore, these parameters are crucial for understanding astrophysical processes. Exploring the correlation of these properties with stellar mass (M_*) can reveal underlying mechanisms in galactic evolution, enriching our cosmic understanding. Therefore, this section describes some of these correlations and shows the important role they play in the study of galaxy evolution.

1.3.1 Mass–SFR relation

There is a well-established correlation between the M_* of galaxies and their SFR, named as main sequence (MS) of SFG. This correlation is positive, meaning that galaxies with higher M_* also have higher SFR. This relationship was first identified by Gavazzi and Scodeggio (1996) in a sample of $\sim 10^3$ galaxies and later confirmed by Brinchmann et al. (2004) in a much larger sample of $\sim 10^5$ galaxies from the SDSS.

Moreover, this relation evolves with redshfit. For the same M_*, the more distant a galaxy is the higher the SFR it shows, or, in other words, galaxies at higher redshfit form stars at a higher rate. In the recent paper by Popesso et al. (2023), they make an exhaustive study compiling information from a total of 28 previous papers between

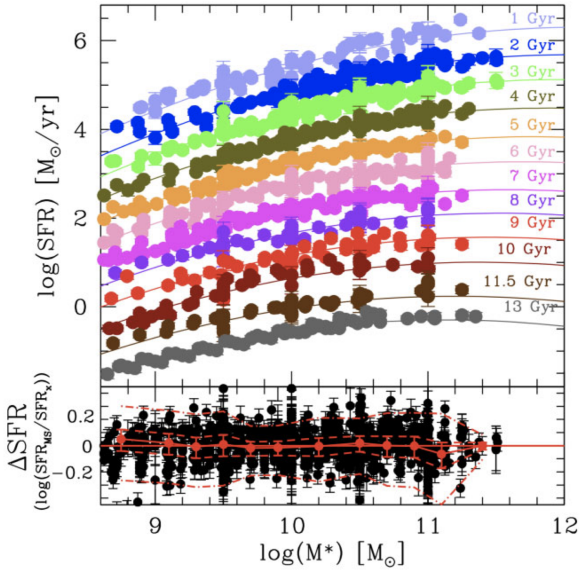

FIGURE 1.3— From the paper of Popesso et al. (2023). The upper panel displays the MS derived by Popesso et al. (2023), represented by continuous lines, applied to different cosmic time ranges, represented by different colours. For clarity in the plot, each MS was shifted 0.4 dex from each other. The lower panel shows the residuals obtained from these fits.

2014 and 2022, including the paper by Speagle et al. (2014) which is also a compilation of 65 papers between 2007 and 2014 (see table 1 from Popesso et al. (2023) and table 4 from Speagle et al. (2014)).

Popesso et al. (2023) obtains a relation for the MS that covers a wide range of masses ($10^{8.5}$ to $10^{11.5}$ $M_\odot$) and redshifts ($0 < z < 6$), whose mathematical expression is:

$$\log \mathrm{SFR}\,(M_*, t) = a_0 + a_1 t - \log\left(1 + \left(M_*/10^{a_2+a_3 t}\right)^{-a_4}\right) \tag{1.6}$$

where t is the cosmic time elapsed from the Big Bang in yr, M_* is the stellar mass in solar masses, $a_0 = 2.693$, $a_1 = -0.186\,\mathrm{yr}^{-1}$, $a_2 = 10.85$, $a_3 = -0.0729\,\mathrm{yr}^{-1}$, and $a_4 = 0.99$. Figure 1.3 displays the Popesso et al. (2023) result, demonstrating the fit of its expression for various redshift ranges. The lower panel shows the obtained residuals.

1.3.2 Mass–metallicity relation

The analysis of gas-phase metallicity revealed a direct correlation with the M_* of galaxies, known as the mass–metallicity relation (MZR). This relation has been extensively studied in the literature (Lequeux et al., 1979; Garnett, 2002; Tremonti et al., 2004; Pilyugin et al., 2004; Lee et al., 2006; Zahid et al., 2014; Sanders et al.,

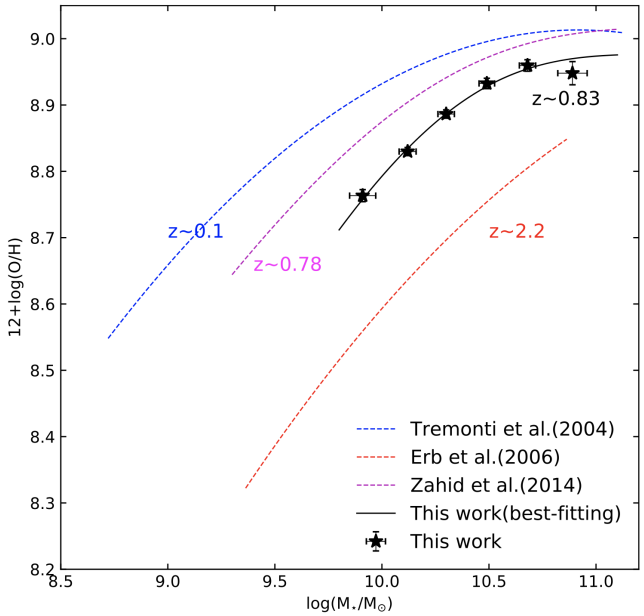

FIGURE 1.4— From the paper of Huang et al. (2019). The clear evolution of the MZR can be observed when analysing samples of objects at different redshifts. It is observed that the lower redshift samples show higher metallicities than the higher redshift samples, for a fixed M_*.

2021, among many others). It is observed that more massive galaxies have higher metallicities than less massive galaxies, i.e. galaxies with higher M_* have a more metallic interstellar medium (ISM) than galaxies with lower M_*. The MZR is not a simple one-to-one correspondence, it is influenced by the balance between the inflow of pristine gas, which is a gas without or with a minimal portion of heavier elements than helium, from the intergalactic medium (IGM) and the outflow of enriched gas from the galaxy due to supernova explosions, star formation burst and AGN feedback (Matsuoka et al., 2009, 2018; Thomas et al., 2019; Hamel-Bravo et al., 2024; Ibrahim and Kobayashi, 2024, among others). Other factors like the IR emission or the downsizing could also play a role in the MZR (for example Spitoni et al., 2020).

The MZR relation has been successfully confirmed up to redshift $z \sim 3$ (Sanders et al., 2021), but new findings with the JWST have extended the range of validity up to redshift $z \sim 10$ (Curti et al., 2024). Furthermore, it has been demonstrated that the MZR evolves with redshift (for example Huang et al., 2019; Sanders et al., 2021; Pistis et al., 2022), such that for a fixed M_*, galaxies at higher redshift exhibit lower metallicities than those at lower redshift. This evolution may be attributed to the higher gas fractions and SFR observed in high-redshift galaxies, as well as the higher rate of poorly processed gas to the ISM.

Figure 1.4, from the research of Huang et al. (2019), illustrates the evolution of

the MZR with redshift by analysing samples of objects situated at varying distances.

1.3.3 Mass–metallicity–SFR relation

The Mass–metallicity–SFR relation represents an extension of the MZR, in which the SFR is taken into consideration. Although the MZR and the MS have been known for a long time, the relation between these three properties has recently been discovered. The first evidence for this correlation was obtained by Ellison et al. (2008), where they observed a slight correlation between metallicity and specific star formation rate (sSFR).

Subsequently, and practically simultaneously, two independent papers, Lara-López et al. (2010) and Mannucci et al. (2010), discovered and described the relationship between M_*, SFR and metallicity. In the study by Lara-López et al. (2010), using a complete magnitude-limited SFG sample from the SDSS-DR7 catalogue, they fitted a plane to the space formed by M_*, SFR and metallicity. The scatter of 0.16 dex in their fit indicated a clear correlation between the parameters, which they named as the Fundamental Plane (FP). Using M_* as the dependent variable, their parameterisation provides a powerful way to derive the M_* of galaxies from the SFR and metallicity. Furthermore, using samples of objects at redshift $z \sim 3$, they found that the FP is universal, i.e. it does not evolve with redshift at least in the studied range.

Concurrently, Mannucci et al. (2010) also employed a sample of SDSS-DR7 to demonstrate that SFGs represent a surface in three-dimensional space generated by M_*, SFR and metallicity. They designated this relationship the Fundamental Metallicity Relation (FMR), for which they obtained a scatter of 0.05 dex and in which the independent parameter is the metallicity.

The results of the FP and FMR analysis indicate a robust relationship in the SFGs for their M_*, SFR and metallicity. Furthermore, the non-evolution of this relation with redshift up to z 3 has been confirmed by several independent works (see for example Cresci et al., 2019; Sanders et al., 2021). However, recent results obtained by Curti et al. (2024) analysing galaxies up to $z \sim 10$ with JWST show that their objects do not follow the FMR, reopening the debate on the universality of the relation between M_*, SFR and metallicity.

1.4 The Lockman–SpReSO project

The Lockman Spectroscopic Redshift Survey using OSIRIS (Lockman–SpReSO) project is an optical spectroscopic follow-up of a sample of mainly FIR-selected objects in the Lockman Hole (LH) field. The LH field is notable for its low hydrogen column density ($N_{\rm H} = 5.8 \times 10^{19}\,{\rm cm}^{-2}$, Lockman et al., 1986), which is lower than

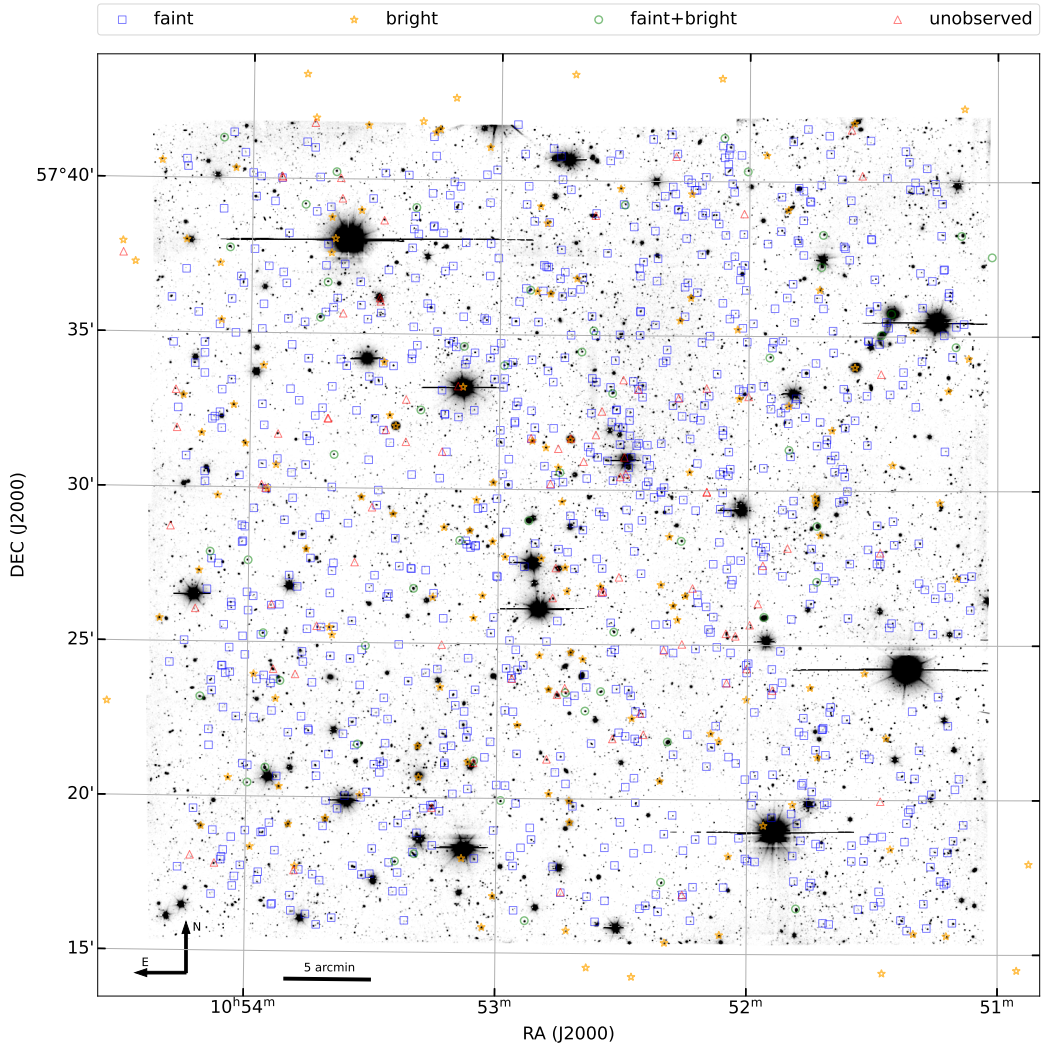

FIGURE 1.5— From Gonzalez-Otero et al. (2023). The image depicts the central region of the LH deep field (24×24 arcmin^2) on which objects from the Lockman–SpReSO catalogue have been highlighted. The blue square indicates the objects observed with OSIRIS/GTC (the faint sample, $R_C > 20$ mag), the yellow stars indicate the objects observed with AF2-WYFFOS/WHT and HYDRA/WIYN (the bright sample,$R_C \leq 20.6$ mag), the green circles indicate the objects observed in both cases, and the red triangles indicate the unobserved objects in the catalogue.

that observed in the Galactic poles ($N_{\rm H} \sim 10^{20}\,{\rm cm}^{-2}$, Dickey and Lockman, 1990).

This characteristic makes the LH field a suitable region for study across the entire electromagnetic spectrum, with observations in the most energetic ranges made possible by telescopes such as *XMM-Newton* and *ROSAT*. The *GALEX* telescope also observed the LH field in its two UV bands. In the optical range, the LH field was observed by multiple telescopes, including the Sloan telescope, the Large Binocular Telescope (LBT), the Subaru telescope and the United Kingdom Infrared Telescope (UKIRT). The IR regime was studied by the *Spitzer* and *Herschel* space telescopes. Even at longer wavelengths, the LH was observed by the Low-Frequency Array (LOFAR) and Very Large Array (VLA) observatories.

As mentioned above, there are numerous studies of the LH field that have been carried out over a range of areas and depths, allowing the creation of a large multi-wavelength database of information and properties of the objects in the field (Fotopoulou et al., 2012; Kondapally et al., 2021). However, few have focused on the deep spectroscopy of the LH field. Prior to the release of the SDSS data, only ~ 600 high-quality spectroscopic redshifts had been recorded for the entire LH field, which covers an area of $\sim 15\,{\rm deg}^2$. The comprehensive SDSS mapping has greatly increased the spectroscopic information, although not to a very deep level ($i \sim 22$ mag), leaving a lack of spectroscopy for faint objects, especially in the central $24\times24\,{\rm arcmin}^2$ region of the field, where the deepest observations of *XMM-Newton*, *Spitzer*, and *Herschel* are available. Covering this lack of spectroscopic information is one of the main objectives of the Lockman–SpReSO project: to study spectroscopically a remarkable sample of objects located in the central region of the LH field with equatorial coordinates (J2000) $10^{\rm h}\,52^{\rm m}\,43^{\rm s}$ $+57^\circ\,28'\,48''$ (Fig. 1.5). A more detailed examination of this topic is presented in Chapter 2.

In the selection of the objects to be observed within the Lockman-SpReSO project, preference was given to those that exhibited the greatest depth of observation of the LH field. The most comprehensive study was conducted with *Herschel*, so the majority of the sample ($> 80\%$) was drawn from the guaranteed-time *Herschel*/PACS Evolutionary Probe (PEP) programme (Lutz et al., 2011) with a robust optical counterpart in the Cousins $R_{\rm C}$ band down to a magnitude $R_{\rm C} = 24.5$. The PEP programme observed the central region of the LH field with a depth of 6 mJy at 5σ at 100 and 160 μm. This characteristic selection leads to another major objective of the Lockman–SpReSO project: the study of the optical properties of a statistically significant sample of galaxies selected for their emission in the IR range. This study is described in detail in the Chapter 3.

In order to provide a more comprehensive scientific foundation for the Lockman-SpReSO project, a number of additional objects were incorporated. These include point X-ray sources candidate cataclysmic stars, high-velocity halo stars, radio sources, very red QSOs, and sub-millimetre galaxies. Table 1.2 provides a detailed

TABLE 1.2— Adapted from Gonzalez-Otero et al. (2023). Summary of the classes of objects that comprise the Lockman–SpReSO catalogue. It should be noted that there are redundancies between the different classes.

Object Class	Count
FIR sources	956
High-Velocity Halo Stars	94
Radio Sources	24
Very red QSOs Candidates	70
Sub-millimetre Galaxies	16
X-ray Point Sources and Cataclysmic Stars Candidates	58

overview of the number of objects that are part of the Lockman–SpReSO catalogue. The construction of the catalogue is discussed in detail in Chapter 2.

The majority of the Lockman–SpReSO observations were conducted with the OSIRIS (Cepa et al., 2000) instrument at the Gran Telescopio de Canarias (GTC) telescope using the multi-object spectroscopy (MOS) mode. The observations were designed in such a way that all objects were observed across the entire optical range. To achieve this, each object was observed with at least two grisms. One grism was dedicated to the blue region of the spectrum (R500B, 3600–7200 Å), with a nominal dispersion of 3.54 Å pixel^{-1}. For the red part of the spectrum, two grisms were used: R500R and R1000R, both covering the range 5000–10000 Å and a dispersion of 2.62 Å pixel^{-1}. From the OSIRIS observations, the brightest Lockman-SpReSO objects in the catalogue ($R_C \leq 20$ mag) were omitted, thus observing only the faintest objects (faint sample). The brightest objects in the catalogue (bright sample) were observed with two medium-resolution multi-fiber spectrographs: AF2-WYFFOS (R300B and R600R, 3800–7000 Å) at the William Herschel Telescope (WHT) with a dispersion $\sim$ 4 Å pixel^{-1} and HYDRA (316@7, 4400–9600 Å) with a dispersion $\sim$ 3 Å pixel^{-1} at Wisconsin, Indiana, Yale, and National optical astronomy observatory (WIYN) telescope. The detailed description of the observing strategy is given in Chapter 2.

In conclusion, the Lockman–SpReSO project was designed to study spectroscopically a remarkable sample of objects selected for their IR emission. The spectroscopic redshift assessment and property measurements such as M_*, SFR, or metallicity are important when it comes to researching the global relations such as MS, MZR, and FP or FMR of the IR objects and to the comparison of the results with those obtained from the literature for otherwise selected objects.

1.5 Aims and outline of the thesis

The aim of this thesis is to exploit the data from the Lockman–SpReSO project in order to study the optical properties of IR selected galaxies in the LH field. In order to achieve this, we list and comment on the main points set for this thesis.

- To perform the complete data reduction of the survey observations by applying the corresponding calibrations and corrections: BIAS, dark, wavelength, and flux calibration.
- To carry out a study on the possibilities for the subtraction of the sky emission in the observations and to apply it.
- To compile a database with all available information on the survey objects in the literature to create a catalogue as comprehensive as possible.
- To inspect the obtained spectra to create a quality index and to determine the spectral lines present and, from them, the spectroscopic redshifts of the objects.
- To carry out a spectral energy distributions (SED) fitting process using the available photometric information and the spectroscopic redshift determined in the previous point, in order to determine properties of the galaxies such as the M_* or the $L_{\rm TIR}$.
- To measure the spectral lines present in the spectra in order to derive properties such as E(B-V) and to correct the observed flux for dust extinction. This also enable SFR and metallicity to be determined.
- To classify the galaxies in the catalogue into SFGs and AGNs using different criteria, both photometric and spectroscopic, using all the available information.
- To study the global relations (MS, MZR, and FP) of the Lockman-SpReSO SFGs and compare the results with those found in the literature for objects not selected for their infrared emission.
- To study the correlations between the EW and velocity of the galactic flows with the host galaxy properties for the sample of Lockman-SpReSO objects with galactic flows.

The thesis is organised as follows. Chapter 2 provides a comprehensive description of the Lockman-SpReSO project. This includes a discussion of the sample selection, observing strategies, data reduction, redshift determination, spectral line measurement, and SED adjustment processes.

In Chapter 3, we present the criteria employed for the classification of the objects into SFGs and AGNs, the extinction correction process of the spectral lines, the determination of the SFR and the different tracers used, the determination of the metallicity and the calibrations used, the study of the MS of the SFGs, the study of the MZR, and the universality of the FP.

In Chapter 4, we present a description of the sample of galaxies that present galactic flows within the project. We then proceed to describe the process of determining the velocity of the flows and the EW of the lines. Finally, we study the correlation between these parameters and galaxy properties such as M*, SFR and sSFR.

Finally, in Chapter 5, we present a summary of the main conclusions of the thesis.

The thesis consists of a compendium of three published articles. Table 1.3 includes all the relevant information on the published articles.

As part of the research group responsible for the thesis, we were afforded the opportunity to collaborate directly with the OSIRIS Tunable Emission Line Object Survey (OTELO) project and the GaLAxy Cluster Evolution Survey (GLACE) project. As part of these collaborations, we have participated as co-authors in the list of works reflected in Table 1.4.

TABLE 1.3— Information of the articles that comprise the compendium of this thesis.

Reference	Status	Journal	Volume	Number	Title	Chapter
Gonzalez-Otero et al. 2023	Published	*A&A*	669	A85	Description, target selection, observations, and catalogue preparation	2
González-Otero et al. 2024a	Accepted	*A&A*	–	–	Main properties of infrared selected star-forming galaxies	3
González-Otero et al. 2024b	Published	*A&A*	684	A31	Galactic flows in a sample of far-infrared galaxies	4

TABLE 1.4— List and information on co-authored articles.

Reference	Status	Journal	Topic	Project
de Diego et al. 2020	Published	*A&A*	Galaxy classification: deep learning	OTELO
Cedrés et al. 2021	Published	*ApJ*	The Star Formation Rate Evolution of Low-mass Galaxies	OTELO
Pilyugin et al. 2021	Published	*A&A*	MaNGA galaxies with off-centered spots of enhanced gas velocity dispersion	Other
Navarro Martínez et al. 2021	Published	*A&A*	Low-luminosity active star-forming galaxies at $z \sim 0.9$	OTELO
de Diego et al. 2021	Published	*A&A*	Nonsequential neural network for galaxy classification and photometric redshifts	OTELO
Cedrés et al. 2024	Accepted	*A&A*	The mass–metallicity relationship and the effect of the environment	GLACE
de Diego et al.	In prep.	*A&A*	Galaxy morphology with spectral data and unsupervised techniques	Other
Cedrés et al.	In prep.	*A&A*	The SFR, sSFR and M_* functions of low-mass galaxies at $0.38 < z < 1.43$	OTELO

2

The Lockman–SpReSO project. Description, target selection, observations, and catalogue preparation

This chapter provides a detailed account of the characteristics of the Lockman–SpReSO project. The survey is designed to conduct a spectroscopic follow-up in the optical range of a sample of objects selected for their FIR emission in the LH field. The spectroscopic study anables the analysis of properties derived from spectral lines in the optical range, including extinction, SFR, and metallicity.

This paper describes in detail the whole process for the elaboration of the final catalogue of objects. The project selected 956 Herschel FIR sources and 188 other interesting objects in the field for the optical spectroscopic follow-up. In addition, the techniques and strategies used for the observations, for which the OSIRIS spectrograph at the GTC telescope has been used, are discussed. However, for a small fraction of objects, the brightest ones, the spectrographs AF2-WYFFOS at the WHT and HYDRA at the WIYN telescopes were used. The data reduction and corresponding calibrations are detailed in this chapter.

Consequently, the spectroscopic redshift was determined for a total of 456 objects through the analysis of their spectral lines, with a redshift range of $0.03 < z < 4.97$. Additionally, the study conducted SED fits to estimate M_* and $L_{\rm TIR}$. The results indicated that the M_* of the galaxies in the sample is within the range of $7.65 < \log(M_*/M_\odot) < 12.07$, while the $L_{\rm TIR}$ is within the range of $8.12 < \log(L_{\rm TIR}/L_\odot) <$

13.06. We found that 55% of the objects are in the LIRG regime, 6% are ULIRGs, and 1% are HLIRGs.

The contents of this chapter have been published as Gonzalez-Otero et al. (2023).

A&A 669, A85 (2023)
https://doi.org/10.1051/0004-6361/202244480

Astronomy & Astrophysics

The Lockman-SpReSO project

Description, target selection, observations, and catalogue preparation

Mauro Gonzalez-Otero[1,2], Carmen P. Padilla-Torres[1,2,3,4], Jordi Cepa[1,2,4], José de Jesús González[5], Ángel Bongiovanni[4,6], Ana María Pérez García[4,7], José Ignacio González-Serrano[4,8], Emilio Alfaro[9], Vladimir Avila-Reese[5], Erika Benítez[5], Luc Binette[5], Miguel Cerviño[7], Irene Cruz-González[8], José A. de Diego[8], Jesús Gallego[10], Héctor Hernández-Toledo[5], Yair Krongold[5], Maritza A. Lara-López[10], Jakub Nadolny[11], Ricardo Pérez-Martínez[4,12], Mirjana Pović[13,9,14], Miguel Sánchez-Portal[4,6], Bernabé Cedrés[4], Deborah Dultzin[5], Elena Jiménez-Bailón[5], Rocío Navarro Martínez[4], Castalia Alenka Negrete[5], Irene Pintos-Castro[15], and Octavio Valenzuela[5]

(Affiliations can be found after the references)

Received 12 July 2022 / Accepted 19 October 2022

ABSTRACT

Context. Extragalactic surveys are a key tool for better understanding the evolution of galaxies. Both deep and wide-field surveys serve to provide a clearer emerging picture of the physical processes that take place in and around galaxies, and to identify which of these processes are the most important in shaping the properties of galaxies.

Aims. The Lockman Spectroscopic Redshift Survey using Osiris (Lockman-SpReSO) aims to provide one of the most complete optical spectroscopic follow-ups of the far-infrared (FIR) sources detected by the *Herschel* Space Observatory in the Lockman Hole (LH) field. The optical spectroscopic study of the FIR-selected galaxies supplies valuable information about the relation between fundamental FIR and optical parameters, including extinction, star formation rate, and gas metallicity. In this article, we introduce and provide an in-depth description of the Lockman-SpReSO project and of its early results.

Methods. We selected FIR sources from *Herschel* observations of the central 24 arcmin ×24 arcmin of the LH field with an optical counterpart up to 24.5 R_C(AB). The sample comprises 956 *Herschel* FIR sources, plus 188 additional interesting objects in the field. These are point X-ray sources, cataclysmic variable star candidates, high-velocity halo star candidates, radio sources, very red quasi-stellar objects, and optical counterparts of sub-millimetre galaxies. The faint component of the catalogue (R_C(AB) ≥ 20) was observed using the OSIRIS instrument on the 10.4 m Gran Telescopio Canarias in multi-object spectroscopy (MOS) mode. The bright component was observed using two multi-fibre spectrographs: the AF2-WYFFOS at the *William Herschel* Telescope and the HYDRA instrument at the WYIN telescope.

Results. From an input catalogue of 1144 sources, we measured a secure spectroscopic redshift in the range $0.03 \lesssim z \lesssim 4.96$ for 357 sources with at least two identified spectral lines. In addition, for 99 sources that show only one emission or absorption line, a spectroscopic redshift was postulated based on the line and object properties, and photometric redshift. In both cases, properties of emission and absorption lines were measured. Furthermore, to characterize the sample in more depth with determined spectroscopic redshifts, spectral energy distribution (SED) fits were performed using the CIGALE software. The IR luminosity and the stellar mass estimations for the sample are also presented as a preliminary description.

Key words. surveys – galaxies: statistics – galaxies: fundamental parameters – techniques: imaging spectroscopy

1. Introduction

A fundamental contribution to our understanding of galaxy formation and evolution is the availability of samples of objects as large and as deep as possible. These censuses, or surveys, may be broadly classified as either photometric or spectroscopic.

Photometric surveys observe an area of the sky by integrating a range of wavelengths, commonly referred as photometric bands, pass-bands, or filters. It is common practice to perform observations of the same field in several filters, thus making the spectral coverage as complete as possible. We can differentiate several types of photometric surveys according to the wavelength range integrated during the observations or the resolving power ($R \equiv \lambda/\delta\lambda$, $\delta\lambda$ being the full width at half maximum (FWHM) of the filter's transmission curve) of the used filters. Thus, broad-band surveys have the lowest resolution power ($R \sim 5$); the Sloan Digital Sky Survey (SDSS; York et al. 2000) and the Dark Energy Spectroscopic Instrument (DESI) Legacy Imaging Surveys (Dey et al. 2019) are some examples. In the case of intermediate-band surveys, the power resolution usually ranges between 20 and 40; examples of such surveys are the ALHAMBRA (Moles et al. 2008) and the COMBO-17 (Wolf et al. 2003) surveys. Narrow-band surveys have the highest resolving power ($R \geq 60$); the PAUS survey (Eriksen et al. 2019), the J-PAS survey (Benitez et al. 2014), and the OTELO survey (Bongiovanni et al. 2019), using 40, 54, and 36 narrow-band filters, respectively, are examples.

This photometric information allows us to construct the spectral energy distribution (SED) and fit it using empirical or theoretical spectral templates. A good coverage of photometric information using different filters over a wide spectral range is crucial for obtaining the best possible fits and to accurately determine the physical properties of objects (e.g. stellar mass and IR luminosity), together with their photometric redshift (z_{phot}).

On the other hand, for each object, spectroscopic surveys yield the spectrum over a wavelength range determined by the instrumental configuration. These spectroscopic surveys generally have brighter flux limits, determined by the achievable resolution. Nevertheless, the multi-object spectroscopy (MOS) mode used in spectroscopic surveys has improved the efficiency of these studies, making it possible to obtain the spectra of tens, hundreds (e.g. the Near-Infrared Spectrograph on the *James Webb* Space Telescope; Ferruit et al. 2022), or thousands (e.g. the DESI spectroscopic study; Abareshi et al. 2022) of objects simultaneously. Spectroscopic surveys allow us to obtain more reliable and more accurate spectroscopic redshifts ($z_{\rm spec}$) thanks to the possibility of very precise measurements of spectral lines in absorption and emission, both intense and weak, which in turn allow us to determine physical properties of the objects (e.g. stellar ages, star formation rate (SFR), extinction, ionization, and gas metallicity).

Numerous spectroscopic surveys of vast numbers of objects have scanned huge areas of the sky; for example, SDSS/BOSS (Dawson et al. 2013) has scanned ∼10 000 deg^2 in the *i*-band down to 19.9 mag. Other surveys have analysed smaller areas, but in greater depth. For example, the z-COSMOS survey (Lilly et al. 2007) conducted studies of the COSMOS field for a total of 30 000 objects in the redshift range zero to three. The VANDELS ESO public spectroscopic survey (McLure et al. 2018) performed a spectroscopic study of sources in the central part of the CANDELS Ultra Deep Survey and the *Chandra* Deep Field South with a redshift range between one and seven.

Surveys that analyse small areas of the sky in great depth generally tend to do so in sky regions of high Galactic latitude with plenty of broad-band multi-wavelength data. One of these areas that is of great interest is known as the Lockman Hole (hereafter LH) extragalactic field. The LH field is a galactic area with a minimal amount of neutral hydrogen column density ($N_{\rm H}$) on the sky (Lockman et al. 1986). This quality makes it one of the best Galactic windows for detecting distant and nearby weak sources, and a perfect target for developing high-sensitivity surveys. The central part of the LH field has a hydrogen column density value of $N_{\rm H} = 5.8 \times 10^{19}$cm^{-2} (Lockman et al. 1986; Dickey & Lockman 1990). This value is moderately lower than that found at the Galactic poles, where $N_{\rm H} \sim 10^{20}$cm^{-2} (Dickey & Lockman 1990). Lower latitudes are unsuitable for this kind of study, given their high extinction.

Because of this exceptional quality, the LH field is of great interest to the scientific community and has been observed over virtually the entire range of the electromagnetic spectrum. In high-energy regimes, missions such as *Chandra*, *XMM-Newton* and ROSAT have targeted the field in a quest for deep data per unit observed solid angle. Furthermore, the GALEX telescope observed the LH in its two UV photometric bands. Sloan, the Large Binocular Telescope (LBT), Subaru, and UKIRT are examples of telescopes that have observed the LH field at optical wavelengths. In addition, the low-IR background of the LH field (0.38 mJy sr^{-1} at 100 µm, Lonsdale et al. 2003) has prompted deep IR observations such as those carried out with the *Spitzer* and *Herschel* space telescopes. However, despite the wealth of existing data and even though the LH field has been observed from the X-ray to the radio region, there is a surprising lack of deep optical spectroscopic data, which presents an unresolved challenge.

The Lockman Spectroscopic Redshift Survey using OSIRIS (Lockman-SpReSO) aims to address the shortage of spectroscopic information on the LH field by performing a deep spectroscopic follow-up, up to magnitude $R_{\rm C} = 24.5$, in the optical and near-IR (NIR) ranges, of a sample of galaxies selected from far-IR (FIR) source catalogues. This survey not only determines the spectroscopic redshifts but also estimates the principal properties of the selected galaxies. To this aim, we took advantage of the large collecting surface of the 10 m class Gran Telescopio de Canarias (GTC) telescope and the excellent performance of the MOS mode of the OSIRIS instrument.

This is the first paper of a series that aims to present the Lockman-SpReSO project and it is structured as follows. In Sect. 2, we outline the main features and scientific motivations of the survey. In Sect. 3, we detail the target selection and the development of the source catalogue. In Sect. 4, we describe the planning of the observations and their main properties for the elaboration of the survey. In Sect. 5, we explain how the data reduction was carried out. In Sect. 6, we describe the first results of the spectral line measurements, the determination of the spectroscopic redshift, and the SED-fitting procedure. In Sect. 7, we summarize the main content of the paper and establish a timeline for the next data release of the survey. Throughout the paper, magnitudes in the AB system (Oke & Gunn 1983) are used. The cosmological parameters adopted in this work are: $\Omega_{\rm M} = 0.3$, $\Omega_\Lambda = 0.7$, and $H_0 = 70$ km s^{-1} Mpc^{-1}.

2. Lockman-SpReSO

Lockman-SpReSO is a deep optical spectroscopic survey of a sample of mainly FIR-selected objects over the LH field. The region studied is the central 24×24 arcmin^2 of the LH field with equatorial coordinates (J2000) $10^{\rm h}52^{\rm m}43^{\rm s}$ $+57°28'48''$ at the centre (north-eastern region).

One of the first studies of optical counterparts of IR sources was that of Armus et al. (1989), who carried out spectroscopic observations of 53 IR galaxies to determine the nature of the emission from these sources. Another relevant study is that of Veilleux et al. (1995), who performed a spectroscopic survey of 200 luminous IRAS galaxies in order to discern when the IR emission is due to nuclear activity in the galaxy and when it is due to intense starbursts. In their work, they found that the probability of the ionization source coming from nuclear activity increases for cases of higher IR luminosity. More recent studies have consisted of spectroscopic follow-ups of *Spitzer* (Berta et al. 2007) and *Herschel* (Casey et al. 2012) sources using the Keck observatory. The work by Berta et al. (2007) focused on the study of 35 luminous infrared galaxies (LIRGs) with $z > 1.4$ and has determined that 62% of the objects with a measurable spectroscopic redshift have an active galactic nucleus (AGN) component. Casey et al. (2012) studied 767 *Herschel* sources by performing a detailed study and estimating luminosity functions for $z < 1.6$. Other studies, using the large statistical database of SDSS, have carried out analyses of IR sources detected with SDSS in the local low-redshift ($z < 0.15$) universe (Rosario et al. 2016, Maragkoudakis et al. 2018).

Many spectroscopic studies have observed the whole LH field in different ranges of the electromagnetic spectrum. From LH observations in the X-ray range made with *XMM-Newton*, a series of papers were published explaining the data obtained (Hasinger et al. 2001), the spectral analysis performed (Mainieri et al. 2002), with a total of 61 spectroscopic redshift identifications, and a catalogue with the fluxes of the sources (Brunner et al. 2008). The ROSAT deep survey also published a series of papers studying LH sources: optical identifications, photometry, and spectroscopy with 43 redshifts measured by Schmidt et al. (1998) and 86 by Lehmann et al. (2001), among others.

Rovilos et al. (2011) made an optical and IR analysis of the properties of AGNs in the LH field detected in the X-ray data described above, and they found 401 optical counterparts to the 409 AGNs detected by *XMM-Newton*. Patel et al. (2011), using the WYFFOS instrument on the *William Herschel* Telescope, carried out observations in the optical range of the XMM-LSS and LH-ROSAT X-ray fields and measured a total of 278 and 15 spectroscopic redshifts, respectively.

Many other studies have performed optical/NIR spectroscopic follow-ups of X-ray sources, given their good quality. Zappacosta et al. (2005), using the DOLORES instrument in its MOS mode at the Telescopio Nazionale Galileo (TNG), observed 215 sources down to $R = 22$ mag, obtained spectroscopic redshifts for 103 objects, and found evidence of a superstructure at $z = 0.8$. Henry et al. (2014) postulated that one of the most distant X-ray clusters at $z = 1.753$ in the LH field (Henry et al. 2010) could actually be a large-scale structure at $z = 1.71$. SDSS has also scanned the entire LH field and obtained spectroscopic redshifts for ∼115 k objects, where only 140 objects down to $r = 21.8$ mag lie within the central 24×24 arcmin^2 of the field (Abdurro'uf et al. 2022).

Of particular relevance to our work is that carried out by Fotopoulou et al. (2012, hereafter FT12), which we describe in more detail in Sect. 3.2. The authors collected all the available photometric and spectroscopic information on the LH field at the time of publication from the UV (GALEX) to NIR (*Spitzer*/IRAC) in a single catalogue, including publicly available good-quality spectroscopic redshifts and the photometric redshifts calculated by themselves.

More recently, Kondapally et al. (2021) has produced another multi-wavelength catalogue of the radio sources detected by the LOw-Frequency ARray (LOFAR; van Haarlem et al. 2013) Two Metre Sky Survey (LoTSS; Shimwell et al. 2017), which observed (among other fields) the LH field at 150 MHz down to an RMS of 22 μJy beam^{-1}. The multi-wavelength catalogue contains photometric information from the UV (GALEX) to the NIR (*Spitzer*/IRAC) and identifies the multi-wavelength counterparts to the radio sources detected by LoTSS. Since it is a more recent work than FT12, the photometric information is more up to date, including measurements in the optical range from the *Spitzer* Adaptation of Red-sequence Cluster Survey[1] (SpARCS; Wilson et al. 2009) and the Red Cluster Sequence Lensing Survey (RCSLenS; Hildebrandt et al. 2016). The merging of FT12 and the multi-wavelength catalogue of Kondapally et al. (2021) ensures that we have the most complete multi-wavelength (from UV to NIR) photometric coverage to perform accurate SED fittings (see Sect. 6.3).

Other studies have been carried out at longer wavelengths. Swinbank et al. (2004), for example, used imaging and NIR spectroscopy to study 30 (four in the LH field) LIRGs preselected from sub-millimetre and radio surveys (Chapman et al. 2003, 2005). Another example is the work of Coppin et al. (2010), who analysed AGN-dominated sub-millimetre galaxy (SMG) candidates using the *Spitzer*/IRAC spectrograph. The northern region of the LH field was studied as part of the SCUBA-2 Cosmology Legacy Survey at 850 μm and a depth reached at 1σ of 1.1 mJy beam^{-1} using the *James Clerk Maxwell* Telescope (JCMT, Geach et al. 2017).

All previous studies have covered different areas and sizes of the LH field for which there were, until the release of SDSS spectroscopic data, ∼600 good-quality spectroscopic redshifts for the whole LH field (∼15 deg^2). Although the number was significantly increased thanks to the contribution of SDSS, the number of spectroscopic redshifts in the central 24×24 arcmin^2 has barely increased with ∼150 new values but with a limiting magnitude $i \sim 22$.

To address the lack of spectroscopic information and also study specific families of optical counterparts, the main objective of the Lockman-SpReSO project is to obtain deep optical spectroscopy of a selected sample of objects in the LH field to complement the deepest observations of the *XMM-Newton*, *Spitzer* and *Herschel* space telescopes, and radio data (Ciliegi et al. 2003). The primary sample of objects (>80% of the total sample) to be observed with the Lockman-SpReSO project consists of sources observed in the *Herschel*/PACS Evolutionary Probe (PEP) programme by Lutz et al. (2011) with robust optical counterparts down to a magnitude of ∼24.5 in the Cousins R_C band. They observed the central 24×24 arcmin^2 region of the field with a depth of 6 mJy (at 5σ) at 100 and 160 μm within the framework of the time-guaranteed *Herschel*/PACS key project PEP. These observations enabled sampling near the maximum of the SED of active star-forming galaxies (SFG) at high redshifts ($z < 3$). This enables the bolometric luminosities to be estimated more accurately. Moreover, the typical spatial resolution of PACS allows us to perform a reliable cross-correlation with optical sources depending on the spectral band. In order to optimize the use of MOS mode observations, the primary catalogue of FIR sources was supplemented with other types of sources in the field under study, as explained in Sect. 3.5.

Redshifts were obtained by optical spectroscopy using various instruments (OSIRIS, Cepa et al. 2000; WYFFOS, Domínquez Palmero et al. 2014 and HYDRA[2]), which are described in Sect. 4. Spectroscopic observations of selected targets in the NIR domain are planned for the near future.

Panchromatic studies (from the X-ray to the radio region) of galaxies have been shown to be a valuable strategy for studying the evolution and properties of these objects. The obtained spectra for selected Lockman-SpReSO objects, complemented with ancillary data, were used to derive the stellar masses, SFRs, gas metallicites, and extinctions. Furthermore, using ratios of spectral lines, we were able to separate SFGs from AGNs using a BPT diagram (Baldwin et al. 1981; Stasińska et al. 2006). This segregation is also possible using different IR or X-ray emission (Ramón-Pérez et al. 2019, and references therein). Among other parameters, SED-fitting techniques allow us to estimate stellar masses, while SFRs can be obtained via either FIR luminosities or optical lines (Kennicutt 1998). Gas metallicities can be measured using different optical relations, the aforementioned R_{23} and N2 methods, and also FIR relations (Pereira-Santaella et al. 2017; Herrera-Camus et al. 2018, for example). Finally, FIR over UV luminosities are considered the best method for determining extinctions (Viaene et al. 2016).

Several studies have shown that LIRGs lie below the mass–metallicity relation for SFGs (Pereira-Santaella et al. 2017, and references therein), although the offset could depend on the selection criteria used. However, these studies are limited to local samples. Ideally, they should be extended in order to ascertain whether this relation depends on FIR luminosity or redshift, or on both. Moreover, the study should encompass the possible differences of the fundamental plane of SFG (Lara-López et al. 2010) for LIRGs and ultra-luminous infrared galaxies (ULIRGs). For example, studies at higher redshifts have shown that spectral

[1] http://www.faculty.ucr.edu/~gillianw/SpARCS/

[2] https://noirlab.edu/science/programs/kpno/telescopes/wiyn-35m-telescope/overview

lines are more attenuated than the continuum (Buat et al. 2020), whereas Eales et al. (2018), using *Herschel* data, make a claim for rapid galaxy evolution in the very recent past.

Some of the scientific objectives of the Lockman-SpReSO project, which are developed in forthcoming papers, include studying the possible evolution of the relation of the masses, extinctions, different SFR indicators, and gas metallicities of *Herschel* galaxies with respect to FIR colours, masses, and FIR and radio luminosities.

Compared to other deep spectroscopic surveys, the Lockman-SpReSO project reaches a depth parameter (Djorgovski et al. 2012) 1.2 times greater than that achieved by the VVDS/ultra-deep survey (Le Fèvre et al. 2013). It is also more advantageous in terms of continuum sensitivity and spectral coverage than z-COSMOS (Lilly et al. 2007) and AEGIS-DEEP (Davis et al. 2007) respectively. These advantages are largely due to the possibility of using the collecting surface of a 10-metre class telescope and a powerful instrument such as OSIRIS. The sensitivities achievable are higher than those attainable by surveys with smaller collecting surfaces (i.e. the SDSS survey), even considering the later releases. In addition, our study is, to date, the most complete, extensive and statistically significant of the optical counterparts of the *Herschel* IR sources.

3. Target selection

As already mentioned, the main objective of the Lockman-SpReSO project is to provide a high-quality optical spectroscopic follow-up of the FIR sources from the *Herschel*-PEP survey (Lutz et al. 2011) with robust optical counterparts in images from OSIRIS in the SDSS r band, up to $R_C = 24.5$ mag. This limiting magnitude was originally chosen to reach an $S/N \sim 3$ in the continuum with the OSIRIS instrument in MOS mode at resolution $R \sim 500$ and an integration time of about 3 h, according to the GTC/OSIRIS Exposure Time Calculator[3] (ETC, version 2.0).

After selecting the FIR sources and studying which of them have optical counterparts, it was necessary to collect all the good-quality information available in the literature to accurately study the redshifts and physical properties of those sources. Data such as photometric redshifts or magnitudes in various bands are essential for this study.

After an exhaustive search of the literature, three catalogues were used to create the bulk of the sample. The first of these is the catalogue of FIR objects from the PEP Survey *Data Release*[4] (DR1) but limited to the central 24×24 arcmin^2 of the LH field. The second catalogue is that of FT12, in which the available information from the LH field was collected (see Sect. 3.2). Finally, the third catalogue was obtained from the broad-band optical images made with OSIRIS (see Sect. 3.3). The fusion of these three catalogues makes up the primary source catalogue of the Lockman-SpReSO project.

In addition, X-ray emitting counterparts of the FIR sources were identified by using the *XMM-Newton* and *Chandra* mission catalogues. Other secondary catalogues were added to the project to optimize the use of the masks and observation times. The following sections describe the sample selection and creation of the final catalogues.

[3] http://www.gtc.iac.es/instruments/osiris/Osiris_ETC.php

[4] www.mpe.mpg.de/ir/Research/PEP/public_data_releases

3.1. Far-infrared sources

As a starting point, we used the data from the DR1 of the PEP survey (Lutz et al. 2011) to select the FIR objects. The PEP programme is a *Herschel* guaranteed time extragalactic survey focused on deep PACS (Poglitsch et al. 2010) 70, 100, and 160 μm observations of blank fields and lensing clusters. One of them is the LH field, of which complementary observations were made within the HerMES survey (Oliver et al. 2010) using the *Herschel*/SPIRE (Griffin et al. 2010) photometer and its channels at 250, 350, and 500 μm.

For the purposes of our study, we adopted the catalogue based on the 24 μm priors from *Spitzer*/MIPS, which includes the positions and fluxes as measured by Egami et al. (2008), and the *Herschel*/PACS photometer fluxes detected by the PEP project at these positions at 100 and 160 μm. This information is also available in the published PEP DR1 data.

After applying the constraint imposed by the coordinates and discarding MIPS sources with no fluxes at 100 and 160 μm, 1181 sources in total were obtained for the FIR catalogue (hereafter PEP-catalogue).

3.2. Multi-wavelength catalogue

One of the most complete studies carried out on the LH field is that of FT12, whose authors collected photometric and spectroscopic information available in the literature. They published a catalogue with all the data, including the photometric redshifts for the sources in our field. Specifically, Tables 5 and 10 from FT12 provide the data for photometric information and photometric redshifts respectively. Table 5 in FT12 contains photometric information from the far-UV (FUV) to the mid-IR, in the best case reaching up to 21 bands. Furthermore, spectroscopic redshifts are also included for those objects with high-quality spectroscopic information analysed in 27 studies and compiled in Table 4 of FT12.

All these data from FT12 were compiled and limited to magnitude $R_C \leq 24.5$ and coordinates within the 24×24 arcmin^2 of the field of study. A multi-wavelength catalogue (hereafter the FT-catalogue) of 28 956 sources was obtained with an astrometric precision better than 0.2 arcsec (Rovilos et al. 2011). The merging of the FT-catalogue and the PEP-catalogue made it possible to limit the FIR sources in R_C magnitude.

3.3. Pre-images of the Lockman Hole field from OSIRIS

A total of 64 images were taken to map the central region of the LH field (J2000 equatorial coordinates: $10^h52^m43^s$ +57°28′48″) using OSIRIS in broad-band mode with the SDSS r filter. Those images were meticulously reduced and astrometrically calibrated with RMS < 0.15 arcsec. The outcome was a mosaic of the studied field with dimensions of approximately 24×24 arcmin^2.

The purpose of the mosaic was to find the optical positions and calibrated magnitudes of the optical counterparts of the FIR sources in the PEP-catalogue in agreement with the imposed flux limit of $R_C \leq 24.5$. The observations were thus designed to achieve a limiting magnitude for the mosaic of $r_{lim} = 25.6$ at 3σ. This limit ensured that all the optical counterparts of the FIR sources were detected. The optical positions determined in this process were those used in the design of the masks for the MOS observation mode.

The extraction of the list of objects and photometric information from the mosaic was implemented using `SExtractor` (Bertin & Arnouts 1996). A total of 33 942 sources

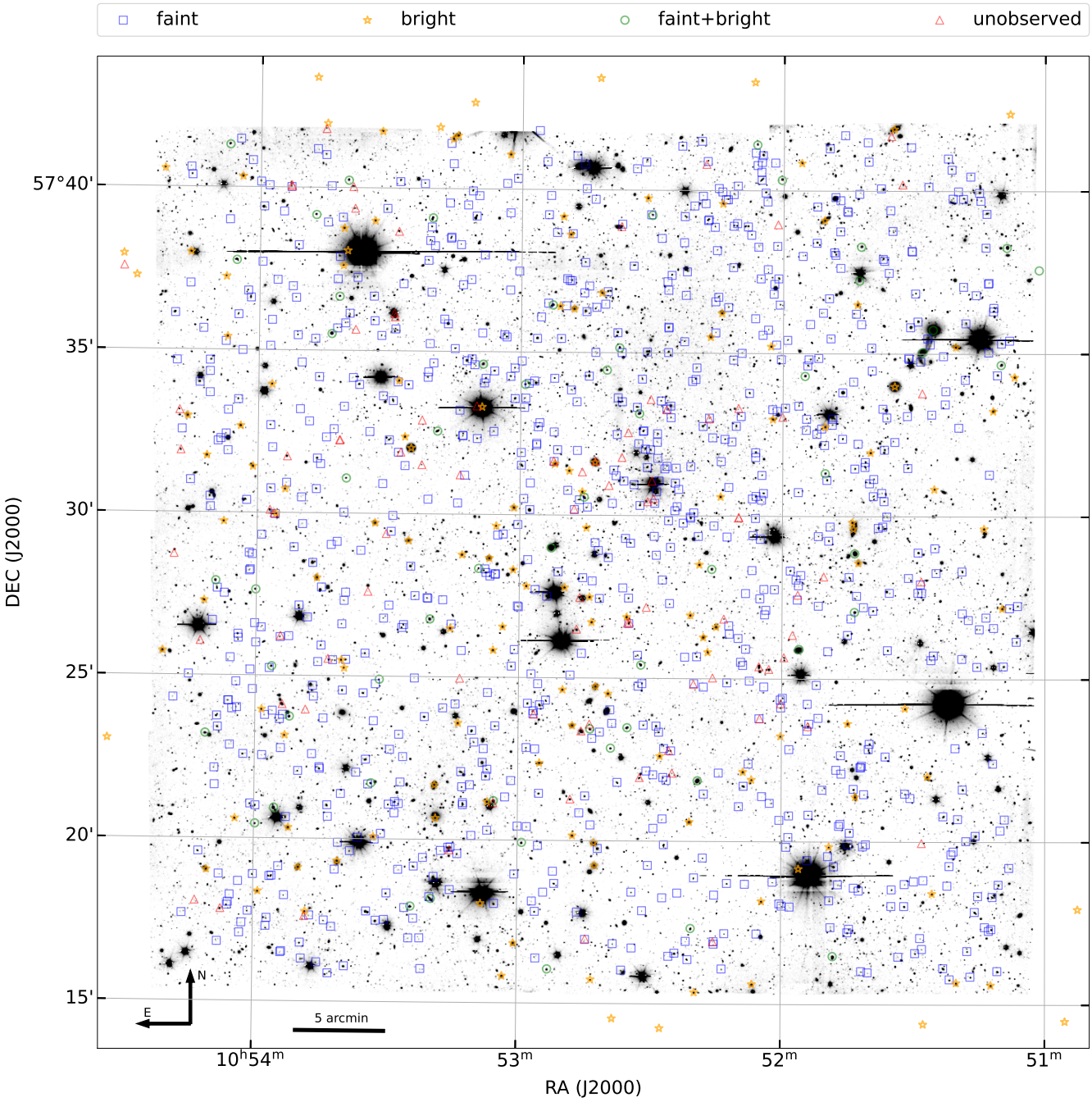

Fig. 1. 24×24 arcmin^2 OSIRIS mosaic (north up, east left) of the studied region of the Lockman-Hole field with equatorial coordinates (J2000) $10^h52^m43^s$ +57°28′48″ at the centre. Objects from the Lockman-SpReSO project input catalogue are highlighted on the mosaic: the blue squares represent objects in the faint subset, the yellow stars are objects in the bright subset, the green circles are objects in both sub-samples, and the red triangles are objects in the catalogue that were left unobserved.

were extracted with RMS < 0.38 arcsec, which defines the OSIRIS-catalogue. The resulting mosaic of the OSIRIS pre-image constitutes the background of the map represented in Fig. 1. The fusion of the OSIRIS-catalogue and the PEP-catalogue allowed the IR sample to be limited to those objects with optical counterparts in the OSIRIS mosaic.

3.4. X-ray counterparts of far-infrared sources

The X-ray observations in the LH field are the deepest and most complete in the field. These data give us an opportunity to identify the FIR sources with X-ray emission, in addition to optical counterparts up to $R_C \leq 24.5$, which are useful for AGN host classification (e.g. Pović et al. 2009a, 2009b; Mahoro et al. 2017 and references therein). In particular, we analysed data from the *XMM-Newton* and *Chandra* missions because of the high quality of their data in the LH field, looking for which sources in the PEP-catalogue have X-ray emission.

The *XMM-Newton* satellite provides the deepest observations in the LH field (Brunner et al. 2008), with a total of 409 sources detected. We matched this catalogue with the PEP-catalogue with a search radius of 2 arcsec, as recommended by Pović et al. (2009a), and found that 64 were objects in common.

From the *Chandra Source Catalogue* (Evans et al. 2010), we selected the sources in our field under the same conditions as imposed on *XMM-Newton* data. We identified a total of 106 *Chandra* objects, of which only 19 were matched with the PEP-catalogue, within a search radius of 2 arcsec.

Finally, we matched both catalogues. We found a total of 66 X-ray sources without redundancies, that is to say 66 FIR sources with emission in the X-ray domain detected by either the *XMM-Newton* or *Chandra* telescopes. All selected objects are also in the FT-catalogue with $R_C \leq 24.5$ mag and in the OSIRIS-catalogue, so the objects are part of the final catalogue as selected objects with IR emission and X-ray counterparts.

3.5. Additional targets

The possibility of working with the GTC's large collecting surface and the efficiency of OSIRIS allows us to complement the Lockman-SpReSO project scientifically with secondary studies. We added interesting complementary targets to take full advantage of the OSIRIS MOS mode and to optimize the design of masks.

Since none of the secondary catalogues impose the criteria of IR emission in their objects, redundancies may arise among the secondary catalogues, and even with the main catalogue. A study of the existence and correction of redundancies was carried out as the last step in the compilation of the final catalogue of the Lockman-SpReSO project.

Two studies on secondary objects are proposed. For those objects whose nature has been determined in previous studies, further information is expected to be added through optical spectroscopy. This is the case for galaxies studied in the sub-millimetre and radio domains. On the other hand, for those objects whose nature is indeterminate, spectroscopy helps us reveal the type of object being analysed and its properties, an example being the very red quasi-stellar object (QSO) candidates. The following subsections describe each of the additional catalogues in detail.

3.5.1. X-ray point sources and cataclysmic variable star candidates

A new cross-match was made between the OSIRIS-catalogue and the catalogue of FT12 in order to assign the photometric information, but with a search radius of 5 arcsec. Two different search methods were applied. The first, looking for point sources, imposed the *CLASSSTAR*> 0.95 constraint and an X-ray detection (a flag in the catalogue of FT12). The result was a list of 45 objects. The second method was the colour criteria of Drake et al. (2014) ($-0.5 < u - g < 0.5$ and $-0.5 < g - r < 0.5$) to identify possible cataclysmic variable (CV) stars. This yielded a total of 21 objects, but eight of these were in common with the point sources. Therefore, this catalogue of secondary objects comprises a total of 58 objects. The spectroscopic study of these objects help us to determine whether or not their nature is stellar, together with a study of the degree of contaminants suffered in the colour-based selection method.

3.5.2. High-velocity halo star candidates

Another secondary scientific objective focused on the study of high-velocity halo stars. Considering as a first criterion the stellarity given by the photometry, we selected 94 sources from the *Initial Gaia Catalogue* (Smart & Nicastro 2014) with high proper motion (>10 mas yr^{-1}) and $R_C > 18$ as the sample of stars in the Lockman-SpReSO project.

Our interest was centred on spectroscopically sampling the halo while focusing on stars with high proper motion, which could include Galactic runaway stars. The spectra of the objects may provide rough radial velocity information, but good enough to classify them as halo or disc stars. On the other hand, this sampling could provide us with a better classification between stars, galaxies, and quasars, while indicating the degree of contamination of the stellar sample defined only by the stellarity parameter.

3.5.3. Radio-source population

Deep radio surveys (for more information see de Zotti et al. 2010 and Padovani 2016) at levels of a few μJy show that there is an excess of sources with respect to the population of powerful radio galaxies. Radio sources above ∼1 mJy are typically classical radio sources powered by AGNs and hosted by elliptical galaxies. Below 1 mJy, radio-source counts start to be dominated by SFGs, similar to the nearby starburst population; in other words, radio emission in these galaxies is directly related to the SFR. Thus, deep radio surveys are relevant to the study of the history of star formation in galaxies. One of these surveys in the LH field is the 6 cm (5 GHz) Very Large Array survey by Ciliegi et al. (2003), who studied 63 radio sources at a depth of ∼11 μJy. We selected objects from this survey with no spectroscopic information in the bibliography and matched them with the FT-catalogue to add the photometric information. The result was a sample with 24 radio sources with optical counterparts up to $R_C = 24.5$ mag in FT12.

3.5.4. Very red quasi-stellar object candidates

As in the case of the optical spectroscopy of radio galaxies, the scope and possibilities of Lockman-SpReSO give us the opportunity to study other obscured sources that are interesting in their own right. We selected a sample of candidates of very red QSOs by following two different selection processes. The first, proposed by Glikman et al. (2013), consists in searching for optical, not necessarily point-like objects, counterparts of radio sources from the Faint Images of the Radio Sky at Twenty[5] (FIRST; Becker et al. 1995) survey using the criteria $R - K_{Vega} > 4.5$ and $J - K_{Vega} > 1.5$. In this way, we found seven very red QSO candidates.

An alternative selection was based on the work of Ross et al. (2015), where the colour selection criterion was $r' - W4 > 7.5$, with $W4$ the 22.19 μm channel of Wide-field Infrared Survey (WISE; Wright et al. 2010). As a reference to $W4$, they used a relation with MIPS 24μm − $W4 = 0.86$ (Brown et al. 2014). For the r band, they used $r' - R_C = -0.2$ (Ovcharov et al. 2008). In terms of this criterion, 63 sources were classified as potential very red QSOs, yielding a total of 70 by merging both methods.

3.5.5. Optical counterparts of sub-millimetre galaxies

As is known, surveys with the *Herschel* Space Observatory have identified an increasing number of SMGs (Negrello et al. 2010, Mitchell-Wynne et al. 2012). The study of these sources is of paramount importance for understanding the formation and evolution of massive, dusty galaxies, which could explain the origin of present-day massive ellipticals (e.g. Ivison et al. 2013). For these reasons, analysis of its spectroscopic properties in the

[5] http://sundog.stsci.edu

Table 1. Summary of the classes in which the 1144 LH catalogue objects have been detected or for which they are candidates.

FIR sources	X-ray FIR counterparts	X-ray point sources and cataclysmic stars	High-velocity halo stars	Radio sources	Very red QSOs	sub-millimetre galaxies
956	66	58	94	24	70	16

Notes. It should be noted that there are redundancies between the different classes.

optical and NIR can be both exciting and challenging, and the Lockman-SpReSO project provides an excellent opportunity to do that at a minimum cost.

The catalogue that was used as a starting point can be found in Table B3 of Michałowski et al. (2012), which contains the LH field objects detected with JCMT/AzTEC at 1.1 mm as part of the SCUBA HAlf Degree Extragalactic Survey (SHADES; Mortier et al. 2005). This survey has a resolution of ∼18 arcsec and reaches a depth of ∼1 mJy. To determine source identifications, they used the catalogues of Austermann et al. (2010), thus exploiting deep radio (1.4 GHz) and 24 μm (0.61 GHz) data, complemented by flux density based methods at 8 μm and $i - K$ colour.

To ensure a fair identification of SMG candidates, only objects with very good detection ($bID = 1$ in Table B1 of Michałowski et al. 2012) were selected. We then cross-matched them with those in the PEP-catalogue with a search radius of 5 arcsec and selected those with $R_C \leq 24.5$. We obtained a sample of 16 sources with good identification in AzTEC and sub-millimetre emission with optical and FIR counterparts. These SMG sources were also selected as FIR sources with optical counterparts in the OSIRIS mosaic, so they are included in the main object catalogue but flagged regarding that distinctive feature for future studies.

3.5.6. Fiducial stars

One of the requirements for quality pointing using the OSIRIS MOS mode is that we have at least three reference points in the field with good accuracy. In this case, these reference points are fiducial stars in the LH field, which help us to point the telescope with accuracy and repeatability.

Each observation had between three or four fiducial stars to guarantee accurate telescope pointing. Thus, we chose 171 sources in the LH field from SDSS-DR12 (Alam et al. 2015). The sample has a coordinate accuracy of 0.3 arcsec and R-band magnitudes between 16 and 19. According to this, the selected fiducials are bright enough to align the mask in a few minutes, but not so bright that they could saturate the acquisition frames when a MOS mask is observed.

3.6. The final input catalogue

To compile the final sample, the three main catalogues (the PEP-, FT- and OSIRIS-catalogues) were merged to obtain a final priority target catalogue. Coordinates from Egami et al. (2008) were used as reference in the cross-match process because of their high astrometric accuracy. We tested the best value of the maximum allowed distance between the different catalogues. We found that 1.5 arcsec was the best compromise. This is slightly greater than the most significant error of the coordinates in the PEP-catalogue (∼1.22 arcsec).

We started by joining the target list from the OSIRIS mosaic and the PEP-catalogue. We matched a total of 991 targets within a distance of 1.5 arcsec. After this, we merged the PEP-catalogue with the FT-catalogue to obtain a list of 1063 common objects. The final step was to bring these two previous matches together into a single catalogue. After the correction for multiplicities, the definitive catalogue of primary sources was made up of a total of 956 objects (the primary catalogue). The whole process is described more schematically in Fig. 2 (up to the green box). The last step was to check for possible redundancies between the additional catalogues and the primary catalogue, namely to see if there were objects that appeared in both the primary catalogue and any of the secondary catalogues, while skipping the SMGs that had already been taken into account. The lower half of Fig. 2 represents the merge of the primary and the secondary catalogues (see the 'Preliminary Object Type' and 'Catalogue' columns in Table 4 to check where the redundancies were found and in what quantity, respectively).

The final target selection from the FIR counterparts in the primary catalogue and complementary sources present in the OSIRIS mosaic, making up the LH-catalogue, includes 1144 sources. The final composition of objects in the LH-catalogue is summarized in Table 1. Each value in the table indicates the number of sources in that category that have become part of the LH-catalogue. However, it is important to note that there are redundancies between the different classes; for example, all the SMGs are part of the FIR objects.

4. Spectroscopic observations

Our survey used the guaranteed time of the OSIRIS instrument team and the Instituto de Astronomía of the Universidad Nacional Autónoma de México (IA-UNAM). The first observations were carried out over the first semester of 2014 (run 2014A in Table 2) and were used to create the OSIRIS mosaic image of the study region of the LH field (Fig. 1).

As mentioned above, our quality requirement was to reach a $S/N \geq 3$ in the continuum for all the objects in the survey. Considering the ETC predictions for the different R_C magnitude intervals of the survey, as well as the spatial distribution of the objects by R_C magnitude in the 24×24 arcmin^2 field, it was determined that, in order to achieve this S/N, it would take of the order of 1 to 1.4 h per mask with $R_C < 20.6$ mag, and up to 3 h per mask for sources with $R_C \geq 20.6$ mag. Figure 3 shows the R_C magnitude distribution for all the objects in the catalogue.

Consequently, to avoid problems in merging bright and faint objects, and with the aim of optimizing the number of masks that needed to be used, the sample was divided into two parts using the magnitude criterion $R_C = 20$ mag as the separation value. We denominated objects with $R_C \geq 20$ mag as the faint subset (993 sources) and objects with $R_C < 20$ mag as the bright subset (151 sources), where each of them was observed with a different telescope. However, there is a slight overlap (up to $R_C = 20.6$ mag, 93 sources in the magnitude range $20 < R_C < 20.6$) between the sub-samples for comparing the results obtained with the different telescopes and checking that they are in good

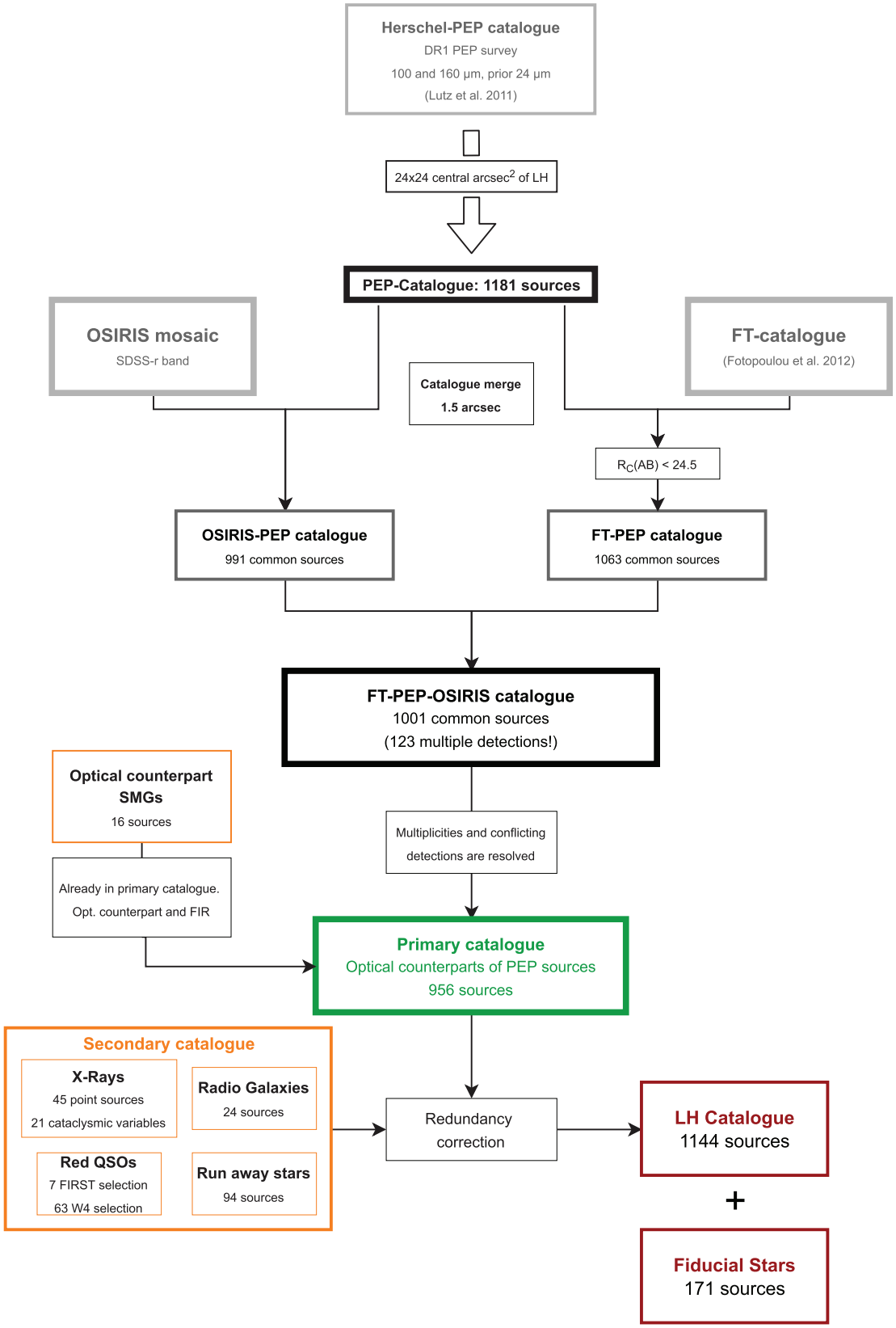

Fig. 2. Merger schedule for the elaboration of the LH-catalogue.

Table 2. Schedule and details of the observing runs over the faint subset observed with OSIRIS/GTC.

Run	Masks (#)	OB/Mask	Grisms	Slits length (arcsec)	Req. night	Exp. time (s)
2014A	–	–	–	–	–	10 304
2014B	10	3 [(1)]	R500B(2) and R1000R(1)	10	Gray	105 600
2015A	7	3 [(2)]		10	Gray	87 400
2015B	6	3		10	Gray	71 400
2016A	3	3	R500B(1) and R500R(2)	10	Dark	24 000
2016B	6	3		10	Dark	50 400
2017B	10	4	R500B(2) and R500R(2)	3	Dark	10 8000
2018B	6	4		3	Dark	64 800

Notes. All the essential information is collected for each run. The number in parentheses in the 'Grisms' column represents the number of times that the observations with the grism were made. The first row corresponds to the observation of the images used to elaborate the mosaic. [(1)] Two masks had 2 OBs (R500B(1) and R500R(1)). [(2)] One masks had 4 OBs (R500B(2) and R500R(2)).

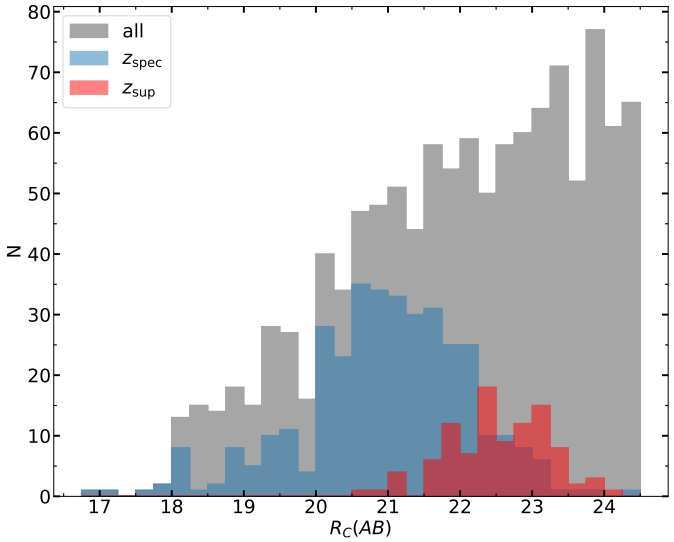

Fig. 3. Distribution of R_C magnitude for the whole Lockman-SpReSO sample (grey), highlighting the objects with z_{spec} measured in this study (blue) and objects with z_{sup} (red, see Sect. 6.1 for details).

agreement. Figure 1 shows the spatial distribution of the objects in each of the subsets, as well as those that are common and those not observed.

4.1. The faint subset

The observations of the faint subset were carried out using the OSIRIS instrument at the GTC telescope in MOS-mode[6]. The first run started in the second semester of 2014 (2014B in Table 2), just after the OSIRIS mosaic observations. In addition, spectroscopic MOS mode observations for Lockman-SpReSO also began shortly after the technical commissioning of the OSIRIS MOS mode (Vaz Cedillo et al. 2018). The schedule and essential information on the runs can be seen in Table 2. The masks were designed using the telescope's software, the OSIRIS Mask Designer (MD; González-Serrano et al. 2004, Gómez-Velarde et al. 2016).

Each mask was observed using two different grisms covering the blue and red part of the optical spectrum at an intermediate resolution. The blue region was observed with the R500B grism, which provides a wavelength coverage of 3600–7200 Å and a nominal dispersion of 3.54 Å pixel^{-1}. The red part was covered with two grisms (R500R and R1000R). The former has a wavelength coverage of 4800–10000 Å and a dispersion of 4.88 Å pixel^{-1}, while the latter has a range of 5100–10000 Å and a dispersion of 2.62 Å pixel^{-1}.

The observing strategy changed because of differences in the sample brightness. In this way we could optimize the design of the masks to attain our quality objective of $S/N > 3$. The first runs were dedicated to observing the brightest objects in the faint subset ($20 \lesssim R_C \lesssim 22$, 403 objects), which have a lower density in the field. It was requested that these observations be done on grey nights and the masks were designed using slits with a length of 10 arcsec. This slit length allowed us to select a region in the 2D spectra where the contribution due to emission sky lines could be obtained in order to subtract them from the object spectra (Sect. 5.1.1). The slit width was set at 1.2 arcsec, as recommended in the official literature for the instrument. This width did not result in a noticeable loss of resolution in the spectrum, and was also in line with the 0.1 arcsec precision of the slit positioning in the OSIRIS MOS mode and the 10% accuracy requirement in positioning.

Three observing blocks (OBs) were scheduled for each mask. Two were observed with the R500B grism and one with the R1000R grism. The former had two scientific images per OB, while the latter had three. Table 2 gives detailed information about the configuration of the runs.

Sky emission subtraction was difficult for faint objects. Moreover, the increase in the number of faint objects in the field implied changing the run's configuration after the 2016B run, when we started to observe the faintest objects in the faint subset ($22 \lesssim R_C \leq 24.5$, 535 objects). Each OB was observed in the *ON-OFF-ON* mode (Sect. 5.1.1), where the *ON-frame* is an actual image and the *OFF-frame* is a consecutive image but with a slight telescope displacement that makes all the slits point to a blank region of the sky. Therefore, each OB had two frames with the spectra of the objects plus sky emission (ON-frames) and one frame with only sky emission spectra (OFF-frame). With this technique, the sky correction for faint objects was greatly improved. Additionally, the sky emission was taken from the *OFF-frame* to enable the slit length to be smaller (3 arcsec) and to allow more slits to be introduced in a given mask design.

The object selection for each mask was made in an effort to minimize the number of masks needed by selecting a field of

[6] www.gtc.iac.es/instruments/osiris/osirisMOS.php

view with greater object density where possible, but taking care not to merge objects with a very large difference in magnitude and so fit the exposure time in agreement with this. Each mask also had to have some slits for the fiducial stars. These slits were circular with a radius of 2 arcsec. In the masks designed for the faint subset, we also introduced special slits that were pointed to empty regions of the sky in both the *ON*- and *OFF-frames*. These slits were used in the sky correction (see Sect. 5.1.1).

In total, 48 masks, covering 92% of the objects, were designed to perform observations of the faint subset. All the observations were designed to achieve an S/N better than three in order to obtain good quality spectral lines, even for the faintest objects. In addition to the type of night set for each observation, both airmass and seeing were always requested to be below 1.2. All observations were made in compliance with the required seeing, 60% with seeing better than 1 arcsec. For the airmass, the constraint was less strict according to the seeing value of that same observation; in other words, if the airmass exceeded the value of 1.2 by never more than 1.35, but the seeing value was good (seeing < 1arcsec), the observation was accepted. In total, 12 OBs were earmarked for repetition because the conditions in which they were performed failed to meet requirements, either because of high airmass and seeing or because the type of night was not as requested.

4.2. The bright subset

The bright subset of targets selected for the LH field, $16.8 \leq R_C \leq 20.6$, were observed using two medium-resolution multi-fibre spectrographs, A2F-WYFFOS (AF2) of the WHT at Roque de Los Muchachos Observatory in La Palma, and HYDRA from the WYIN telescope at Kitt Peak Observatory in Tucson.

The selected targets were divided into a 'blue sample' ($16.8 < r_{SDSS} < 20.0$) and a 'red sample' ($20.0 < r_{SDSS} < 20.6$). Three fibre configurations were prepared for the blue sample and two for the red sample, to be observed with AF2/WHT. In total, 96 targets were allocated for the blue sample and 50 for the red sample, ~60% of the total bright sample plus the overlap with the faint subset, but not all the scheduled observations could be completed.

To complete the observations of the bright subset, we used the HYDRA spectrograph on the WYIN telescope. The sample designed for WYIN was composed of objects not observed with the WHT and some were observed to compare results between telescopes in order to make the most of the observations. Finally, 134 sources with $16.8 < R_C < 20.6$ were observed with WYIN.

Regarding the bright part of the catalogue, these objects were expected to be at a lower redshift than in the faint part. Still, as for the faint subset, all observations were set to reach an S/N of better than five to obtain quality measurements of the spectral lines.

Figure 1 also shows the spatial distribution of the objects in the bright part. The yellow stars represent the objects in the bright subset, and the green circles represent common objects in both the bright and faint catalogues.

4.2.1. Multi-fibre optical spectroscopy with AF2-WYFFOS

We conducted multi-fibre medium-resolution spectroscopy with the AF2 wide-field multi-fibre spectrograph. The AF2 spectrograph contains 150 science fibres of a diameter of 1.6 arcsec, and ten fiducial fibres dedicated to acquiring and tracking guide stars. The AF2 spectrograph has a nominal field of view of 1 deg^2, but because of optical distortion and the restriction to avoid the region beyond 25 arcmin, to prevent vignetting of the telescope system and instrument, the configuration file was designed to consider only the area within the central 20 arcmin^2. Despite these restrictions, three optimized AF2 pointings were planned to cover the central 24×24 arcmin^2 of the LH field. With AF2, it is necessary to use the special software *af2-configure*[7] (from the Isaac Newton Group) to create the map of targets to be observed. This software allowed us to optimally place, beforehand, between 50 and 70 fibres per observation on the selected targets. After allocating all the objects in the best way, the remaining fibres were used to observe blank areas in the observation field to obtain sky spectra.

Observations were performed in three configurations over seven nights in 2016 and 2017 in service mode. More details of the observations are listed in Table 3. The R600R and R300B gratings were used with a spectral resolution of 4.4 and 3.6 Å, respectively. The spectra were centred at wavelength ~5400 Å and covered the range from 3800 to 7000 Å, using a 2×2 binning of the CCD camera.

4.2.2. Multi-fibre optical spectroscopy with HYDRA

Owing to the decommissioning of AF2 before the planned observations of the bright subset were completed, we had to conduct our observations using a similar instrument. The HYDRA spectrograph on the WYIN telescope was chosen. The Lockman sample for HYDRA had 134 sources with $16.8 < R_C \leq 20.6$.

The HYDRA spectrograph has 90 active fibres. The targets were observed down to a spectrograph configuration of λ_{start} = 4400 Å, to λ_{end} = 9600 Å, using the the grism 316@7 with a resolution of $R \sim 900$ and $\delta\lambda \sim 3$ Å, the lowest resolution but the largest available spectral range.

The images were taken with 3×1800 s exposures for each configuration, adding two series of arcs, and were taken over a total of 8 h with overheads. We needed four configurations in two half nights. The observations were carried out during the first half of the nights of 8 and 9 May 2018, with a clear sky and a seeing of ~1 arcsec. A summary of the observations is given in Table 3.

5. Data reduction

Since the survey data have been obtained using different instruments and telescopes, the nature of the data of each subset is different. Thus, although some procedures are common, the data reduction is described separately for each group of data.

5.1. Faint subset reduction

Basic data reduction tasks were carried out using the IRAF-based pipeline GTCMOS (see Gómez-González et al. 2016) developed by Divakara Mayya of the Instituto Nacional de Astrofísica, Óptica y Electrónica (INAOE), Mexico. For each OB, the first step was to couple the image of the two OSIRIS CCDs into a single one to make it more manageable. We created a master bias and subtracted it from science images, and corrected it for flat-field. The wavelength calibration was performed using Hg, Ar, Xe, and Ne lamp spectra for each grism and mask with a median RMS of ~0.05.

The correction for cosmic rays was carried out using our own python code. To this aim, we relied on the fact that each

[7] https://www.ing.iac.es/Astronomy/instruments/af2/af2_documentation.html

Table 3. Schedule and details of the observations over the bright subset.

Telescope	Name	Date	Configuration	Grisms	Exp. time (sec)
AF2/WHT	data 1	15/05/2016	$blue_1$	R600R	2×1000
	data 2	02/06/2016	$blue_1$	R300B	3×1000
	data 3	19/01/2017	$blue_1$	R600R	3×2000
	data 4	20/01/2017	red_1	R600R	4×1800+1×1100
	data 5	05/02/2017	red_1	R300B	5×1800
	data 6	21/02/2017	$blue_1$	R300B	2×1000
	data 7	30/05/2017	$blue_2$	R600R, R300B	2×2000,3×1000
HYDRA/WYIN	blue1	07/05/2018	$blue_1$	R316R	3×1800
	blue2	07/05/2018	$blue_2$	R316R	3×1800
	red1	08/05/2018	red_1	R316R	3×1800
	mixed	08/05/2018	mix_1	R316R	3×1800

observation block had at least two science images. This allowed us to compare the same column in both 2D spectra, while looking for pixels more than 3σ of the median. These pixels are classified as cosmic rays.

5.1.1. Sky subtraction and flux calibration

The sky emission subtraction of an object's spectrum is both necessary and challenging. The line strength variation of the emission of OH over time is significant, making it painstaking work. As set out above, we performed two different kinds of sky emission subtraction, one for each slit length.

For the 10-arcsec slits, the subtraction was more direct as we could select regions in the 2D spectra where there was only signal from the sky. To separate the contribution of the observed object in the slit and the sky signal, iterative sigma-clipping was applied column by column. Then, once we obtained the contribution of the sky, we applied a linear fit and finally subtracted it from the original column. The linear fit was implemented to improve the correction because there is a slight curvature in the outer parts of the CCDs that introduces a distortion in the 2D spectra. The difference between the sky over the column when averaging the sky signal causes the value obtained to diverge from the sky emission and the subtraction fails.

A potential problem with this method occurs when the observed object has a faint continuum because it could be erroneously selected as a sky contribution by the sigma-clipping algorithm, thus resulting in a loss of object information. Furthermore, since the density of faint objects in the field is higher than that of bright objects, the adopted solution was to use 3-arcsec slits observed with the already mentioned *ON-OFF-ON* strategy.

The length limits of the 3-arcsec slits constrained the possibility of selecting sky signal in the 2D spectra. Observing with the *ON-OFF-ON* strategy, we had available direct sky emission spectra (OFF-frame) that could be subtracted directly from the images of the objects (ON-frames). However, the residuals obtained with direct subtraction are considerable. This difference in the sky signal between two consecutive frames is due to the significant variability of the sky emission over the time of the exposures. The solution to this problem was to introduce slits pointing to a region without objects (sky-slits), even in the ON-frames, in such a way that the sky-slits collected sky emission in both ON- and OFF-frames. Thus, if we compare the sky spectra obtained by the sky-slit in one of the ON-frames with the spectra obtained by the same slit, the result in the OFF-frame is a matrix of sky variation coefficients that can be applied to the OFF-frame spectra to correct the variation of the sky emission over time. Each mask should have at least one sky-slit per OSIRIS CCD to deal with the existing spatial variation of the sky emission, in addition to the time variation.

This method of sky emission subtraction gives even better results than the sky subtraction obtained in the case of 10-arcsec slits, where the sky can be selected in the 2D spectra. With the *ON-OFF-ON* strategy, the 2D spectra to be corrected for sky contribution and the 2D sky spectra used have the same shape because they come from the same slit with precisely the same characteristics (i.e. slit irregularities, CCD curvature, and differential refraction of the light). In Fig. 4, we can see an example of the sky subtraction for a 3-arcsec-long slit. The top panel is a slice of the 2D raw spectrum, where the sky emission completely hides the emission from the observed object. The central panel shows the result after applying the previous sky emission subtraction. It can be seen how the emission of the object is now fully visible owing to the good correction applied. The lower panel shows the 1D spectrum for that object with really strong spectral lines. The spectroscopic redshifts of the objects are determined from the observed lines in the spectra. In this case, the redshift obtained is $z_{\rm spec} = 0.275$.

Flux calibration is the last step when working with 2D spectra, just before obtaining the 1D spectra. For each OB, at least one standard star was observed to perform that task. Calibration was applied using the standard IRAF procedure.

5.1.2. 1D spectra obtained

Once the results of the previous data reduction steps were deemed satisfactory, we proceeded to obtain the final 1D spectra, which allowed us to know the nature of the observed objects and their main physical characteristics in the optical domain.

As we have mentioned, each object was observed at least twice per OB. Furthermore, each mask was observed between three and four times with different grisms, as scheduled in Table 2. Each object should finally have between three and eight observations per grism. The latter scenario is possible because an object could be observed more than once, just to fill in possible free spaces in the masks.

The desired outcome was a single 1D spectrum per grism. An 'average-sigma-clipping' algorithm was applied to achieve this goal. The algorithm runs through each wavelength, discarding the flux points more than 2 σ from the median and averaging the

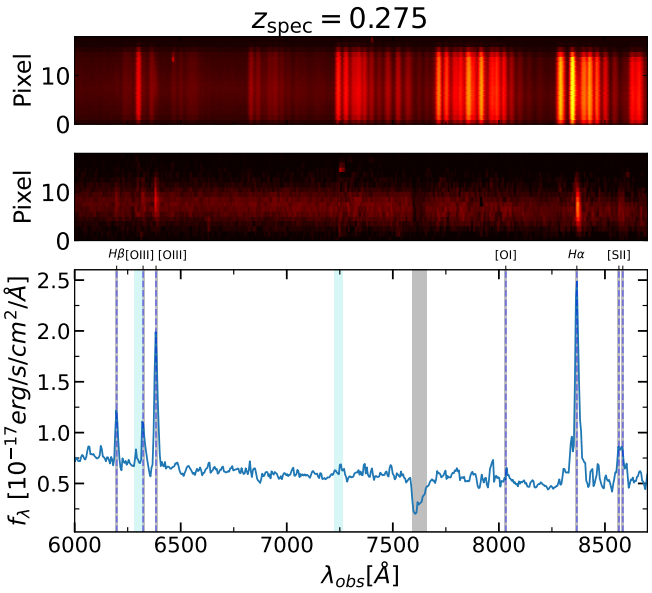

Fig. 4. Example of the sky emission correction process for an object of the faint subset. Top: slice of the observed 2D raw spectrum with a 3-arcsec slit using OSIRIS in MOS mode. The intensity of the emission from the sky makes it impossible to appreciate the contribution of the observed object. Mid: result obtained by applying the sky subtraction described in the text. This allowed us to recover the emission of the observed object. Bottom: final 1D spectrum obtained for this object. The redshift obtained is $z_{spec} = 0.275$ using the observed emission lines.

remaining points into a single point. The most common problems occurred when the object was observed in more than one mask and some of the observations were taken with a bright moon or a zero-order from a nearby slit with a bright target contaminating the spectrum. All these problems were managed using the average-sigma-clipping algorithm. In Fig. 5 we can see an example of the final 1D spectrum of an object at $z_{spec} = 0.421$, observed with the R500R and R500B grisms, represented by blue and red lines, respectively. The individual observations of this object with each grism, on which the average-sigma-clipping algorithm was applied, are plotted in grey. It can be seen how the algorithm has managed to correct for residuals from sky emission or cosmic ray detection.

5.2. Bright subset reduction

The reduction of the bright part was carried out using IRAF and the `hydra.dohydra`[8] package. This package was specifically developed for the reduction of data obtained with the HYDRA instrument. However, it allowed us to change its configuration and adapt it to the observations made with AF2. In this way, just by changing the parameters related to each instrument, this same tool was used for the different observing instruments of the bright part of our sample.

The `hydra.dohydra` task was used for scattered light subtraction, extraction, fibre throughput correction and wavelength calibration. It is a command language script that collects and combines the functions and parameters of many general-purpose tasks to provide a single complete data reduction path. The tool also allowed us to do a sky correction, but in this case, we only used the result of the combination of the fibres associated with the sky to obtain the average sky spectrum that we latter used as a final correction with the `Skycorr` [9] tool (Noll et al. 2014), which gave us better results in terms of the S/N quality of the final spectrum than those given by `dohydra`.

Before obtaining the final spectrum, the He and Ne lamp spectra were used for the wavelength calibration by employing an third-order Legendre polynomial for most of the objects in the range $0.03 \leq \mathrm{RMS} \leq 0.07$. Flux calibration of fibre instruments is complicated to apply, as it depends directly on the quantum efficiency of each fibre at the time of measurement and its relationship with the others; that is, it is a function that depends directly on time and is internally variable fibre to fibre in the same way. Adding to this the fact that the observing routine of the bright subset was also very complicated, we decided that it was not necessary to apply this correction. Thus, these data are used to determine properties that do not require flux calibration such as spectroscopic redshifts, line widths, and flux ratios.

We likewise removed cosmic rays from individual images using the IRAF `lacos-spec` task (van Dokkum 2001). We obtained the average spectrum of each of the objects observed in the R600R and R300B networks for AF2-WYFFOS and the R316R network in HYDRA with the same reduction method. Figure 6 shows an example of a 1D spectrum for a source in the bright subset observed with WYIN/HYDRA and the R316R grism.

6. Lockman-SpReSO catalogue

In this section, we present the first results obtained from the reduction of the Lockman-SpReSO data. Once the 1D spectra were acquired, the treatment was the same for objects in the bright part and those in the faint part, so the results shown in this section come from both subsets.

The whole process of obtaining a final spectrum per grism was executed automatically by the software infrastructure developed for this task described above. Although each component was tested and analysed, it was decided to conduct a visual inspection of all the results to look for possible errors in the process. Other important reasons for the visual inspection were to determine the spectroscopic redshifts of the objects by looking for the main spectral features, checking which spectra showed a stellar continuum and which did not, giving an initial quality flag of the spectral lines, and taking note of the objects with uncommon properties. In addition, further rounds of visual inspection were carried out after the fitting and measuring of the lines to make sure that everything worked correctly. The 'Object cont.' column in Table 4 shows the number of objects in which the stellar continuum was detected by the object category within Lockman-SpReSO.

The quality criterion imposed on the spectral lines in the visual inspection helped us to filter the objects according to that criterion. Possible values for the flag are: (1) no line appears in the spectrum; (2) the line has some error or is difficult to measure, or both (e.g. lines partially or totally under strong sky emission); (3) the line is weak but detectable; (4) the line is clearly visible with a moderate signal; and (5) an intense line with a high signal. This criterion defined the quality of the lines until we performed the line fits and obtained the equivalent widths (EWs) and S/N values.

[8] https://astro.uni-bonn.de/~sysstw/lfa_html/iraf/noao.imred.hydra.dohydra.html

[9] https://www.eso.org/sci/software/pipelines/skytools/skycorr

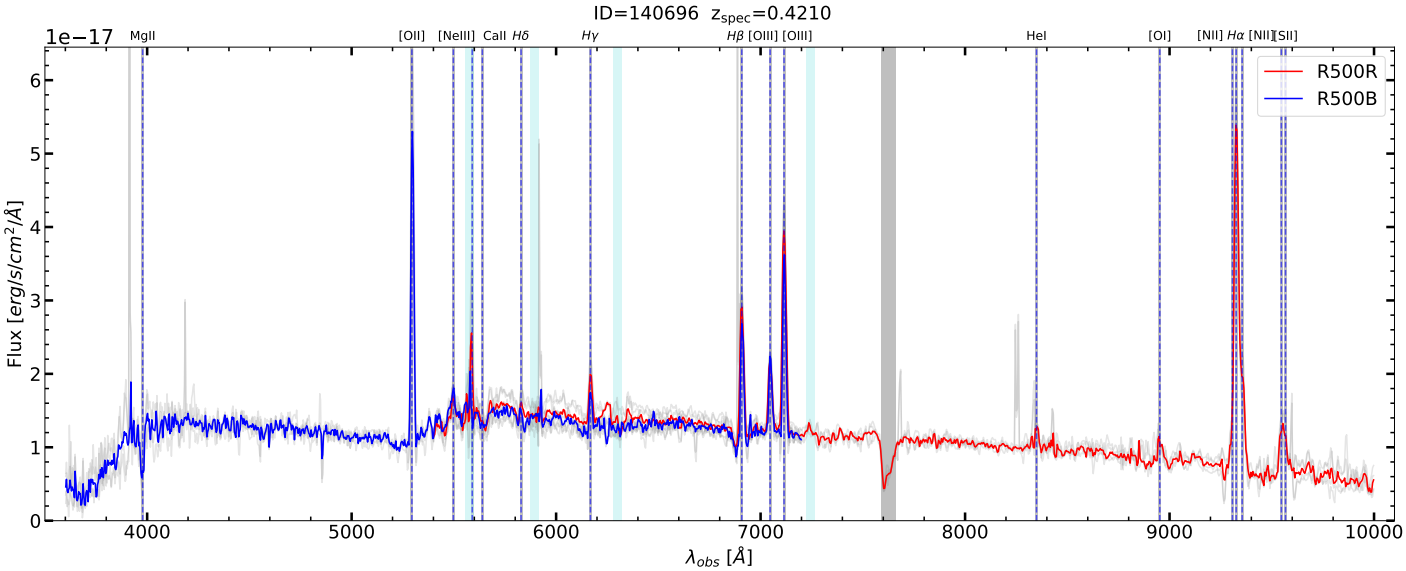

Fig. 5. Final 1D spectrum for an SFG in the faint subset at a spectroscopic redshift, $z_{\rm spec}$ = 0.421. Blue and red lines are the final spectra for the R500B and R500R grisms, respectively. Individual observations with the grisms are plotted in grey, where some residuals of sky emission or cosmic ray detection are visible, but not in the final spectra owing to the application of the 'average-sigma-clipping' algorithm. The vertical dashed blue lines mark the most prominent spectral features in this wavelength range at that redshift. The vertical cyan bands show the areas where sky emission is most important, and the wider grey band corresponds to the telluric absorption band.

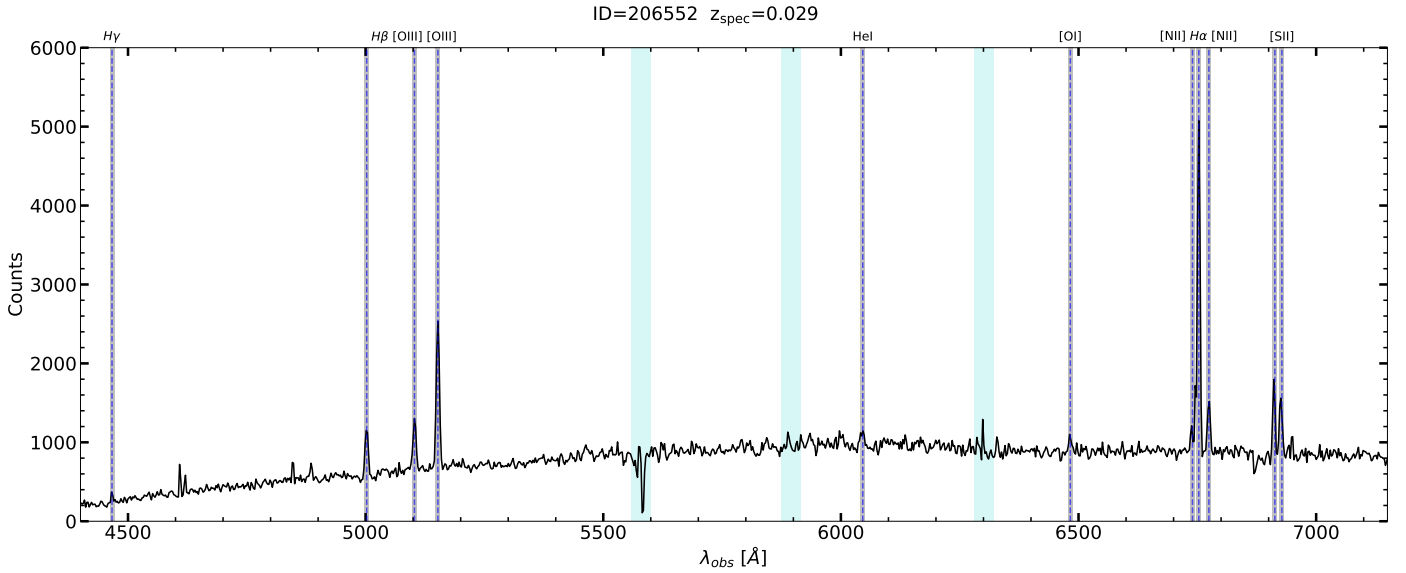

Fig. 6. Final 1D spectrum for a SFG in the bright subset at a spectroscopic redshift $z_{\rm spec}$ = 0.029. This object was observed with WYIN/HYDRA using the R316R grism. The vertical cyan bands show the areas where sky emission predominates.

6.1. Redshift determinations

To determine the spectroscopic redshifts, we imposed the condition that the spectrum should have at least two spectral features. The reason for doing so was to minimize, as much as possible, cases of false determinations due to ambiguous detection. It was also decided that, for objects with spectroscopic redshift in the literature, the presence of one line coinciding with the redshift would be the only condition. In total, 357 spectroscopic redshifts were obtained using both criteria and these are shown in Table 4, where they are split up by the object category and the subset to which they belong.

We verified how many of these objects had a previous spectroscopic redshift determination. To do so, we used Table 5 of FT12, which lists the works with spectroscopic studies that existed up to the date of publication for the LH field. In addition, we updated this information with those objects for which the SDSS survey provided redshifts, and finally we searched the NASA/IPAC Extragalactic Database[10] (NED) for the available information of the objects for which the redshift was determined in this work. A total of 89 objects already had their redshifts determined and coincided with those determined in this study. Hence, for 268 objects (~75%), the spectroscopic redshift was determined for the first time.

Figure 7 shows the comparison between the spectroscopic redshifts ($z_{\rm spec}$) measured in this study and the photometric redshifts ($z_{\rm phot}$) from FT12. The error bars plotted for $z_{\rm phot}$

[10] https://ned.ipac.caltech.edu

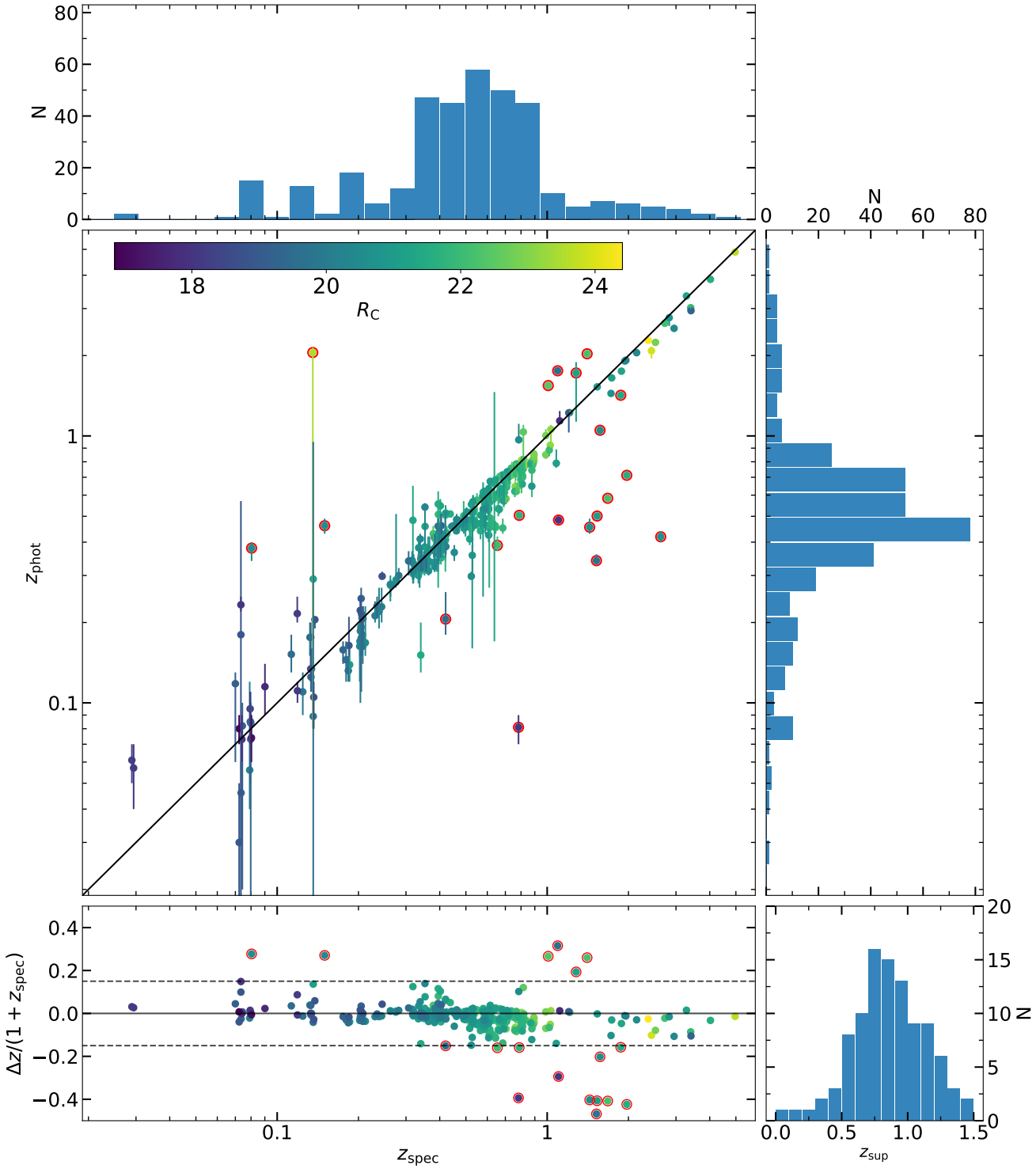

Fig. 7. Comparison between the photometric redshifts from FT12 and the spectroscopic redshifts measured in this study. The error bars in z_{phot} represent the range of 90% significance. The error bars in z_{spec} are not appreciable, and the median value is 3×10^{-4}. The colour code represents the R_C magnitude. In the bottom left panel, the difference between z_{phot} and z_{spec} divided by z_{spec} against z_{spec} is plotted. Dashed lines represent the limit in the outlier definition (see Sect. 6.1) and empty red circles represent the outliers. Because of the scale of the ordinate axis, there are points beyond the range of visualization. In the bottom right panel, the distribution of z_{sup} is shown.

represent the range of 90% significance reported by LePhare code (Arnouts et al. 1999; Ilbert et al. 2006). The errors in z_{spec} are also plotted, but are smaller than the data-point size, with a median value of 3×10^{-4}. The bottom panel shows the scatter of the difference between photometric and spectroscopic redshifts. The dashed grey lines represent the limit value defined by Hildebrandt et al. (2010) for flagging an outlier, defined by

$$\frac{|\Delta z|}{1 + z_{spec}} \geq 0.15,$$

where $|\Delta z| = |z_{phot} - z_{spec}|$. Applying this criterion, we found 4% of outliers in the spectroscopic redshift range $z_{spec} < 0.5$, 2% at

Table 4. Summary of the observed objects and the spectroscopic redshifts measured in this study, sorted by the preliminary categories described in Sect. 3.5.

CAT	Preliminary object Type	Catalogue	Observed	Observed faint	Observed bright	Object cont.	z_{spec}	z_{spec} faint	z_{spec} bright	z_{sup}
1	X-rayPoint + CatVarStars	45	43	41	6	39	30	28	4	3
2	High-Velocity Stars	93	85	14	80	80	1	–	1	–
3	Radio Galaxies	17	13	13	1	7	5	5	1	1
4	FIR	902	838	772	106	503	305	258	76	90
5	1 + 4	12	11	11	1	11	7	7	1	3
7	3 + 4	4	4	3	1	4	3	2	1	1
12	1 + 2	1	1	1	1	1	1	1	–	–
20	RedQSOs(W4)	23	21	21	–	2	2	2	–	–
21	RedQSOs(FIRST)	5	5	5	–	1	–	–	–	–
23	20 + 3	2	1	1	–	1	–	–	–	–
24	20 + 4	38	33	33	–	5	1	1	–	1
25	21 + 2	1	1	–	1	1	1	–	1	–
26	21 + 3	1	1	1	–	1	1	1	–	–
	TOTAL	1144	1057	916	197	656	357	305	85	99

Notes. The 'Catalogue' column represents all objects in Lockman-SpReSO. The 'Object cont.' column indicates how many objects per category have the stellar continuum detected in their spectra. The 'z_{sup}' column indicates the number of objects for which the redshift has been determined from a single spectral line. It should be noted that an object could be observed in the faint and the bright subset so that the sum may be greater than the total. The same happens to the columns with the spectroscopic redshift.

$0.5 < z_{spec} < 1.0$ and 34% for $z_{spec} > 1$. Outliers were marked with empty red circles in the Fig. 7. As expected, the determination of photometric redshifts is problematic for distant objects, even considering one out of three of the more distant objects as an outlier. Nevertheless, this result can be useful when using the photometric redshift to derive other quantities; for example, when the determination of the spectroscopic redshifts is not very clear because the spectral lines are not intense enough, or in cases where only one line is present in the spectrum, as we discuss below.

There are 105 objects in the LH-catalogue for which we detected only one emission-line feature in their spectra without any complementary information in the literature. An attempt was made to give a redshift value (z_{sup}) based on the properties of the line found (intensity, observed wavelength, photometric redshift, object magnitudes, and credibility). This preliminary analysis made it possible to give a reliable redshift for 99 objects with only one spectral line. The bottom right panel of Fig. 7 shows the distributions obtained for z_{sup}, where 71% of the objects have $z_{sup} < 1.0$ and the fraction of outliers in the photometric distribution are less than 3%, so a redshift based on the line found in the spectra is very helpful. For all other objects, the photometric redshift was used with care, more weight being given to the other information available for that object. The last column in Table 4 shows how the objects with z_{sup} are distributed among the different categories and their number. Figure 3 shows the distribution of the R_C magnitude for the objects with z_{spec} (blue) and z_{sup} (red) values measured in this study.

In some cases, the determination of the spectroscopic redshift allowed us to clarify the nature of the objects under study. For example, for some of the candidate CV stars we, determined a range of values for z_{spec} ($0.5263 \leq z_{spec} \leq 1.9387$), which made it clear that they cannot be stars, but distant compact sources.

Although we already had z_{spec} measured, the final value for each object was calculated as a weighted mean of each of the redshifts obtained for each line after fitting. This is discussed further in the next section.

6.2. Line measurement

To measure the lines, we fitted them with a non-linear least-squares minimization routine implemented in Python (*LMFIT*[11], Newville et al. 2014). Each line was fitted with a Gaussian profile plus a linear model to take into account possible continuum variations, all of which resulted in a total of five parameters to be determined: the position of the centre, the sigma, the amplitude for the Gaussian component, and the slope and intercept for the linear model.

The parameters were set free, but initial values were needed. The initial values were adapted and certain constraints were imposed for minimizing the computing time for each fitted spectral line. For example, as we knew z_{spec}, the centre of the line could be obtained and used as the initial value for the centre of the Gaussian component in the fitting process. One of the restrictions applied concerned the value for the amplitude of Hβ when the Hα line was available in the object's spectrum. The lines were usually fitted from the most intense to the least intense so that the value of the Hβ amplitude could not be greater than the calculated Hα amplitude, thus restricting the space of values that the fitting programme had to explore. The same was applied to the other lines of the Balmer series and even for forbidden lines pairs such as [O III] λ4959 Å and [O III] λ5007 Å and [N II] λ6548 Å and [N II] λ6583 Å among others. Another constraint applied was related to the σ of the Gaussians for the spectral lines that came from the same regions of the galaxy,such as the abovementioned forbidden line pairs. The initial σ value of the Gaussian with which we fitted their line profiles should be almost identical because their nature is the same. Another important parameter that remained fixed during the fitting and was external to it, was the wavelength window used for each line fit. The size of this region depended on the line type, the redshift, and the object type.

With the spectral resolution used in our observations, there were spectral lines very close in wavelength that could not be

[11] https://lmfit.github.io/lmfit-py/index.html#

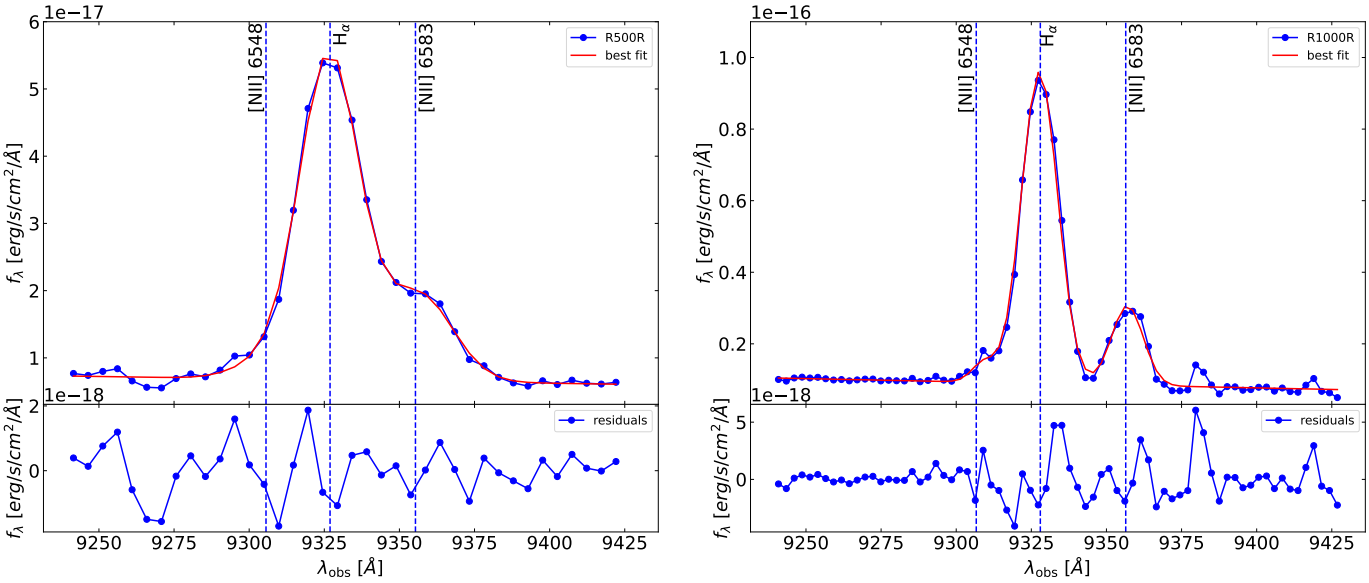

Fig. 8. Observed flux fitted to the same object of the faint subset with different grisms in the region of Hα + [N II] λ6548,6583. In the upper panels, blue dots and the blue line represent the observed flux, and the red line represents the best fit. The residuals of the fits are plotted in the bottom panels.

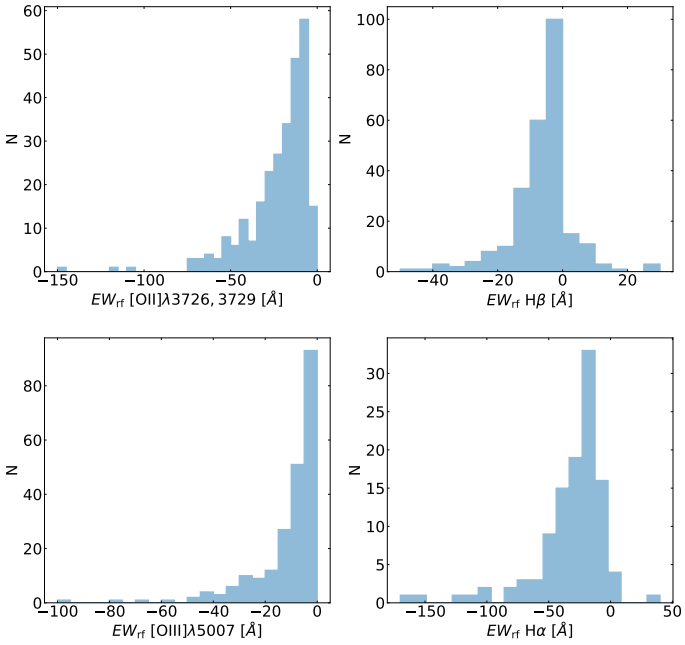

Fig. 9. Distribution of the rest-frame EWs for some of the most intense lines in the optical range for all the objects in the LH-catalogue with a measured spectroscopic redshift.

resolved because they were blended into a single feature. In these cases, we had to fit more than one Gaussian model at same time, one for each line plus a linear model. Even in cases where the resolution was sufficient to separate the components, they were so close that a separate fit was difficult to perform. One example is shown in Fig. 8, where the emission feature corresponds to a group of three spectral lines: Hα + [N II] λ6548,6583 Å. In the left panel, the grism used to observe the objects is the R500R, which has approximately half the resolution of the grism used on the right (the R1000R grism). In both cases, the blue dots are the observed flux, the red line is the best fit, and the bottom panels represent the residuals of both fits. It is important to note that, when observed with the lowest resolution, the components were blended into the same feature but that, when performing a fit, the three components were well recovered. In the right panel, the improvement of resolution allowed us to separate the [N II] λ6583 Å line from the Hα line, but not enough to perform independent fits. Another case in which multiple Gaussians were fitted simultaneously concerned objects with broad lines. As usual in these situations, we fitted one Gaussian for the narrow component and another for the broad component.

Figure 9 shows the rest-frame EWs obtained for some of the strongest lines in the optical range. By definition, emission lines have a negative EW, and absorption lines have a positive EW. For this reason, only the Hα and Hβ lines have positive values in Fig. 9 because the forbidden lines [O II] λ3726,3729 Å and [O III] λ5007 Å cannot be in absorption. Finally, in Table 5 a sample of the information available in the database is presented. Principal information for both the FT and PEP-catalogues is included.

6.3. Stellar-mass and IR luminosity distributions

In order to further characterize the scope of Lockman-SpReSO, basic parameters such as stellar mass and luminosity are essential. One of the most common ways to obtain them is by using SED fits to derive the physical properties of the objects from best-fit models. In the work of Shirley et al. (2019), the authors performed a unification of the fields studied by *Herschel* (1270 deg^2 and 170 million objects) and produced a general catalogue (HELP). In addition, they carried out SED-fitting studies on this catalogue (Małek et al. 2018) to determine the properties of the objects using a previously determined photometric redshift (Duncan et al. 2018).

Spectroscopic redshift gives us the advantage that, for a chosen cosmology, we know the distance of the object, which is very important for SED fitting and accurate translation of rest-frame models to the observed wavelength. Thus, a SED-fitting process was carried out to take advantage of the good photometric

Table 5. Sample of the information in Lockman-SpReSO

ID	RA	Dec	CAT	mag	mag err	FIR	FIR err	zphot	z	z err	z type	line	z line	z line err
units	(deg)	(deg)				(mJy)	(mJy)							
(1)	(2)	(3)	(4)	(5)	(6)	(7)	(8)	(9)	(10)	(11)	(12)	(13)	(14)	(15)
84957	163.07966	57.36440	4	19.085	0.002	260	30	0.082	0.07464	0.00006	spec	[O III] λ4959	0.0746	0.0002
												[O III] λ5007	0.0747	0.0001
												[S II] λ6716	0.0746	0.0002
												[S II] λ6731	0.0746	0.0002
128229	163.16754	57.61459	4	20.854	0.004	730	20	0.474	0.482938	0.000009	spec	Ca II λ3934	0.48505	-
												Ca II λ3968	0.48368	-
												Hβ	0.48305	0.00002
												Hα	0.48291	0.00001

ID	line obs. centre	line obs. centre err	line flux	line flux err	$FWHM$ line	line $FWHM$ err	line EW	line S/N	line quality
units	(Å)	(Å)	(erg s^{-1} cm^2 $\times$ 10^{-17})	(erg s^{-1} cm^2 $\times$ 10^{-17})	(Å)	(Å)	(Å)	(Å)	
(1)	(16)	(17)	(18)	(19)	(20)	(21)	(22)	(23)	(24)
84957	5329	1	17	3	21	3	−2.54	12	5
	5381.5	0.5	29	2	19	1	−7.03	19	5
	7217	1	15	2	17	2	−5.21	13	5
	7234	1	16	2	17	2	−5.75	14	5
128229	5842	-	2	-	2	-	1.32	1	1
	5887	-	2	-	3	-	1.85	1	1
	7209.5	0.1	38.2	0.9	10.0	0.2	−55.67	19	5
	9732.36	0.07	91	1	16.4	0.2	−241.34	35	5

Notes. Column 1 is the unique identification number for each object in the catalogue. Columns 2 and 3 give the optical coordinates (J2000) of the object. Coordinates of counterparts in other bands, available in FT12, and FIR coordinates are also included. Column 4 is the flag to indicate to which catalogue the object belongs: (1) X-ray point sources or CV star candidates; (2) high-velocity halo stars; (3) poorly studied radio galaxies; (4) FIR-objects; (5) objects in both CAT = 1 and CAT = 4; (7) objects in both CAT = 3 and CAT = 4; (12) objects in both CAT = 1 and CAT = 2; 20) very red QSOs selected using the Glikman et al. (2013) method; (21) very red QSOs selected using the Ross et al. (2015) criteria; (23) objects in both CAT = 20 and CAT = 3; (24) objects in both CAT = 20 and CAT = 4; (25) objects in both CAT = 21 and CAT = 2; and (26) objects in both CAT = 21 and CAT = 3. Columns 5 and 6 are the AB magnitudes and errors for al the bands available in FT12 from FUV (GALEX) to 8 μm (*Spitzer*; see Sect. 3 in FT12 for more details). Columns 7 and 8 give the FIR fluxes and errors at 24, 100, and 160 μm from the PEP work expressed in mJy (Lutz et al. 2011). Column 9 is the photometric redshift calculated in FT12. Columns 10 and 11 are the object redshift and the error measured in this work. Column 12 is the flag to mark how the redshift has been obtained. Two values are possible: 'spec' and 'sup'. Columns 13–24 are the main parameters of the fitted line using the model explained in the text. Each parameter of the Gaussian and line model is included in the table, as well as the EW and S/N obtained in the fitting process, and the quality criterion assigned in the first visual inspection.

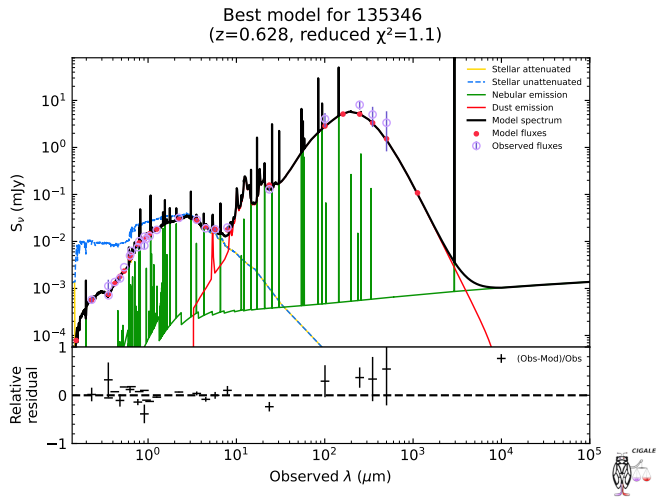

Fig. 10. Example of the best SED fit from CIGALE for a galaxy with $z_{\rm spec} = 0.628$ measured in this work. The best model is plotted as a solid black line, the photometric information of the object is plotted as empty violet circles, and the red filled circles are the fluxes obtained by the best model. The individual contributions of the models used are also plotted where the yellow line represents the attenuated stellar component, the blue dashed line is the unattenuated stellar component, the red line is the dust emission, and the green line illustrates the nebular emission. The relative residuals of the flux for the best model are plotted at the bottom.

coverage collected in FT12, plus the FIR information at 24, 100 and 160 μm, together with the spectroscopic redshift determined in this study.

As explained in Sect. 2, the Kondapally et al. (2021, hereafter K21) multi-wavelength catalogue includes recent observations of the LH field in the optical range. The SpARCS and RCSLenS surveys observed the LH field using both the CFHT/MegaCam instrument and the broad-band filters u, g, r, i, and z, also included in the FT12 catalogue from observations made with SDSS. The SpARCS and RCSLenS bands were therefore added to the Lockman-SpReSO catalogue by cross-matching both catalogues. The process was restricted to a maximum distance of 1.5 arcsec, the same as that used when we merged the PEP-catalogue with the FT- and OSIRIS-catalogues. It was found that 97% of the objects had a counterpart in K21 at an angular distance of less than 1.5 arcsec. Another reason for the fusion of catalogues was the completeness of the K21 sample with respect to the Lockman-SpReSO catalogue; in other words, for the u, g, r, i, and z bands, we have information for 30, 38, 40, 40, and 39% of the objects, respectively, within SDSS observations from FT12. In SpARCS and RCSLenS, we have information for 97, 97, 97, 86, and 94% of the objects. This effect is also present within the GALEX data in the FUV and NUV bands, with information for 13 and 27% of the objects, respectively, in the FT12 catalogue, and in K21 we have information for 74 and 74% of the objects, respectively.

To try to cover the FIR range as well as possible, the Lockman-SpReSO catalogue was cross-matched with the HELP catalogue in order to get the flux in the 250, 350, and 500 μm *Herschel*/SPIRE bands. These photometric points helped to model the IR emission on the red side of the peak for the vast majority of objects in our spectroscopic sample. We found that 98.9% of our objects have a HELP counterpart at an angular distance of less than 1.5 arcsec and 96.6% have a HELP counterpart at less than 0.7 arcsec. The maximum separation was chosen to be 1.5 arcsec. Also, for the SMGs in the LH-catalogue, the JCMT/AzTEC 1.1 mm band value of Michałowski et al. (2012) was taken into account. Table A.1 compiles all the filters used in the SED fittings.

Therefore, for objects in the LH-catalogue with a calculated spectroscopic redshift, we fitted their SEDs using the CIGALE software (Code Investigating GALaxy Emission, Burgarella et al. 2005, Boquien et al. 2019). This code allowed us to perform SED fits from the UV to the radio (X-ray regimes are included in the latest update; we do not, however, use them in this study, Yang et al. 2020, 2022). The code is based on the assumption of energy balance, that is to say that UV, optical and NIR light attenuated by dust is re-emitted in the redder ranges of the IR region. For each of the components involved in the SED fitting, CIGALE allowed us to choose between different models incorporated in the software. CIGALE performs a minimization of the χ^2 statistic to select the best-fitting model. In addition, CIGALE also performs a Bayesian-based study to obtain a probability distribution of the physical parameters derived from the SED fit using all the models and their errors. Thus, using the available photometric and the spectroscopic redshift, we were able to obtain essential information about the objects in the LH-catalogue.

For the stellar component, we used the `sfhdelayed` model, a star formation history (SFH) model with a nearly linear growth until a certain time (τ), after which it drops smoothly, plus an exponential starburst. This model allowed us to fit both late-type galaxies (small τ) and early-type galaxies (large τ; Boquien et al. 2019). As in our study we are working with mostly infrared-emitting galaxies, we adopted a recent starburst to model the young population of stars (i.e. SFGs). The intrinsic component of the stars was computed using the library of (Bruzual & Charlot 2003, model `bc03`) with infra- and supra-solar metallicities and the IMF of Chabrier (2003). Nebular emission was also taken into account by adding the model to the CIGALE calculation. Extinction was incorporated using the `dustatt_modified_starburst` model, which is based on the extinction law of Calzetti et al. (2000), to which the curve of Leitherer et al. (2002) between the Lyman break and 150 nm was added; in addition, both the slope and the UV bump could be modified. For the dust contribution, we used the Dale et al. (2014) templates (`dale2014` model) based on nearby SFGs that also added an AGN component. More sophisticated AGN models were not used because the purpose of these SED fits was the characterization of the Lockman-SpReSO sample as a whole, while assuming the AGN fraction-free parameter provided by the models of Dale et al. (2014) were adequate. Future studies of the Lockman-SpReSO project will carry out detailed investigations on object classification, and more individualized SED fits will study each type of object more precisely. A summary of the selected models and the set of values used for the parameters of the models are given in Table B.1. An example of the SED-fitting process is shown in Fig. 10, where the best fit obtained for a source in the Lockman-SpReSO catalogue is plotted together with the contribution of each of the models used. The lower part of Fig. 10 shows the relative residuals of the flux obtained in the fit.

Most of our objects were selected for their emission in the *Herschel* bands (i.e. they are FIR emitters). Therefore, one of the first parameters to determine and describe the sample is the total IR luminosity ($L_{\rm TIR}$). There are different methods for obtaining the IR luminosity. Some of them derive $L_{\rm TIR}$ by using a monochromatic proxy (Chary & Elbaz 2001), and others, as in the work developed by Galametz et al. (2013, see

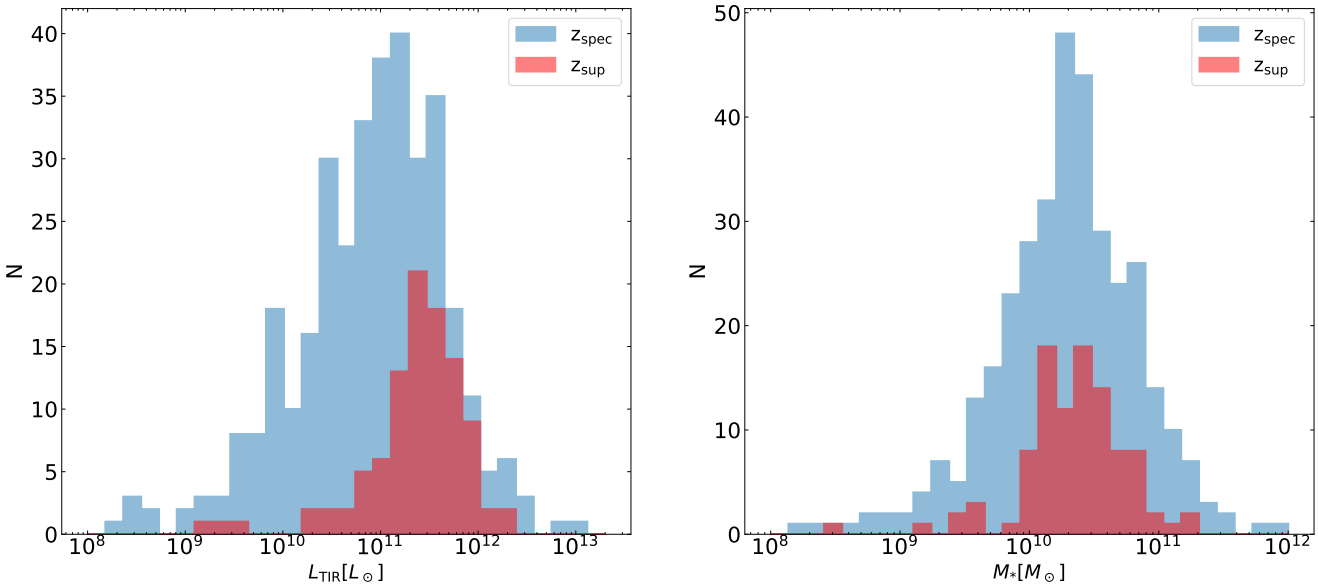

Fig. 11. Distribution of the total IR luminosity of the objects in the LH-catalogue derived from the SED fit using CIGALE (left). Objects with z_{spec} are in blue, and the sample with z_{sup} is in red. The distribution of the stellar mass for the same objects was also derived from SED fitting (right).

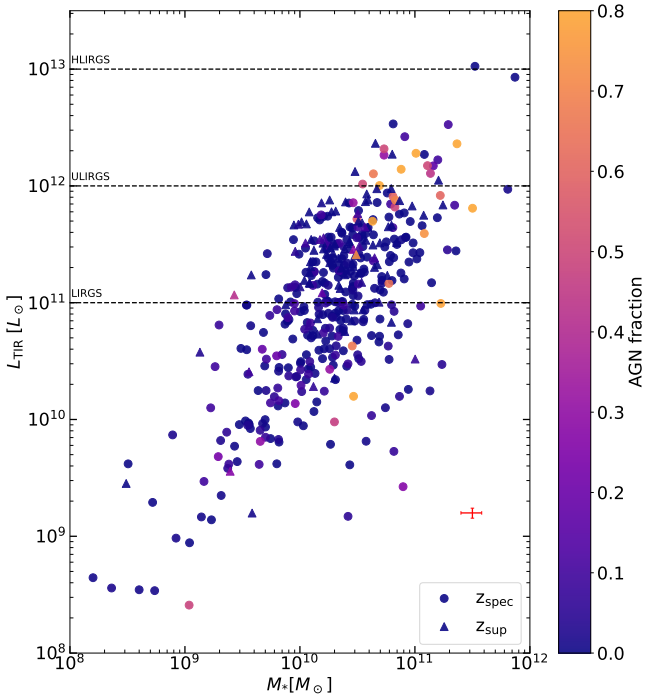

Fig. 12. Representation of the stellar mass and IR luminosity, both obtained from the CIGALE fits. The circles indicate the objects with z_{spec} calculated in this work, and the triangles represent the z_{sup} objects. The median error on both axes is shown in red. The colour code indicates the fraction of AGN we obtained from the SED fits using the IR templates of Dale et al. (2014). The boundary lines on which the LIRG, ULIRG, and HLIRG sources are defined are highlighted.

also the references therein), the IR luminosity is obtained from an analytic expression based on *Spitzer* and *Herschel* data. These studies are usually designed to use the rest-frame bands, which means that when we study distant galaxies, the bands are redshifted, and a correction is needed.

To surmount this difficulty, as we had the SED fits available, we could integrate the luminosity of the best fit in the IR range (usually between 8 and 1 000 µm) and directly obtain the L_{TIR}. CIGALE already returns this luminosity and its error both from the best-fitting model and from the Bayesian approach. The left panel of Fig. 11 shows the IR luminosity distribution obtained for the z_{spec} sample in blue and for the z_{sup} sample in red. We find that most of our objects (55%) are in the LIRG regime ($L_{TIR} > 10^{11} L_{\odot}$), 6% are ULIRGs ($L_{TIR} > 10^{12} L_{\odot}$), and less than 1% are hyper-luminous infrared galaxies (HLIRGs,$L_{TIR} > 10^{13} L_{\odot}$).

Another parameter of importance for the general description of the sample is the stellar mass (M_*) of the objects. As for the IR luminosity, we used the value derived from the SED fit with CIGALE. Figure 11 (right panel) shows the mass distribution obtained for the z_{spec} objects in blue and for the z_{sup}sample in red. Considering both distributions, 75% of the objects have stellar masses greater than $\log(M_*/M_{\odot}) = 9.93$, 25% of them have a stellar mass greater $\log(M_*/M_{\odot}) = 10.54$, and the median value is $\log(M_*/M_{\odot}) = 10.28$.

Figure 12 plots M_* versus L_{TIR} obtained from the SED fittings by colour coding the AGN fraction derived from the IR templates used (Dale et al. 2014). It can be seen that the AGN fraction increases for the most luminous galaxies, which in turn are the most massive. This would be in agreement with the findings of Veilleux et al. (1995), who showed that the probability of the source of ionization being due to nuclear activity increases with IR luminosity.

The information studied in this section will be used in forthcoming papers of the Lockman-SpReSO series. Stellar mass, IR luminosity, line measurements, and SED fits will play a key role in studying the physical properties of both FIR sources and secondary catalogue objects.

7. Summary and timeline

This paper presents the Lockman-SpReSO project and focuses on its scientific motivation, target selection, observational design and the first results from the reduction of the spectra. Lockman-SpReSO was created to try to fill the notable lack of spectroscopic information in one of the best large-scale fields, the Lockman Hole field, for high depth studies owing to its low

hydrogen column density. In this way, spectroscopic redshifts and the main physical parameters such as gas metallicity, extinctions, SFR, and even SED fits can be studied for a specific selection of targets.

The Lockman-SpReSO catalogue contains 1144 sources of various kinds. All Lockman-SpReSO observations were carried out from 2014 to 2018, and all data have been satisfactorily reduced. The spectroscopic data obtained have been analysed and have produced spectroscopic redshifts for a total of 357 objects, from $z_{\rm spec}$ = 0.0290 to $z_{\rm spec}$ = 4.9671. For 99 objects with only one characteristic feature in their spectra, an attempt was made to determine the redshift and resulted in a redshift range from $z_{\rm sup}$ = 0.0973 to $z_{\rm sup}$ = 1.4470. Furthermore, for those objects whose redshift was determined, only ∼25% have a spectroscopic redshift available in the literature. Finally, the spectral lines of the objects were measured in order to establish the initial database of Lockman-SpReSO.

We performed an SED-fitting process using the spectroscopic redshift and CIGALE software, taking advantage of the wide photometric spectral coverage from the FUV to the FIR. The fit results allowed us to derive the IR luminosities and the stellar masses of the sources. Based on the $L_{\rm TIR}$ values derived from the SED fitting, about 55% of the objects are LIRGs, 6% are ULIRGs and less than 1% are HLIRGs. The stellar mass distribution has a minimum and a maximum value of $\log(M_*/M_\odot)$ = 7.65 and $\log(M_*/M_\odot)$ = 12.07, respectively, with a median value of $\log(M_*/M_\odot)$ = 10.28.

A data release is expected for late 2022 or early 2023, where the results of the type classification, extinction, gas metallicity and SFR determinations for the objects on which we have sufficient information will be presented. Studies will also be carried out in order to analyse the different classes of sources in the secondary catalogues. We shall try to perform observations in the NIR using other facilities for the objects with known redshifts that have emission lines in that wavelength range.

Acknowledgements. We thank the anonymous referee for their useful report. This work was supported by the Evolution of Galaxies project, of references AYA2017-88007-C3-1-P, AYA2017-88007-C3-2-P, AYA2018-RTI-096188-BI00, PID2019-107408GB-C41, PID2019-106027GB-C41, PID2021-122544NB-C41, and MDM-2017-0737 (Unidad de Excelencia María de Maeztu, CAB), within the *Programa estatal de fomento de la investigación científica y técnica de excelencia del Plan Estatal de Investigación Científica y Técnica y de Innovación (2013-2016)* of the Spanish Ministry of Science and Innovation/State Agency of Research MCIN/AEI/ 10.13039/501100011033 and by 'ERDF A way of making Europe'. This article is based on observations made with the Gran Telescopio Canarias (GTC) at Roque de los Muchachos Observatory on the island of La Palma, with the *Willian Herschel* Telescope (WHT) at Roque de los Muchachos Observatory on the island of La Palma and on observations at Kitt Peak National Observatory, NSF's National Optical-Infrared Astronomy Research Laboratory (NOIRLab Prop. ID: 2018A-0056; PI: González-Serrano, J.I.), which is operated by the Association of Universities for Research in Astronomy (AURA) under a cooperative agreement with the National Science Foundation. This research has made use of the NASA/IPAC Extragalactic Database (NED), which is funded by the National Aeronautics and Space Administration and operated by the California Institute of Technology. J.N. acknowledges the support of the National Science Centre, Poland through the SONATA BIS grant 2018/30/E/ST9/00208. E.B. and I.C.G. acknowledge support from DGAPA-UNAM grant IN113320. M.P. acknowledges the support from the Space Science and Geospatial Institute under the Ethiopian Ministry of Innovation and Technology (MInT). E.A. and M.P. acknowledge the support from the State Agency for Research of the Spanish MCIU through the Center of Excellence Severo Ochoa award to the Instituto de Astrofísica de Andalucía (SEV-2017-0709). J.A.D. acknowledges the support of the Universidad de La Laguna through the Proyecto de Internacionalización y Excelencia, Programa Tomás de Iriarte 2022. The authors thank Terry Mahoney (at the IAC's Scientific Editorial Service) for his substantial improvements of the manuscript.

References

Abareshi, B., Aguilar, J., Ahlen, S., et al. 2022, AJ, 164, 207
Abdurro'uf, Accetta, K., Aerts, C., et al. 2022, ApJS, 259, 35
Alam, S., Albareti, F. D., Allende Prieto, C., et al. 2015, ApJS, 219, 12
Armus, L., Heckman, T. M., & Miley, G. K. 1989, ApJ, 347, 727
Arnouts, S., Cristiani, S., Moscardini, L., et al. 1999, MNRAS, 310, 540
Austermann, J. E., Dunlop, J. S., Perera, T. A., et al. 2010, MNRAS, 401, 160
Baldwin, J. A., Phillips, M. M., & Terlevich, R. 1981, PASP, 93, 5
Becker, R. H., White, R. L., & Helfand, D. J. 1995, ApJ, 450, 559
Benitez, N., Dupke, R., Moles, M., et al. 2014, arXiv e-prints [arXiv:1403.5237]
Berta, S., Lonsdale, C. J., Siana, B., et al. 2007, A&A, 467, 565
Bertin, E., & Arnouts, S. 1996, A&AS, 117, 393
Bongiovanni, Á., Ramón-Pérez, M., Pérez García, A. M., et al. 2019, A&A, 631, A9
Boquien, M., Burgarella, D., Roehlly, Y., et al. 2019, A&A, 622, A103
Brown, M. J. I., Jarrett, T. H., & Cluver, M. E. 2014, PASA, 31, e049
Brunner, H., Cappelluti, N., Hasinger, G., et al. 2008, A&A, 479, 283
Bruzual, G., & Charlot, S. 2003, MNRAS, 344, 1000
Buat, V., Corre, D., Boquien, M., & Małek, K. 2020, IAU Symp., 341, 70
Burgarella, D., Buat, V., & Iglesias-Páramo, J. 2005, MNRAS, 360, 1413
Calzetti, D., Armus, L., Bohlin, R. C., et al. 2000, ApJ, 533, 682
Casey, C. M., Berta, S., Béthermin, M., et al. 2012, ApJ, 761, 140
Cepa, J., Aguiar, M., Escalera, V. G., et al. 2000, Proc. SPIE, 4008, 623
Chabrier, G. 2003, PASP, 115, 763
Chapman, S. C., Windhorst, R., Odewahn, S., Yan, H., & Conselice, C. 2003, ApJ, 599, 92
Chapman, S. C., Blain, A. W., Smail, I., & Ivison, R. J. 2005, ApJ, 622, 772
Chary, R., & Elbaz, D. 2001, ApJ, 556, 562
Ciliegi, P., Zamorani, G., Hasinger, G., et al. 2003, A&A, 398, 901
Coppin, K., Pope, A., Menéndez-Delmestre, K., Alexander, D. M., & Dunlop, J. 2010, AIP Conf. Ser., 1240, 80
Dale, D. A., Helou, G., Magdis, G. E., et al. 2014, ApJ, 784, 83
Davis, M., Guhathakurta, P., Konidaris, N. P., et al. 2007, ApJ, 660, L1
Dawson, K. S., Schlegel, D. J., Ahn, C. P., et al. 2013, AJ, 145, 10
de Zotti, G., Massardi, M., Negrello, M., & Wall, J. 2010, A&ARev., 18, 1
Dey, A., Schlegel, D. J., Lang, D., et al. 2019, AJ, 157, 168
Dickey, J. M., & Lockman, F. J. 1990, ARA&A, 28, 215
Djorgovski, S. G., Mahabal, A. A., Drake, A. J., et al. 2012, IAU Symp., 285, 141
Domínquez Palmero, L., Cano, D., Fariña, C., et al. 2014, SPIE Conf. Ser., 9147, 914778
Drake, A. J., Gänsicke, B. T., Djorgovski, S. G., et al. 2014, MNRAS, 441, 1186
Duncan, K. J., Brown, M. J. I., Williams, W. L., et al. 2018, MNRAS, 473, 2655
Eales, S., Smith, D., Bourne, N., et al. 2018, MNRAS, 473, 3507
Egami, E., Bock, J., Dole, H., et al. 2008, Ultra-Deep MIPS Imaging of the Lockman Hole (USA: Spitzer Proposal)
Eriksen, M., Alarcon, A., Gaztanaga, E., et al. 2019, MNRAS, 484, 4200
Evans, I. N., Primini, F. A., Glotfelty, K. J., et al. 2010, ApJS, 189, 37
Ferruit, P., Jakobsen, P., Giardino, G., et al. 2022, A&A, 661, A81
Fotopoulou, S., Salvato, M., Hasinger, G., et al. 2012, ApJS, 198, 1
Galametz, M., Kennicutt, R. C., Calzetti, D., et al. 2013, MNRAS, 431, 1956
Geach, J. E., Dunlop, J. S., Halpern, M., et al. 2017, MNRAS, 465, 1789
Glikman, E., Urrutia, T., Lacy, M., et al. 2013, ApJ, 778, 127
Gómez-González, V. M. A., Mayya, Y. D., & Rosa-González, D. 2016, MNRAS, 460, 1555
Gómez-Velarde, G., García-Alvarez, D., & Cabrerra-Lavers, 2016 ASP Conf. Ser., 507, 191
González-Serrano, J. I., Sánchez-Portal, M., Castañeda, H., et al. 2004, Exp. Astron., 18, 65
Griffin, M. J., Abergel, A., Abreu, A., et al. 2010, A&A, 518, L3
Hasinger, G., Altieri, B., Arnaud, M., et al. 2001, A&A, 365, L45
Henry, J. P., Aoki, K., Finoguenov, A., et al. 2014, ApJ, 780, 58
Henry, J. P., Salvato, M., Finoguenov, A., et al. 2010, ApJ, 725, 615
Herrera-Camus, R., Sturm, E., Graciá-Carpio, J., et al. 2018, ApJ, 861, 95
Hildebrandt, H., Arnouts, S., Capak, P., et al. 2010, A&A, 523, A31
Hildebrandt, H., Choi, A., Heymans, C., et al. 2016, MNRAS, 463, 635
Ilbert, O., Arnouts, S., McCracken, H. J., et al. 2006, A&A, 457, 841
Ivison, R. J., Swinbank, A. M., Smail, I., et al. 2013, ApJ, 772, 137
Kennicutt, Robert C., J. 1998, ARA&A, 36, 189
Kondapally, R., Best, P. N., Hardcastle, M. J., et al. 2021, A&A, 648, A3
Lara-López, M. A., Cepa, J., Bongiovanni, A., et al. 2010, A&A, 521, L53
Le Fèvre, O., Cassata, P., Cucciati, O., et al. 2013, A&A, 559, A14
Lehmann, I., Hasinger, G., Schmidt, M., et al. 2001, A&A, 371, 833
Leitherer, C., Li, I. H., Calzetti, D., & Heckman, T. M. 2002, ApJS, 140, 303
Lilly, S. J., Le Fèvre, O., Renzini, A., & Zamorani, G. 2007, ApJS, 172, 70

Lockman, F. J., Jahoda, K., & McCammon, D. 1986, ApJ, 302, 432
Lonsdale, C. J., Smith, H. E., Rowan-Robinson, M., et al. 2003, PASP, 115, 897
Lutz, D., Poglitsch, A., Altieri, B., et al. 2011, A&A, 532, A90
Mahoro, A., Pović, M., & Nkundabakura, P. 2017, MNRAS, 471, 3226
Mainieri, V., Bergeron, J., Hasinger, G., et al. 2002, A&A, 393, 425
Małek, K., Buat, V., Roehlly, Y., et al. 2018, A&A, 620, A50
Maragkoudakis, A., Zezas, A., Ashby, M. L. N., & Willner, S. P. 2018, MNRAS, 475, 1485
McLure, R. J., Pentericci, L., Cimatti, A., et al. 2018, MNRAS, 479, 25
Michałowski, M. J., Dunlop, J. S., Ivison, R. J., et al. 2012, MNRAS, 426, 1845
Mitchell-Wynne, K., Cooray, A., Gong, Y., et al. 2012, ApJ, 753, 23
Moles, M., Benítez, N., Aguerri, J. A. L., et al. 2008, AJ, 136, 1325
Mortier, A. M. J., Serjeant, S., Dunlop, J. S., et al. 2005, MNRAS, 363, 563
Negrello, M., Hopwood, R., De Zotti, G., et al. 2010, Science, 330, 800
Newville, M., Stensitzki, T., Allen, D. B., & Ingargiola, A. 2014, https://doi.org/10.5281/zenodo.11813
Noll, S., Kausch, W., Kimeswenger, S., et al. 2014, A&A, 567, A25
Oke, J. B., & Gunn, J. E. 1983, ApJ, 266, 713
Oliver, S. J., Wang, L., Smith, A. J., et al. 2010, A&A, 518, L21
Ovcharov, E. P., Nedialkov, P. L., Valcheva, A. T., et al. 2008, MNRAS, 386, 819
Padovani, P. 2016, A&ARev., 24, 13
Patel, H., Clements, D. L., Rowan-Robinson, M., & Vaccari, M. 2011, MNRAS, 415, 1738
Pereira-Santaella, M., Rigopoulou, D., Farrah, D., Lebouteiller, V., & Li, J. 2017, MNRAS, 470, 1218
Poglitsch, A., Waelkens, C., Geis, N., et al. 2010, A&A, 518, L2
Pović, M., Sánchez-Portal, M., Pérez García, A. M., et al. 2009a, ApJ, 706, 810
Pović, M., Sánchez-Portal, M., Pérez García, A. M., et al. 2009b, ApJ, 702, L51
Ramón-Pérez, M., Bongiovanni, Á., Pérez García, A. M., et al. 2019, A&A, 631, A11
Rosario, D. J., Mendel, J. T., Ellison, S. L., Lutz, D., & Trump, J. R. 2016, MNRAS, 457, 2703
Ross, N. P., Hamann, F., Zakamska, N. L., et al. 2015, MNRAS, 453, 3932
Rovilos, E., Fotopoulou, S., Salvato, M., et al. 2011, A&A, 529, A135
Schmidt, M., Hasinger, G., Gunn, J., et al. 1998, A&A, 329, 495
Shimwell, T. W., Röttgering, H. J. A., Best, P. N., et al. 2017, A&A, 598, A104
Shirley, R., Roehlly, Y., Hurley, P. D., et al. 2019, MNRAS, 490, 634
Smart, R. L., & Nicastro, L. 2014, A&A, 570, A87
Stasińska, G., Cid Fernandes, R., Mateus, A., Sodré, L., & Asari, N. V. 2006, MNRAS, 371, 972
Swinbank, A. M., Smail, I., Chapman, S. C., et al. 2004, ApJ, 617, 64
van Dokkum, P. G. 2001, PASP, 113, 1420
van Haarlem, M. P., Wise, M. W., Gunst, A. W., et al. 2013, A&A, 556, A2
Vaz Cedillo, J. J., Bongiovanni, A. M., Ederoclite, A., et al. 2018, SPIE Conf. Ser., 10705, 107050X
Veilleux, S., Kim, D. C., Sanders, D. B., Mazzarella, J. M., & Soifer, B. T. 1995, ApJS, 98, 171
Viaene, S., Baes, M., Bendo, G., et al. 2016, A&A, 586, A13
Wilson, G., Muzzin, A., Yee, H. K. C., et al. 2009, ApJ, 698, 1943
Wolf, C., Meisenheimer, K., Rix, H. W., et al. 2003, A&A, 401, 73
Wright, E. L., Eisenhardt, P. R. M., Mainzer, A. K., et al. 2010, AJ, 140, 1868
Yang, G., Boquien, M., Buat, V., et al. 2020, MNRAS, 491, 740
Yang, G., Boquien, M., Brandt, W. N., et al. 2022, ApJ, 927, 192
York, D. G., Adelman, J., Anderson, John E., J., et al. 2000, AJ, 120, 1579
Zappacosta, L., Maiolino, R., Finoguenov, A., et al. 2005, A&A, 434, 801

[1] Instituto de Astrofísica de Canarias, 38205 La Laguna, Tenerife, Spain
e-mail: mauro.gonzalez@iac.es; mauromarago@gmail.com
[2] Departamento de Astrofísica, Universidad de La Laguna (ULL), 38205 La Laguna, Tenerife, Spain
[3] Fundación Galileo Galilei-INAF Rambla José Ana Fernández Pérez, 7, 38712 Breña Baja, Tenerife, Spain
[4] Asociación Astrofísica para la Promoción de la Investigación, Instrumentación y su Desarrollo, ASPID, 38205 La Laguna, Tenerife, Spain
[5] Instituto de Astronomía, Universidad Nacional Autónoma de México, Apdo. Postal 70-264, 04510 Ciudad de México, Mexico
[6] Institut de Radioastronomie Millimétrique (IRAM), Av. Divina Pastora 7, Núcleo Central 18012, Granada, Spain
[7] Centro de Astrobiología (CSIC/INTA), 28692 ESAC Campus, Villanueva de la Cañada, Madrid, Spain
[8] Instituto de Física de Cantabria (CSIC-Universidad de Cantabria), 39005, Santander, Spain
[9] Instituto de Astrofísica de Andalucía (CSIC), 18080 Granada, Spain
[10] Departamento de Física de la Tierra y Astrofísica, Instituto de Física de Partículas y del Cosmos, IPARCOS. Universidad Complutense de Madrid (UCM), 28040 Madrid, Spain
[11] Astronomical Observatory Institute, Faculty of Physics, Adam Mickiewicz University, ul. Słoneczna 36, 60-286 Poznań, Poland
[12] ISDEFE for European Space Astronomy Centre (ESAC)/ESA, PO Box 78, 28690 Villanueva de la Cañada, Madrid, Spain
[13] Space Science and Geospatial Institute (SSGI), Entoto Observatory and Research Center (EORC), Astronomy and Astrophysics Research Division, PO Box 33679, Addis Abbaba, Ethiopia
[14] Physics Department, Mbarara University of Science and Technology (MUST), Mbarara, Uganda
[15] Centro de Estudios de Física del Cosmos de Aragón (CEFCA), Plaza San Juan 1, 44001 Teruel, Spain

Appendix A: Photometric information

Table A.1. Photometric filters used in the SED-fitting process and the number of objects with information in each of them.

Telescope	Instrument	Filter				
GALEX	*GALEX*	FUV 842			NUV 842	
LBT	LBCB	U 1072			B 1040	
	LBCR	V 1011		Y 1011		z 1028
Subaru	Suprime	Rc 1144		Ic 1081		z 1134
SLOAN	SLOAN	u 350	g 442	r 470	i 470	z 454
CFHT	MegaCAM	u 1102	g 1118	r 1105	i 980	z 1069
UKIRT	WFCAM	J 1106			K 1107	
Spitzer	IRAC	3.6 µm 972	4.5 µm 931	5.8 µm 952	8 µm 909	
	MIPS	24 µm 956				
Herschel	PACS	100 µm 760			160 µm 606	
	SPIRE	250 µm 889		350 µm 889	500 µm 889	
JCMT	AzTEC	1.1 mm 18				

Appendix B: CIGALE input parameters

Table B.1. Schedule of the parameters and models used in the CIGALE SED fitting.

Model used	Parameter information	Values
SFH:	e-folding time main population	250, 500, 1000, 2000, 4000, 6000, 8000 [Myrs]
delayed SFH with	age of the main population	250, 500, 1500, 4000, 8000, 10000 [Myrs]
optional exponential burst	e-folding time of late burst	25, 50 [Myrs]
	age of the late burst	10, 20, 50 [Myrs]
	mass fraction late burst	0.0, 0.01, 0.05
SSP:	IMF	Chabrier (2003)
Bruzual & Charlot (2003)	metallicity	0.0001, 0.0004, 0.004, 0.008, 0.02, 0.05
Dust attenuation:	E(B-V) lines	0, 0.1, 0.2, 0.3, ..., 2.4, 2.5
power law modified	E(B-V) factor (line to continuum)	0.44
Calzetti et al. (2000)	UV bump wavelength	217.5 [nm]
	UV bump FWHM	35
	UV bump amplitude	0, 1.5, 3
	Power law modification slope	-0.2, 0
	R_V	3.1
Dust emission	AGN fraction	0, 0.1, 0.3, 0.5, 0.8, 0.9
Dale et al. (2014)	Alpha slope	0.125, 0.625, 1.0, 1.25, 1.5, 1.75, 2.0, 2.5, 3.0, 3.5, 4.0

3

The Lockman–SpReSO project. Main properties of infrared selected star-forming galaxies.

In this chapter a comprehensive study is conducted using galaxy data from the Lockman–SpReSO project, which comprises a sample of galaxies observed through optical spectroscopy after being FIR selected. Specifically the study focuses on star-forming galaxies (SFGs), mainly within the domain of LIRGs. For these galaxies parameters like extinction, star formation rate (SFR), and metallicity are studied.

The idea is to examine how these properties evolve with respect to each other and compare them to those of low-redshift FIR and non-FIR-selected galaxy samples. In order to minimise contamination from AGN, distinct selection criteria are applied. Various methods are employed to estimate the dust extinction, SFR, and gas-phase metallicity for the SFGs. We investigate correlations between SFRs and M_*, as well as how metallicity evolves based on M_*. Furthermore, the analysis encompasses the investigation of the three-dimensional relationship between M_*, SFR, and metallicity.

Out of the initial spectroscopic data set of 409 objects, we are able to identify and remove 69 AGNs which finally brings us down to a sample of 340 SFGs. The study reveals that the FIR-selected SFGs from Lockman–SpReSO show signs of evolution at redshifts $z > 0.4$, deviating above the MS, particularly within the starburst galaxy region. In addition, the expected behaviour of sSFR with redshift, flattening with increasing redshift, is barely observed, especially for $\log M_*(M_\odot) \geq 10.5$. Furthermore, FIR-selected SFGs exhibit lower metallicities than expected based on their M_*

and redshift. Finally, the investigation of the three-dimensional M_*–SFR–metallicity relation indicates consistency with existing literature.

The contents of this chapter have been published as González-Otero et al. (2024a).

Astronomy & Astrophysics manuscript no. main
April 21, 2024

The Lockman–SpReSO project

Main properties of infrared selected star-forming galaxies

Mauro González-Otero[1,2,3], Jordi Cepa[1,2,3], Carmen P. Padilla-Torres[1,2,3,4], Maritza A. Lara-López[5], J. Jesús González[6], Ángel Bongiovanni[7,3], Bernabé Cedrés[7,3], Miguel Cerviño[8], Irene Cruz-González[6], Mauricio Elías-Chávez[6], Martín Herrera-Endoqui[6], Héctor J. Ibarra-Medel[6], Yair Krongold[6], Jakub Nadolny[9], C. Alenka Negrete[6], Ana María Pérez García[8,3], José A. de Diego[6], J. Ignacio González-Serrano[10,3], Héctor Hernádez-Toledo[6], Ricardo Pérez-Martínez[11,3], and Miguel Sánchez-Portal[7,3]

[1] Instituto de Astrofísica de Canarias, E-38205 La Laguna, Tenerife, Spain
[2] Departamento de Astrofísica, Universidad de La Laguna (ULL), E-38205 La Laguna, Tenerife, Spain
[3] Asociación Astrofísica para la Promoción de la Investigación, Instrumentación y su Desarrollo, ASPID, E-38205 La Laguna, Tenerife, Spain
[4] Fundación Galileo Galilei-INAF Rambla José Ana Fernández Pérez, 7, E-38712 Breña Baja, Tenerife, Spain
[5] Departamento de Física de la Tierra y Astrofísica, Instituto de Física de Partículas y del Cosmos, IPARCOS. Universidad Complutense de Madrid (UCM), E-28040, Madrid, Spain.
[6] Instituto de Astronomía, Universidad Nacional Autónoma de México, Apdo. Postal 70-264, 04510 Ciudad de México, Mexico
[7] Institut de Radioastronomie Millimétrique (IRAM), Av. Divina Pastora 7, Núcleo Central E-18012, Granada, Spain
[8] Centro de Astrobiología (CSIC/INTA), E-28692 ESAC Campus, Villanueva de la Cañada, Madrid, Spain
[9] Astronomical Observatory Institute, Faculty of Physics, Adam Mickiewicz University, ul. Słoneczna 36, 60-286 Poznań, Poland
[10] Instituto de Física de Cantabria (CSIC-Universidad de Cantabria), E-39005, Santander, Spain
[11] ISDEFE for European Space Astronomy Centre (ESAC)/ESA, P.O. Box 78, E-28690 Villanueva de la Cañada, Madrid, Spain
e-mail: mauro.gonzalez-ext@iac.es, mauromarago@gmail.com

Received —; accepted —

ABSTRACT

Aims. In this article we perform a comprehensive study using galaxy data from the Lockman–SpReSO project, a far-infrared (FIR) selected sample of galaxies observed using optical spectroscopy. We analysed a sub-sample of star-forming galaxies (SFGs) with secure spectroscopic redshifts, mostly in the luminous infrared galaxies domain. From these galaxies, parameters such as extinction, star formation rate (SFR), and metallicity were derived. The present paper examines how these properties evolve in relation to each other, and in comparison with low-redshift FIR and non-FIR-selected samples of galaxies.
Methods. We applied distinct selection criteria to attain an SFG sample with minimal AGN contamination. Multiple approaches were used to estimate the intrinsic extinction, SFR and gas-phase metallicity for the SFGs. In conjunction with findings in the literature, we examined the correlation between SFRs and stellar masses (M_*), as well as the metallicity evolution depending on M_*. Finally, the 3D relationship between M_*, SFR and metallicity, is also studied.
Results. From the initial spectroscopic sample of 409 FIR-selected objects from the Lockman–SpReSO catalogue, 69 (17%) AGNs have been identified and excluded, which is nearly double the percentage found in local studies, leaving a sample of 340 SFGs. The analysis of the M_*–SFR relationship revealed that Lockman–SpReSO IR-selected SFGs show signs of evolution at redshifts $z > 0.4$, shifting above the main sequence, with a mean value of ~ 0.4 dex. They are located within the starburst galaxy region since 78% of the galaxies fall into this category. In addition, no evident flattening was found in the relation to specific SFR with redshift for $\log M_*(M_\odot) \gtrsim 10.5$. In line with the M_*–metallicity relation (MZR) outcomes published in previous studies for optically selected SFGs, however, during the analysis of the MZR, it was found that IR-selected SFGs exhibit lower metallicities than those anticipated on the basis of their M_* and redshift. During the investigation of the 3D M_*–SFR–metallicity relation (FP), it was established that the research sample is consistent with relations in the existing literature, with an average scatter of ~ 0.2 dex. However, a re-calibration of the FP when using the SFR obtained from the IR luminosity is required and, in this case, no attenuation in the correlation for $\log M_*(M_\odot) \gtrsim 10.5$ is observed. This result points to a possible evolution of the more massive fraction of the sample in the sense of decreasing the present-day star formation with respect to the averaged star formation in the past.

Key words. galaxies: fundamental parameters – galaxies: evolution – galaxies: star formation – techniques: spectroscopic

1. Introduction

Studying the evolution of galaxies is challenging, since it involves possible variations with redshift of relationships involving global indicators, such as star formation rate (SFR), metallicity (Z), stellar mass (M_*) and other related parameters. Estimating these indicators, each with its specific uncertainties and intrinsic limitations, is a difficult task, as is shown later in this paper.

Extensive research on the evolution of the main sequence (MS), comparing star formation rate (SFR) and stellar mass (M_*), has been undertaken. Numerous studies, such as those of Brinchmann et al. (2004); Speagle et al. (2014); Popesso et al.

(2023), have investigated this indicator, including Cedrés et al. (2021), who found no evolution of this indicator, even for low-mass galaxies below $z \simeq 1.43$.

The mass–metallicity relationship (MZR), which reflects the enrichment of galactic gas compared to the mass within stars, serves as an additional observational indicator of evolution (Duarte Puertas et al. 2022, and references therein). The results so far obtained indicate that metallicity rises with M_* and cosmic time (for example, Sanders et al. 2021), and is inversely correlated with SFR, as evidenced by the fundamental mass–metallicity–SFR (FP or FMR) relationship (Lara-López et al. 2010; Mannucci et al. 2010). The MZR definition suggests that gas accretion, outflows and metal astration probably influence it, but it could also be affected by factors such as downsizing or infrared (IR) luminosity. However, its possible evolution remains uncertain. For instance, at the lower redshift ($z \sim 0.4$) and low-mass end ($\log(M_*) < 8$), Nadolny et al. (2020) found no evidence of MZR evolution. This was also confirmed at higher redshifts up to $z = 2.3$ by Cresci et al. (2019) and up to $z = 3.3$ by Sanders et al. (2021), including the low-mass end. However, according to Pistis et al. (2022), the MZR is subject to biases resulting from S/N ratio and quality flags in the spectra, leading to overestimated metallicities or to the selection of high-metallicity galaxies. These authors, however, observed that the relationship between metallicity and specific SFR (sSFR) is relatively insensitive to such biases. Nevertheless, Henry et al. (2021) found evolution in MZR and FMR at redshifts $1.3 < z < 2.3$ using a larger sample than those of previous authors, and extended to low mass galaxies. In addition, these authors confirmed this evolution for a sub-sample of galaxies with high S/N spectra.

The situation described above is even more complex for far-IR (FIR) selected galaxies. Luminous infrared galaxies (LIRGs) and ultra-luminous infrared galaxies (ULIRGs) are galaxies with total infrared luminosities ($L_{\rm TIR}$, from 8 to 1000 μm) between 10^{11}–10^{12} and 10^{12}–10^{13} solar luminosities ($L_\odot$), respectively. Both LIRGs and ULIRGs are considered interacting/merging or post-merger galaxies (see for example, Kilerci Eser et al. 2014; Pereira-Santaella et al. 2019; Nadolny et al. 2023, and references therein). From a sample of nine (U)LIRGs at redshifts $0.2 < z < 0.4$, Pereira-Santaella et al. (2019) concluded that 10–25% are isolated discs and the rest interacting or merging systems, with SFR(Hα) $\sim$ SFR($L_{\rm TIR}$) but with interstellar medium (ISM) conditions different from those in local galaxies. From a sample of 20 LIRGs at low–intermediate redshifts ($0.25 < z < 0.65$) that were classified to be in the regime between normal and starburst galaxies, however, Lee et al. (2017) concluded that only 10% show signs of interaction. From a sample of 118 local ULIRGs with mean redshift $z \simeq 0.18$ selected from SDSS DR10, Kilerci Eser et al. (2014) found that SFR(Hα) is in mean 8 times lower that SFR($L_{\rm TIR}$), and that Z determined from optical lines using R_{23} (see Section 5.2) is on average about 0.3 dex lower with respect to local SDSS galaxies. From a study of five local ULIRGs, however, Chartab et al. (2022) claim that the lower metallicity observed in ULIRGs is an artefact originating from metallicity determinations using optical instead of FIR lines. Nevertheless, determining metallicity using FIR lines remains controversial. Herrera-Camus et al. (2018) still reports lower metallicity in (U)LIRGs, even when using FIR lines. This is in contrast to Chartab et al. (2022), who used different lines.

The objective of this paper is to study the relations among different determinations of SFR, M_* and metallicity for a statistically significant sample of star-forming galaxies(SFGs) at intermediate redshifts, selected according to their IR emission and having a robust redshift determination. The study will further analyse possible differences with respect to optically selected samples, other LIRG-selected samples and their possible evolution.

This paper is organized as follows. In Section 2 the data available for this work are presented. The different methods of discriminating SFGs with respect to active galactic nuclei (AGN) are described in Section 3. The extinction correction adopted is explained in Section 4. Sections 5 and 6 explain the different gas metallicity and SFR estimators, respectively. Section 7 presents the results of the global indicators MS, MZR and FP. Finally, our conclusions are given in Section 8. Throughout the paper, magnitudes are given in the AB system (Oke & Gunn 1983). The cosmological parameters adopted are: $\Omega_{\rm M} = 0.3$, $\Omega_\Lambda = 0.7$, and $H_0 = 70$ km s^{-1} Mpc^{-1}. We assume a Chabrier (2003) initial mass function (IMF) for the estimation of both SFR and M_*.

2. Data selection

The data used in this paper are drawn from the Lockman–SpReSO project described in Gonzalez-Otero et al. (2023), to which the reader is referred for a detailed description of the observations, reduction and catalogue compilation. Further details on the optical and FIR wavelength coverage, fluxes, optical spectral resolution, area covered and ancillary data available are also explained in Gonzalez-Otero et al. (2023).

In summary, the Lockman–SpReSO project involves an optical spectroscopic follow-up of 956 sources selected by their FIR flux using *Herschel Space Observatory* data. In addition, 188 objects of interest, with a limiting magnitude in the Cousins R band ($R_{\rm C}$) of $R_{\rm C} < 24.5$ mag and all located in the Lockman Hole field were included in the sample. The spectroscopic observations were conducted using the WHT/A2F-WYFFOS[1] (Domínquez Palmero et al. 2014) and WYIN/HYDRA[2] instruments for objects within the brighter subset of the catalogue ($R_{\rm C} < 20.6$ mag). While for objects in the fainter subset ($R_{\rm C} > 20$ mag), GTC/OSIRIS[3] (Cepa et al. 2000) was used.

Of the 1144 sources of Lockman–SpReSO, spectroscopic analysis allowed the determination of spectroscopic redshift for 456 objects, where 357 come from objects with at least two identified spectral lines and 99 were obtained using only one spectral line secured using all available photometric information. To ensure a robust determination, we have used the available photometric bands information, generally from FUV to FIR (see appendix A in Gonzalez-Otero et al. 2023), the photometric redshifts available in the literature, and the intensity and shape of the spectral line. In this paper we analyse the 456 regardless of how the redshift was obtained. Furthermore, with the spectroscopic redshifts obtained, Gonzalez-Otero et al. (2023) conducted spectral energy distribution (SED) fitting using the available photometric data spanning from the ultraviolet to the FIR wavelength range. This was carried out using the CIGALE software (Code Investigating GALaxy Emission, Burgarella et al. 2005, Boquien et al. 2019). In particular, this SED fitting method provides more accurate measurements of M_* and $L_{\rm TIR}$ than previous determinations also derived from SED fittings but based on photometric redshifts.

The Lockman–SpReSO project catalogue includes a set of sources that were not selected based on their infrared emission. These objects were added to complement the observational masks and are also of interest. The selection comprises radio

[1] https://www.ing.iac.es/Astronomy/instruments/af2
[2] https://www.wiyn.org/Instruments/wiynhydra.html
[3] http://www.gtc.iac.es/instruments/osiris/osiris.php

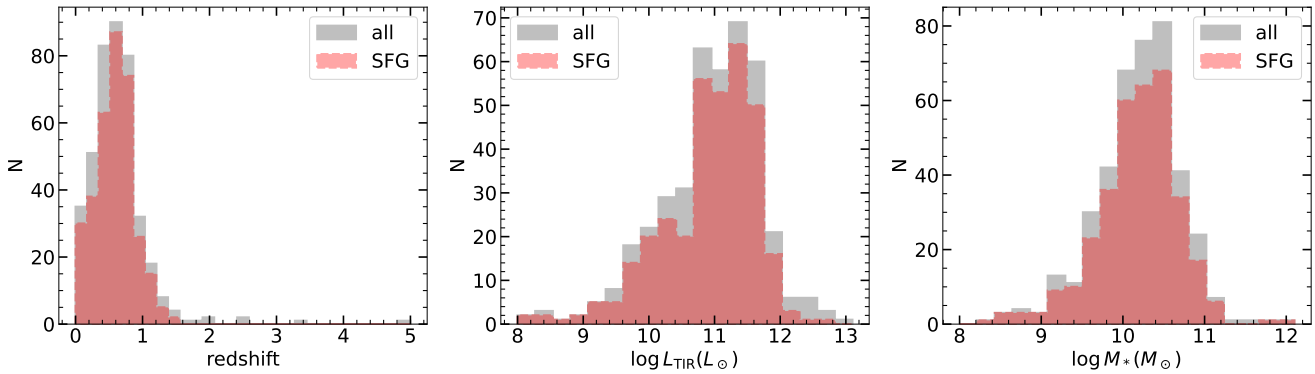

Fig. 1. Distributions of the spectroscopic redshift, L_{TIR} and M_*. In grey the sample of 409 objects collected from the Lockman–SpReSO catalogue with a determined spectroscopic redshift is represented. The objects selected as SFG are represented in red (see Sect. 3 for details).

galaxies, obscured quasars, and distant galaxies that were initially thought to be X-ray binaries and cataclysmic star candidates (for more details see Gonzalez-Otero et al. 2023) Out of the 456 objects with determined spectroscopic redshift in the catalogue, 47 belong to this sample of non IR selected objects. Therefore, for the purpose of this work, they must be removed from the studied sample.

Thus, for the development of this work we selected 409 objects for which the spectroscopic redshift had been determined, spanning the range $0.03 \lesssim z \lesssim 4.96$ with a median redshift of 0.6. In this sample, 54% of the sources are LIRGs, 6% ULIRGs and 1% hyper-luminous infrared galaxies (HLIRGs, $L_{TIR} > 10^{13}\ L_\odot$) with a median value $\log L_{TIR}(L_\odot) = 11.1$. The M_* of this sample lies in the range $8.23 \lesssim \log M_*(M_\odot) \lesssim 12.1$ with a median value $\log M_*(M_\odot) = 10.26$. The distributions of these properties are shown in Fig. 1, where the sample of 409 objects is represented by the grey distribution. In addition, a signal-to-noise ratio (S/N) greater than 3 was applied to all spectroscopic lines used in the subsequent sections.

3. Star-forming galaxies and AGN discrimination

The sample selected in the previous section did not differentiate between SFGs and AGNs. However, for the study proposed in this article, it is essential to distinguish between AGNs and SFGs in order to calculate accurately the extinction, SFR and metallicity. The investigation of the AGN population in the Lockman–SpReSO project will be presented in separate papers scheduled for imminent publication.

To classify the objects as AGNs or SFGs, we used a combination of photometric, spectroscopic, and SED fitting data gathered from Gonzalez-Otero et al. (2023), as described below. Photometric criteria, based on X-ray and IR information of the objects, were utilized, along with spectroscopic criteria, which involved analyzing spectral lines to perform this classification.

3.1. Photometric criteria

3.1.1. X-ray discrimination criteria

The use of X-ray data to differentiate between SFG and active galactic nuclei is common practice. The strong X-ray emission from the accretion disc regions surrounding the central black holes serves as a robust indicator of the nature of the objects. One of the initial studies in this area was conducted by Maccacaro et al. (1988), who used the ratio of X-ray-to-optical flux (X/O ratio) as a means of distinguishing AGN from other sources of X-ray emission. Subsequent studies have also used the X/O ratio to differentiate AGN from other X-ray sources (Stocke et al. 1991; Lehmann et al. 2001; Szokoly et al. 2004; Xue et al. 2011; Luo et al. 2017; Chen et al. 2018; Ramón-Pérez et al. 2019; Elías-Chávez et al. 2021).

In our study, we adopted the criterion described by Luo et al. (2017), who conducted research within the spectroscopic redshift range of $0 \lesssim z \lesssim 5$. In their work the X/O ratio is given by:

$$\log \mathrm{X/O} = \log F_\mathrm{X} + 0.4\, R_\mathrm{C} + 4.77 > -1,$$

where F_X is the X-ray flux within the range 0.2–12 keV and R_C is the magnitude in the R_C band, which is used as a tracer for the optical flux. The X-ray data of the sample were obtained from observations made by the *XMM-Newton* space telescope over the Lockman field and the 4XMM-DR10 catalogue (Webb et al. 2022).

The left panel of Fig. 2 shows the X-ray flux versus the R_C magnitude. The dashed lines mark the regions where $\log \mathrm{X/O} > -1$ and $\log \mathrm{X/O} > 1$. Using the above criterion, we have classified objects above the $\log \mathrm{X/O} > -1$ threshold as AGN. The colour code in the figure represents the spectroscopic redshift of the objects. This diagnostic diagram classified 21 objects as AGN.

The ratio between the X-ray flux and the near-IR flux (X/NIR ratio), using the K_s band as an indicator of the NIR (Luo et al. 2017), could also be used to separate AGN from SFGs. The criterion for this separation is defined as:

$$\log \mathrm{X/NIR} = \log F_\mathrm{X} + 0.4\, K_\mathrm{s} + 5.29 > -1.2$$

The outcome after applying this criterion is shown in the right panel of Fig. 2, where the X-ray flux is plotted against the K_s magnitude. The dashed lines represent the limits in the X/NIR ratio, and the colour code in the figure represents the spectroscopic redshift. Following the definition in Luo et al. (2017), the objects in the range $\log \mathrm{X/NIR} > -1.2$ were categorised as AGN. A total of 21 objects were classified as AGN using this criterion.

The final criterion applied using X-ray information is that defined by Xue et al. (2011), who defined a threshold for the X-ray luminosity (L_X) to distinguish AGN from other X-ray sources. According to this criterion, any source with $L_\mathrm{X} \geq 3 \times 10^{42}$ erg/s is classified as an AGN. In Fig. 2 this criterion is represented by red circles over the points. The application of this criterion resulted in the classification of 24 objects as AGN. A total of 25 unique objects were classified as AGN by at least one of the above criteria based on X-ray information.

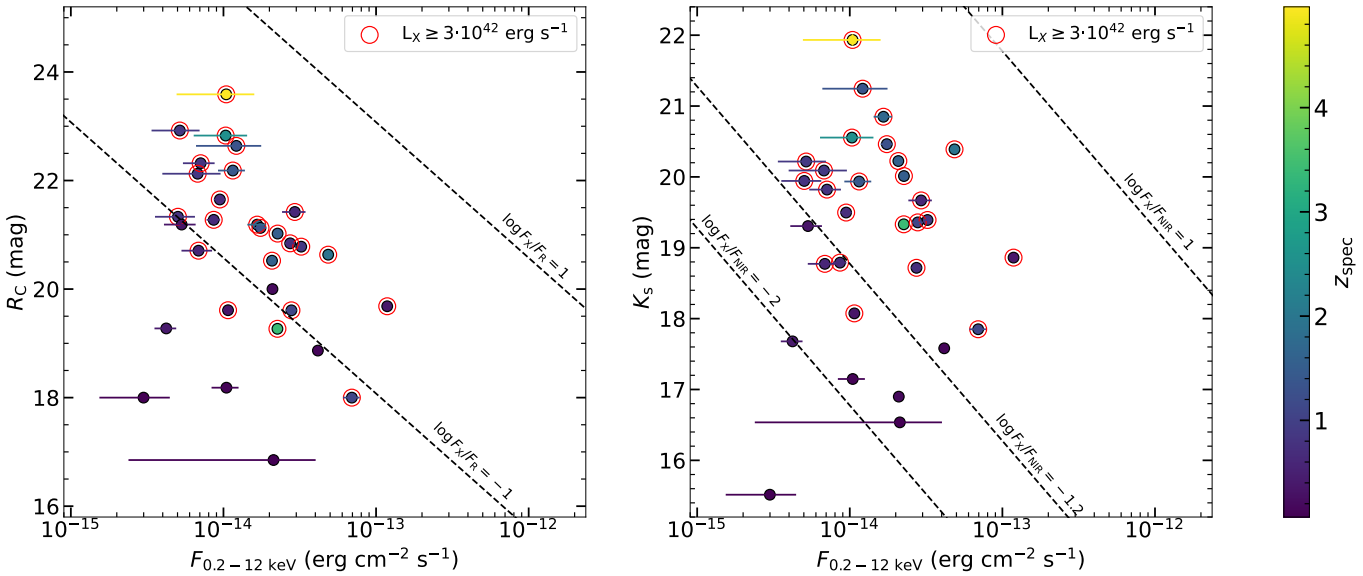

Fig. 2. AGN classification based on X/O and X/NIR ratios. The left panel illustrates the relationship between X-ray flux (0.2 to 12 keV) and R_C magnitude. Dashed lines represent the thresholds for $\log(X/O) > -1$ and $\log(X/O) > 1$, with objects above $\log(X/O) > -1$ classified as AGN. Red circles highlight points meeting the AGN criterion $L_X > 3 \times 10^{42}$ erg s^{-1} of Xue et al. (2011). Colour coding indicates the spectroscopic redshift of the objects. The right panel displays the X-ray flux plotted against K_s magnitude. Objects above the $\log(X/NIR) > -1.2$ threshold are categorised as AGN. Red circles and colour coding remain consistent with the left panel.

3.1.2. Infrared discrimination criteria

One of the characteristics of AGN that helps us to distinguish them from SFGs is the fact that they tend to be redder in the NIR and MIR. This is because the SED of AGN from the UV down to $\sim 5\,\mu$m is usually dominated by a power-law continuum, whereas SFGs show a black-body continuum with a peak above $\sim 1.6\,\mu$m due to the underlying stellar population (Stern et al. 2005).

Using the above information, investigations have been carried out using the IR information to separate AGN from SFGs. Donley et al. (2012) used the four *Spitzer*/IRAC bands (3.6, 4.5, 5.8, and 8.0 μm) to distinguish AGN from SFGs, by updating the Lacy et al. (2004) and Stern et al. (2005) criteria, which suffer from contamination by normal SFGs in deep IRAC data. They defined an empirical region where AGN lie in the *Spitzer*/IRAC colour space:

$$x \geq 0.08;\ y \geq 0.15$$

$$y \geq 1.21\,x - 0.27$$

$$y \leq 1.21\,x + 0.27$$

$$f_{4.5\,\mu m} > f_{3.6\,\mu m};\ f_{5.8\,\mu m} > f_{4.5\,\mu m};\ f_{8.0\,\mu m} > f_{5.8\,\mu m}$$

where $x = \log\left(f_{5.8\,\mu m}/f_{3.6\,\mu m}\right)$ and $y = \log\left(f_{8.0\,\mu m}/f_{4.5\,\mu m}\right)$. The definition of this criterion is independent of the redshift within the sample under study. In Fig. 3 we plot the above flux ratios and the region defined by Donley et al. (2012) where the objects are classified as AGN. Based on the results of this diagnostic diagram, 19 objects were classified as AGN.

The criterion developed by Messias et al. (2012) has been further applied to the sample. This criterion is a classification method that uses information from the *Spitzer*/IRAC 4.5 and 8.0 μm bands, and the 24 μm *Spitzer*/MIPS band to define a region where the AGN would be found, called the IRAC-MIPS criterion

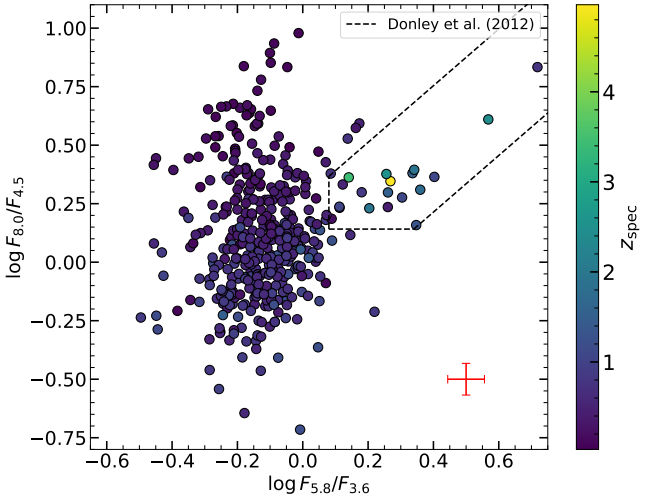

Fig. 3. Criteria for separating AGN from SFGs, using *Spitzer*/IRAC bands, updated by Donley et al. (2012). The x-axis represents the ratio of fluxes in the 5.8 μm and 3.6 μm bands, while the y-axis represents the ratio of fluxes in the 8.0 μm and 4.5 μm bands. The area bounded by the black dashed lines corresponds to the selection criterion defined by Donley et al. (2012). The colour coding represents the spectroscopic redshift of the objects. The average 1σ size is shown in red at the bottom right.

("IM" criterion), with an additional criterion based on the K_s band ("KIM" criterion):

$$[8.0] - [24] > -2.9\,([4.5] - [8.0]) + 2.8$$

$$[8.0] - [24] > 0.5$$

$$K_s - [4.5] > 0$$

where [4.5], [8.0], [24], and K_s are the AB magnitudes in the 4.5 and 8.0 μm IRAC bands, the 24 μm MIPS band, and the K_s

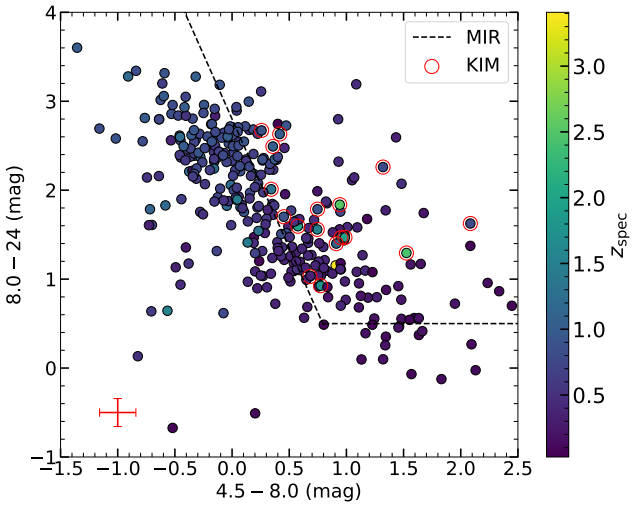

Fig. 4. Separation criteria from Messias et al. (2012) using the *Spitzer*/IRAC 4.5 and 8.0 μm bands, the *Spitzer*/MIPS 24 μm band, and the K_s band. The dashed line outlines the area where AGN could be found based on the IM criteria. The red empty circles indicate the objects that also met the KIM criteria. The colour coding represents the spectroscopic redshift of the objects. The average 1σ size is shown in red at the bottom left.

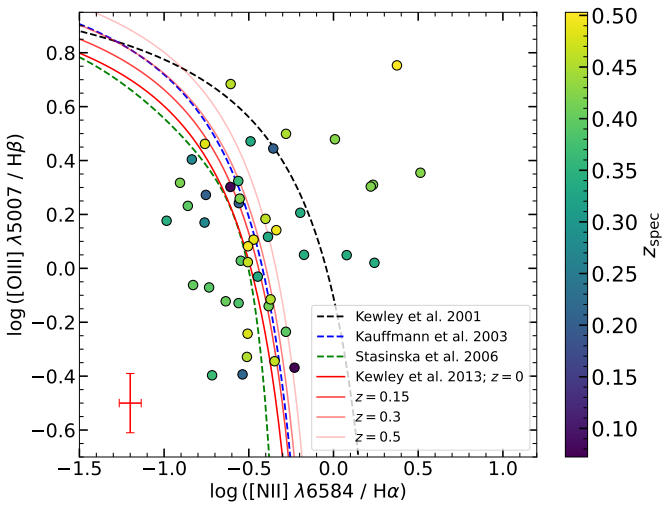

Fig. 5. Representation of the BPT diagram defined by Baldwin et al. (1981) to separate SFGs from AGN. The orange, blue and black dashed lines represent the Stasińska et al. (2006), Kauffmann et al. (2003) and Kewley et al. (2001) selection criteria, respectively. The red solid lines represent the Kewley et al. (2013) selection criteria for redshifts 0, 0.15, 0.3, and 0.5. The colour coding represents the spectroscopic redshift of the objects. The average 1σ size is shown in red at the bottom left.

band, respectively. This criterion minimizes the contamination of the selected AGN sample by normal and SFGs at low redshifts thanks to the addition of the criterion using the K_s band, while it strongly separates SFGs from AGN at high redshifts. The fact that it is independent of redshift fits perfectly with the Lockman–SpReSO data, since the sample is not constrained by redshift. In Fig. 4 we plot the colour between the 4.5 and 8.0 μm bands against the colour between the 8.0 and 24 μm bands. The dashed line represents the area defined by the IM criterion and the objects with and empty red circle are those that also satisfied the KIM criterion. Thus, using the Messias et al. (2012) criterion, a total of 17 objects were classified as AGN. This leaves a total of 26 unique objects classified as AGN using the IR photometric discrimination criteria.

3.2. Spectroscopic criteria

Spectral emission lines emanating from intricate interactions between photons and ionized atoms serve as diagnostics of the ionization sources, chemical composition and physical conditions within galaxies. In the context of distinguishing between AGN and SFGs, the precise identification of ionization mechanisms becomes particularly crucial.

One of the most widely used diagrams for this purpose, based on spectral emission lines, is the well-known Baldwin, Phillips & Terlevich (BPT) diagram (Baldwin et al. 1981). This diagram uses the ratios of optical emission lines to distinguish between SFGs and AGN, where the most common ratios are [O III]λ5007/Hβ and [N II]λ6584/Hα. AGN exhibit a higher [O III]λ5007/Hβ ratio owing to intense radiation from the accretion disc whereas SFGs have a lower [O III]λ5007/Hβ ratio, as their emission lines are mainly influenced by ionization from young stars. Similarly, the [N II]λ6584/Hα ratio is higher in AGN compared to SFGs, a result of stronger emission lines from the ionized gas around the black hole, leading to distinctive regions occupied by AGN and SFGs in this diagram.

Figure 5 shows the BPT diagram for the sample of objects from Lockman–SpReSO used in this paper. The criteria from Kewley et al. (2001), Kauffmann et al. (2003), Stasińska et al. (2006), and Kewley et al. (2013) to separate SFGs from AGN are shown. The Kewley et al. (2001) criterion is the least restrictive for SFGs, allowing composite galaxies to be included in the selection. Criteria such as those of Stasińska et al. (2006) or Kauffmann et al. (2003) are more restrictive and filter out SFGs more efficiently. We decided to use the Kewley et al. (2013) selection criterion, since it takes into account the evolution of the line ratios with redshift. This is especially important for our sample, which extends up to a $z \sim 0.5$, and the Kewley et al. (2013) criterion allowed us to better separate SFGs from AGN. According to this diagnostic diagram, 26 objects were classified as SFGs and 19 objects were classified as AGN or composite galaxies.

As a complement to the BPT diagram, the classification diagram developed by Cid Fernandes et al. (2010), named the EWαn2 diagram, is very valuable for objects with a limited number of emission lines available. This method uses only the Hα line and the [N II] line. Using these two lines, a degeneracy appears between Seyfert and AGNs which the authors solved by adding the Hα rest-frame equivalent width (EW). The separation between SFGs and AGNs is established by criteria based on the [N II] / Hα ratio (Kewley et al. 2001; Kauffmann et al. 2003; Stasińska et al. 2006). In this case, we adopted the more restrictive criteria of Stasińska et al. (2006), which define SFGs to occupy the region with log [N II]/H$\alpha \leq -0.4$, and AGN are defined to be in the region with log [N II]/H$\alpha \geq -0.2$. Figure 6 shows the sample objects on the EWαn2 diagram, where the different separation criteria mentioned above have been marked. The application of this diagnostic diagram resulted in the classification of 31 objects as not being SFGs.

In summary, compiling all the results, we have obtained 25 objects classified as AGN using X-ray-based criteria, 26 using IR-based criteria, and an additional 33 AGN based on spectroscopic criteria. This yields a total of 69 unique objects classified as not SFGs from the sample of 409 objects taken from

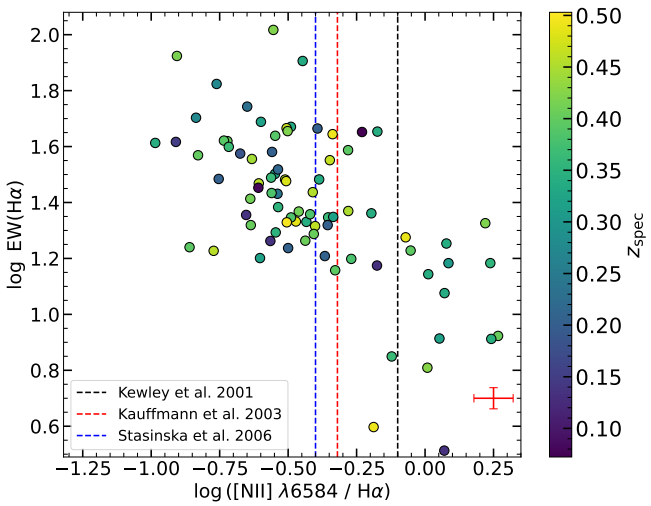

Fig. 6. EWαn2 criterion defined by Cid Fernandes et al. (2010) for the classification of SFGs and AGN. The Stasińska et al. (2006) criterion (blue dashed line) has been adopted for the separation, as it is the most restrictive for SFGs. The Kauffmann et al. (2003, red dashed line) and Kewley et al. (2006, black dashed lines) criteria are also shown. The colour coding represents the spectroscopic redshift of the objects. The average 1σ size is shown in red at the bottom right.

the Lockman–SpReSO catalogue, representing 17% of the sample. This value is slightly higher than the values of 11.4% and 11.5% found by Lara-López et al. (2013a) for the SDSS and GAMA surveys, respectively. However, this result is highly dependent on the selection criteria of the initial sample. Sabater et al. (2019) revealed that 20% of their radio-galaxy sample with a counterpart in SDSS were AGN, whilst Magliocchetti et al. (2018) found for the VLA-COSMOS catalogue that 33% of the galaxies were AGN. The spectroscopic redshift, that spans the range $0.03 \lesssim z \lesssim 1.52$ with a median value ~ 0.6, $L_{\rm TIR}$, and M_* distributions of the SFG selected are shown in the Fig. 1, where they are marked in red.

4. Extinction correction

In the study of galaxies, spectral lines serve as invaluable tools, providing crucial information about their physical properties, chemical composition, and ionization processes. Nonetheless, accurate interpretation of spectral lines can be significantly hindered by the presence of extinction effects caused by interstellar dust within the galaxies themselves. Extinction occurs when dust particles in the interstellar medium absorb and scatter light, leading to a reddening of the observed spectra. This reddening effect can introduce systematic biases in the measurements of emission lines, potentially misleading the derived physical parameters of galaxies, such as SFR and metallicities.

Correcting for extinction effects therefore becomes of paramount importance in obtaining reliable and precise measurements of emission lines. In this section, we present our methodology for correcting extinction in the spectral lines of galaxies.

4.1. Stellar absorption of underlying older components

Before tackling the task of extinction correction, we need to consider the contribution of the old stellar population to line measurements. One of the properties of this type of stellar population is absorption in the Balmer series lines, which is often superimposed on the emission lines produced by the excitation of gas by the hotter, younger stars.

To correct for this effect, we have adopted the criterion of Hopkins et al. (2003, 2013), using a constant value of 2.5 Å for the EW correction, $\mathrm{EW_c}$, to account for the absorption contribution arising from the underlying stellar population. It is important to note that this form of correction is recommended primarily for cases where it is desired to study the properties of a large sample of objects as a whole. For detailed analyses of individual objects, more refined measurements of the underlying absorption should be preferred.

Correction of the Balmer line fluxes for the effect of the underlying stellar absorption has been performed using:

$$F = F_{\rm obs}\left(1 + \frac{\mathrm{EW_c}}{\mathrm{EW}}\right), \tag{1}$$

where F is the underlying absorption-corrected flux, $F_{\rm obs}$ is the observed flux of a Balmer line, $\mathrm{EW_c}$ is the applied correction of 2.5 Å, and EW is the equivalent width of the line.

4.2. Extinction calculation

To perform the extinction correction on the emission lines of SFGs, we have made use of the empirical relationships established by Calzetti et al. (1994), who state that the intrinsic flux ($F_{\rm int}$) at a given wavelength (λ) can be obtained as follows

$$F_{\rm int}(\lambda) = F(\lambda)\, 10^{0.4\,A(\lambda)} = F(\lambda)\, 10^{0.4\,k(\lambda)\,E(B-V)}, \tag{2}$$

where $F(\lambda)$ is the observed flux at that wavelength corrected for the underlying stellar absorption, $A(\lambda)$ is the extinction at that wavelength, and $k(\lambda)$ is the reddening curve evaluated at that wavelength. In this work we have used the reddening curve defined by Calzetti et al. (2000). Finally, $E(B-V)$ is the colour excess; that is, the variation that the $B-V$ colour suffers due to the effect of the dust.

The estimation of the extinction from the Balmer decrement of the emission lines observed in the spectra of the objects is one of the most reliable methods because, for a fixed electronic temperature, quantum physics gives the theoretical values for the ratios of the lines. Thus, the colour excess is obtained using the Hα/Hβ ratio:

$$E(B-V) = \frac{2.5}{k(\lambda_{\rm H\beta}) - k(\lambda_{\rm H\alpha})}\, \log_{10}\left(\frac{(\mathrm{H\alpha/H\beta})_{\rm obs}}{(\mathrm{H\alpha/H\beta})_{\rm th}}\right), \tag{3}$$

where $k(\lambda_{\rm H\beta})$ and $k(\lambda_{\rm H\alpha})$ are the values of the reddening curve evaluated at Hβ and Hα wavelengths, respectively; $(\mathrm{H\alpha/H\beta})_{\rm obs}$ is the observed Balmer decrement, and $(\mathrm{H\alpha/H\beta})_{\rm th}$ is the quantum-physical value of the Balmer decrement in the case of non-extinction. The standard case adopted in the study of SFGs is the recombination Case B described by Osterbrock (1989), where $(\mathrm{H\alpha/H\beta})_{\rm th} = 2.86$ is defined for an electron temperature $T = 10^4$ K and an electron density $n_e = 10^2$ cm^{-3}.

The sample of SFGs has a redshift distribution with a median value of ~ 0.6, which means that more than half of the sample does not have the Hα line available because it is outside the spectral range covered for objects at redshifts $\gtrsim 0.5$. Other orders of the Balmer decrement are proposed to calculate the extinction; for example, the ratio Hβ/Hγ. The theoretical value for this ratio, defined under the recombination Case B of Osterbrock (1989), is $(\mathrm{H\beta/H\gamma})_{\rm th} = 2.13$. Subsequent orders of the Balmer decrement were not considered because the lines are weaker and usually have a low S/N ratio.

Figure 7 shows the distributions and the relation for the $E(B-V)$ obtained using the Hα/Hβ and Hβ/Hγ ratios. The number of sources for which the $E(B-V)$ can be obtained is limited. Therefore, we have considered other ways of calculating $E(B-V)$ for the extinction correction.

From the SED fits performed by Gonzalez-Otero et al. (2023) using CIGALE (the CIGALE configuration is depicted in their appendix B), the $E(B-V)$ of the nebular lines was obtained for each source. CIGALE also performs a parameter determination by Bayesian inference, taking into account all the models with which an attempt has been made to fit the SED of an object. This value obtained from Bayesian inference is the one we have taken as $E(B-V)$. The relation with the other tracers and the distribution obtained for the $E(B-V)$ provided by the SED fits using CIGALE can be seen in Figure 7.

The ultimate method to measure $E(B-V)$ is based on the IR/UV ratio. By investigating the balance between the IR and UV wavelengths, one can gain an understanding of the extinction phenomenon as the dust absorbs the UV radiation from hot stars and re-emits it in the IR spectrum. We adopt the parameterisation method developed by Hao et al. (2011) to determine the colour excess, and this is accomplished by using the IR/UV ratio. This method provides a colour excess for the continuum and for comparing it with the one obtained previously, a commonly used conversion factor is applied:

$$E(B-V)_{\rm c} = 0.44 \times E(B-V), \tag{4}$$

where $E(B-V)_{\rm c}$ represents the colour excess of the continuum. Figure 7 shows the distribution obtained and the comparison with the other tracers studied. The $E(B-V)$ value obtained from the SED fits with CIGALE is the one used to correct for the extinction of the line fluxes (Eq. 2) used in the following sections of the paper. Moreover, it is in good agreement with the IR/UV tracer, as shown in Fig. 7.

5. Gas phase metallicities estimation

In this section, we examine the calibrations used to determine the gas-phase metallicity of the SFGs in our sample. This determination is based on the oxygen abundance, 12 + log (O/H).

The direct method of estimating the electron temperature (T_e) of the ionized gas requires achieving high resolution and S/N ratio. However, this method uses weak auroral lines such as [O III] λ4363 or [N II] λ5755, which are difficult to observe, so other methods have been proposed. Some of them are empirical calibrations of the T_e method, while others are based on photoionisation models. This variety of methods leads to a lack of universality in the metallicity calibrator. In addition, the discrepancies introduced by the variations between methods lead to deviations in the fundamental metallicity relation and its associated projections, adding complexity to the study.

5.1. Empirical methods

One of the empirical methods analysed in this study is the Pilyugin & Grebel (2016, hereafter P16) calibration, which derives the abundance of oxygen using the intensities of strong emission lines in H II regions. They separated the calculation of the metallicity for the upper and lower branches characteristic of the methods based on oxygen determination. The upper branch is thus defined as $\log(N_2) < -0.6$, where $N_2 = $ [N II] $\lambda\lambda$6548, 84/Hβ. The metallicity equation is

$$12 + \log({\rm O/H}) = 8.589 + 0.022\,\log(R_3/R_2) + 0.399\,\log(N_2) + (-0.137 + 0.164\,\log(R_3/R_2) + 0.589\,\log(N_2))\,\log(R_2)\,. \tag{5}$$

The lower branch definition is $\log(N_2) > -0.6$ and the metallicity equation is:

$$12 + \log({\rm O/H}) = 7.932 + 0.944\,\log(R_3/R_2) + 0.695\,\log(N_2) + (0.970 - 0.291\,\log(R_3/R_2) + 0.19\,\log(N_2))\,\log R_2. \tag{6}$$

In both equations the coefficients are $R_2 =$ [O II] $\lambda\lambda$3727, 29/Hβ and $R_3 =$ [O III] $\lambda\lambda$4959, 5007/Hβ. The distribution of the metallicity obtained is plotted in the left panel in the upper row in Fig. 8.

The relationship derived by Pettini & Pagel (2004, hereafter PP04) is the second empirical tracer we studied based on the O3N2 estimator. It is particularly useful because it can be applied to high-redshift galaxies, as it employs spectral lines that are in close proximity to one another, eliminating the need for complex procedures such as extinction corrections or flux calibrations, which are challenging when observing high-redshift galaxies in the infrared. Their parameterisation of the metallicity is:

$$12 + \log({\rm O/H}) = 8.73 - 0.32 \times {\rm O3N2}, \tag{7}$$

where O3N2 = $\log\left[({\rm [O\,III]}\,\lambda5007/{\rm H}\beta)\,/\,({\rm [N\,II]}\,\lambda6584/{\rm H}\alpha)\right]$ and is valid only for galaxies with O3N2 < 2. The result is plotted in the middle panel of the upper row in Fig. 8.

5.2. Theoretical photoionisation models-based methods

Tremonti et al. (2004, hereafter T04) developed an objective calibration of oxygen abundance by fitting the most intense emission lines in the optical range with theoretical model approaches. The fitting models were created by combining single stellar population (SSP) models from Bruzual & Charlot (2003) with photoionisation models from CLOUDY (Ferland et al. 1998). The parameterisation of the oxygen abundance is based on the R_{23} estimator, where $R_{23} =$ ([O II] $\lambda\lambda$3727, 29 + [O III] $\lambda\lambda$4959, 5007) /Hβ. The metallicity is calculated using the following equation:

$$12 + \log({\rm O/H}) = 9.185 - 0.313\,x - 0.264\,x^2 - 0.321\,x^3 \tag{8}$$

where $x = \log(R_{23})$ and is valid only for the upper branch of the double-valued R_{23}-abundance relation. The previous definition of the upper branch is not applicable to objects with redshift $z \gtrsim 0.45$, as the [N II] lines lie outside the Lockman–SpReSO spectra. To differentiate between the upper and lower branches, we have set the criteria defined by the region $\log R_{23} > 0.85$ and $\log M_* < 9.3$ for the upper branch. The motivation for these criteria can be found in Appendix A. The right panel in the upper row in Fig. 8 shows the metallicity distribution obtained.

The metallicity estimates derived from the R_{23} estimator, enable the calculation of metallicity for a larger number of Lockman–SpReSO objects, owing to the use of shorter wavelength spectral lines that are still visible in the optical, for objects at higher redshifts.

The Kobulnicky & Kewley (2004, hereafter KK04) parameterisation is an iterative technique for determining the oxygen abundance that also relies on the R_{23} estimator. The R_{23} calibrator is sensitive to the ionization state of the gas, characterized by

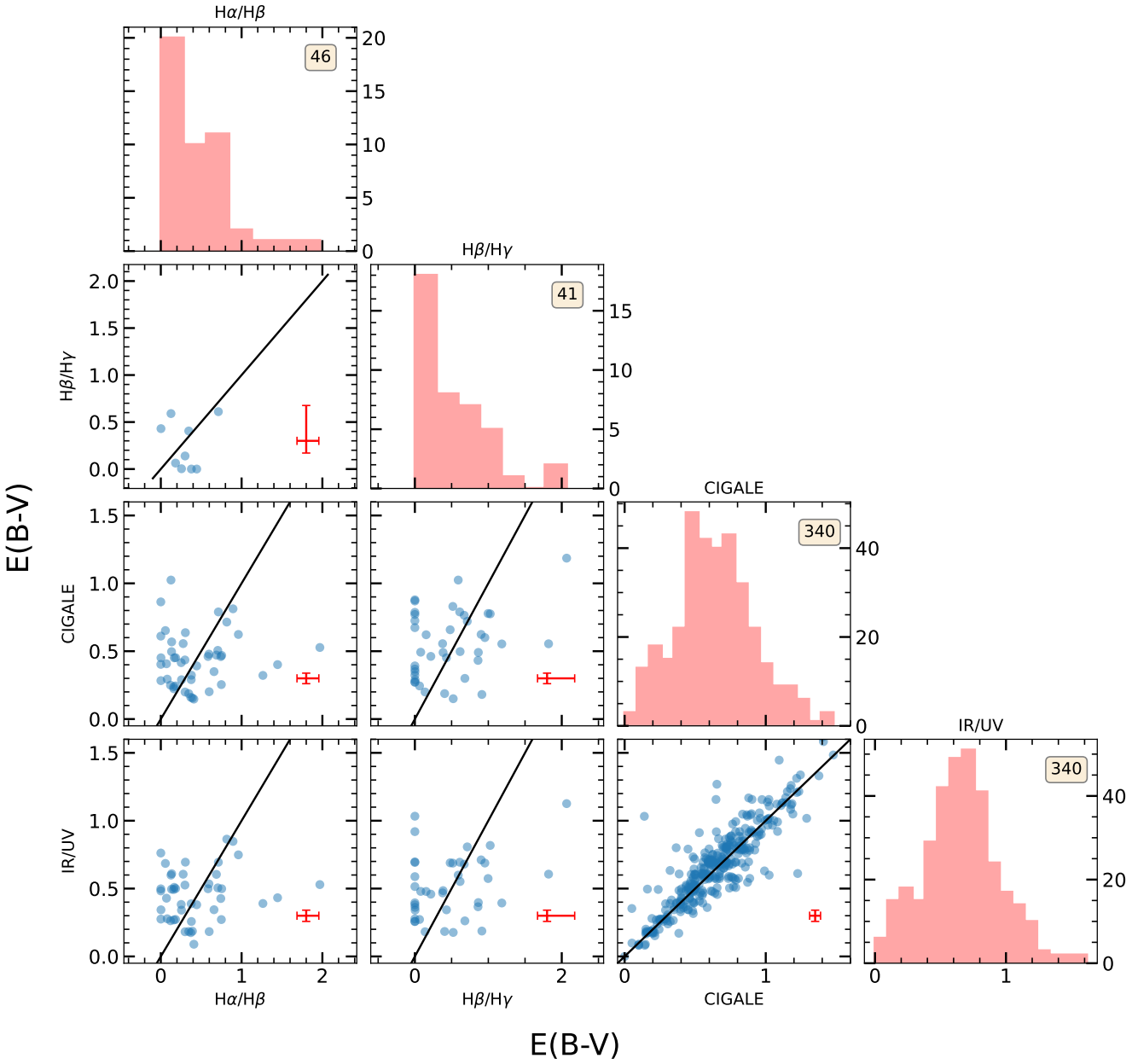

Fig. 7. Histograms and comparisons of the colour excesses obtained using the tracers analysed in this article. The black lines indicate the relationship $x = y$. The values in the inset boxes refer to the number of objects for which the colour excess could be calculated with the respective tracer. The average 1σ size is shown in red at the bottom right of each panel.

the ionization parameter (q), which is the number of hydrogren-ionizing photons passing through a unit area per second divided by the hydrogen density of the gas. The ionization parameter is determined through the [O II]/[O III] ratio of lines, which is in turn influenced by the metallicity of the gas, through the subsequent equation:

$$\begin{aligned}\log q = &\left[32.81 - 1.153\,y^2\right.\\ &\left.+\,[12 + \log(\mathrm{O/H})]\left(-3.396 - 0.025\,y + 0.1444\,y^2\right)\right]\\ &\times\left[4.603 - 0.3119\,y - 0.163\,y^2\right.\\ &\left.+\,[12 + \log(\mathrm{O/H})]\left(-0.48 + 0.0271\,y + 0.02037\,y^2\right)\right]^{-1},\end{aligned} \quad (9)$$

where $y = \log([\mathrm{O\,III}]\,\lambda5007/\,[\mathrm{O\,II}]\,\lambda3727)$. An initial metallicity value is required for the ionization parameter calculation. To determine it, we analyse which branch the object belongs to, according to the already established criteria, and assign an initial value of 12 + log (O/H)= 8.2 for the lower branch and 12 + log (O/H)= 8.7 for the upper branch. The obtained ionization parameter value is then used to determine the metallicity via the following parameterisation:

$$\begin{aligned}12 + \log(\mathrm{O/H})_{\mathrm{lower}} = &\ 9.40 + 4.65\,x - 3.17\,x^2\\ &- \left(0.272 + 0.547\,x - 0.513\,x^2\right)\log q,\end{aligned} \quad (10)$$

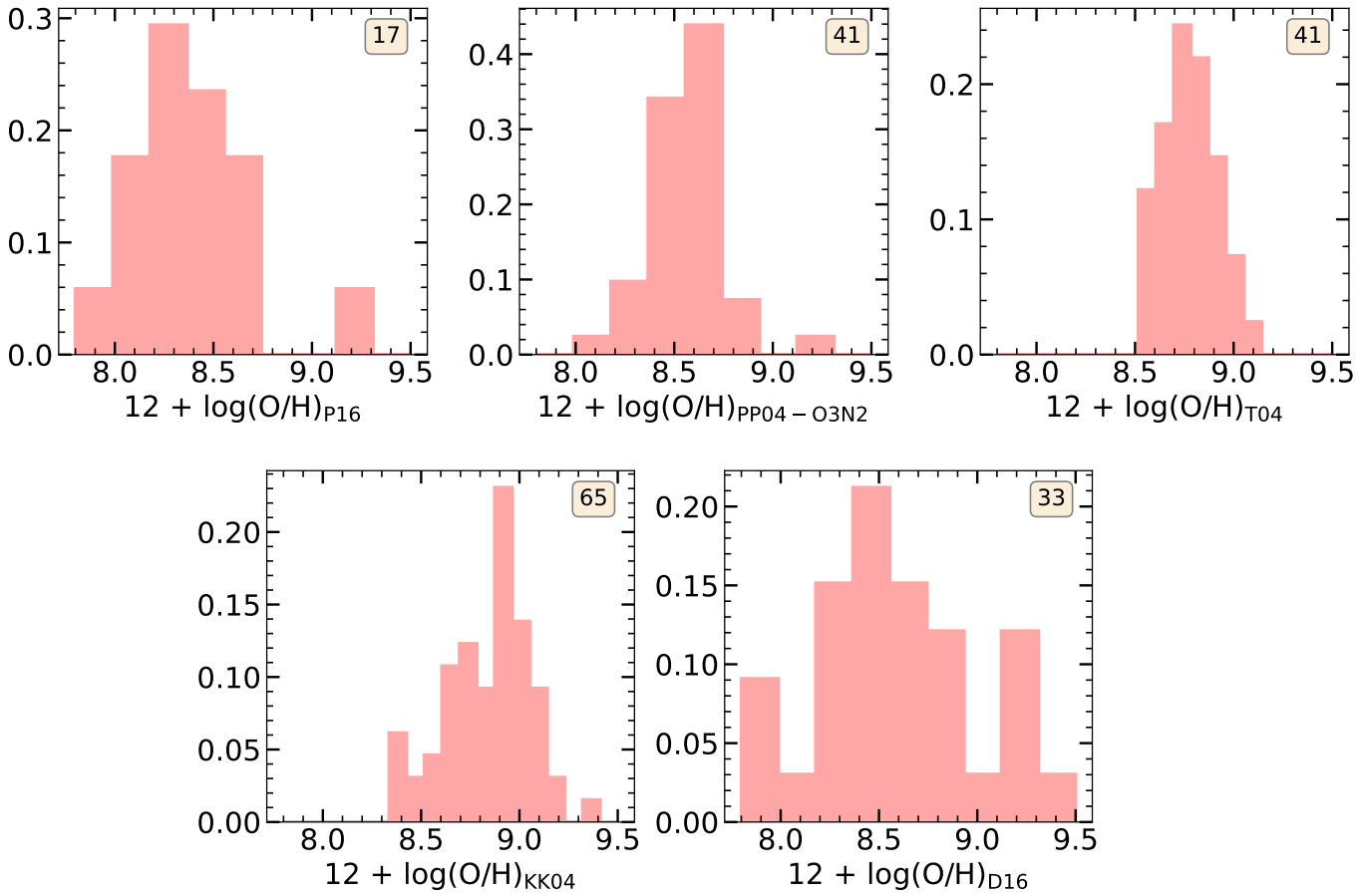

Fig. 8. Normalized histograms of the metallicities obtained in this article for the SFGs of the Lockman–SpReSO project. From left to right and from top to bottom, the parameterisations are from Pilyugin & Grebel (2016), Pettini & Pagel (2004), Tremonti et al. (2004), Kobulnicky & Kewley (2004), and Dopita et al. (2016). The values in the inset boxes refer to the number of objects for which the gas-phase metallicity could be calculated with the respective tracer.

$$12 + \log(\mathrm{O/H})_{\mathrm{upper}} = 9.72 - 0.777\,x - 0.951\,x^2 - 0.072\,x^3 - 0.811\,x^4 - \left(0.0737 - 0.0713\,x - 0.141\,x^2 + 0.0373\,x^3 - 0.058\,x^4\right)\log q, \quad (11)$$

where $x = \log R_{23}$, and upper and lower sub-indices indicate the branch. This process is repeated until $12 + \log(\mathrm{O/H})$ converges. The obtained distribution is shown in the left panel in the bottom row of Fig. 8.

Finally, we implemented the Dopita et al. (2016, hereafter D16) criterion to determine the oxygen abundance. This methodology utilizes lines which are redder than those used in the previously mentioned techniques, namely Hα, [N II]λ6484 and the [S II] $\lambda\lambda$ 6717,31 doublet. These lines are also similar in wavelength, hence extinction correction can be neglected. The computation of metallicity is thus established by the following relation:

$$12 + \log(\mathrm{O/H}) = 8.77 + y + 0.45\,(y + 0.3)^5, \quad (12)$$

where $y = \log([\mathrm{N\,II}]/[\mathrm{S\,II}]) + 0.264\,\log([\mathrm{N\,II}]/\mathrm{H}\alpha)$. The left panel in the bottom row in Fig. 8 shows the distribution obtained.

6. Star Formation rate

6.1. Spectral lines

The Hα line is the primary SFR indicator in the optical range of the local universe. The emission of the Hα line originates from the H II regions, wherein massive newly formed stars ionize the gas, resulting in the production of Balmer and other emission lines. The Hα emission is moreover uninfluenced by the metallicity of the gas or the star formation history. There are many calibrations that use the Hα flux to determine the SFR. One of the most commonly used methods, and the one adopted in this paper, is the calibration proposed by Kennicutt & Evans (2012):

$$\log\left[\mathrm{SFR}\left(M_\odot\,\mathrm{yr}^{-1}\right)\right] = \log\left[L_{\mathrm{H}\alpha}\left(\mathrm{erg\,s}^{-1}\right)\right] - 41.27. \quad (13)$$

However, the Hα line falls outside the optical spectrum for objects with redshifts $z \gtrsim 0.5$. The majority of objects in the Lockman–SpReSO sample have higher redshifts, so we have to rely on other spectral lines to calculate the SFR. The Hβ line, available for objects up to redshift $z \sim 1$, can be used as a tracer of SFR. Assuming a relation with the Hα line, typically under the recombination Case B of Osterbrock (1989), the same used for extinction correction, the SFR derived using Hβ is:

$$\log\left[\mathrm{SFR}\left(M_\odot\,\mathrm{yr}^{-1}\right)\right] = \log\left[L_{\mathrm{H}\beta}\left(\mathrm{erg\,s}^{-1}\right)\right] - 41.27 + \log 2.86, \quad (14)$$

where the 2.86 factor is the theoretical value for the Hα/Hβ ratio in the supposed recombination Case B.

Under the same considerations, the SFR can be determined from the Hγ line flux. This line is observable for objects with a

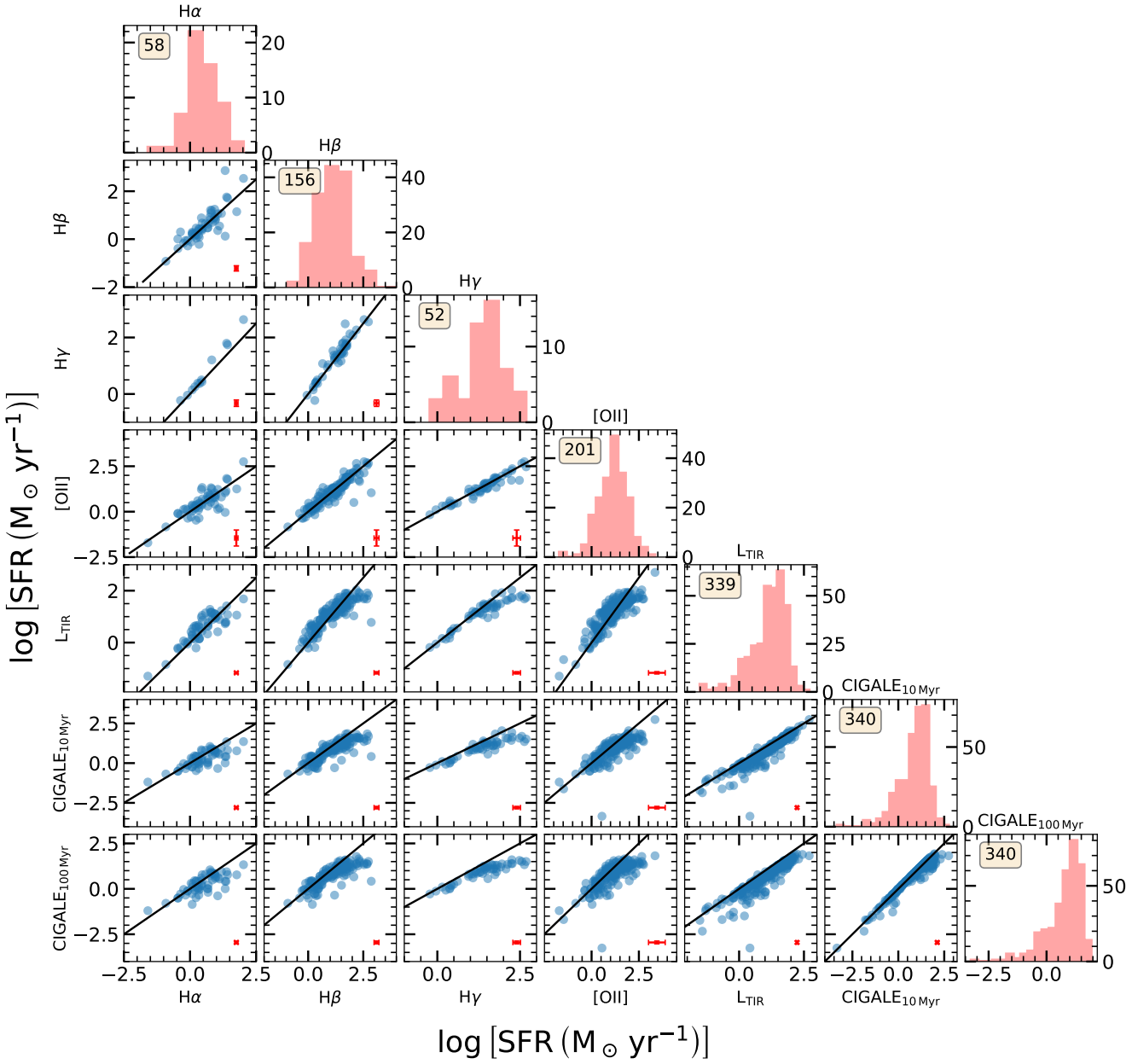

Fig. 9. Histograms and comparisons of the SFR obtained using different traces for the SFG from the Lockman–SpReSO project. The values in the histogram panels indicate the total number for which the SFR could be calculated with the respective tracer. The solid black lines represent the $x = y$ relation. The values in the inset boxes refer to the number of objects for which the SFR could be calculated with the respective tracer. The average 1σ size is shown in red at the bottom right of each panel.

redshift of up to $z \sim 1.3$; however, it is comparatively fainter, more affected by extinction and less detectable in the Lockman–SpReSO spectra. The equation for determining the SFR is:

$$\log\left[\mathrm{SFR}\left(M_\odot\,\mathrm{yr}^{-1}\right)\right] = \log\left[L_{\mathrm{H}\gamma}\left(\mathrm{erg\,s}^{-1}\right)\right] - 41.27 + \log 2.86 + \log 2.13, \quad (15)$$

where 2.13 is the theoretical values for the Hβ/Hγ ratio in the supposed recombination Case B.

Another spectral line that can be utilized to determine the SFR is the [O II] $\lambda\lambda$3726, 29 doublet, which appears in the same regions as Hα and represents similar star formation timescales. However, it is less correlated with the emission created by the ionization of gas from massive stars. On the other hand, extinction in the region where this doublet is located is significant and depends greatly on the metallicity and the ionization parameter. Nevertheless, there are parameterisations that use the [O II] flux to determine the SFR with good results. For this research, we have adopted the parameterisation obtained by Figueira et al. (2022), who took into account the metallicity of their SFG sample for their study. The equation is:

$$\log\left[\mathrm{SFR}\left(M_\odot\,\mathrm{yr}^{-1}\right)\right] = 0.96\,\log\left[L_{[\mathrm{O\,II}]}\left(\mathrm{erg\,s}^{-1}\right)\right] - 39.69. \quad (16)$$

6.2. CIGALE data products

Indicators based on photometric luminosity in selected bands are also used as tracers for SFR. One of the most commonly used is

$L_{\rm TIR}$, based on energy balance studies: UV emission from the hottest stars, absorbed by dust, is re-emitted in the IR regime of the electromagnetic spectrum. It should be noted that the timescale of the SFR studied using $L_{\rm TIR}$ is greater ($\sim$ 100 Myr) than that derived from the optical spectral lines ($\sim$ 10 Myr).

In this paper we use the relationship between SFR and $L_{\rm TIR}$ described by Kennicutt & Evans (2012). The mathematical expression is:

$$\log\left[\mathrm{SFR}\left(M_\odot\,\mathrm{yr}^{-1}\right)\right] = \log\left[L_{\rm TIR}\left(\mathrm{erg\,s}^{-1}\right)\right] - 43.41, \quad (17)$$

where $L_{\rm TIR}$ was obtained from the paper of Gonzalez-Otero et al. (2023). They performed a SED-fitting process on the Lockman–SpReSO objects, from which, among other parameters, $L_{\rm TIR}$ was obtained.

Among the results given by CIGALE there is also an estimate of the SFR. CIGALE provides the estimate of the instantaneous SFR and the SFR averaged over 10 and 100 Myr. For comparison with the results obtained with the spectral lines and the $L_{\rm TIR}$, we have selected the SFR averaged over 10 and 100 Myr, respectively.

Figure 9 shows the results obtained for the SFR with the different methods analysed in this section. The histograms represent the distributions obtained by each method, while the plots show the relationships between the different tracers. As we have already mentioned, we need to bear in mind that the SFR derived from spectral lines study very similar time ranges (0–10 Myr), whereas the SFR derived from $L_{\rm TIR}$ studies longer times (0–100 Myr), so the comparison between these tracers is purely indicative.

Table 1 presents an excerpt from the Lockman–SpReSO SFG catalogue. The table displays the quantities obtained in this work for the galaxy properties studied in Sects. 4, 5, and 6.

7. Global relations

7.1. Main sequence in star-forming galaxies

In this section, we examine the relationship between M_* and the SFR of galaxies, as well as its possible evolution with redshift. There is a well-established positive correlation between M_* and SFR, meaning that galaxies with higher stellar masses form stars at a higher rate than low stellar mass galaxies (see, for example, the comprehensive work of Speagle et al. 2014 or more recently Popesso et al. 2023, and references therein). Likewise, its evolution with redshift is widely acknowledged. For a given M_* value, galaxies at higher redshifts form stars at a faster rate compared to galaxies at lower redshifts. This correlation is widely recognized as the main sequence of SFGs. The MS has been a subject of intense study, covering approximately five orders of magnitude in M_* and spanning a redshift range from 0 to 6 (see table 4 of Speagle et al. 2014 and table 1 of Popesso et al. 2023).

In this paper, we adopt the MS model developed by Popesso et al. (2023), whose work involves a comprehensive synthesis of results from 28 studies focusing on the MS, aimed at investigating how this relation evolves over an extensive span of mass values, ranging from $10^{8.5}$ to $10^{11.5}$ $M_\odot$, and redshifts within the range $0 < z < 6$. The mathematical relationship they derived is as follows:

$$\log \mathrm{SFR}\,(M_*, t) = a_0 + a_1 t - \log\left(1 + \left(M_*/10^{a_2+a_3 t}\right)^{-a_4}\right) \quad (18)$$

where t is the cosmic time elapsed from the big bang in yr, M_* is the stellar mass in solar masses, $a_0 = 2.693$, $a_1 = -0.186$, $a_2 = 10.85$, $a_3 = -0.0729$, and $a_4 = 0.99$.

In Fig. 10, we present the SFR derived through line fluxes and $L_{\rm TIR}$ plotted against M_*. As the MS described by Popesso et al. (2023) depends on cosmic time, that is redshift,we have divided the sample into subsets by redshift ranges. For each of these subsets, we have overlaid the MS evaluated at the redshift of the subset. The MS is depicted with lines that match the colour of their respective subsets. The colour bands indicate the 0.09 dex scatter as determined by Popesso et al. (2023). For each subset, we have shown the minimum detectable SFR with a horizontal dashed line using the same colour code by redshift bin. The lowest SFR detectable using spectral line fluxes was obtained using the average EW for each line from Reddy et al. (2018), in combination with the 1σ level continuum limit $R_C < 24.5$ mag set out in the Lockman–SpReSO project description (Gonzalez-Otero et al. 2023). For the calculation of the minimum detectable SFR based on $L_{\rm TIR}$, we set the limit values of 0.6 mJy and 2 mJy for the 100 μm and 160 μm bands from the *Herschel*/PACS instrument, respectively, as described by the PEP team[4] and converted to $L_{\rm TIR}$ using the Galametz et al. (2013) calibrations. Additionally, the inset histograms provide insights into the redshift distribution within each of the subsets.

Irrespective of the method employed to derive the SFR, it is evident that the MS from Popesso et al. (2023) fits well for objects at low redshifts ($z < 0.4$) where the mean shift showed by these objects from the MS is $\sim$ 0.03 dex. Table 2 displays the mean shift values and corresponding errors for each of the SFRs analysed in this study. The SFR derived from Hγ exhibits the largest distance. This is because there are not enough objects with $z < 0.4$ to provide sufficient statistics for this SFR tracer. However, as we examine samples at higher redshifts, the trend shows that objects tend to be above the MS. A significant fraction of the total sample (78%) populates the starburst regime when the SFR derived from the $L_{\rm TIR}$ flux is examined, that is the region above the MS, and showing a mean shift from the MS of $\sim$ 0.4 dex for objects at $z > 0.4$. Table 2 shows the mean shift values for objects at $z > 0.4$ based on the studied SFR tracers. The table also includes mean values for the full samples. The mean shift for Hα, which is mainly populated by low redshift objects, is very low. However, the other SFR determinations show a bigger median shifts from the MS as they compile objects at higher redshifts.

The objects in the sample with redshifts $z > 0.4$ tend to be located near the starburst galaxy region. That is, they exhibit higher SFRs than that expected based on their M_* and redshift, showing shifts of up to $\sim$ 2 dex, although Lee et al. (2017) found that galaxies departing from the MS by less than 0.6 dex may still be considered normal, not starburst. The SFRs obtained exceed the minimum detectable SFR by 1 to 2 orders of magnitude, proving that there is no noise-induced selection bias in our results. It is worth noting that the detection of galaxies heavily obscured by dust would be limited (up to 40% of the initial sample), given that (Fig. 1) most of our sample are LIRG or even FIR galaxies. Local ULIRGs are known to be outliers of the MS relation (Elbaz et al. 2007), as are starbursts (Rodighiero et al. 2011; Guo et al. 2013). For instance, it was found by Kilerci Eser et al. (2014) that local ULIRGs with $M_* \sim 10^{10.5-11.5}$ are more than an order of magnitude higher than the MS, and that the majority of ULIRGs are interacting pairs or post-mergers. However, the present study reveals that the intermediate redshift LIRGs exceed the MS, in average, by 0.5 dex, even at lower stellar masses than those examined by the authors. In contrast, the FIR and LIRGs at low redshift do not demonstrate this trait fol-

[4] https://www.mpe.mpg.de/ir/Research/PEP/DR1/

Table 1. Sample of the values derived in this study for the properties of the SFGs in the Lockman–SpReSO catalogue.

objid	z_{spec}	$\log M_*(M_\odot)$	$\log L_{TIR}(L_\odot)$	$E(B-V)_{H\alpha/H\beta}$	$E(B-V)_{H\beta/H\gamma}$	$E(B-V)_{CIGALE}$	$E(B-V)_{IR/UV}$	$12+\log(O/H)_{P16}$	$12+\log(O/H)_{PP04}$
(1)	(2)	(3)	(4)	(5)	(6)	(7)	(8)	(9)	(10)
96702	0.54950± 0.00005	10.00 ± 0.13	10.92 ± 0.12	-	-	$0.62^{+0.09}_{-0.08}$	$0.67^{+0.11}_{-0.11}$	-	-
99389	0.81001± 0.00005	10.59 ± 0.08	11.64 ± 0.05	-	-	$0.88^{+0.04}_{-0.04}$	$0.91^{+0.14}_{-0.12}$	-	-
132869	0.41953± 0.00008	10.48 ± 0.04	10.84 ± 0.03	-	-	$0.40^{+0.03}_{-0.03}$	$0.40^{+0.07}_{-0.08}$	-	-
94458	0.67084± 0.00004	10.77 ± 0.08	11.73 ± 0.02	-	-	$0.76^{+0.02}_{-0.02}$	$0.89^{+0.09}_{-0.11}$	-	-
123801	0.61025± 0.00006	10.65 ± 0.09	11.12 ± 0.06	-	-	$0.75^{+0.08}_{-0.08}$	$0.72^{+0.10}_{-0.12}$	-	-

Table 1. *continued*

objid	$12+\log(O/H)_{T04}$	$12+\log(O/H)_{KK04}$	$12+\log(O/H)_{D16}$	$\log[SFR_{H\alpha}(M_\odot yr^{-1})]$	$\log[SFR_{H\beta}(M_\odot yr^{-1})]$	$\log[SFR_{H\gamma}(M_\odot yr^{-1})]$	$\log[SFR_{[OII]}(M_\odot yr^{-1})]$
(1)	(11)	(12)	(13)	(14)	(15)	(16)	(17)
96702	-	$8.74^{+0.22}_{-0.32}$	-	-	1.08 ± 0.19	-	1.25 ± 0.47
99389	-	-	-	-	1.91 ± 0.21	-	1.93 ± 0.45
132869	-	-	-	-	-	-	-
94458	-	-	-	-	1.68 ± 0.06	-	1.44 ± 0.44
123801	-	-	-	-	-	-	1.08 ± 0.47

Table 1. *continued*

objid	$\log[SFR_{L_{TIR}}(M_\odot yr^{-1})]$	$\log[SFR_{CIGALE}(M_\odot yr^{-1})]$	$\log[SFR_{CIGALE(10Myrs)}(M_\odot yr^{-1})]$	$\log[SFR_{CIGALE(100Myrs)}(M_\odot yr^{-1})]$
(1)	(18)	(19)	(20)	(21)
96702	1.10 ± 0.12	0.87 ± 0.14	0.87 ± 0.14	0.83 ± 0.12
99389	1.82 ± 0.05	1.59 ± 0.07	1.59 ± 0.07	1.58 ± 0.07
132869	1.02 ± 0.03	0.74 ± 0.05	0.74 ± 0.05	0.73 ± 0.05
94458	1.91 ± 0.02	1.61 ± 0.04	1.61 ± 0.04	1.59 ± 0.06
123801	1.30 ± 0.06	0.95 ± 0.13	0.96 ± 0.13	0.94 ± 0.13

Notes. Column (1) is the unique identification number for each object in the Lockman–SpReSO catalogue. Column (2) is the spectroscopic redshift of the object. Column (3) is the stellar mass obtained from the SED fittings using CIGALE. Column (4) is the IR luminosity obtained from the SED fittings using CIGALE. Columns (5)–(8) are the colour excess calculated in this work (see Sect. 4). Columns (9)–(13) are the metallicities derived in this work following different calibrations (see Sect. 5). Columns (14)–(21) are the SFR derived in this work following different calibrations (see Sect. 6).

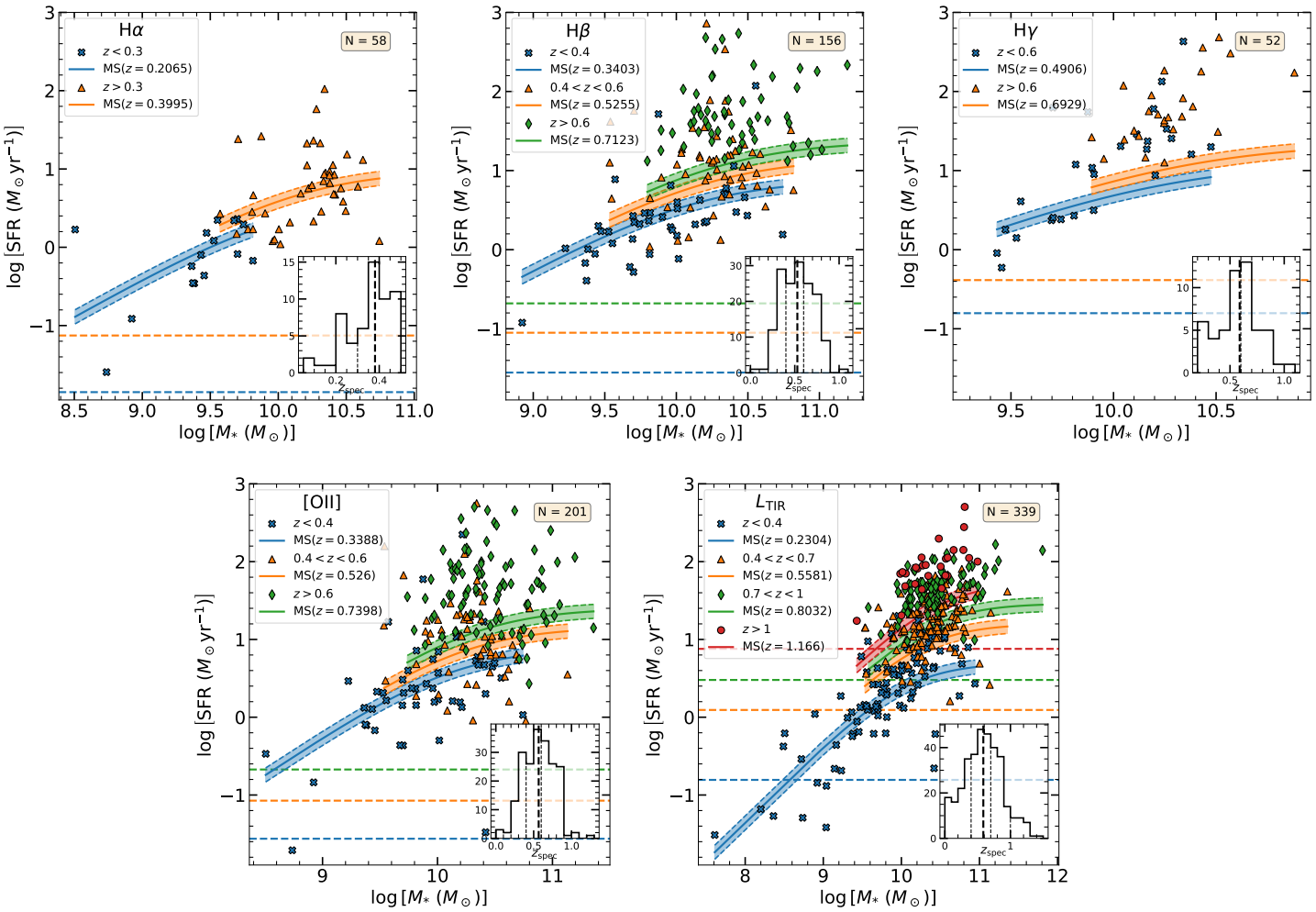

Fig. 10. SFR–M relation for different SFR determination methods. From left to right and top to bottom, the SFR determined using Hα, Hβ, Hγ, [O II], and $L_{\rm TIR}$ fluxes is displayed. Inside each panel the sample was divided into redshift ranges. The solid lines represent the MS from Popesso et al. (2023) evaluated at the mean redshift of each subsample, denoted by the points, using the same colour as the MS. The shaded areas and dashed lines represent 0.09 dex of scatter obtained by Popesso et al. (2023). The horizontal dashed lines designate the minimum detectable SFR for each redshift bin and SFR tracer, using the same colour scheme. The inset histograms show the redshift distribution for the complete sample in each panel. The vertical thick black dashed line indicates the redshift mean, and the vertical thin lines indicate the sample division boundaries. The numbers at the top indicate the total number of objects in each panel.

Table 2. Mean values and errors of the shifts found with respect to the MS, obtained for the different SFR tracers. The mean values have been tabulated for objects with z=0.4 as separator, as well as the mean value for the whole sample.

SFR	Mean shifts (dex)		
tracer	$z < 0.4$	$z > 0.4$	All z
Hα	-0.05 ± 0.06	0.20 ± 0.10	0.04 ± 0.06
Hβ	-0.02 ± 0.06	0.49 ± 0.06	0.35 ± 0.05
Hγ	0.12 ± 0.12	0.65 ± 0.06	0.60 ± 0.06
[O II]	0.01 ± 0.08	0.38 ± 0.04	0.29 ± 0.04
$L_{\rm TIR}$	0.10 ± 0.03	0.40 ± 0.02	0.32 ± 0.02

lowing the MS with a low scatter, as we have seen before. This indicates an evolutionary tendency of LIRGs, which has unique features compared to that of ULIRGs.

In the same way as the SFR–M_* relation increases with redshift, the sSFR increases steadily up to $z \sim 2$ and then tends to flatten out (Speagle et al. 2014; Popesso et al. 2023, and references therein). In Fig. 11 we have plotted the sSFR, using the SFR derived by $L_{\rm TIR}$, against redshift and coloured by M_* for the Lockman–SpReSO and Oi et al. (2017) objects. The galaxies from Oi et al. (2017) are a sample of AKARI-detected mid-IR SFG at $z \sim 0.88$ with Subaru/FMOS spectroscopic observations. The MS defined by Popesso et al. (2023) is also plotted with $\log M_*(M_\odot)$ set to the median value of the sample (10.28), and 9, 10 and 11, showing the evolution with redshift and M_*. The relationship of Elbaz et al. (2011) shown in Fig. 11 was produced by examining infrared SEDs for a sample of objects in the redshift range $0 < z < 2.5$. For the study, they assumed a slope of 1 in the SFR–M_* relation and constant over the whole redshift range; that is, independent of mass:

$$\mathrm{sSFR}\,(\mathrm{yr}^{-1}) = 26 \cdot 10^{-9} \times t^{-2.2} \qquad (19)$$

where t is the cosmic time. They mark as starbursts those galaxies which, for the same redshift, have an sSFR twice that of the MS, represented by the upper edge of the grey-shaded area. As

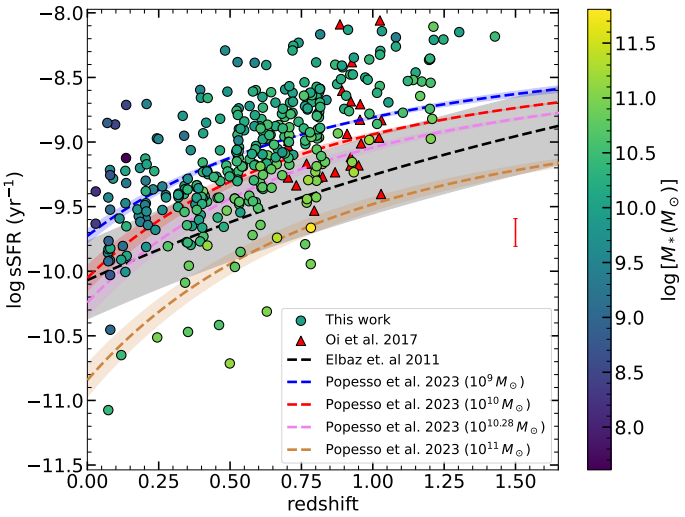

Fig. 11. Redshift and M_* evolution of the sSFR for SFG. The circles represent the Lockman–SpReSO galaxies, colour coded by M_*. The MS defined by Popesso et al. (2023) is shown in magenta for the mean M_* and in blue, red and brown for log $M_*(M_\odot)$ set to 9, 10 and 11, respectively. The black line is the MS defined by Elbaz et al. (2011) for IR galaxies, assuming independence with M_*. The grey shaded region marks the area above which the galaxies are classified as starbursts. The Lockman sample tends to populate this region regardless of the MS used. The galaxies from Oi et al. (2017), shown as red triangles, follow the behaviour of the Lockman–SpReSO objects.

for the case of the SFR–M_* relation, the Lockman–SpReSO objects have sSFRs that tend to be higher than the MS shown in the figure, so we are studying galaxies with very intense outbursts of star formation; that is, starburst galaxies. However, although the data follow the general trend of decreasing sSFR with increasing M_*, no evident flattening can be observed with redshift, and only the most massive galaxies seem to fit the Popesso et al. (2023) and Elbaz et al. (2011) relations, while for galaxies with stellar mass values that are below the median, sSFR is higher than the models showing a median scatter of 0.31 dex and 0.56 dex from Popesso et al. (2023) and Elbaz et al. (2011), respectively.

7.2. Mass–metallicity relation for infrared galaxies

The existence of a relation between M_* and metallicity of galaxies is well known in a wide range of spectroscopic redshifts ($0 < z < 3$), with lower-mass galaxies having lower metallicity and more massive galaxies having higher metallicity. However, the evolution of this relation with redshift is still a matter of debate. This discussion also extends to the analysis of IR objects and the evolution of the M_*–metallicity relation for these objects and the differences with optically selected ones.

As a benchmark to low redshift ($z \sim 0.1$), we have used the OSSY catalogue (Oh et al. 2011), an improved and quality-assessed set of emission and absorption line measurements in SDSS galaxies. The M_* of these objects were taken from SDSS Data Release 10 (Ahn et al. 2014), obtained by SED fits using the Sloan photometric bands[5]. In addition, to make the comparison between IR-selected samples of galaxies, we matched the OSSY catalogue with the *Herschel* Extra-galactic Legacy Project (HELP) database (Shirley et al. 2019). The HELP group has merged the information from the various fields observed by *Herschel* to create a general catalogue in which, in addition to the IR information of the objects, they have added all the information in other photometric bands obtained by other surveys, from UV to FIR. Using this information, they performed a SED fit analysis of the sources catalogued in the HELP database using CIGALE software, providing new measurements of M_*, $L_{\rm TIR}$ and extinction, among other parameters (Małek et al. 2018).

To analyse the MZR, we used the metallicity obtained by the iterative method of KK04 and T04, both based on the R_{23} tracer, since it provides the most complete set in terms of number of objects and is widely used in the literature, together with the M_* obtained by the SED fitting process in Gonzalez-Otero et al. (2023). Figure 12 shows the MZR diagram obtained for both metallicity estimators. The metallicity of Oi et al. (2017) was calculated using the N2 tracer calibrated by PP04. For comparison with the Lockman–SpReSO sample, the metallicities have been converted from N2 to R_{23} by performing a calibration using the full OSSY sample and a second-order polynomial fit, see Appendix B for details. It can be seen, from both panels, that the metallicities derived for the Lockman–SpReSO and Oi et al. (2017) samples are compatible, and tend to be lower than those of the OSSY sample, with the exception being the highest M_*, which corresponds to the area with the densest concentration of OSSY galaxies. Moreover, this result agrees with that obtained by Oi et al. (2017), who find that the metallicities for their IR-selected objects are compatible with those obtained by T04 for normal SFGs in the local Universe ($z \sim 0.1$) and higher than those of Zahid et al. (2011) for a sample of DEEP2 galaxies with $z \sim 0.78$. However, the Oi et al. (2017) data represent the highest redshift and the highest stellar mass of the Lockman–SpReSO sample. At lower stellar masses the metallicity is lower by ~ 0.25 dex. Both properties show a positive Spearman's rank correlation coefficient of 0.36 at a significance of 3.5σ for the metallicity of KK04 and 0.34 at a significance of 2.9σ for the metallicity of T04. In addition, we proceeded to test whether IR objects behave differently from optical objects when studying the MZR. To this end, we analysed the behaviour of the IR properties in MZRs obtained from samples of objects not selected according to their IR flux.

In Fig. 13 we show the MZR diagram using the metallicities from KK04 upper branch, and from T04 for the Lockman–SpReSO and Oi et al. (2017) objects. In addition, we have binned the M_* for the OSSY catalogue, for both the full catalogue and the catalogue merged with HELP, considering the median metallicity in each bin (only bins those with more than 40 galaxies are represented). This reveals that the metallicity of the bins with an IR detection is lower than that obtained for the full catalogue in the two metallicity tracers studied, as can be seen in the two panels of Fig. 13. For a sample of nearby LIRGs and ULIRGs at a redshift of around 0.1, Rupke et al. (2008) also found that these types of galaxies exhibited a median metallicity offset of 0.4 dex from the MZR discovered T04.

The Zahid et al. (2014) model, originally computed using an IMF of Chabrier (2003) and the metallicity calibration of KK04, is also included in Fig. 13 for local SDSS galaxies ($z \sim 0.08$) and distant galaxies from the SHELS ($z \sim 0.29$), DEEP2 ($z \sim 0.78$) and COSMOS ($z \sim 1.55$) surveys. The linear relationship obtained by Savaglio et al. (2005) for the MZR is also shown in Figure 13. They studied 60 SFGs in the redshift range $0.4 < z < 1.0$ using the metallicity calibration of KK04 and an IMF Baldry & Glazebrook (2003, 1.13 times that of Chabrier 2003). As a benchmark for high redshift we have shown the MZR from the Erb et al. (2006) paper, an analysis of 87 rest-frame UV-selected

[5] The IMF used by Ahn et al. (2014) in the SED fitting process is that of Kroupa (2001). To transform from Kroupa (2001) to Chabrier (2003) a multiplicative factor of 0.94 or -0.02 in dex must be applied.

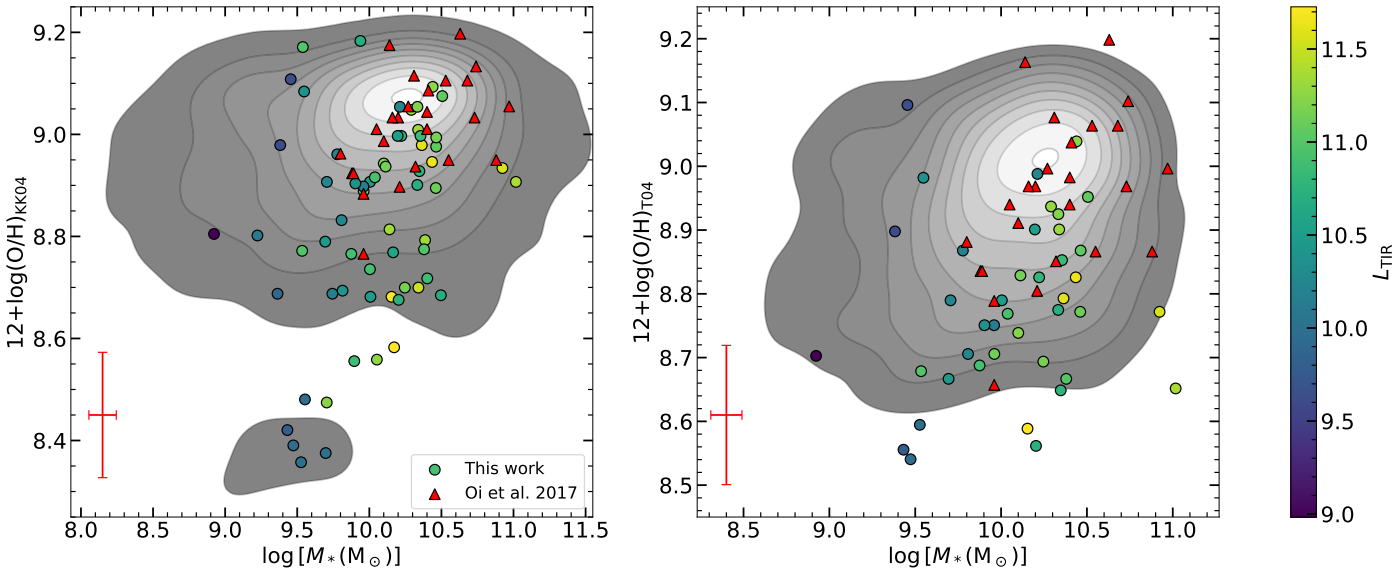

Fig. 12. MZR using the metallicity parameterisation from Kobulnicky & Kewley (2004, left) and Tremonti et al. (2004, right). In both panels the galaxies from Lockman–SpReSO are colour coded according to $L_{\rm TIR}$. The red triangles are the galaxies from the paper by Oi et al. (2017). The shadows and contours in the background represent the merged galaxies from the OSSY catalogue (Oh et al. 2011) and the HELP catalogue (Shirley et al. 2019). The mean error is shown in red at the bottom left.

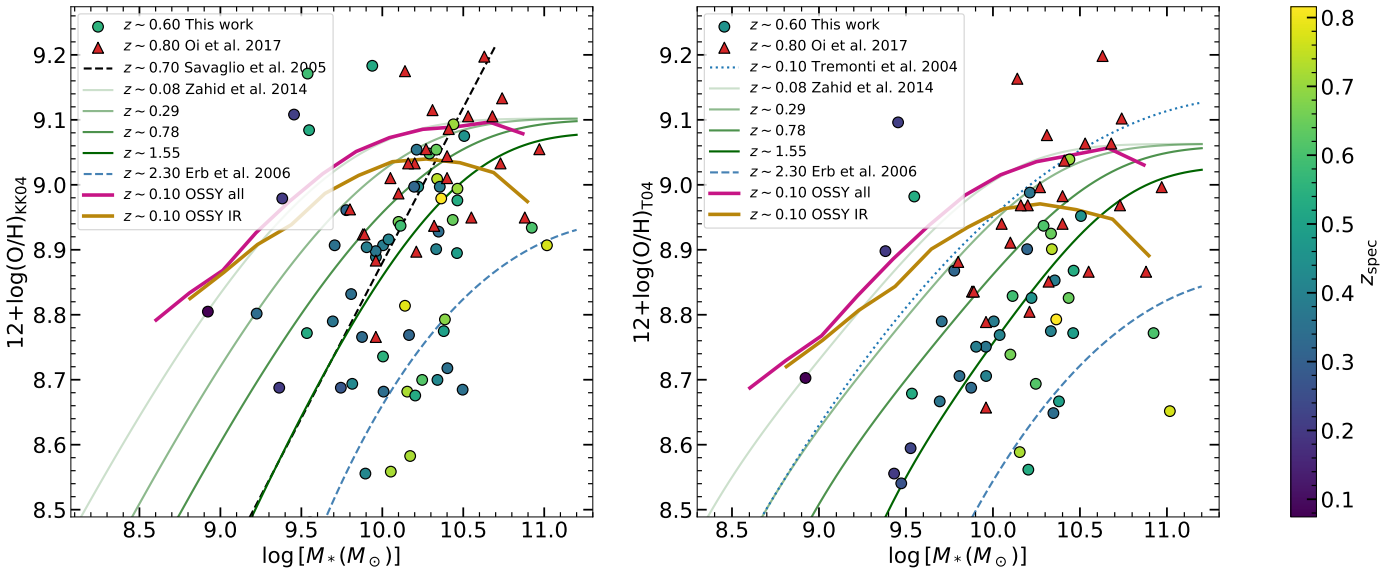

Fig. 13. MZR diagram using the Kobulnicky & Kewley (2004, left) and Tremonti et al. (2004, right) metallicity calibrations. The blue dots represent our Lockman–SpReSO data at a median redshift ∼ 0.6 and the red triangles represent the Oi et al. (2017) IR galaxies at a median redshift ∼ 0.8. The magenta line represents the median metallicity for each mass binning of the whole OSSY catalogue, while the brown line represents the same binning but only for the OSSY objects with IR information in HELP. The green lines represent the MZR model from Zahid et al. (2014) applied to galaxies from the SDSS ($z \sim 0.08$), SHELS ($z \sim 0.29$), DEEP2 ($z \sim 0.78$) and COSMOS ($z \sim 1.55$) surveys. The black dashed line represents the linear MZR model obtained by Savaglio et al. (2005) for 60 galaxies with an average redshift of $z \sim 0.7$. In both the OSSY catalogue and the Lockman objects, it can be seen that, except at the higher masses of the sample, IR objects tend to be less metallic than optical objects at the same redshift. The blue dashed line shows the MZR obtained by Erb et al. (2006) for a sample of UV-selected SFGs at $z \sim 2.3$.

SFG with a mean redshift $z \sim 2.23$ from Keck/LRIS observations that also confirms the evolution of the MZR with cosmic time. The KK04 to T04 metallicity transformation was calibrated in the same way as was done previously for the metallicity from Oi et al. (2017), as shown in Appendix B. It can be seen that the result obtained by Zahid et al. (2014) for their SDSS sample and our result for the full OSSY sample are in good agreement, while again the OSSY IR objects have lower metallicities than the full OSSY sample. The MZR model at $z \sim 1.55$ is the best fit for the lower-mass Lockman–SpReSO data ($M_* \lesssim 10^{10.2}\,M_\odot$) showing a median dispersion from the MZR of 0.04 dex, while for Oi et al. (2017) and the Lockman–SpReSO data of similar masses both models $z \sim 1.55$ and $z \sim 0.78$ fit the behaviour of the data well, showing the same absolute dispersion from both MZRs (0.07 dex). This is due to the short evolution of the MZR and the dispersion of the data in this range of M_*. This

again indicates that the metallicities of Lockman–SpReSO data at $M_* \lesssim 10^{10.2}\,M_\odot$ are lower than predicted by the models, especially when we analyse the MZR using the T04 metallicity calibration, where the Lockman–SpReSO objects show a median dispersion of 0.02 dex with respect to the MZR at $z \sim 1.55$. At higher M_*, the redshift evolution of the MZR is smaller. It is evident in the displayed MZRs in Fig. 13 that the most massive galaxies attain almost their current metallicity at redshift $z \sim 1$ (Zahid et al. 2014; Maiolino & Mannucci 2019).

7.3. The M_*–SFR–metallicity relation

As we have seen above, there is a strong relationship between M_* and SFR, as well as between M_* and metallicity, both of which have been extensively studied in the literature. However, it is only relatively recently that a clear dependence between SFR and metallicity has become evident. The initial hints of this relationship were discovered by Ellison et al. (2008), who found a slight connection between sSFR and metallicity. Shortly afterwards, almost simultaneously and independently, Lara-López et al. (2010) and Mannucci et al. (2010) found and described the mutual relationship between SFR, M_*, and metallicity.

Lara-López et al. (2010) used a complete magnitude-limited sample of SFGs, with the r-band falling in the range 14.5 to 17.77 mag, sourced from the SDSS-DR7 catalogue. This sample spanned a redshift range of $0.04 < z < 0.1$. Using the M_* as the dependent variable on SFR and metallicity, they fitted a plane to the distribution formed in the 3D space of these parameters. With a scatter of 0.16 dex in their fit, they found the existence of a clear relationship between the three galaxy properties, which they named the Fundamental Plane (FP). Furthermore, when Lara-López et al. (2010) compared their findings with data from studies at higher redshifts, extending up to $z \sim 3$, they ascertained that the FP exhibited no evolution with redshift. In subsequent papers Lara-López et al. (2013a,b), revisited the FP. This revision involved expanding the studied sample by adding data from the GAMA survey, which is two orders of magnitude deeper than the SDSS (up to $z \sim 0.35$). They also applied principal component analysis (PCA) in their investigation, resulting in a reduction in the scatter within the Fundamental Plane. The FP offers the ability to estimate the M_* of SFGs using both SFR and metallicities, with a dispersion of 0.2 dex, as demonstrated by Lara-López et al. (2013a).

Using the SDSS–DR7 sample for the redshift range $0.07 < z < 0.3$, Mannucci et al. (2010), and the Mannucci et al. (2011) application for a low-mass sample, they determined that SFGs delineate a surface in 3D space defined by M_*, metallicity, and SFR. This relation was designated the Fundamental Metallicity Relation (FMR). The scatter they identified was ~ 0.05 dex, a value in line with the uncertainties inherent in the galaxy properties analysed. Mannucci et al. (2010) used metallicity as the dependent variable in relation to M_* and SFR.

The findings from both the FP and the FMR point to a robust connection for SFGs among SFR, M_*, and metallicity. Equally significant is the observation that this connection remains unaltered with redshift, persisting up to $z \sim 3$, which is also confirmed by several independent works (see for example Hunt et al. 2012; Cresci et al. 2019; Sanders et al. 2021, among many others).

In this paper, to study the relationship between SFR, M_* and metallicity, we used the plane described by Lara-López et al. (2010), where M_* is studied as a function of SFR and metallicity

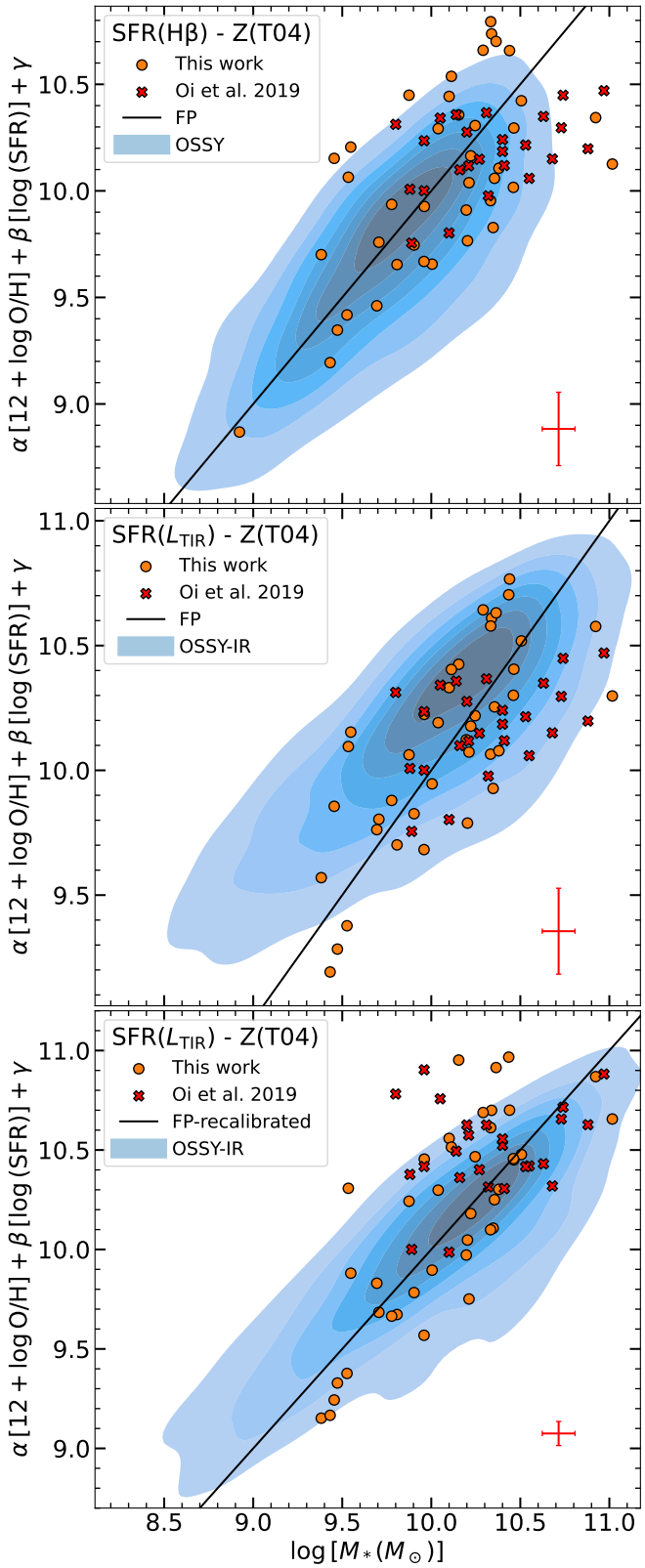

Fig. 14. Projection of the FP onto the M_* coordinate against the observed M_*. In the top panel we have used the SFR derived from the Hβ flux, the metallicity using the Tremonti et al. (2004) calibration and the Lara-López et al. (2013a) parameterisation. The orange dots are the Lockman–SpReSO SFGs, the red crosses are the Oi et al. (2017) data and the blue contours at the bottom are the OSSY data. The middle panel shows the same, but with the IR-derived SFR. In the lower panel we show the recalibration of the FP using the OSSY data with IR information to obtain a calibrated FP with the L_{TIR}-derived SFR. A more detailed discussion is given in the text.

using the following expression:

$$\log M_* = \alpha\,[12 + \log(\mathrm{O/H})] + \beta\,[\log \mathrm{SFR}] + \gamma \quad (20)$$

where $\alpha = 1.3764$, $\beta = 0.6073$, and $\gamma = -2.5499$ obtained from the revision of the FP by Lara-López et al. (2013a).

In the top panel of Fig. 14 we have plotted the fundamental plane (Eq. 20) for the metallicity calibration obtained by T04 and SFR obtained using the Hβ luminosity. It can be seen that the fundamental plane reproduces very well both the sample of local OSSY objects, represented by the background contours, and the sample of IR-selected Lockman–SpReSO galaxies when using the SFR derived from the Hβ flux, obtaining an average scatter of the plane of 0.20 dex, which is only slightly larger than the average uncertainty found for the M_* determined by SED fits (0.1 dex). However, when using L_{TIR}, the Fundamental Plane does not reproduce the behaviour of the data, as can be seen in the middle panel of Figure 14. This is due to the definition of the FP by Lara-López et al. (2013a), which specifically uses the Hα flux and the T04 metallicity for its construction. In order to carry out a fair comparison, it is necessary to recalibrate Eq. 20, because we have to take into account that when analysing L_{TIR} and the Balmer lines, we are studying not only different star formation timescales, but also different regions of the galaxies, although they are related. Assuming that the metallicity derived using optical lines is representative of the whole galaxy, and using the OSSY sample with IR information, we have refitted Eq. 20. We have used the SFR derived from the IR luminosity and M_* obtained by the HELP team using SED fits with CIGALE (Małek et al. 2018; Shirley et al. 2019). The new parameters obtained are $\alpha = 0.3640$, $\beta = 0.9071$ and $\gamma = 6.1029$. The result is shown in the lower panel of Fig. 14, where we have plotted the recalibration of the Fundamental Plane with the IR derived SFR and T04 metallicity calibrator. It can be seen that the FP now reproduces very well the behaviour of the Lockman–SpReSO data with an average scatter of 0.17, although for the Oi et al. (2017) data there seems to be a wider scatter, mainly owing to the metallicity transformation used for comparison. This result shows that the Fundamental Plane makes it possible to calculate the M_* of galaxies with a low level of uncertainty.

Salim et al. (2014) re-analysed the SDSS galaxies and found that for $M_* \gtrsim 10.5\,M_\odot$ the relationship between sSFR and metallicity appears to be weak or non-existent, a result also found in simulations by Matthee & Schaye (2018), who argue that it is due to contamination by AGN. Although in this paper the FP study using the SFR from Hβ flux (top panel in Fig. 14) seems to support this trend, the FP study using the SFR from L_{TIR} flux (bottom panel in Fig. 14) does not support this trend; and neither does our sample include AGN.

From the previous two subsections, we have shown that Lockman–SpReSO SFGs tend to have lower metallicities than normal galaxies and SFRs above the MS for redshifts $z > 0.4$, typical of starburst galaxies. Despite these unusual properties, the Fundamental Plane remains valid, although it was formulated using samples of objects very different from those studied here. Moreover, neither do we find any difference in the observed trends between the different SFR tracers. This also supports the non-evolutionary theory of the Fundamental Plane, since no redshift trends are evident. This result is in agreement with that found by Hunt et al. (2012) for a sample of $\sim$ 1000 extreme and rare objects. They selected local quiescent SFGs and blue compact dwarfs, luminous compact emission line galaxies at $z = 0.3$ and Lyman-break galaxies spanning a redshift range of $1 < z < 3$. In plots such as MZR or MS, these objects appear as outliers owing to their extreme properties. However, these objects follow the FP with good accuracy, a result that extrapolates the relationship between SFR, M_* and metallicity to extreme class objects.

The most accepted explanation for the non-evolution of the FP lies in the balance between SFR and metallicity at different stages of galaxy evolution (see the review by Maiolino & Mannucci 2019, and references therein). In general, galaxies at high redshift are composed of stars formed from poorly processed gas (that is of low metallicity), which is also associated with high SFR, as observed at these evolutionary stages. On the other hand, if we look at galaxies in the local Universe, stars are formed from highly processed material (that is, of high metallicity). Moreover, the availability of gas to form stars in local galaxies is more limited than in high-redshift galaxies, which implies lower SFR. This shows the balance, with high redshift galaxies having high SFRs at low metallicities, and local galaxies having low SFRs at higher metallicities. The fact that the evolution of SFR and metallicity with redshift go in opposite directions, helps to explain the non-evolution of the Fundamental Plane, although the parameterization can vary depending on the timescale of the SFR indicator used, as can be seen in the bottom panel of Figure 14.

8. Summary and conclusions

In this paper, we present the first study of the SFGs of the Lockman–SpReSO project. This project is an optical spectroscopic follow-up of *Herschel* FIR-selected sources with optical counterparts of $R_C < 24.5$ mag. The scope of the present work was to determine fundamental parameters such as extinction, metallicity, and SFR, and to study the relationships among them. To this aim, we used the FIR-selected galaxies for which the spectroscopic redshift was determined by Gonzalez-Otero et al. (2023), with the result that, in a total of 409 objects, the redshifts lay in the range $0.03 < z < 4.96$. The objects in the Lockman–SpReSO catalogue have photometric information over a wide spectral range, from X-ray to FIR bands. Apart from the optical spectroscopy, the derived redshifts and line fluxes, SED fits were also performed, from which, among other properties, M_* and L_{TIR} of the galaxies were obtained. These results have yielded a spectroscopic study with a higher number of carefully FIR-selected SFGs.

For the study, 69 objects (17%) identified as AGN based on the criteria outlined in Sec. 3 were excluded from the sample. This percentage is notably higher than that of local samples but is dependent largely on the selection criteria used. Finally, the resulting sample consists of 340 SFGs, with almost half of the sample being LIRGs.

From the analysis of the relationship between M_* and SFR, it resulted that SFGs at low redshifts, $z < 0.4$, follow the MS defined by Popesso et al. (2023), with a shift of ~ 0.1 dex, based on the emission line fluxes and L_{TIR} SFRs. However, at higher redshifts, the sample presents significant evolution by increasing the fraction of starburst galaxies, with 78% of the galaxies falling into this classification using the SFR derived from L_{TIR}. The shift from the MS is approximately 0.4 dex for each object. Therefore, SFGs from Lockman–SpReSO exhibiting significant burst of star formation, as would be expected for a FIR-selected sample. This result can also be observed when analysing the sSFR and its evolution over cosmic time, even when compared to the MS, such as that of Elbaz et al. (2011), which is designed for IR objects, although they assume that the MS is independent of M_*. However, in the present sample, no apparent flattening of sSFR with redshift for $\log M_*(M_\odot) \gtrsim 10.5$ is observed.

The MZR relationship, derived using T04 and KK04 metallicity calibrators, compared with data from Oi et al. (2017), shows that both samples are compatible. The comparison with the OSSY sample (Oh et al. 2011) containing IR information in the HELP database (Shirley et al. 2019) shows that Lockman–SpReSO galaxies have lower metallicities. Moreover, comparing with MZR from the literature Tremonti et al. (2004); Savaglio et al. (2005); Erb et al. (2006); Zahid et al. (2014), Lockman–SpReSO FIR-selected SFGs exhibit lower metallicities than anticipated for their redshift and M_*, since the MZR defined by Zahid et al. (2014) at $z \sim 1.55$ fits Lockman–SpReSO galaxies with a scatter of 0.1 dex. This result is particularly evident for masses $M_* \lesssim 10^{10.2}\,M_\odot$. At higher masses, where the Lockman–SpReSO and Oi et al. (2017) data overlap, due to the dispersion of the data and the short range of evolution of the MZRs at those M_*, the metallicity is equally fit by the MZR at $z \sim 1.55$ and at $z \sim 0.78$, closer to the mean redshift of the sample. Nonetheless, there is a limited number of Lockman–SpReSO galaxies in this region, while the majority of Oi et al. (2017) galaxies are present in this area. The present study also conducted the MZR comparison using both OSSY galaxies with IR photometric information, as well as the entire OSSY sample, showing that local galaxies with IR information also showcased decreased metallicities. This finding confirms the notion that IR galaxies have a tendency to show lower metallicities than optical galaxies.

Finally, by incorporating the SFR as an additional parameter in the MZR, which then becomes the FP, the dispersion is substantially reduced. The 3D correlation has been investigated following the work of Lara-López et al. (2010), who established the FP, where M_* is the dependent variable on both SFR and metallicity. Based on our analysis of the T04 metallicity and the SFR derived from Hβ flux, we have concluded that the FP is valid for the Lockman–SpReSO LIRG sample, despite the objects exhibiting strong SFR outbursts and lower metallicities compared to optical galaxies, showing a median scatter about the FP of ~ 0.20 dex. However, a recalibration of the FP is required to be able to use the SFR derived from $L_{\rm TIR}$. It has been established, then, that the FP is valid for LIRG objects. Nevertheless, when using $L_{\rm TIR}$ the known saturation of the relation $\log M_*(M_\odot) \gtrsim 10.5$ is not observed, contrary to the findings of Salim et al. (2014) and Matthee & Schaye (2018), for non-IR-selected galaxies. This could point towards an evolution of the more massive fraction of the sample, in the sense of decreasing present-day star formation with respect to the averaged star formation in the past. The balance between the SFR excess and the metallicity deficit justifies the applicability of the FP (Lara-López et al. 2010, 2013b; Maiolino & Mannucci 2019, among many others), further supporting the reasoning behind its non-evolution.

Acknowledgements. We thank the anonymous referee for their useful report. This work was supported by the Evolution of Galaxies project, of references: PRE2018-086047, AYA2017-88007-C3-1-P, AYA2017-88007-C3-2-P, AYA2018-RTI-096188-BI00, PID2019-107408GB-C41, PID2019-106027GB-C41 and, PID2021-122544NB-C41, PID2022-136598NB-C33, within the *Programa estatal de fomento de la investigación científica y técnica de excelencia del Plan Estatal de Investigación Científica y Técnica y de Innovación (2013-2016)* of the Spanish Ministry of Science and Innovation/State Agency of Research MCIN/AEI/ 10.13039/501100011033 and by 'ERDF A way of making Europe'. This article is based on observations made with the Gran Telescopio Canarias (GTC) at Roque de los Muchachos Observatory on the island of La Palma, with the Willian Herschel Telescope (WHT) at Roque de los Muchachos Observatory on the island of La Palma and on observations at Kitt Peak National Observatory, NSF's National Optical-Infrared Astronomy Research Laboratory (NOIRLab Prop. ID: 2018A-0056; PI: González-Serrano, J.I.), which is operated by the Association of Universities for Research in Astronomy (AURA) under a cooperative agreement with the National Science Foundation. This research has made use of the NASA/IPAC Extragalactic Database (NED), which is funded by the National Aeronautics and Space Administration and operated by the California Institute of Technology. J.N acknowledge the support of the National Science Centre, Poland through the SONATA BIS grant 2018/30/E/ST9/00208. YK aknowledges support from PAPIIT grant 102023. ICG and EB acknowledge financial support from DGAPA-UNAM grant IN-119123 and CONAHCYT grant CF-2023-G-100. The authors thank Terry Mahoney (at the IAC's Scientific Editorial Service) for his substantial improvements of the manuscript.

References

Ahn, C. P., Alexandroff, R., Allende Prieto, C., et al. 2014, ApJS, 211, 17
Baldry, I. K. & Glazebrook, K. 2003, ApJ, 593, 258
Baldwin, J. A., Phillips, M. M., & Terlevich, R. 1981, PASP, 93, 5
Boquien, M., Burgarella, D., Roehlly, Y., et al. 2019, A&A, 622, A103
Brinchmann, J., Charlot, S., White, S. D. M., et al. 2004, MNRAS, 351, 1151
Bruzual, G. & Charlot, S. 2003, MNRAS, 344, 1000
Burgarella, D., Buat, V., & Iglesias-Páramo, J. 2005, MNRAS, 360, 1413
Calzetti, D., Armus, L., Bohlin, R. C., et al. 2000, ApJ, 533, 682
Calzetti, D., Kinney, A. L., & Storchi-Bergmann, T. 1994, ApJ, 429, 582
Cedrés, B., Pérez-García, A. M., Pérez-Martínez, R., et al. 2021, ApJ, 915, L17
Cepa, J., Aguiar, M., Escalera, V. G., et al. 2000, in Proc. SPIE, Vol. 4008, Optical and IR Telescope Instrumentation and Detectors, ed. M. Iye & A. F. Moorwood, 623–631
Chabrier, G. 2003, PASP, 115, 763
Chartab, N., Cooray, A., Ma, J., et al. 2022, Nature Astronomy, 6, 844
Chen, C. T. J., Brandt, W. N., Luo, B., et al. 2018, MNRAS, 478, 2132
Cid Fernandes, R., Stasińska, G., Schlickmann, M. S., et al. 2010, MNRAS, 403, 1036
Cresci, G., Mannucci, F., & Curti, M. 2019, A&A, 627, A42
Domínquez Palmero, L., Cano, D., Fariña, C., et al. 2014, in Society of Photo-Optical Instrumentation Engineers (SPIE) Conference Series, Vol. 9147, Ground-based and Airborne Instrumentation for Astronomy V, ed. S. K. Ramsay, I. S. McLean, & H. Takami, 914778
Donley, J. L., Koekemoer, A. M., Brusa, M., et al. 2012, ApJ, 748, 142
Dopita, M. A., Kewley, L. J., Sutherland, R. S., & Nicholls, D. C. 2016, Ap&SS, 361, 61
Duarte Puertas, S., Vilchez, J. M., Iglesias-Páramo, J., et al. 2022, A&A, 666, A186
Elbaz, D., Daddi, E., Le Borgne, D., et al. 2007, A&A, 468, 33
Elbaz, D., Dickinson, M., Hwang, H. S., et al. 2011, A&A, 533, A119
Elías-Chávez, M., Longinotti, A. L., Krongold, Y., et al. 2021, ApJ, 919, 18
Ellison, S. L., Patton, D. R., Simard, L., & McConnachie, A. W. 2008, ApJ, 672, L107
Erb, D. K., Shapley, A. E., Pettini, M., et al. 2006, ApJ, 644, 813
Ferland, G. J., Korista, K. T., Verner, D. A., et al. 1998, PASP, 110, 761
Figueira, M., Pollo, A., Małek, K., et al. 2022, A&A, 667, A29
Galametz, M., Kennicutt, R. C., Calzetti, D., et al. 2013, MNRAS, 431, 1956
Gonzalez-Otero, M., Padilla-Torres, C. P., Cepa, J., et al. 2023, A&A, 669, A85
Guo, K., Zheng, X. Z., & Fu, H. 2013, ApJ, 778, 23
Hao, C.-N., Kennicutt, R. C., Johnson, B. D., et al. 2011, ApJ, 741, 124
Henry, A., Rafelski, M., Sunnquist, B., et al. 2021, ApJ, 919, 143
Herrera-Camus, R., Sturm, E., Graciá-Carpio, J., et al. 2018, ApJ, 861, 95
Hopkins, A. M., Driver, S. P., Brough, S., et al. 2013, MNRAS, 430, 2047
Hopkins, A. M., Miller, C. J., Nichol, R. C., et al. 2003, ApJ, 599, 971
Hunt, L., Magrini, L., Galli, D., et al. 2012, MNRAS, 427, 906
Kauffmann, G., Heckman, T. M., Tremonti, C., et al. 2003, MNRAS, 346, 1055
Kennicutt, R. C. & Evans, N. J. 2012, ARA&A, 50, 531
Kewley, L. J., Dopita, M. A., Sutherland, R. S., Heisler, C. A., & Trevena, J. 2001, ApJ, 556, 121
Kewley, L. J., Groves, B., Kauffmann, G., & Heckman, T. 2006, MNRAS, 372, 961
Kewley, L. J., Maier, C., Yabe, K., et al. 2013, ApJ, 774, L10
Kilerci Eser, E., Goto, T., & Doi, Y. 2014, ApJ, 797, 54
Kobulnicky, H. A. & Kewley, L. J. 2004, ApJ, 617, 240
Kroupa, P. 2001, MNRAS, 322, 231
Lacy, M., Storrie-Lombardi, L. J., Sajina, A., et al. 2004, ApJS, 154, 166
Lara-López, M. A., Cepa, J., Bongiovanni, A., et al. 2010, A&A, 521, L53
Lara-López, M. A., Hopkins, A. M., López-Sánchez, A. R., et al. 2013a, MNRAS, 434, 451
Lara-López, M. A., López-Sánchez, Á. R., & Hopkins, A. M. 2013b, ApJ, 764, 178
Lee, N., Sheth, K., Scott, K. S., et al. 2017, MNRAS, 471, 2124
Lehmann, I., Hasinger, G., Schmidt, M., et al. 2001, A&A, 371, 833
Luo, B., Brandt, W. N., Xue, Y. Q., et al. 2017, ApJS, 228, 2
Maccacaro, T., Gioia, I. M., Wolter, A., Zamorani, G., & Stocke, J. T. 1988, ApJ, 326, 680
Magliocchetti, M., Popesso, P., Brusa, M., & Salvato, M. 2018, MNRAS, 473, 2493

Maiolino, R. & Mannucci, F. 2019, A&A Rev., 27, 3
Małek, K., Buat, V., Roehlly, Y., et al. 2018, A&A, 620, A50
Mannucci, F., Cresci, G., Maiolino, R., Marconi, A., & Gnerucci, A. 2010, MNRAS, 408, 2115
Mannucci, F., Salvaterra, R., & Campisi, M. A. 2011, MNRAS, 414, 1263
Matthee, J. & Schaye, J. 2018, MNRAS, 479, L34
Messias, H., Afonso, J., Salvato, M., Mobasher, B., & Hopkins, A. M. 2012, ApJ, 754, 120
Nadolny, J., Lara-López, M. A., Cerviño, M., et al. 2020, A&A, 636, A84
Nadolny, J., Michałowski, M. J., Rizzo, J. R., et al. 2023, ApJ, 952, 125
Oh, K., Sarzi, M., Schawinski, K., & Yi, S. K. 2011, ApJS, 195, 13
Oi, N., Goto, T., Malkan, M., Pearson, C., & Matsuhara, H. 2017, PASJ, 69, 70
Oke, J. B. & Gunn, J. E. 1983, ApJ, 266, 713
Osterbrock, D. E. 1989, Astrophysics of gaseous nebulae and active galactic nuclei
Pereira-Santaella, M., Rigopoulou, D., Magdis, G. E., et al. 2019, MNRAS, 486, 5621
Pettini, M. & Pagel, B. E. J. 2004, MNRAS, 348, L59
Pilyugin, L. S. & Grebel, E. K. 2016, MNRAS, 457, 3678
Pistis, F., Pollo, A., Scodeggio, M., et al. 2022, A&A, 663, A162
Popesso, P., Concas, A., Cresci, G., et al. 2023, MNRAS, 519, 1526
Ramón-Pérez, M., Bongiovanni, Á., Pérez García, A. M., et al. 2019, A&A, 631, A11
Reddy, N. A., Shapley, A. E., Sanders, R. L., et al. 2018, ApJ, 869, 92
Rodighiero, G., Daddi, E., Baronchelli, I., et al. 2011, ApJ, 739, L40
Rupke, D. S. N., Veilleux, S., & Baker, A. J. 2008, ApJ, 674, 172
Sabater, J., Best, P. N., Hardcastle, M. J., et al. 2019, A&A, 622, A17
Salim, S., Lee, J. C., Ly, C., et al. 2014, ApJ, 797, 126
Sanders, R. L., Shapley, A. E., Jones, T., et al. 2021, ApJ, 914, 19
Savaglio, S., Glazebrook, K., Le Borgne, D., et al. 2005, ApJ, 635, 260
Shirley, R., Roehlly, Y., Hurley, P. D., et al. 2019, MNRAS, 490, 634
Speagle, J. S., Steinhardt, C. L., Capak, P. L., & Silverman, J. D. 2014, ApJS, 214, 15
Stasińska, G., Cid Fernandes, R., Mateus, A., Sodré, L., & Asari, N. V. 2006, MNRAS, 371, 972
Stern, D., Eisenhardt, P., Gorjian, V., et al. 2005, ApJ, 631, 163
Stocke, J. T., Morris, S. L., Gioia, I. M., et al. 1991, ApJS, 76, 813
Szokoly, G. P., Bergeron, J., Hasinger, G., et al. 2004, ApJS, 155, 271
Tremonti, C. A., Heckman, T. M., Kauffmann, G., et al. 2004, ApJ, 613, 898
Webb, N. A., Coriat, M., Traulsen, I., et al. 2022, VizieR Online Data Catalog, IX/63
Xue, Y. Q., Luo, B., Brandt, W. N., et al. 2011, ApJS, 195, 10
Zahid, H. J., Dima, G. I., Kudritzki, R.-P., et al. 2014, ApJ, 791, 130
Zahid, H. J., Kewley, L. J., & Bresolin, F. 2011, ApJ, 730, 137

Appendix A: Branch selection criteria

P16 use the value of the N_2 parameter ([N II] $\lambda\lambda$6548.84/Hβ) as a method of separating the upper and lower branches, with objects with $\log N_2 < -0.6$ belonging to the lower branch and objects with $\log N_2 > -0.6$ belonging to the upper branch. However, for objects with a redshift $z \gtrsim 0.45$, the [N II] is no longer visible, so this method is not applicable. To separate the higher redshift objects into branches, we have used the OSSY data and analysed how the two branches behave in different plots to obtain a separation criterion. In the left panel of Fig. A.1, where we plot the metallicity obtained with the P16 calibration against M_*, we can see that the objects in the lower branch do not exceed M_* values around $\log M_*(M_\odot) \sim 9.3$. In the middle panel, we plot the parameter R_{23} against the same metallicity to check the regime of the objects as a function of branch. It can be seen that in this plot the objects in the lower branch tend to be in the $R_{23} \gtrsim 0.8$ region. On the right we have plotted the two previous variables that we could use to constrain the branches. It is clear that by using a value of $R_{23} > 0.85$ and M_* of $\log M_*(M_\odot) < 9.3$ we could separate between the branches objects at higher redshifts where the [N II] lines are not visible.

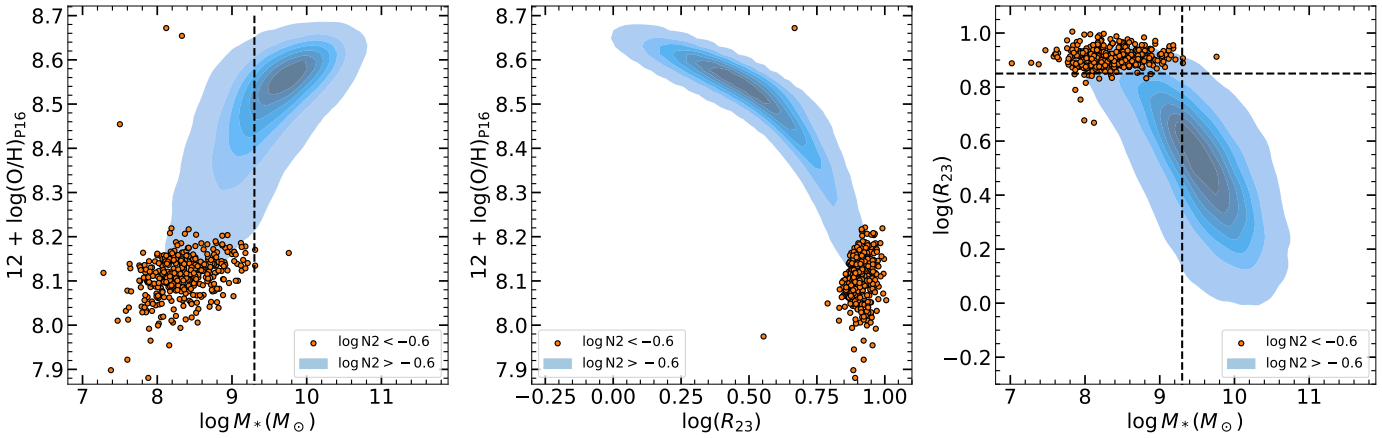

Fig. A.1. Criteria for separating galaxies into the upper and lower branches. On the left we have plotted the metallicity obtained with the Pilyugin & Grebel (2016) calibration against M_*. In orange we have plotted the OSSY data that meet the $\log N_2 < -0.6$ criterion, defined by Pilyugin & Grebel (2016) as the branch separation. The blue contours in the background represent the OSSY objects in the upper branch, and the vertical dashed line marks a M_* value of $\log M_*(M_\odot) = 9.3$, which seems to mark a limit for the objects in the lower branch. In the middle panel we show the relationship between the same metallicity and the parameter R_{23}. In the right panel we have plotted the parameter R_{23} against M_*. The vertical line at $\log M_*(M_\odot) = 9.3$ and the horizontal line at $R_{23} = 0.85$ mark the region where the lower branch objects tend to be.

Appendix B: Metallicity calibrations

In order to compare the metallicities obtained with different parameterisations, we have performed calibrations between different methods using the OSSY database.

The calibration for the transformation from PP04 metallicity, based on the N2 tracer, to the metallicities of KK04 and T04 is shown in the Fig. B.1. The calibrations obtained in the fits are:

$$[12 + \log(\mathrm{O/H})]_{\mathrm{KK04}} = -83.91818785 + 20.37854882 \times [12 + \log(\mathrm{O/H})]_{\mathrm{PP04-N2}} - 1.11361199 \times [12 + \log(\mathrm{O/H})]^2_{\mathrm{PP04-N2}} \quad \text{(B.1)}$$

$$[12 + \log(\mathrm{O/H})]_{\mathrm{T04}} = -58.34509817 + 14.154599852 \times [12 + \log(\mathrm{O/H})]_{\mathrm{PP04-N2}} - 0.7367259 \times [12 + \log(\mathrm{O/H})]^2_{\mathrm{PP04-N2}} \quad \text{(B.2)}$$

The calibration for the transformation from KK04 metallicity to T04 metallicity is shown in the left panel of Fig. B.2. The inverse transformation is also shown in the right panel of Fig. B.2. The calibrations obtained in the fits are:

$$[12 + \log(\mathrm{O/H})]_{\mathrm{T04}} = 86.72778038 - 18.61508955 \times [12 + \log(\mathrm{O/H})]_{\mathrm{KK04}} + 1.10771049 \times [12 + \log(\mathrm{O/H})]^2_{\mathrm{KK04}} \quad \text{(B.3)}$$

$$[12 + \log(\mathrm{O/H})]_{\mathrm{KK04}} = -48.25364669 + 12.06139695 \times [12 + \log(\mathrm{O/H})]_{\mathrm{T04}} - 0.63255371 \times [12 + \log(\mathrm{O/H})]^2_{\mathrm{T04}} \quad \text{(B.4)}$$

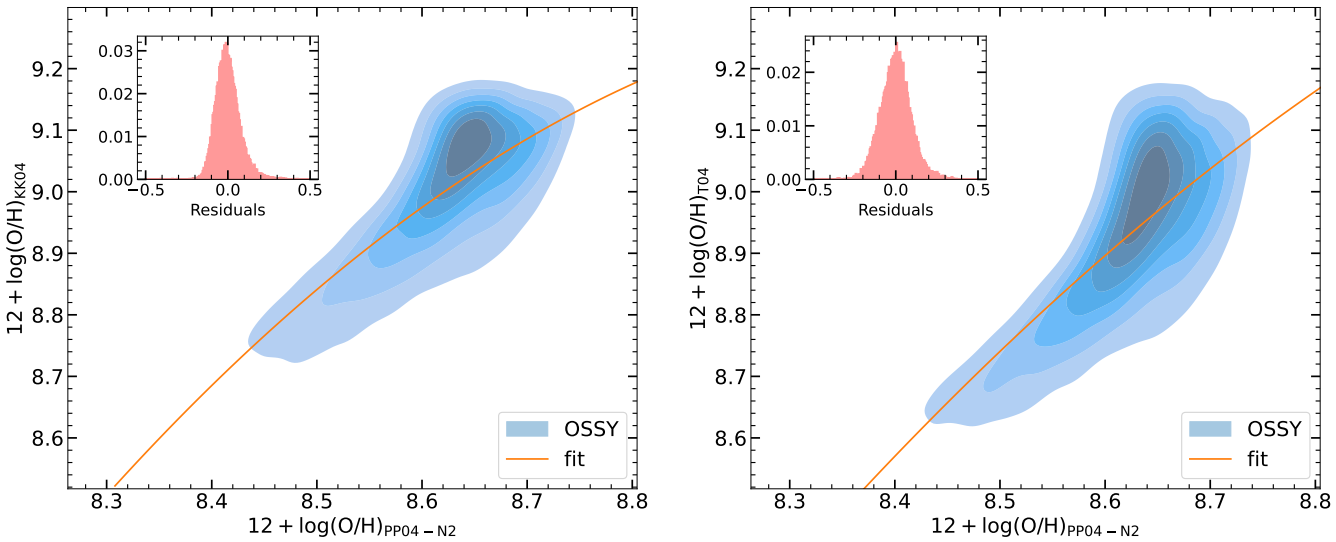

Fig. B.1. Cross-calibration of metallicity determination methods. On the left, we illustrate the transformation from metallicities following the Tremonti et al. (2004) method to those based on Kobulnicky & Kewley (2004). On the right, we depict the conversion from Kobulnicky & Kewley (2004) metallicities to those derived using the Tremonti et al. (2004) method. The blue circles represent data points sourced from the OSSY catalogue, while the orange line represents a third-order polynomial fit to the OSSY data.

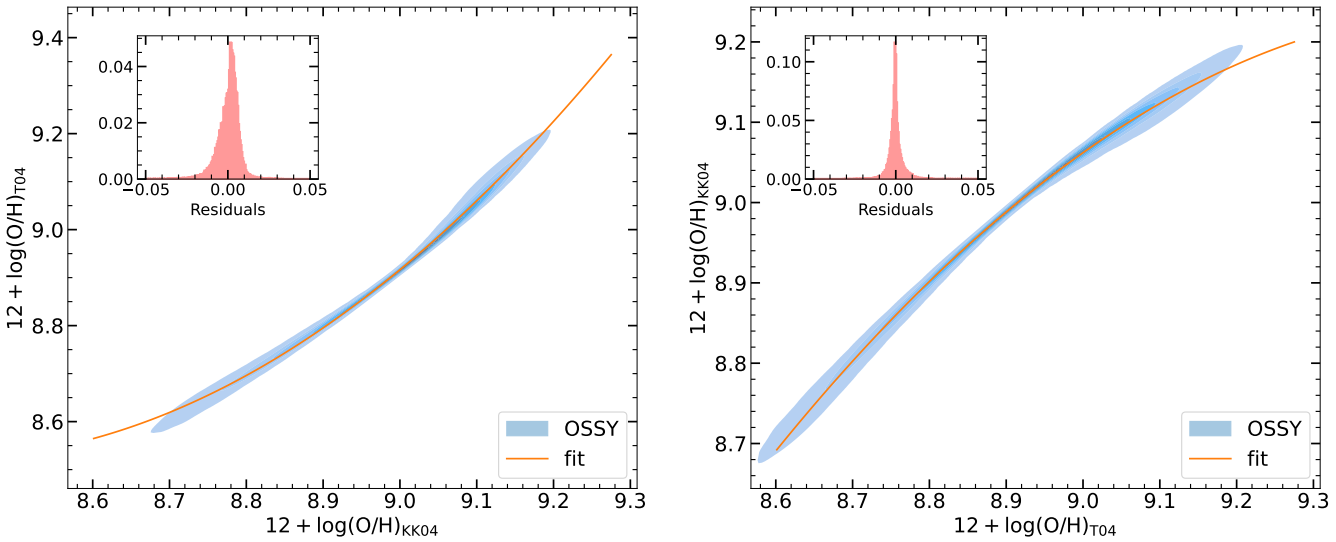

Fig. B.2. Cross-calibration of metallicity determination methods. On the left, we illustrate the transformation from metallicities following the Tremonti et al. (2004) method to those based on Kobulnicky & Kewley (2004). On the right, we depict the conversion from Kobulnicky & Kewley (2004) metallicities to those derived using the Tremonti et al. (2004) method. The blue circles represent data points sourced from the OSSY catalogue, while the orange line represents a third-order polynomial fit to the OSSY data.

4

The Lockman–SpReSO project. Galactic flows in a sample of far-infrared galaxies

In this chapter, we analyse Lockman–SpReSO sources with galactic flows by examining the Fe II and Mg II absorption lines in their spectra. Among the 456 objects with determined spectroscopic redshifts, Fe II and Mg II lines were observed in 21 objects, with redshifts in the range $0.5 \lesssim z \lesssim 1.44$.

This study aims to explore material ejection from star-forming regions and material infall into galaxies through analysis of Fe II and Mg II absorption lines. It also investigates correlations between galactic wind velocities, EWs, and galaxy properties such as M_*, SFR, and sSFR for a sample of FIR-selected objects. The analysed objects have M_* spanning $9.89 < \log(M_*/M_\odot) < 11.50$ and SFRs in the range $1.01 < \log(\mathrm{SFR}) < 2.70$.

Measurements of spectral lines including Mg II $\lambda\lambda$2796, 2803, Mg I λ2852, Fe II $\lambda\lambda$2374, 82, Fe II $\lambda\lambda$2586, 2600, and Fe II λ2344 are conducted to determine EW and velocity of flows in SFGs. Bootstrap simulations using Spearman's rank correlation coefficient (ρ_s) are performed to explore the correlations with galaxy properties. Additionally, the covering factor, gas density, and optical depth for the measured Fe II doublets were calculated for the sample.

The analysis reveals strong correlations between the EW of Mg II lines and both M_* ($\rho_s = 0.43, 4.5\sigma$) and SFR ($\rho_s = 0.42, 4.4\sigma$). For Fe II lines, strong correlations are observed with SFR ($\rho_s \approx 0.65, > 3.9\sigma$), with weaker correlations for M_* ($\rho_s \approx 0.35, > 1.9\sigma$). No notable correlations are found between velocity measurements of

Mg II lines and galaxy properties. However, a strong negative correlation is found between the velocity of Fe II lines and the SFR of galaxies ($\rho_s \approx -0.45, \approx 3\sigma$). The results are consistent with previous studies, although focusing solely on FIR-selected objects. Finally, a candidate "loitering outflow", a recently discovered sub-type of FeLoBAL quasars, is detected at a redshift of $z = 1.4399$, exhibiting emission in C III] and low line velocities ($|v| \leq 2000\,\mathrm{km\ s^{-1}}$)

The contents of this chapter have been published as González-Otero et al. (2024b).

A&A, 684, A31 (2024)
https://doi.org/10.1051/0004-6361/202347826

Astronomy & Astrophysics

The Lockman–SpReSO project

Galactic flows in a sample of far-infrared galaxies

Mauro González-Otero[1,2], Carmen P. Padilla-Torres[1,2,3,4], José Ignacio González-Serrano[4,5], Jordi Cepa[1,2,4], Ana María Pérez García[4,6], J. Jesús González[7], Erika Benítez[7], Ángel Bongiovanni[4,8], Miguel Cerviño[6], Irene Cruz-González[7], Jesús Gallego[9], Martín Herrera-Endoqui[7], Héctor J. Ibarra-Medel[7], Yair Krongold[7], Maritza A. Lara-López[9], Jakub Nadolny[10], Castalia Alenka Negrete[7], Ricardo Pérez-Martínez[4,11], Mirjana Pović[12,13,14], Miguel Sánchez-Portal[4,8], Bernabé Cedrés[4,8], José A. de Diego[7], Héctor Hernández-Toledo[7], and Rocío Navarro Martínez[4]

[1] Instituto de Astrofísica de Canarias, 38205 La Laguna, Tenerife, Spain
e-mail: mauro.gonzalez-ext@iac.es; mauromarago@gmail.com
[2] Departamento de Astrofísica, Universidad de La Laguna (ULL), 38205 La Laguna, Tenerife, Spain
[3] Fundación Galileo Galilei-INAF, Rambla José Ana Fernández Pérez, 7, 38712 Breña Baja Tenerife, Spain
[4] Asociación Astrofísica para la Promoción de la Investigación, Instrumentación y su Desarrollo, ASPID, 38205 La Laguna, Tenerife, Spain
[5] Instituto de Física de Cantabria (CSIC-Universidad de Cantabria), 39005 Santander, Spain
[6] Centro de Astrobiología (CSIC/INTA), 28692 ESAC Campus, Villanueva de la Cañada, Madrid, Spain
[7] Instituto de Astronomía, Universidad Nacional Autónoma de México, Apdo. Postal 70-264, 04510 Ciudad de México, Mexico
[8] Institut de Radioastronomie Millimétrique (IRAM), Av. Divina Pastora 7, Núcleo Central 18012, Granada, Spain
[9] Departamento de Física de la Tierra y Astrofísica, Instituto de Física de Partículas y del Cosmos, IPARCOS, Universidad Complutense de Madrid (UCM), 28040 Madrid, Spain
[10] ISDEFE for European Space Astronomy Centre (ESAC)/ESA, PO Box 78, 28690 Villanueva de la Cañada, Madrid, Spain
[11] Astronomical Observatory Institute, Faculty of Physics, Adam Mickiewicz University, ul. Słoneczna 36, 60-286 Poznań, Poland
[12] Space Science and Geospatial Institute (SSGI), Entoto Observatory and Research Center (EORC), Astronomy and Astrophysics Research Division, PO Box 33679, Addis Abbaba, Ethiopia
[13] Instituto de Astrofísica de Andalucía (CSIC), 18080 Granada, Spain
[14] Physics Department, Mbarara University of Science and Technology (MUST), Mbarara, Uganda

Received 29 August 2023 / Accepted 8 January 2024

ABSTRACT

Context. The Lockman–SpReSO project is an optical spectroscopic survey of 956 far-infrared (FIR) objects within the Lockman Hole field limited by magnitude $R_C(AB) < 24.5$. Fe II and Mg II absorption lines have been detected in 21 out of 456 objects with a determined spectroscopic redshift in the catalogue. The redshifts of these objects are in the range $0.5 \lesssim z \lesssim 1.44$.
Aims. The aim of this study is to investigate material ejection from star-forming regions and material infall into galaxies by analysing the Fe II and Mg II absorption lines. Additionally, we explore whether the correlations found in previous studies between these galactic wind velocities, line equivalent widths (EWs), and galaxy properties such as stellar mass (M_*), star formation rate (SFR), and specific star formation rate (sSFR) are valid for a sample with FIR-selected objects. The objects analysed span an M_* range of $9.89 < \log(M_*/M_\odot) < 11.50$ and an SFR range of $1.01 < \log(\mathrm{SFR}) < 2.70$.
Methods. We performed measurements of the Mg II $\lambda\lambda$2796, 2803, Mg I λ2852, Fe II $\lambda\lambda$2374, 82, Fe II $\lambda\lambda$2586, 2600, and Fe II λ2344 spectral lines present in the spectra of the selected sample to determine the EW and velocity of the flows observed in the star-forming galaxies. Subsequently, we conducted 10^7 bootstrap simulations using the Spearman's rank correlation coefficient (ρ_s) to explore correlations with galaxy properties. Furthermore, we calculated the covering factor, gas density, and optical depth for the measured Fe II doublets.
Results. Our analysis reveals strong correlations between the EW of Mg II lines and both M_* ($\rho_s = 0.43$, 4.5σ) and SFR ($\rho_s = 0.42$, 4.4σ). For the Fe II lines, we observed strong correlations between the EW and SFR ($\rho_s \sim 0.65$, $>3.9\sigma$), with a weaker correlation for M_* ($\rho_s \sim 0.35$, $>1.9\sigma$). No notable correlations were found between velocity measurements of the Mg II line and M_*, SFR, or sSFR of the objects ($\rho_s \sim 0.1$). However, a strong negative correlation was found between the velocity of the Fe II lines and the SFR of the galaxies ($\rho_s \sim -0.45$, $\sim 3\sigma$). Our results align with those of previous studies, although only FIR-selected objects are investigated here. Finally, we detect a candidate 'loitering outflow', a recently discovered subtype of the iron low-ionisation broad absorption line (FeLoBAL) quasars, at a redshift of $z = 1.4399$, exhibiting emission in C III] and low line velocities ($|v| \lesssim 200\,\mathrm{km\,s^{-1}}$).

Key words. techniques: spectroscopic – galaxies: evolution – galaxies: starburst – galaxies: statistics

1. Introduction

To understand how galaxies evolve, we need to study the processes that galaxies undergo over time. Galactic winds are one of the mechanisms that play a fundamental role in their evolution. When giant stars explode as supernovae, they eject material enriched in heavy elements into the galactic halo, enriching the intergalactic medium through a mechanism known

as galactic winds (Veilleux et al. 2005). Subsequently, this ejected material can be reaccreted by the gravitational potential of the host galaxy, leading to a 'reinjection', or inflow, of enriched material to refuel the galaxy and trigger the birth of the new generation of stars. The study of this material cycle is a major challenge in cosmology (Péroux & Howk 2020). Investigation of the frequency with which this cycle occurs, its characteristics, and its dependence on host galaxy properties, such as stellar mass (M_*) or star formation rate (SFR), will help us to better understand the dynamical and chemical evolution of the galaxies, the circumgalactic medium, and the intergalactic medium (Tumlinson et al. 2017; Veilleux et al. 2020).

Studies of galactic outflows have shown that this phenomenon is a common feature of star-forming galaxies (SFGs) across cosmic time. In the local Universe, Chen et al. (2010) showed the ubiquity of outflows in galaxies with a high SFR. Martin et al. (2012) found winds in about half of their sample of approximately 200 objects with redshifts between 0.4 and 1.4. These authors found no relationship between the rate of detection of outflows and the physical properties of galaxies, but reported a strong relationship with the viewing angle, strengthening the idea of the presence of biconical outflows in SFGs.

The kinematics of galactic winds allow them to be studied in the spectrum of their host galaxy. The spectral lines produced by the flow itself are blueshifted (redshifted) in cases where the material is ejected (captured) by the galaxy. Studies were therefore carried out on individual objects to look for properties of the flows and their possible dispersion (Martin et al. 2012; Erb et al. 2012; Rubin et al. 2014; Chisholm et al. 2015; Finley et al. 2017a,b; Prusinski et al. 2021; Xu et al. 2022; Davis et al. 2023, among others), and on coadded spectra of similar objects to look for general properties of galactic flows (Weiner et al. 2009; Rubin et al. 2010; Erb et al. 2012; Zhu et al. 2015; Prusinski et al. 2021, among others). This latter approach is useful for distant objects where the signal-to-noise ratio is poor, as it enables the acquisition of generalised information from the whole sample, although unique properties of each individual object may be forfeited.

Many studies have focused on the analysis of low-ionisation resonant absorption spectral lines. Optical features such as Ca II $\lambda\lambda$3933, 69 or Na I $\lambda\lambda$5890, 96 (Martin 2005; Chen et al. 2010) are useful because of their presence in low-redshift SFGs. There are other interesting low-ionisation absorption lines in the UV range that are becoming available to ground observations for objects at redshifts $z \gtrsim 0.3$. The Mg II $\lambda\lambda$2796, 2803 doublet is one of the most widely used (Weiner et al. 2009; Erb et al. 2012; Rubin et al. 2014; Zhu et al. 2015; Finley et al. 2017a; Prusinski et al. 2021) because it is the most common ionised state of magnesium under a wide range of environmental conditions and also has a large oscillator strength. At bluer wavelengths, the Fe II lines (Fe II λ2344, Fe II $\lambda\lambda$2586, 2600, Fe II $\lambda\lambda$2374, 82) are found to confer an advantage in that they are less sensitive to emission filling (Erb et al. 2012; Martin et al. 2012; Rubin et al. 2014; Zhu et al. 2015; Finley et al. 2017a; Prusinski et al. 2021). For the study of more distant objects, far-UV transitions such as Si II, Al II, C II, C IV, and Lyα, are commonly used to the study of outflows (Shapley et al. 2003; Steidel et al. 2010; Jones et al. 2012; Leclercq et al. 2020, among others).

One of the properties of the outflows derived from the analysis of the spectral lines is the velocity difference between the outflow and the host galaxy. Some studies have found that the velocity of the outflows tends to increase with M_* and the SFR of the host galaxy (Martin 2005; Rupke et al. 2005a; Weiner et al. 2009; Chisholm et al. 2015), implying that galaxies with higher SFRs have more energy to eject material via supernovae and also contain a greater amount of material. However, this correlation has not been found in other studies, where the outflow velocity is found to be independent of M_* or the SFR of the host galaxy (Rupke et al. 2005b; Chen et al. 2010; Martin et al. 2012; Rubin et al. 2014; Prusinski et al. 2021). These correlations show a significant intrinsic scatter ($\sigma \sim 0.2$ dex, Chisholm et al. 2015; Heckman et al. 2015), meaning that large samples of objects must be studied with a wide range of analysed parameters. Davis et al. (2023) discovered a scatter that is half of that obtained by these latter, previous studies, resulting in a large sample that spans almost three orders of magnitude in M_* and SFR. In their study of a sample with a wide range of M_* ($\log M_* \sim 6-10\,M_\odot$) and SFR ($\log \mathrm{SFR} \sim 0.01-100\,M_\odot\,\mathrm{yr}^{-1}$), Xu et al. (2022) found a correlation of high significance between outflow velocity and both SFR and M_*.

Most studies that investigate the correlations between galaxy properties and outflow properties tend to focus on normal SFGs. Furthermore, for distant objects ($z > 0.5$), SFGs are selected based on the UV emission observed in the optical range, which introduces a bias towards a specific type of object. Therefore, it is crucial to conduct studies on objects selected using different criteria. In the paper of Banerji et al. (2011), the authors analyse a sample of 19 submillimetre galaxies and 21 submillimetre faint radio galaxies with an average redshift of $z \sim 1.3$. A correlation was found between the velocity of the outflows and SFR, which is consistent with the results seen for lower redshift Ultra-Luminous Infrared Galaxies (ULIRGs).

In the present paper, we describe how we identified and analysed the galactic flows of objects within the framework of the Lockman–SpReSO project Gonzalez-Otero et al. (2023). We used a sample of IR-selected SFGs with Fe II and Mg II absorption lines in their spectra. We fitted these lines to determine the EW and the velocity of the flow relative to that of the system. We explore the correlation between these line properties and the physical parameters of the host galaxies using the flow data from Lockman–SpReSO, Rubin et al. (2014, hereafter RU14) and Prusinski et al. (2021, hereafter PR21) together. In addition to creating a statistically significant set of objects (~200), we include SFGs chosen for their far-infrared (FIR) brightness, which complements the sample. This is important, as studies of flow in IR-selected distant objects are limited, and such studies are usually carried out on a composite spectrum that lacks the individual properties of the objects. We also determine the covering factor, optical depth, and ion densities for the Fe II doublets.

This is the second paper in the Lockman–SpReSO project series and is structured as follows. In Sect. 2, we describe the sample, the selection criteria, and the comparison samples. In Sect. 3, we describe the flow properties and Sect. 3 shows the line-fitting process. In Sect. 4, we describe the analysis of the correlations between flow and galaxy properties. In Sects. 4.1 and 4.2, we describe our analysis of the EWs and velocities of the flows, respectively, and in Sect. 4.3, we describe our study of the local covering factor, optical depths, and ion densities. Our results and conclusions are summarised in Sect. 5. Magnitudes in the AB system (Oke & Gunn 1983) are used throughout the paper. The cosmological parameters adopted in this work are: $\Omega_\mathrm{M} = 0.3$, $\Omega_\Lambda = 0.7$, and $H_0 = 70\,\mathrm{km\,s^{-1}\,Mpc^{-1}}$. Both the SFR and M_* assume a Chabrier (2003) initial mass function (IMF).

2. Sample selection and description

2.1. Lockman–SpReSO data

The galaxies studied in this paper have been selected from the Lockman–SpReSO project object catalogue. Detailed description of the observations, reduction and catalogue compilation can be found in the presentation paper Gonzalez-Otero et al. (2023). In summary, the Lockman–SpReSO project focuses on a spectroscopic follow-up of 956 objects selected from FIR observations of the Lockman Hole field with the *Herschel* Space Observatory, plus a sample of 188 interesting objects in the field, with a sample limiting magnitude in the Cousins R band of $R_C < 24.5$. The spectroscopic observations were made with the WHT/A2F-WYFFOS[1](Domínquez Palmero et al. 2014) and WYIN/HYDRA[2] instruments for the bright subset of the catalogue ($R_C < 20.6$ mag) and with the GTC/OSIRIS[3] instrument (Cepa et al. 2000) for the faint subset ($R_C > 20$ mag). The objects studied here belong to the faint subset, where the resolving power used ($R \equiv \lambda/\delta\lambda$, $\delta\lambda$ being the spectral resolution at wavelength λ) was $R = 500$ ($\sim$4 Å pix^{-1}) for the blue grism with a FWHM resolution at the central wavelength of 560 km s^{-1}, covering the electromagnetic spectra from 3600 Å to 7200 Å. Two different red grisms were used with $R = 500$ and $R = 1000$ ($\sim$3 Å pix^{-1}) and a FWHM resolution at the central wavelength of 511 km s^{-1} and 267 km s^{-1}, respectively, covering from $\sim$5000 Å to 10 000 Å. The spectral analysis made it possible to determine the spectroscopic redshift for 456 objects.

The objects for this work were selected by visual inspection among those with a spectroscopic redshift obtained in the framework of the Lockman–SpReSO project, and which also had the Mg II $\lambda\lambda$2796, 2803 doublet in emission or absorption along with some of the Fe II lines in the near-UV range. The observations cover a wavelength that establishes the minimum redshift of the objects we could study. Objects having these properties can only be studied at redshifts greater than 0.4.. A total of 21 objects were selected in which both the Mg II $\lambda\lambda$2796, 2803 doublet and the Fe II lines were found. In all of them, the absorption Fe II $\lambda\lambda$2586, 2600 doublet was detected; in 19 of them, the Mg II $\lambda\lambda$2796, 2803 doublet was found in absorption, and in the remaining two, one (ID 206641), showed a total emission component and the other (ID 120237) both emission and absorption components. Other UV absorption lines were also measured in this study; the Mg I λ2852 was detected in 15 objects, the Fe II $\lambda\lambda$2374, 82 doublet was detected in 11 objects, and the Fe II λ2344 line was detected in seven of them.

The sample spans the spectroscopic redshift range between 0.5 and 1.44 (see Table 1). For the determination and study of the galactic flows, it is important to have a good determination of the velocity of the object or, in essence, a good determination of the redshift. All the selected objects show strong emission in the [O II] $\lambda\lambda$3726, 29 doublet. This emission is normally produced in the photoionised gas near the star-forming regions, so this is a good determinant of the velocity of the system. Other emission lines, such as the most intense Balmer lines (Hα, Hβ and Hγ), available for the lower redshift objects, or the [O III] $\lambda\lambda$4959, 5007, were also used to determine the systemic velocity (or redshift).

Using the selection criteria described above, the selected sample could be contaminated by AGNs, because this type of object can also show emission or absorption in both Mg II and Fe II lines. We used the classification performed by Gonzalez-Otero et al. (in prep.), in which the objects in the Lockman–SpReSO project catalogue were divided into SFGs and AGNs, using different photometric and spectroscopic criteria. For the former, the X-ray-to-optical flux ratio (Szokoly et al. 2004), the X-ray total luminosity (Luo et al. 2017), near-infrared (NIR) and FIR data (Donley et al. 2012; Messias et al. 2012) were used. For the spectroscopic ones, the BPT (Baldwin et al. 1981), the Cid Fernandes et al. (2011) diagrams, and visual inspection were used. With these criteria, objects 120237, 206641, and 206679 were classified as AGNs.

Basic properties of the galaxies were retrieved from the work of Gonzalez-Otero et al. (2023) and compiled here in Table 1. They used their spectroscopic redshift determinations to perform SED fits of the UV to FIR photometric data using the CIGALE software (Code Investigating GALaxy Emission, Burgarella et al. 2005, Boquien et al. 2019), providing more accurate measurements of M_* and the total infrared luminosity (L_{TIR}) of the objects than that provided by conventional photometric redshifts. The CIGALE parameter configuration is shown in the Appendix B of Gonzalez-Otero et al. (2023). The M_* of the objects samples the range $9.89 < \log(M_*/M_\odot) < 11.50$ and the L_{TIR} values are in a range value between $10.84 < \log(L_{TIR}/L_\odot) < 12.53$, with 18 objects compatible with Luminous Infrared Galaxies (LIRGs) and two others compatible with ULIRGs. The individual cutouts of the objects and their SED fittings obtained in the framework of Gonzalez-Otero et al. (2023) are compiled in Appendix A.

The SFR and metallicity of these objects were also obtained from the work of Gonzalez-Otero et al. (in prep.). The SFR of the Lockman–SpReSO project galaxies were studied using the flux of the Balmer lines, L_{TIR}, and the [O II] doublet flux as tracers. In Fig. 1 we have compared the complete Lockman–SpReSO sample with the spectroscopic redshift determined by Gonzalez-Otero et al. (2023) with the sample of objects selected in this paper with absorption in Mg II and Fe II and classified as SFG.

The metallicity was analysed following several criteria, although because of the redshift range of the objects studied in this paper only four of them have a metallicity measurement available. Studies such as Pettini & Pagel (2004) and Pilyugin & Grebel (2016), which use spectral lines over the whole optical range, can be applied to only one of the objects in the sample (ID 123207). Studies based on the R23 method, such as Tremonti et al. (2004) and Kobulnicky & Kewley (2004), which use the blue lines in the optical spectrum, can be applied to four of the objects studied. The SFRs collected in Table 1 were obtained using L_{TIR}, the calibration of Kennicutt & Evans (2012) and the IMF of Chabrier (2003). The metallicities given in Table 1 were obtained using the calibration of Tremonti et al. (2004) and the errors are estimated using Monte Carlo simulations.

In Fig. 2 we show the basic properties (M_*, redshift, SFR, and sSFR) of the objects from Lockman–SpReSO (blue data), together with data from papers that have also carried outflow studies in SFG (see Sect. 2.2 for a detailed description).

2.2. The comparison samples

In order to have a frame of reference with which to compare, we have included in our work samples from other papers that have studied the galaxy winds produced in SFG.

The numerous sample of 105 galaxies from RU14 was used. They selected objects from existing spectroscopic catalogues for

[1] https://www.ing.iac.es/Astronomy/instruments/af2
[2] https://www.wiyn.org/Instruments/wiynhydra.html
[3] http://www.gtc.iac.es/instruments/osiris/osiris.php

Table 1. Basic information on the objects selected from the Lockman–SpReSO catalogue, ordered by increasing redshift.

ID	RA	Dec	z_{spec}	R_C	A_V	$\log(M_*)$	$\log(L_{TIR})$	$\log(SFR)$	$12+\log(O/H)$
	(deg)	(deg)		(mag)	(mag)	($M_\odot$)	($L_\odot$)	($M_\odot\,yr^{-1}$)	
(1)	(2)	(3)	(4)	(5)	(6)	(7)	(8)	(9)	(10)
123207	163.15606	57.58581	0.4914	20.39	1.8	10.38 ± 0.12	10.98 ± 0.06	1.15 ± 0.06	$8.77^{+0.06}_{-0.07}$
96864	163.51695	57.43780	0.5870	20.83	1.9	10.11 ± 0.10	11.15 ± 0.02	1.32 ± 0.02	$8.94^{+0.06}_{-0.08}$
101926	163.18977	57.46801	0.6049	21.20	1.2	9.89 ± 0.07	10.84 ± 0.03	1.01 ± 0.03	–
120080	163.08320	57.56991	0.6108	21.22	2.7	10.29 ± 0.08	11.30 ± 0.05	1.47 ± 0.05	$9.03^{+0.04}_{-0.05}$
118338	163.51918	57.55793	0.6153	21.01	2.7	10.78 ± 0.07	11.35 ± 0.05	1.52 ± 0.05	–
95738	162.89970	57.43148	0.6165	21.15	2.1	10.25 ± 0.14	11.15 ± 0.05	1.32 ± 0.05	$8.85^{+0.07}_{-0.10}$
109219	163.54524	57.50826	0.6443	21.09	2.8	10.79 ± 0.06	11.40 ± 0.03	1.58 ± 0.03	–
94458	162.78952	57.42330	0.6708	21.29	3.6	10.77 ± 0.08	11.73 ± 0.02	1.91 ± 0.02	–
92467	162.96713	57.41357	0.6908	20.90	2.7	10.57 ± 0.06	11.59 ± 0.06	1.76 ± 0.06	–
120257	163.33868	57.56994	0.7204	21.41	2.0	10.12 ± 0.12	11.26 ± 0.06	1.44 ± 0.06	–
95958	163.43787	57.43224	0.7800	21.56	2.1	10.51 ± 0.12	11.42 ± 0.06	1.59 ± 0.06	–
116662	162.97753	57.54978	0.8053	22.29	1.9	9.95 ± 0.18	10.99 ± 0.08	1.17 ± 0.08	–
133957	162.94574	57.64587	0.8116	21.74	3.0	10.49 ± 0.17	11.56 ± 0.05	1.73 ± 0.05	–
186820	163.25419	57.67225	0.8146	21.86	3.2	10.41 ± 0.04	11.54 ± 0.02	1.71 ± 0.02	–
97778	163.41833	57.44325	0.8194	22.11	3.1	10.64 ± 0.13	11.36 ± 0.09	1.53 ± 0.09	–
77155	162.95000	57.32068	0.8683	21.33	2.5	10.43 ± 0.17	11.85 ± 0.04	2.03 ± 0.04	–
102473	163.50675	57.47030	0.8881	22.42	2.9	10.25 ± 0.10	11.56 ± 0.06	1.73 ± 0.06	–
120237 [(a)]	163.44230	57.56971	1.0810	21.05	1.2	10.19 ± 0.13	11.75 ± 0.04	1.92 ± 0.04	–
206641 [(a)]	163.31984	57.59742	1.2023	18.96	1.2	11.50 ± 0.04	11.81 ± 0.03	–	–
78911	162.92261	57.33095	1.2124	22.13	4.1	10.81 ± 0.06	12.53 ± 0.04	2.70 ± 0.04	–
206679 [(a)]	163.12537	57.65379	1.4399	20.54	2.9	11.29 ± 0.04	12.52 ± 0.03	–	–

Notes. Column (1) is the unique identification number for each object in the Lockman–SpReSO main catalogue (Gonzalez-Otero et al. 2023). Columns (2) and (3) give the optical coordinates (J2000) of the object. Column (4) is the spectroscopic redshift of the objects determined by Gonzalez-Otero et al. (2023). Column (5) is the AB magnitude in the R_C band. Column (6) is the extinction obtained from the SED fits using the CIGALE and the Calzetti et al. (2000) extinction law. Column (7) is the stellar mass obtained from the SED fits using CIGALE. Column (8) is the total IR luminosity derived from the SED fits using CIGALE. Column (9) is the SFR derived using the IR calibration from Kennicutt & Evans (2012) and the IMF from Chabrier (2003). Column (10) is the gas phase metallicity derived using the calibration from Tremonti et al. (2004). [(a)]Objects classified as AGN by González-Otero et al. (in prep).

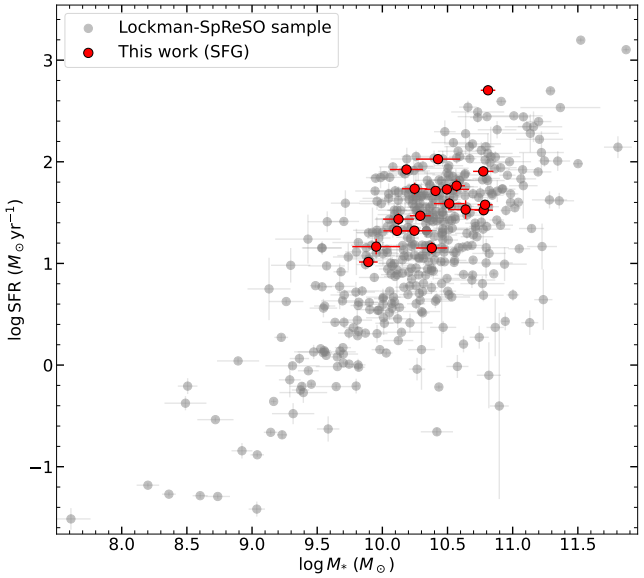

Fig. 1. SFR versus M_* of the SFGs selected for this study (red) compared to the Lockman–SpReSO sample (grey). The galaxies exhibiting Mg II and Fe II absorption lines populate the region with the highest density of objects in the parent sample.

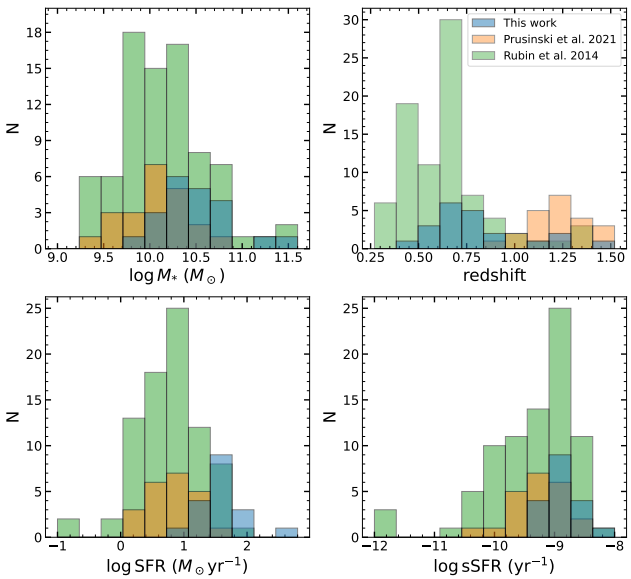

Fig. 2. Main properties of the studied objects. The blue bars represent the objects from Lockman–SpReSO survey, the orange bars represent the objects from PR21 and the green bars are the objects from RU14. The top left panel shows the M_* of the objects, the top right shows the spectroscopic redshift, the bottom left shows the SFR and, the bottom right shows the sSFR.

which HST deep observations are available in order to study the morphology, orientation, and spatial distribution of the star formation. They selected objects with redshifts $z > 0.3$ to ensure Mg II coverage and with B-band magnitude <23. The M_* and the SFR were obtained from a SED fitting procedure in the wavelength range between 2400 Å and 24 µm assuming the IMF of Chabrier (2003). The EW of the lines were derived using the feature-finding algorithm outlined in Cooksey et al. (2008). To normalise the line doublets for the study, the authors used continuum windows located in proximity to the lines region. To determine the flow

velocity, two models were used to fit the lines: one with a single component per line and another with two components per line to separate the systemic component at zero velocity from the flow component. The profile of the lines was fitted using a Voigt shape. Additionally, the maximum flow velocity was also determined. To compare with the data obtained from the Lockman–SpReSO objects, we used the results from their one-component fit for consistency (see Sect. 3). The distributions of the main properties of the sample are shown in Fig. 2 in green.

In addition, we also used the data from PR21, a sample of 22 galaxies from the Skelton et al. (2014) data of the CANDELS and COSMOS surveys. These were selected based on their SFR ($>1\,M_\odot\,\mathrm{yr}^{-1}$), with photometric redshift range $0.7 \lesssim z_{\rm phot} \lesssim 1.5$ at 99% confidence and magnitude $R_C \leq 24$. The SFR was computed from the *Hubble* Space Telescope (HST) Hα emission-line maps using the Kennicutt (1998) recipe and the M_* was retrieved from the 3D-HST catalogue (Skelton et al. 2014). This SFR has been multiplied by the correction factor (0.68) given in Kennicutt & Evans (2012) to make the used IMF consistent. To study the outflows, they examined the bluest line of the Mg II $\lambda\lambda$2796, 2803 doublet, along with the Fe II absorption lines present in the spectra of the sample. The outflow velocity was estimated from the centroids of the lines, and the EW was measured by directly integrating the lines. Weighted averages of the velocity and EW for the Fe II lines of each object were obtained due to their saturation. The distributions of the main properties of the sample are shown in Fig. 2 in orange.

The M_* distribution is similar for three samples, unlike the SFR distribution where a larger difference is found, as can be seen in Fig. 2. The Lockman–SpReSO sample populates the highest SFR region, which is understandable given the selection criterion for objects with FIR emission. The range of SFRs between the samples presented allows us to cover a much wider range of parameters. In Fig. 3 we can see the relationship between SFR and M_* for the objects in the three data sets. The dashed line represents the Murray et al. (2011) limit for the production of winds in galaxies, adapted from the Eq. (3) of RU14. It can be seen that the full sample agrees well with the theoretical limit, filling the upper right region in the diagram. The solid lines represents the main sequence developed by Popesso et al. (2023) for the minimum, average, and maximum redshifts of the sample ($z \sim 0.3,\ 0.8,\ 1.5$, respectively) and the shaded area represents a scatter of 0.09 dex. Almost 85% of the sample is located over the MS, that is the region of starburst galaxies.

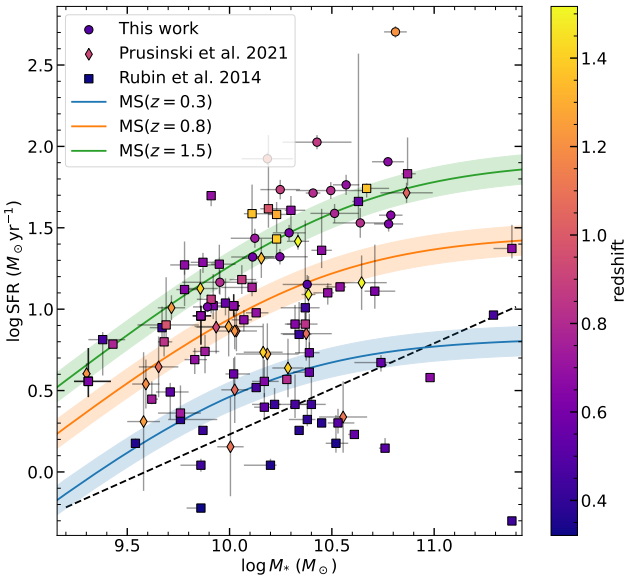

Fig. 3. Diagram of M_* versus SFR of the sample studied, colour coded according to the spectroscopic redshift. The data from Lockman–SpReSO are represented by circles, PR21 data are represented by diamonds, and RU14 data are represented by squares. The dotted line represents the Murray et al. (2011) limit for producing winds in galaxies. The blue, red, and green solid lines and shaded areas are the Popesso et al. (2023) fit for the main sequence and its scatter of 0.09 dex calculated at the minimum, median, and maximum redshift of the sample, respectively.

3. Inflow and outflow study

To determine whether our objects have inflows or outflows we need to know the velocity difference, if any, between the selected absorption lines and the velocity of the system. To do this, the redshift of the object and the centre of the lines are required. The redshift was retrieved from Gonzalez-Otero et al. (2023) (see the paper for details) and is given in Table 1. The properties of the Mg II and Fe II lines were derived for this paper by fitting the spectral lines (see the Sect. 3 for details).

As we have already seen, the Fe II and Mg II lines are useful for studying the galactic flows. Some studies have described the UV lines and their main properties in detail (Erb et al. 2012; Martin et al. 2012; Zhu et al. 2015, and references therein). As with UV lines, their analysis with ground-based telescopes is limited to objects with redshifts $\gtrsim 0.4$ owing to the attenuation of the UV component by the atmosphere; otherwise, it is necessarily to observe with space telescopes. Another major problem with these lines is the resonant emission that occurs in some of them, which fills in the absorption and makes it difficult to accurately measure the line. In Fig. 5 of Zhu et al. (2015) and their Appendix A are gathered the energy-level diagrams of the Fe II, Mg II, and Mg I atoms for the transitions that we studied for this paper. Lines that do not produce fluorescent emission (those that can only be de-excited to the ground state) are more affected by emission filling. When this happens, the line profile may be modified.

Absorption is produced by the gas between the observer and the galaxy while emission can come from other parts of the galaxy, leading to a difference between the centres of the absorption and emission components. Among the lines used in our study, the one most affected by this effect is the Fe II λ2382 line, since the only way to de-excite it is by resonant emission. In addition, the Fe II λ2344 line produces a fluorescent emission at 2381.49 Å, which also affects the Fe II λ2382 line. Even the Fe II λ2600 line could suffer from emission filling as the fluorescent emission it produces at 2626 Å has a very low probability of occurring. Lines such as Fe II λ2373 and Fe II λ2586 suffer very little from this effect because the fluorescent emission de-excitation channels have high probabilities of occurrence (high *Einstein* A coefficient), so the lines suffer very little from emission filling.

However, when analysing the spectral lines of our sample, we found no emission filling effect. Figure 4 shows examples where both Fe II and Mg II lines are detected with no apparent emission filling effect. This was also seen in analyses of nearby galaxies, where the Na I $\lambda\lambda$ 5890,96 lines showed little emission filling (Heckman et al. 2000; Martin 2005, 2006; Chen et al. 2010). This has been attributed to the presence of regions of high gas density and high neutral sodium concentration where the long path length of the scattered photons leads to a high probability of absorption by dust. The Lockman–SpReSO survey objects are selected for their IR emission, in other words they are dusty, as indicated by a mean extinction of $A_V \sim 2.7$ mag.

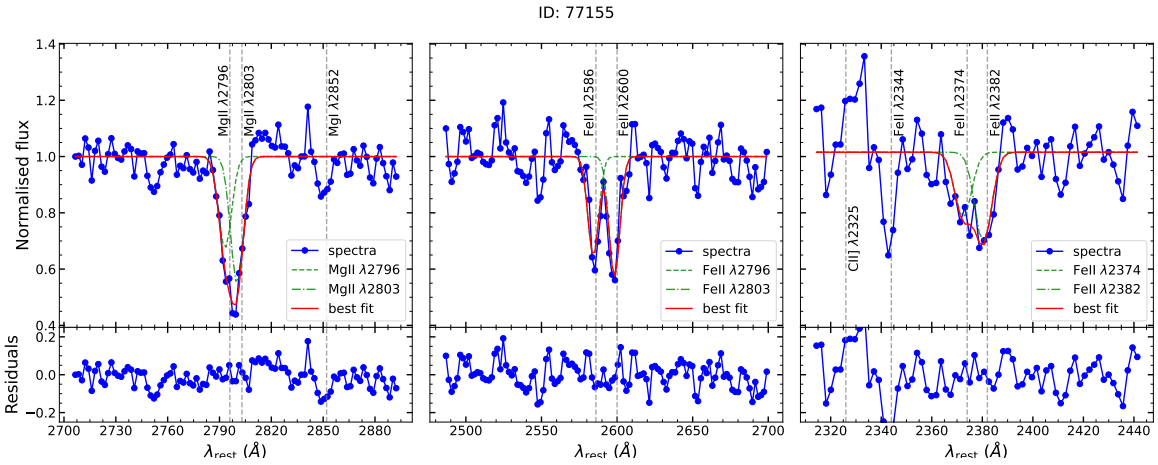

Fig. 4. Example fit for the doublets studied in this study for source 77155. On the left is the Mg II $\lambda\lambda$2796, 2803 fit with the residuals at the bottom. The Mg I λ2852 line is also visible in this slice of the spectrum. In the centre, the fit for Fe II $\lambda\lambda$2586, 2600, also with the residuals of the fit at the bottom. On the right, using the same schedule, the case of Fe II $\lambda\lambda$2374, 82 with a low S/N ratio. You can also see the C II] λ2325 in emission and Fe II λ2344 in absorption.

Furthermore, as we have discussed previously (see Table 1), we see that most of the objects are LIRGs or even ULIRGs, which favours the non-production of emission filling according to the above reasoning. In the work of Prochaska et al. (2011), they find that the Fe II fluorescence lines scale with the amount of emission filling. As they are not detected in the spectra of our sample, this supports the fact that no emission filling effect is found in the spectral lines.

Fitting of absorption lines

The lines were measured using the same procedure as that used by Gonzalez-Otero et al. (2023) where the Python package *LMFIT*[4] (Newville et al. 2014) was used for the measurement of the most intense spectral lines. *LMFIT* allows us to perform a non-linear least-squares minimisation line fitting routine with the desired model. The lines were fitted using a Gaussian model for the absorption component and a linear zero-slope continuum model. As we have seen, in the work of Rubin et al. (2014) and others (Chen et al. 2010; Xu et al. 2022, for example), each line is also fitted with a two component model: one fixed zero velocity component representing the ISM of the galactic region and a variable velocity component representing the galactic flow. However, the resolution of our study does not allow this type of component decomposition. The normalisation of the spectra was performed only in the analysis windows of each line or doublet line. The flat continuum model obtained in the fitting was used to normalise by the continuum.

Mg II $\lambda\lambda$2796, 2803, Fe II $\lambda\lambda$2374, 82, and Fe II $\lambda\lambda$2586, 2600 are doublets of spectral lines whose components are very close in wavelength. This implies that at the dispersion used (~3–4 Å pix^{-1}), depending also on the redshift, these doublets can appear blended. Therefore, in the case of these doublets, we fitted the two lines together with the continuum at the same time, that is two Gaussian components (one for each line) plus a linear model. In order to reduce the computational time, we have used the known relations of the lines as initial parameters of the models, but allowed them to fluctuate. As each doublet line is produced in the same region and under the same conditions in the galaxy, in the absence of emission filling or other phenomena, the width should be the same, that is, the same initial sigma value for the two Gaussian components. The same reasoning applies to the central wavelength of the line, where the length between peaks is known, although it is a free parameter in the fit. None of the fit parameters were fixed, so they were all allowed to vary during the fitting process. Finally, as the redshift is known, the spectra were transferred to rest-frame to measure the lines.

Figure 4 shows an example of the line fit for ID 77155. The different degrees of blending found in this particular source are representative for our sample. Each panel shows the fit of one of the doublets studied in this paper. Upper panels represent the fit performed and lower panels represent the residuals of the fit itself. The fit results of Mg II $\lambda\lambda$2796, 2803, Fe II $\lambda\lambda$2586, 2600 and Fe II $\lambda\lambda$2374, 82 (with the lowest S/N ratio) are shown from left to right.

In addition, from the line-fitting procedure we determined the rest-frame equivalent width (EW) of the lines to be analysed in relation to the physical properties of the galaxies. The values obtained and its errors are collected in Table 2. The error in the EW was calculated by propagating the error obtained for the Gaussian component and the continuum of each line when the EW was calculated (both errors were calculated in the line fitting process). As can be seen, the values of the EW are biased towards higher values, mainly due to the resolution of the Lockman–SpReSO spectra.

Finally, using the centre of the Gaussian components obtained in the fit, we determined the velocity of the lines and hence the velocity difference between the material wind and the system. The errors in velocity have been propagated from the central wavelength error obtained in the fit of each line. In Table 3 we list the velocities obtained and its errors for the lines analysed.

4. Galactic flows properties analysis

4.1. Equivalent width analysis

There are studies in the literature that has led to claims of correlations between EW and certain galaxy properties. RU14 found

[4] https://lmfit.github.io/lmfit-py/index.html

Table 2. Rest-frame EW of the absorption lines measured for the objects from the Lockman–SpReSO catalogue.

ID	Fe II λ2344 (Å)	Fe II λ2374 (Å)	Fe II λ2382 (Å)	Fe II λ2586 (Å)	Fe II λ2600 (Å)	Mg II λ2796 (Å)	Mg II λ2803 (Å)	Mg I λ2852 (Å)
123207	–	–	–	3.9 ± 1.2	3.5 ± 1.1	6.1 ± 1.1	4.5 ± 1.2	0.6 ± 0.8
96864	–	–	–	5.7 ± 1.7	5.2 ± 1.7	6.5 ± 1.8	6.0 ± 1.9	1.9 ± 0.5
101926	–	1.8 ± 1.4	1.8 ± 1.4	9.1 ± 2.2	1.8 ± 1.4	4.4 ± 1.2	4.2 ± 1.3	0.8 ± 0.6
120080	–	–	–	2.6 ± 1.4	3.6 ± 1.4	4.3 ± 1.2	2.9 ± 1.4	0.8 ± 1.3
118338	–	–	–	3.5 ± 1.3	4.3 ± 1.4	6.8 ± 1.6	5.9 ± 1.7	1.2 ± 0.6
95738	–	–	–	4.6 ± 1.2	4.6 ± 1.2	5.1 ± 1.3	6.3 ± 1.1	1.1 ± 0.7
109219	–	–	–	3.5 ± 1.2	1.3 ± 1.2	3.9 ± 1.7	7.3 ± 1.3	–
94458	–	–	–	1.6 ± 1.2	4.6 ± 1.0	3.5 ± 1.4	3.4 ± 1.4	1.4 ± 1.1
92467	–	–	–	2.2 ± 1.8	5.3 ± 1.1	3.2 ± 1.4	2.8 ± 1.4	0.5 ± 1.4
120257	3.0 ± 1.2	1.5 ± 1.9	6.3 ± 1.5	5.7 ± 1.7	5.6 ± 1.2	7.9 ± 1.3	4.4 ± 2.0	1.7 ± 0.7
95958	–	2.3 ± 0.9	2.1 ± 0.9	2.2 ± 1.4	4.2 ± 1.0	5.1 ± 1.6	6.5 ± 1.2	1.7 ± 0.9
116662	–	1.8 ± 1.3	2.2 ± 1.3	2.8 ± 1.3	5.6 ± 1.1	3.6 ± 1.4	5.0 ± 1.4	2.1 ± 1.0
133957	–	–	–	9.3 ± 1.3	5.1 ± 1.4	7.6 ± 1.4	3.3 ± 1.9	–
186820	–	–	–	2.7 ± 1.1	1.7 ± 1.1	3.7 ± 1.3	3.9 ± 1.2	–
97778	–	1.3 ± 1.2	1.6 ± 1.1	2.5 ± 1.4	4.8 ± 1.2	3.5 ± 1.2	4.5 ± 1.1	1.5 ± 1.1
77155	2.6 ± 1.8	3.5 ± 1.6	5.1 ± 1.5	5.3 ± 1.6	7.5 ± 1.4	6.7 ± 1.2	6.8 ± 1.2	2.2 ± 0.6
102473	1.6 ± 1.3	3.5 ± 1.2	3.5 ± 1.2	6.3 ± 1.2	6.3 ± 1.0	5.5 ± 1.3	5.1 ± 1.3	4.3 ± 0.6
120237 [(a)]	4.0 ± 1.0	2.6 ± 1.1	2.3 ± 1.1	3.7 ± 0.9	5.1 ± 0.7	–	–	–
206641 [(a)]	0.3 ± 0.1	0.2 ± 0.2	0.9 ± 0.1	0.4 ± 0.3	1.8 ± 0.2	–	–	–
78911	5.6 ± 1.3	2.1 ± 1.5	5.2 ± 1.3	9.6 ± 1.9	9.0 ± 1.9	9.4 ± 2.0	9.9 ± 1.9	6.5 ± 1.3
206679 [(a)]	5.1 ± 0.4	4.4 ± 1.5	7.1 ± 0.9	5.9 ± 1.0	7.1 ± 1.0	7.4 ± 1.4	7.0 ± 1.5	–

Notes. [(a)]Objects classified as AGN by González-Otero et al. (in prep.).

that the EW of the absorption of Mg II is correlated with M_* with a significance of 3.2σ under a parameter of the Spearman's rank correlation coefficient[5] (ρ_s) of $\rho_s = 0.44$ and with the SFR at a significance of 3.5σ ($\rho_s = 0.48$). For the EW of Fe II they found a correlation with SFR at a significance of 2.4σ ($\rho_s = 0.46$) while for M_* they found no correlation, claiming that this may be because of the small M_* range of their sample. PR21 performed a similar analysis with other data and found a similar correlation between the EW of Mg II λ2796 ($\rho_s = 0.67$ at 3.2σ) and Fe II ($\rho_s = 0.65$ at 2.9σ) with the SFR. However, they found no significant correlation between EW and M_*.

As we have seen, our objects are dusty and the effect of emission filling is not very important. Nevertheless, we focus our analysis on the Mg II λ2796, the blue line of the doublet, which is less affected by this phenomenon. In Fig. 5, from left to right, we have plotted the EW of the Mg II λ2796 line against M_*, SFR, and specific SFR (sSFR) for the objects together from the Lockman–SpReSO, PR21 and RU14 samples. It can be seen that the Lockman–SpReSO galaxies populate regions of the plots that the Rubin and Prusinski objects barely do. The Lockman objects have larger EWs than the other samples, while the properties of the galaxies are comparable (see Fig. 2). The EW of the Lockman objects is biased towards higher values due to the low resolution of the observations, with values close to 10 Å and minimum values around 2 Å. However, this allows us to sample other regions of the parameter space and to study in more detail how the galaxy properties relate to the EW of the lines.

To test whether there is a correlation between the EW and the properties of the galaxies, Spearman tests were performed by grouping the three data sets. To estimate the confidence intervals of the correlation, the bootstrap method was applied 10^7 times. The blue histograms in the inset of each panel of Fig. 5 represent the probability distribution function (PDF) of the Spearman parameter obtained in the bootstrap simulations and the dashed lines mark the mode of the PDF. The expected distribution for the case where there is no correlation between the variables[6] is plotted in orange and the mode of Spearman parameter distribution and the significance are typed. It can be seen that for M_* the data suggest a positive correlation with the EW, a mode of $\rho_s = 0.43$ being obtained at a significance of 4.5σ, indicating that the greater the mass of the object, the greater the capacity to generate material winds. This result differs from that obtained in the framework of PR21, but confirms that found by RU14, mainly owing to the joint study of all the data, which adds more statistics to the entire range of values, both EW and M_*. A positive correlation was also found when examining the SFR with a mode of $\rho_s = 0.42$ at a significance of 4.4σ. As we have already discussed, Lockman data add more statistic significance in the high SFR area of the graph, thus better defining the behaviour in this area. The correlation found is not as strong as the one discovered in the work of PR21 and RU14, but the significance is higher owing to the larger data set. In the case of sSFR, no correlation was found with the EW of Mg II. The distribution obtained from the bootstrap simulations and that expected in the

[5] Spearman's correlation coefficient is a statistical method used to measure the strength and direction of the relationship between two variables. It assesses if there is a consistent monotonic relationship between the ranks of the variables, without assuming a linear association. The correlation coefficient ranges from −1 to 1, with positive values indicating a direct relationship, negative values indicating an inverse relationship, and 0 indicating no monotonic relationship. The test provides a p-value to determine the statistical significance of the observed correlation. It is commonly used when dealing with non-linear or non-normally distributed data.

[6] For large samples ($n \geq 30$), the expected distribution of the Spearman parameter tends to be a normal one $N\left(0, 1/\sqrt{n-1}\right)$.

Table 3. Absorption line velocities measured for the objects from the Lockman–SpReSO catalogue.

ID	Fe II λ2344 (km s^{-1})	Fe II λ2374 (km s^{-1})	Fe II λ2382 (km s^{-1})	Fe II λ2586 (km s^{-1})	Fe II λ2600 (km s^{-1})	Mg II λ2796 (km s^{-1})	Mg II λ2803 (km s^{-1})	Mg I λ2852 (km s^{-1})
123207	–	–	–	-177 ± 144	2 ± 85	-131 ± 293	-226 ± 296	-161 ± 364
96864	–	–	–	-192 ± 110	-122 ± 119	18 ± 85	131 ± 92	-46 ± 33
101926	–	131 ± 100	-18 ± 89	59 ± 170	-148 ± 84	-322 ± 5	-269 ± 68	-210 ± 88
120080	–	–	–	107 ± 53	-43 ± 95	-199 ± 70	-118 ± 109	67 ± 159
118338	–	–	–	61 ± 59	1 ± 165	-24 ± 53	25 ± 61	9 ± 127
95738	–	–	–	-232 ± 93	-147 ± 108	-305 ± 235	-220 ± 219	-210 ± 34
109219	–	–	–	463 ± 207	-134 ± 150	-322 ± 39	-316 ± 723	–
94458	–	–	–	23 ± 169	-382 ± 173	-62 ± 149	-16 ± 155	-217 ± 78
92467	–	–	–	-467 ± 70	-202 ± 76	-114 ± 92	-166 ± 105	-159 ± 496
120257	-222 ± 92	379 ± 511	321 ± 111	-224 ± 249	-31 ± 73	89 ± 63	286 ± 119	151 ± 134
95958	–	-233 ± 148	-54 ± 164	-317 ± 139	-238 ± 83	-279 ± 116	-232 ± 98	78 ± 110
116662	–	-499 ± 215	-303 ± 173	-178 ± 154	-199 ± 118	-322 ± 416	-98 ± 390	331 ± 143
133957	–	–	–	-171 ± 289	-228 ± 99	-90 ± 87	97 ± 213	–
186820	–	–	–	315 ± 227	-23 ± 124	-214 ± 75	-34 ± 88	–
97778	–	-478 ± 252	-295 ± 208	-346 ± 132	-430 ± 213	-214 ± 225	-36 ± 172	-420 ± 247
77155	-131 ± 117	-363 ± 222	-186 ± 147	-99 ± 46	-296 ± 50	-201 ± 98	-214 ± 18	-170 ± 93
102473	63 ± 100	306 ± 117	378 ± 60	-232 ± 12	68 ± 154	-141 ± 63	-78 ± 67	-210 ± 42
120237 [(a)]	-343 ± 133	-130 ± 234	-378 ± 182	-297 ± 95	-312 ± 60	–	–	–
206641 [(a)]	-384 ± 55	-379 ± 147	-327 ± 30	-313 ± 51	-170 ± 52	–	–	–
78911	-256 ± 27	-13 ± 190	258 ± 76	116 ± 17	89 ± 95	12 ± 63	93 ± 59	15 ± 47
206679 [(a)]	-54 ± 33	-75 ± 39	35 ± 23	3 ± 18	-166 ± 23	-44 ± 32	-66 ± 34	–

Notes. [(a)]Objects classified as AGNs by González-Otero et al. (in prep.).

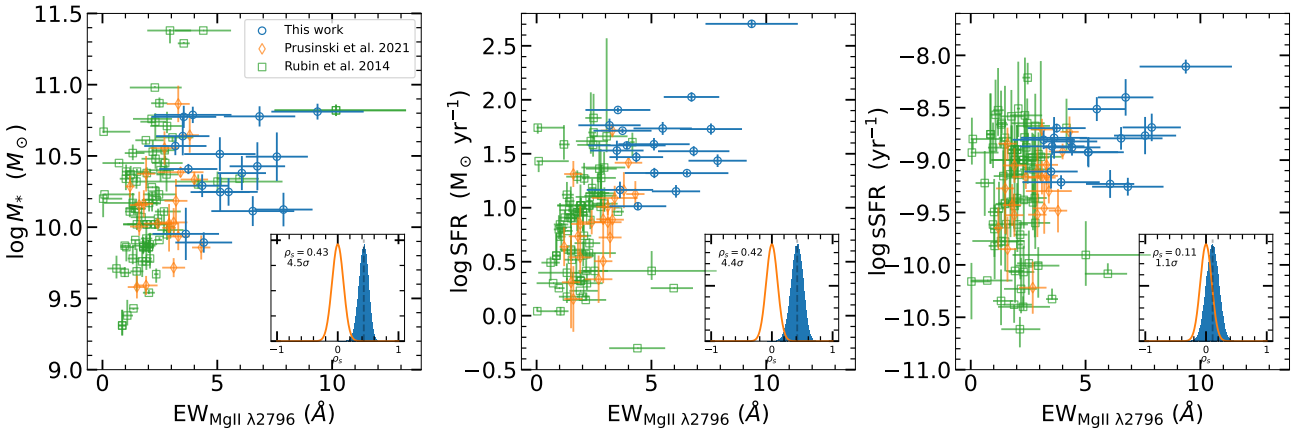

Fig. 5. Plot of the Mg II λ2796 EW versus M_*, SFR, and sSFR (from left to right). The empty blue circles are the results obtained here, the empty orange diamonds are the results of PR21 and the green empty squares are the results of RU14. The inset graph in each panel contains the probability distribution of the Spearman parameter from the bootstrap procedure in blue (see the text for more details) and the expected distribution in the uncorrelated case is shown in orange. The value of the mode of the obtained distribution and the significance in sigmas for the obtained correlation are also included. See the Sect. 4.1 for a discussion of correlation.

case of non-correlation are very close with a mode of $\rho_s = 0.11$ at a significance of 1.1σ.

In Fig. 6 we plot the EW of Fe II λ2586 with respect to the properties of the galaxies in our study, together with the RU14 data, using the same procedure and symbols as in Fig. 5. It is observed that the EW correlates with M_* in a similar way to that found for Mg II, with $\rho_s = 0.43$ at 3.3σ of significance. This result differs from that of RU14, who found no correlation between the parameters ($\rho_s = 0.07$ at 0.4σ). The significant difference in the EW between the data from RU14 and Lockman–SpReSO, mainly due to the different nature of the objects according to the selection criteria, coupled with the increase in the statistics, means that we can further populate the diagram and recover the correlation found between the EW of Mg II and M_*. The correlation between the SFR and the EW of Fe II is the strongest found in this study, with a positive correlation where a mode of $\rho_s = 0.69$ was found in the bootstrap simulations at 5.3σ of significance. Once more, galaxies with higher SFRs can produce stronger winds. For the sSFR, there is still no significant correlation with the EW ($\rho_s = 0.33$ at 2.5σ).

PR21 carried out the study of the Fe II lines using an EW-weighted average because they found the Fe II lines to be saturated in their spectra. In order to compare our data with their results, we calculated an EW-weighted average of the Fe II lines present in our objects and we show the results found in Fig. 7. The correlation with M_* is very weak ($\rho_s = 0.31$) with a significance of 1.9σ. In

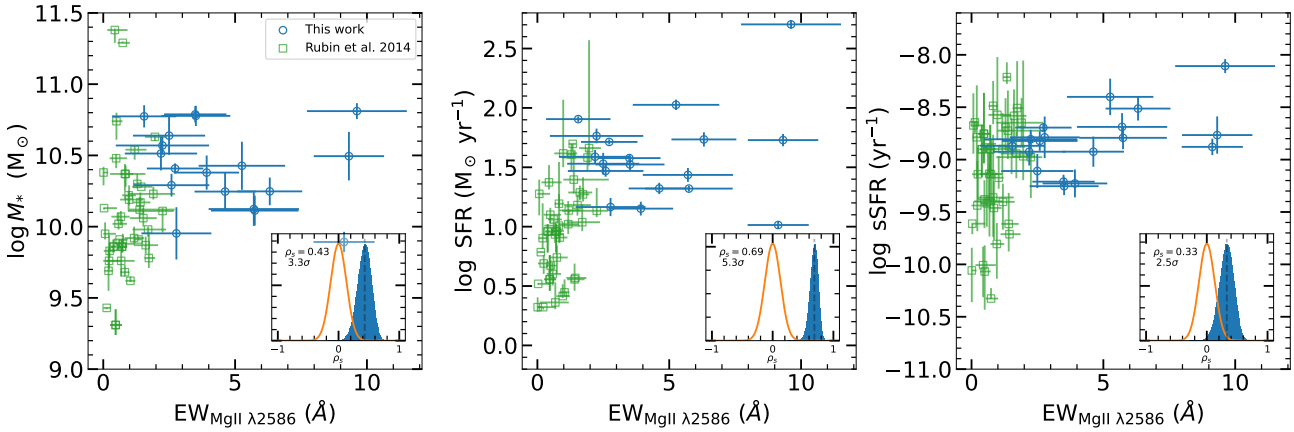

Fig. 6. Plot of the Fe II λ2586 EW versus M_*, SFR, and sSFR (from left to right). The empty blue circles are the results of this paper and the empty green squares are the results of RU14. The inset plots represent the same idea as in Fig. 5. See the Sect. 4.1 for a discussion of correlation.

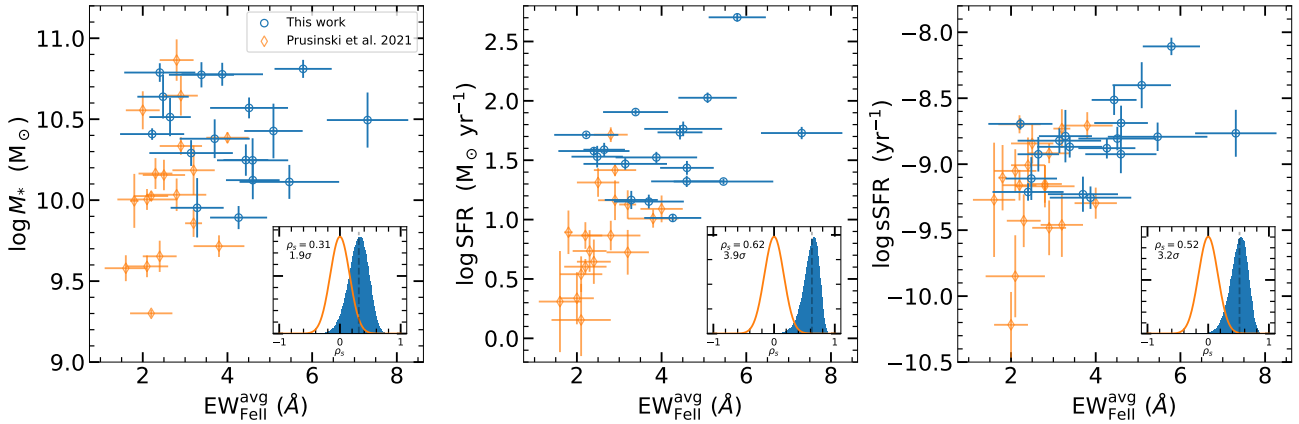

Fig. 7. Weighted EW average of the Fe II lines versus M_*, SFR, and sSFR (from left to right). The empty blue circles are the results of this paper and the empty orange diamonds are the results of PR21. The inset plots represent the same idea as in Fig. 5. See the Sect. 4.1 for a discussion of correlation.

this comparison, the bootstrap distribution and the expected distribution are wider than in the previous cases, mainly because of the smaller data set used. For the SFR we find a significant correlation ($\rho_s = 0.62$) at 3.9σ. This result is consistent with the results of PR21 and with the previous comparison with what RU14 found. This correlation supports the hypothesis that Fe II lines are more intense at higher SFRs of galaxies. The sSFR also shows a slight correlation ($\rho_s = 0.52$) at 3.2σ with the average EW, which we did not find in the previous comparisons. This relation may be due to the smaller statistics we have for log (sSFR) < -9.5, with only two sources in this region.

4.2. Velocity analysis

As we show above, the spectral resolution of the Lockman–SpReSO spectra is not the commonly used resolution for the analysis of outflows. It can lead to large errors in the measurement of properties derived from spectral lines, such as the velocity of the ejected material, as can be seen from Table 3. Despite this severe limitation our sample increases the number of objects that can be studied in this still investigated topic. The initial results provide a fundamental basis for future research with higher resolution, which will help to reduce the margin of error and provide more accurate knowledge about the physical conditions of our sample. Using the velocities obtained we have estimated which objects are receiving an inflow of material, which are ejecting material from the galaxy star-forming regions, and which have velocities compatible with zero (no wind).

Following the criteria used for the EW analysis, we studied the Fe II λ2586 and Mg II λ2796 lines to distinguish between galaxies with outflows, inflows, and gas at the systemic velocity. Analysing the Fe II λ2586 line, of the 18 objects retrieved from Lockman–SpReSO, nine show material outflows, five show material inflows, and four show velocities compatible with zero, namely absorption only. In the analysis of the Mg II λ2796 line, ten objects show outflows, one shows an inflow, and seven have velocities compatible with zero. Considering the three objects classified as AGN, two (120237 and 206641) show an outflows in the Fe II λ2586 line and object 206679 has velocities compatible with zero. The Mg II λ2796 line is available only in pure absorption for the object 206679, and has an outflow-compatible velocity. The discrepancy between the Fe II and Mg II results can be attributed to the high degree of blending of the Mg II doublet lines with respect to the Fe II doublet lines, mainly because of the small wavelength separation between the centres of the Mg II lines (~7 Å) and the resolution at which they are observed in Lockman–SpReSO. Furthermore, object 206679, at redshift ~1.44, could be a Fe II low-ionisation broad absorption-line quasar (FeLoBALQ) candidate that shows an AGN-type nature by the presence of C III] emission, also noticed by

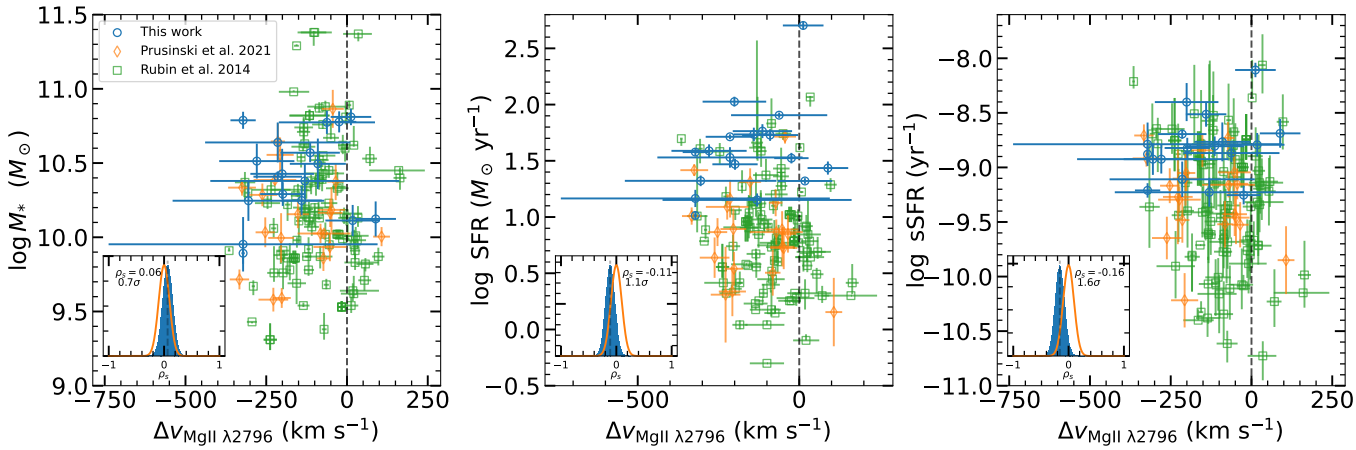

Fig. 8. Mg II λ2796 velocity versus M_*, SFR, and sSFR (from left to right). The symbols and colour coding are the same as for Fig. 5. See Sect. 4.2 for a discussion of correlation analysis.

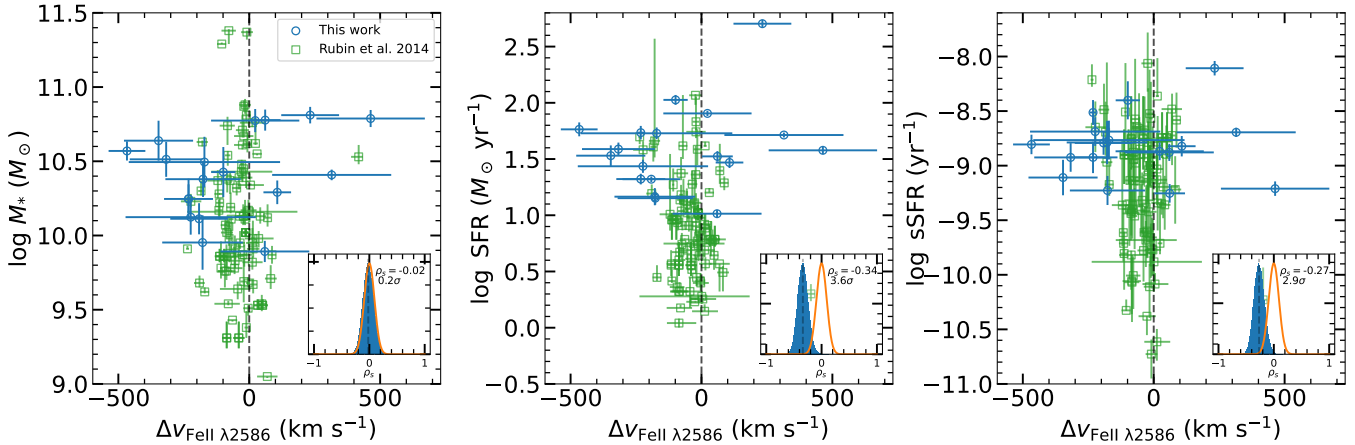

Fig. 9. Fe II λ2586 velocity versus M_*, SFR, and sSFR (from left to right). The symbols and colours are as in Fig. 5. See Sect. 4.2 for a discussion of correlation.

Schmidt et al. (1998), and might be an example of a loitering outflow representing a new class of FeLoBALQs described by Choi et al. (2022). The peculiarity of these FeLoBALQs is that they have low flow velocities and high column density winds located at $\log(R_{\rm d}) \lesssim 1$ pc where $R_{\rm d}$ is the distance to the centre.

In Fig. 8 we plot the Mg II λ2796 velocities using the data from Lockman–SpReSO, PR21, and RU14 against the physical parameters of the galaxies, where the possible existence of a correlation is analysed in the same way as the EW (see Sect. 4.1). To investigate the correlation between outflow velocity and galaxy properties, we restrict the sample to objects that satisfy $\delta v < 50\,{\rm km\,s^{-1}}$, excluding inflows from the study while accounting for measurement errors. The result is that the Mg II λ2796 velocity is not correlated with M_*, SFR, or sSFR as the distributions obtained from the bootstrap simulations are similar to those expected in the uncorrelated case. The same analysis is carried out for the Fe II λ2586 line using the RU14 and Lockman data and is shown in Fig. 9. Examining the distributions of the bootstrap simulations, we find that there is no significant correlation between the Fe II λ2586 velocity and the M_*. However, there is a negative correlation between velocity and SFR with $\rho = -0.34$ at 3.6σ of significance. The study on sSFR shows a weaker negative correlation ($\rho = -0.27$) at 2.9σ.

If we examine the mean velocity of all Fe II lines weighted by the error, we can use the PR21 and Lockman–SpReSO data in conjunction. As can be seen in Fig. 10, there is a strong correlation of the velocity with the M_* ($\rho = -0.43$) and SFR ($\rho = -0.57$) . The significance identified is lower due to the limited statistics available in this case and the narrow range of values that can be studied for the parameters. These results differ from that obtained in the framework of PR21, where no correlations were found with a significance greater than 1.4σ. They argue that the lack of correlation is due to the short range of SFR in their objects, which, when combined with the intrinsic scatter of the relationship between SFR and velocity, makes it difficult to find a correlation. Additionally, the study may be affected by a systemic component of the ISM that scales with the SFR, as expected from the Schmidt-Kennicut law (Kennicutt & Evans 2012). This component may have a greater impact on studies that use a single component fit of the spectral lines.

In contrast of our results, Rupke et al. (2005b) studying 78 starburst-dominated LIRGs and analysing the Na I absorption, found that the outflow velocity and properties of these galaxies are independent. However, Martin (2005), analysing 18 ULIRGs, found that the Na I velocity follows a relation $\Delta v \sim {\rm SFR}^{0.35}$. Weiner et al. (2009), studying a coadded spectra of 1406 galaxies at $z \sim 2$ from the DEEP2 redshift survey, also found that Mg II absorption in outflows is stronger and reaches higher velocities for more massive galaxies; they obtained a similar relationship for the velocity $\Delta v \sim {\rm SFR}^{0.3}$.

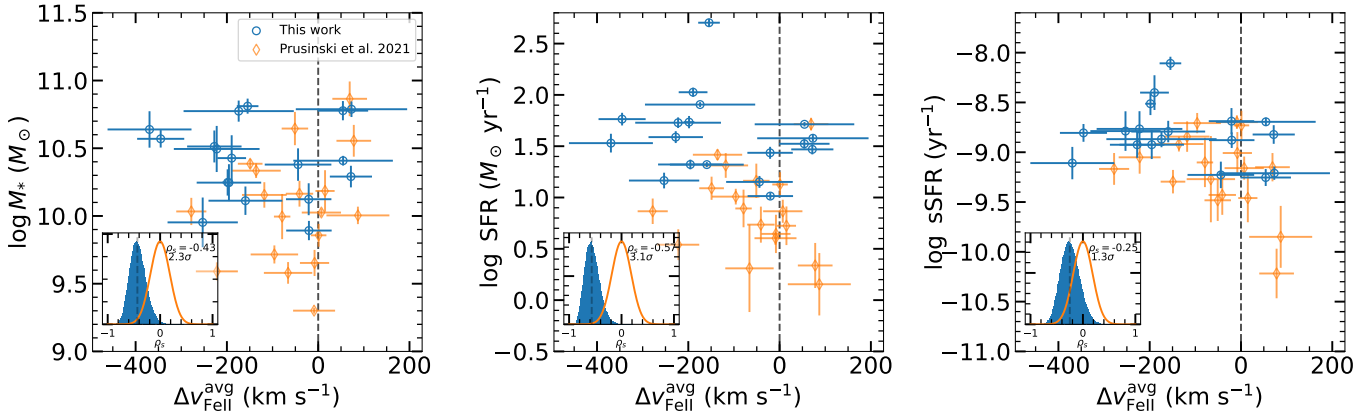

Fig. 10. Average Fe II velocity versus M_*, SFR, and sSFR (from left to right). The symbols and colours are as in Fig. 5. See the Sect. 4.2 for a discussion of correlation.

Heckman et al. (2015), studying the UV absorption lines of 39 low-redshift starburst galaxies, found that there is a strong correlation of the velocity they measured with the SFR and SFR surface density ($\Sigma_{\rm SFR}$), but a weak correlation with M_*. This result is supported by Chisholm et al. (2015), who analysed the Si II absorption lines in 48 nearby SFGs. They found a correlation with a significance of 3–3.5σ between the outflow velocity and galaxy properties such as SFR and M_*. Davis et al. (2023) created a sample with a wide range in M_* and SFR. They studied 46 late-stage galaxy mergers in conjunction with data from ten other papers about outflow winds and discovered a significant correlation between outflow velocities and SFR.

As can be seen, our results are inn good agreement with those found in other studies. The Lockman-SpReSO data is crucial for this study. Figures 8–10 demonstrate that the FIR-selected galaxies occupy regions in the charts where there were previously few objects, particularly in the higher SFR regions. This provides a more comprehensive sampling of the parameter space, allowing for a more detailed analysis of the general properties of galactic flows. In addition to higher SFRs, the velocities of the Fe II line tend to be higher than those of PR21 and RU14 sample (Figs. 9 and 10), increasing the available range of velocities in the correlation study.

4.3. Local covering factor and optical depth

The observed depth of an absorption line depends on the optical depth (τ) of an absorbing cloud, and also on the fraction of the background source which the cloud covers, C. For a continuum-normalised spectrum, the residual intensity I of the absorption feature is given by

$$I = (1 - C) + C\mathrm{e}^{-\tau}.$$

If two absorption lines are observed closely in wavelength, for example two components of a multiplet of the same ion, for which the ratio of the optical depth is known (α), we can solve for C and τ. The ratio of optical depths is the ratio of the oscillator strengths f of the lines which can be found, for example, in Morton (2003) and references therein. If $f_{\rm b} = \alpha f_{\rm r}$ then $\tau_{\rm b} = \alpha\tau_{\rm r}$, and the residual intensities in the red and blue components of the line are:

$$I_{\rm r} = (1 - C) + C\mathrm{e}^{-\tau_{\rm b}/\alpha}$$

and

$$I_{\rm b} = (1 - C) + C\mathrm{e}^{-\tau_{\rm b}}.$$

These equations must be solved numerically. See a more detailed discussion in Benn et al. (2005).

In our case, we observe the pairs of absorption lines Mg II $\lambda\lambda$2796, 2803, Fe II $\lambda\lambda$2374, 82, and Fe II $\lambda\lambda$2586, 2600. By measuring the residual intensities and knowing the oscillator strengths, we then estimate the covering factors (C), optical depths (τ_0) and ionic column densities (N). As our spectral resolution is not high enough, covering factors should be taken as lower limits.. Results are shown in Table 4 where we show only the results for the Fe II absorption lines, because in most cases blending of the Mg II doublet makes it impossible to obtain a physical solution or is unreliable. In some cases it is also very difficult even for Fe II lines.

From the above we have estimated ion column densities (see Table 4). Our data, limited by low spectral resolution and the lack of other ionised species, do not allow us to constrain ionisation parameters or electron densities. We can, however, crudely estimate hydrogen column densities by assuming solar metallicity, no depletion of Fe, and 100% of ionisation for the singly ionised iron (Eq. (13) in Martin et al. 2012). For our outflows, H I column densities are estimated to be in the range $\log(N(\mathrm{H\,I})) \sim 19.7$–$20.5\,\mathrm{cm}^{-2}$, and in some cases can be up to $\log(N(\mathrm{H\,I})) = 21$. These large values seem unlikely, so we would expect higher than solar metallicities. Alternatively, for a control test, we can estimate H I column densities using the relationship defined in Ménard & Chelouche (2009) between H I column densities and rest frame Mg II EW. We measured Mg II EWs to be on average ~5 Å, giving $\log(N(\mathrm{H\,I})) \sim 20.7\,\mathrm{cm}^{-2}$, consistent with our previous estimate.

Ionic densities and covering factors are similar to those in the literature (Martin et al. 2012). Also, average densities are $\log(N) \lesssim 16\,\mathrm{cm}^{-2}$ so that we could conclude that we observed similar galactic outflows as in previous studies; that is, typical mass flux in the low-ionisation outflows can be of the order of $\sim 23\,M_\odot\,\mathrm{yr}^{-1}$ (Eq. (12) from Martin et al. 2012).

5. Summary and conclusions

In this paper, we present a study of the galactic flows in objects from the Lockman–SpReSO project (Gonzalez-Otero et al. 2023). The objects were selected for having Fe II lines in absorption, and Mg II lines in absorption and emission. We find 21 objects with redshift in the range $0.5 \lesssim z \lesssim 1.45$, of which three are classified as AGN (González-Otero, in prep.). The objects in the sample span an M_* range of $9.89 < \log(M_*/M_\odot) < 11.50$ and

Table 4. Covering factor, optical depth, and ionic column density obtained in the analysis of the Fe II doublet lines.

ID	Fe II λ2374			Fe II λ2382			Fe II λ2586			Fe II λ2600		
	C	τ_0	$\log N$ (cm^{-2})	C	τ_0	$\log N$ (cm^{-2})	C	τ_0	$\log N$ (cm^{-2})	C	τ_0	$\log N$ (cm^{-2})
123207	–	–	–	–	–	–	0.33	1.2	15.7	0.33	4.2	15.4
96864	–	–	–	–	–	–	0.3	∞	>16	0.3	∞	>15.7
101926	0.31	2.5	16.0	0.31	2.7	15.7	0.3	∞	>16	0.3	∞	>15.8
120080	–	–	–	–	–	–	0.33	∞	>16	0.33	∞	>16.2
118338	–	–	–	–	–	–	0.20	∞	>16	0.20	∞	>15.6
95738	–	–	–	–	–	–	0.28	4.8	16.2	0.28	16.6	16.0
109219	–	–	–	–	–	–	0.19	1.8	15.9	0.19	6.3	15.7
94458	–	–	–	–	–	–	0.24	1.2	15.4	0.24	4.1	15.6
92467	–	–	–	–	–	–	0.30	1.3	15.4	0.30	4.4	15.5
120257	0.54	0.25	15.3	0.54	2.6	15.2	0.43	0.7	15.7	0.43	2.3	15.3
95958	0.17	3	16.4	0.17	31	16.1	0.35	0.7	15.3	0.35	2.5	15.2
116662	0.20	1.6	16.0	0.20	17	15.8	0.32	1.1	15.5	0.32	3.5	15.5
133957	–	–	–	–	–	–	0.38	1.3	15.9	0.38	4.5	15.5
186820	–	–	–	–	–	–	0.19	1.5	15.8	0.19	5.3	15.3
97778	0.15	1.8	16.0	0.15	19	15.8	0.25	2.5	15.7	0.25	8.6	15.8
77155	0.34	1.1	16.0	0.34	12	15.8	0.43	2.9	15.9	0.43	10	15.8
102473	0.26	3.2	16.3	0.26	34	16.1	0.34	0.7	15.8	0.34	2.2	15.5
120237 [(a)]	0.17	4.4	16.5	0.17	47	16.3	0.30	1.0	15.7	0.30	3.4	15.5
206641 [(a)]	0.08	0.2	15.2	0.08	2.2	15.1	0.08	0.8	15.2	0.08	2.9	15.6
78911	0.41	0.5	15.6	0.41	5.6	15.5	0.53	1.8	15.9	0.53	6.2	15.7
206679 [(a)]	0.41	0.9	16.0	0.41	10	15.8	0.60	1.3	15.6	0.60	4.5	15.4

Notes. [(a)]Objects classified as AGN by González-Otero et al. (in prep.).

Table 5. Summary of the Spearman rank correlation coefficient and the significance found in the study of the Mg II λ2796 line.

ρ_s	Mg II λ2796					
	PR21		RU14		This work	
	EW	Δv	EW	Δv	EW	Δv
M_*	–	–	$0.44_{3.2\sigma}$	–	$0.43_{4.5\sigma}$	$0.06_{0.7\sigma}$
SFR	$0.67_{3.2\sigma}$	–	$0.48_{3.5\sigma}$	–	$0.42_{4.4\sigma}$	$-0.11_{1.1\sigma}$
sSFR	–	–	–	–	$0.11_{1.1\sigma}$	$-0.16_{1.6\sigma}$

are (U)LIRGs ($10.84 < \log(L_{\rm TIR}/L_\odot) < 12.53$) with relatively high log(SFR) between 1.01 and 2.70. We determined the systemic velocities of the objects and measured the EW and velocities of the Fe II $\lambda\lambda$2374, 82, Fe II $\lambda\lambda$2586, 2600, Fe II λ2344, Mg II $\lambda\lambda$2796, 2803, and Mg I λ2852 spectral lines.

The EWs and line velocities were used to explore possible correlations with the M_*, SFR, and sSFR values of the galaxies. In order to obtain statistically significant results, we performed a joint analysis of our sample of 18 objects with an additional 22 and 105 galaxies from PR21 and RU14, respectively. Bootstrap simulations were performed on the Spearman rank test to check for the existence of correlations between the properties. The inclusion of Lockman–SpReSO objects, selected for their FIR emission, adds great value to the sample, because to the best of our knowledge there are very few such studies based on LIRGs in the literature (e.g. Banerji et al. 2011). This helps us to validate whether the results obtained with other types of objects are also valid for the FIR-selected objects.

Using the three samples as a whole, we find the EW of Mg II λ2796 to correlate strongly, $\rho_s = 0.43$ ($\rho_s = 0.42$) and significantly at 4.5σ (4.4σ) with M_* (SFR). This result is in good agreement with the findings of RU14, but is only in agreement with those of PR21 with respect to the SFR relationship; these latter authors found no correlation of EW with M_*. The Lockman–SpReSO sample enables a more in-depth examination of the correlations between EW and galaxy properties. The EWs of these objects occupy regions of the parameter space where object density is very low, with higher values than in the RU14 and PR21 samples. This enables us to expand the boundaries of the relationships. The Mg II λ2796 line velocity has no correlation ($\rho_s \sim -0.1$) with the properties of the galaxies in the sample. Davis et al. (2023) find a positive correlation between velocity and SFR for the Mg II line. The discrepancy observed could be attributed to the effect of emission-line infilling, which dilutes the lines and introduces errors. Table 5 contains a summary of the Spearman coefficient obtained in the analysis of the Mg II λ2796 line.

For the analysis of the Fe II lines, separate studies were carried out for the PR21 and RU14 samples. In the sample with Lockman–SpReSO and RU14 data, a positive correlation $\rho_s = 0.43$ ($\rho_s = 0.69$) and a significant one at 3.3σ (5.3σ) were found with the M_* (SFR) and the EW of Fe II λ2586. With the sSFR, the correlation found is not very strong ($\rho_s = 0.33$) and of marginal significance (2.5σ). The velocity has no significant correlation with M_*, but a strong correlation ($\rho = -0.34$) with high significance (3.6σ) is found with SFR. This result implies that the velocity of Fe II spectral lines remains decoupled from M_* but not from SFR; in other words, the energy to which the material is exposed depends more on SFR than on M_*. A summary of the correlations can be seen in Table 6. To study the Lockman–SpReSO and PR21 sample as a whole, we performed weighted averages of the EW and velocities of the Fe II lines measured in the Lockman–SpReSO objects. We find that $\rm EW_{avg}$ is strongly correlated with the SFR ($\rho_s = 0.62$) at 3.9σ and more marginally

Table 6. Summary of the Spearman rank correlation coefficient and the significance found in the study of the Fe II λ2586 line.

	Fe II λ2586			
ρ_s	RU14		This work	
	EW	Δv	EW	Δv
M_*	$0.07_{0.4\sigma}$	–	$0.43_{3.3\sigma}$	$0.02_{0.2\sigma}$
SFR	$0.46_{2.4\sigma}$	–	$0.69_{5.3\sigma}$	$-0.34_{3.6\sigma}$
sSFR	–	–	$0.33_{2.5\sigma}$	$-0.27_{2.9\sigma}$

Table 7. Summary of the Spearman rank correlation coefficient and the significance found in the study of the weighted average of the Fe II lines.

	Fe II$_{avg}$			
ρ_s	PR21		This work	
	EW$_{avg}$	Δv_{avg}	EW$_{avg}$	Δv_{avg}
M_*	$\leq 1.4\sigma$	$\leq 1.4\sigma$	$0.31_{1.9\sigma}$	$-0.43_{2.3\sigma}$
SFR	$0.65_{2.9\sigma}$	$\leq 1.4\sigma$	$0.62_{3.9\sigma}$	$-0.57_{3.1\sigma}$
sSFR	$\leq 1.4\sigma$	$\leq 1.4\sigma$	$0.52_{3.2\sigma}$	$-0.25_{1.3\sigma}$

correlated with the M_* ($\rho_s = 0.31$) and sSFR ($\rho_s = 0.52$) at 1.9σ and 3.2σ, respectively. The average velocity also shows strong correlations with M_* ($\rho = -0.43$) and SFR ($\rho = -0.57$). This is consistent with the results above that show that the velocity is dependent on the properties of the SFR. In general, thanks to the inclusion of the Lockman–SpReSO objects selected for their FIR emission – of which little is known compared to galactic flows in distant FIR objects –, we can confirm the results of previous studies and find discrepancies with others. A summary of the correlations obtained for the weighted average of Fe II lines is provided in Table 7.

Although the spectral resolution and dispersion used in the Lockman–SpReSO observations ($R \sim 500$, ~ 4 Å pix^{-1}) are not commonly used for outflow analysis, where higher resolutions are usually required, we were able to detect the existence of nine (ten) galactic outflows, five (one) inflows, and four (seven) absorption-only objects based on the velocities obtained for the Fe II λ2586 (Mg II λ2796) line. In addition, of the three objects classified as AGN, object 206679 was found to be a clear candidate 'loitering outflow', a new class of iron low-ionisation broad absorption (FeLoBAL) quasar characterised by low flow velocities ($v \lesssim 2000$ km s^{-1}) and high-column-density winds located at $\log(R_d) \lesssim 1$ pc.

Finally, it is important to highlight that this study was not initially planned, but rather emerged from the serendipitous discovery of these objects in the Lockman–SpReSO data. Despite the unplanned nature of the study, the findings provide valuable insights into the characteristics and behaviour of these objects. Higher-resolution observations will help us to better constrain and study the velocities of the objects with increased accuracy, and will provide more information about the FeLoBAL quasar candidate. However, this study undoubtedly sheds more light on the study of galactic flows by adding objects of a different nature compared to those studied so far, as they are objects selected for their FIR emission.

Acknowledgements. We thank the anonymous referee for their useful report. This work was supported by the Evolution of Galaxies project, of references AYA2017-88007-C3-1-P, AYA2017-88007-C3-2-P, AYA2018-RTI-096188-BI00, PID2019-107408GB-C41, PID2019-106027GB-C41, PID2021-122544NB-C41, PID2021-122544NB-C43, PID2022-136598NB-C33, and MDM-2017-0737 (Unidad de Excelencia María de Maeztu, CAB), within the Programa estatal de fomento de la investigación científica y técnica de excelencia del Plan Estatal de Investigación Científica y Técnica y de Innovación (2013-2016) of the Spanish Ministry of Science and Innovation/State Agency of Research MCIN/AEI/ 10.13039/501100011033 and by 'ERDF A way of making Europe'. This work is based on observations made with the Gran Telescopio Canarias (GTC) at Roque de los Muchachos Observatory on the island of La Palma, with the *William Herschel* Telescope (WHT) at Roque de los Muchachos Observatory on the island of La Palma and on observations at Kitt Peak National Observatory, NSF's National Optical-Infrared Astronomy Research Laboratory (NOIRLab Prop. ID: 2018A-0056; PI: González-Serrano, J.I.), which is operated by the Association of Universities for Research in Astronomy (AURA) under a cooperative agreement with the National Science Foundation. This research has made use of the NASA/IPAC Extragalactic Database (NED), which is funded by the National Aeronautics and Space Administration and operated by the California Institute of Technology. E.B. and I.C.G. acknowledge support from DGAPA-UNAM grant IN119123. J.N. acknowledges the support of the National Science Centre, Poland through the SONATA BIS grant 2018/30/E/ST9/00208 Y.K. acknowledges support from DGAPA-PAPIIT grant IN102023. The authors thank Terry Mahoney (at the IAC's Scientific Editorial Service) for his substantial improvements of the manuscript.

References

Baldwin, J. A., Phillips, M. M., & Terlevich, R. 1981, PASP, 93, 5
Banerji, M., Chapman, S. C., Smail, I., et al. 2011, MNRAS, 418, 1071
Benn, C. R., Carballo, R., Holt, J., et al. 2005, MNRAS, 360, 1455
Boquien, M., Burgarella, D., Roehlly, Y., et al. 2019, A&A, 622, A103
Burgarella, D., Buat, V., & Iglesias-Páramo, J. 2005, MNRAS, 360, 1413
Calzetti, D., Armus, L., Bohlin, R. C., et al. 2000, ApJ, 533, 682
Cepa, J., Aguiar, M., Escalera, V. G., et al. 2000, Proc. SPIE, 4008, 623
Chabrier, G. 2003, PASP, 115, 763
Chen, Y.-M., Tremonti, C. A., Heckman, T. M., et al. 2010, AJ, 140, 445
Chisholm, J., Tremonti, C. A., Leitherer, C., et al. 2015, ApJ, 811, 149
Choi, H., Leighly, K. M., Terndrup, D. M., et al. 2022, ApJ, 937, 74
Cid Fernandes, R., Stasińska, G., Mateus, A., & Vale Asari, N. 2011, MNRAS, 413, 1687
Cooksey, K. L., Prochaska, J. X., Chen, H.-W., Mulchaey, J. S., & Weiner, B. J. 2008, ApJ, 676, 262
Davis, J. D., Tremonti, C. A., Swiggum, C. N., et al. 2023, ApJ, 951, 105
Domínquez Palmero, L., Cano, D., Fariña, C., et al. 2014, SPIE Conf. Ser., 9147, 914778
Donley, J. L., Koekemoer, A. M., Brusa, M., et al. 2012, ApJ, 748, 142
Erb, D. K., Quider, A. M., Henry, A. L., & Martin, C. L. 2012, ApJ, 759, 26
Finley, H., Bouché, N., Contini, T., et al. 2017a, A&A, 605, A118
Finley, H., Bouché, N., Contini, T., et al. 2017b, A&A, 608, A7
Gonzalez-Otero, M., Padilla-Torres, C. P., Cepa, J., et al. 2023, A&A, 669, A85
Heckman, T. M., Lehnert, M. D., Strickland, D. K., & Armus, L. 2000, ApJS, 129, 493
Heckman, T. M., Alexandroff, R. M., Borthakur, S., Overzier, R., & Leitherer, C. 2015, ApJ, 809, 147
Jones, T., Stark, D. P., & Ellis, R. S. 2012, ApJ, 751, 51
Kennicutt, R. C., Jr 1998, ARA&A, 36, 189
Kennicutt, R. C., & Evans, N. J. 2012, ARA&A, 50, 531
Kobulnicky, H. A., & Kewley, L. J. 2004, ApJ, 617, 240
Leclercq, F., Bacon, R., Verhamme, A., et al. 2020, A&A, 635, A82
Luo, B., Brandt, W. N., Xue, Y. Q., et al. 2017, ApJS, 228, 2
Martin, C. L. 2005, ApJ, 621, 227
Martin, C. L. 2006, ApJ, 647, 222
Martin, C. L., Shapley, A. E., Coil, A. L., et al. 2012, ApJ, 760, 127
Ménard, B., & Chelouche, D. 2009, MNRAS, 393, 808
Messias, H., Afonso, J., Salvato, M., Mobasher, B., & Hopkins, A. M. 2012, ApJ, 754, 120
Morton, D. C. 2003, ApJS, 149, 205
Murray, N., Ménard, B., & Thompson, T. A. 2011, ApJ, 735, 66
Newville, M., Stensitzki, T., Allen, D. B., & Ingargiola, A. 2014, https://doi.org/10.5281/zenodo.11813
Oke, J. B., & Gunn, J. E. 1983, ApJ, 266, 713
Péroux, C., & Howk, J. C. 2020, ARA&A, 58, 363
Pettini, M., & Pagel, B. E. J. 2004, MNRAS, 348, L59
Pilyugin, L. S., & Grebel, E. K. 2016, MNRAS, 457, 3678
Popesso, P., Concas, A., Cresci, G., et al. 2023, MNRAS, 519, 1526
Prochaska, J. X., Kasen, D., & Rubin, K. 2011, ApJ, 734, 24

Prusinski, N. Z., Erb, D. K., & Martin, C. L. 2021, AJ, 161, 212
Rubin, K. H. R., Weiner, B. J., Koo, D. C., et al. 2010, ApJ, 719, 1503
Rubin, K. H. R., Prochaska, J. X., Koo, D. C., et al. 2014, ApJ, 794, 156
Rupke, D. S., Veilleux, S., & Sanders, D. B. 2005a, ApJ, 632, 751
Rupke, D. S., Veilleux, S., & Sanders, D. B. 2005b, ApJS, 160, 115
Schmidt, M., Hasinger, G., Gunn, J., et al. 1998, A&A, 329, 495
Shapley, A. E., Steidel, C. C., Pettini, M., & Adelberger, K. L. 2003, ApJ, 588, 65
Skelton, R. E., Whitaker, K. E., Momcheva, I. G., et al. 2014, ApJS, 214, 24
Steidel, C. C., Erb, D. K., Shapley, A. E., et al. 2010, ApJ, 717, 289
Szokoly, G. P., Bergeron, J., Hasinger, G., et al. 2004, ApJS, 155, 271
Tremonti, C. A., Heckman, T. M., Kauffmann, G., et al. 2004, ApJ, 613, 898
Tumlinson, J., Peeples, M. S., & Werk, J. K. 2017, ARA&A, 55, 389
Veilleux, S., Cecil, G., & Bland-Hawthorn, J. 2005, ARA&A, 43, 769
Veilleux, S., Maiolino, R., Bolatto, A. D., & Aalto, S. 2020, A&A Rev., 28, 2
Weiner, B. J., Coil, A. L., Prochaska, J. X., et al. 2009, ApJ, 692, 187
Xu, X., Heckman, T., Henry, A., et al. 2022, ApJ, 933, 222
Zhu, G. B., Comparat, J., Kneib, J.-P., et al. 2015, ApJ, 815, 48

Appendix A: Cutouts and SED fits of the Lockman–SpReSO objects

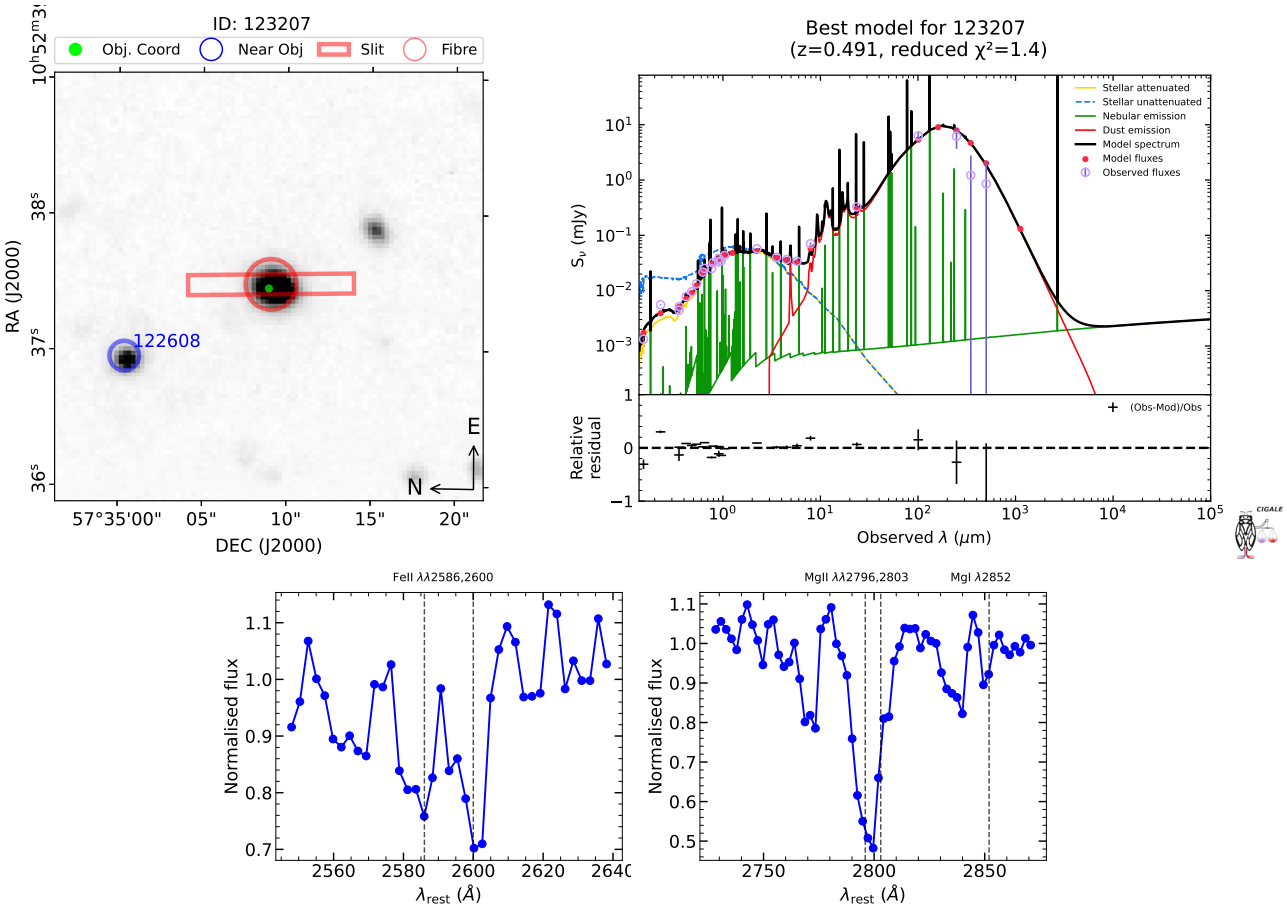

Fig. A.1. Cutouts (top left), SED fits (top right), and spectra slices (bottom) for the object ID 123207 studied in this paper. The cutouts are made on the GTC image of the Lockman-SpReSO survey field (see Gonzalez-Otero et al. 2023 for details). The green dot represents the optical coordinates of the object. The blue circle marks nearby objects in the Lockman-SpReSO catalogue. The red rectangle represents the position and size of the slit used to observe the object. There are two types of slit: a small slit of 3 arcsec and a large slit of 10 arcsec (see Gonzalez-Otero et al. 2023 for more details). The red circle represents the position of the fibre. In the SED fits the best model is plotted as a solid black line, the photometric information of the object is plotted as empty violet circles, and the red filled circles are the fluxes obtained by the best model. The individual contributions of the models used are also plotted where the yellow line represents the attenuated stellar component, the blue dashed line is the unattenuated stellar component, the green line illustrates the nebular emission, and the red line is the dust emission. The relative residuals of the flux for the best model are plotted at the bottom. The spectral slices show the absorption lines studied in this paper. The spectra have been normalised to the continuum. The grey vertical dashed lines represent the rest-frame wavelength of the lines.

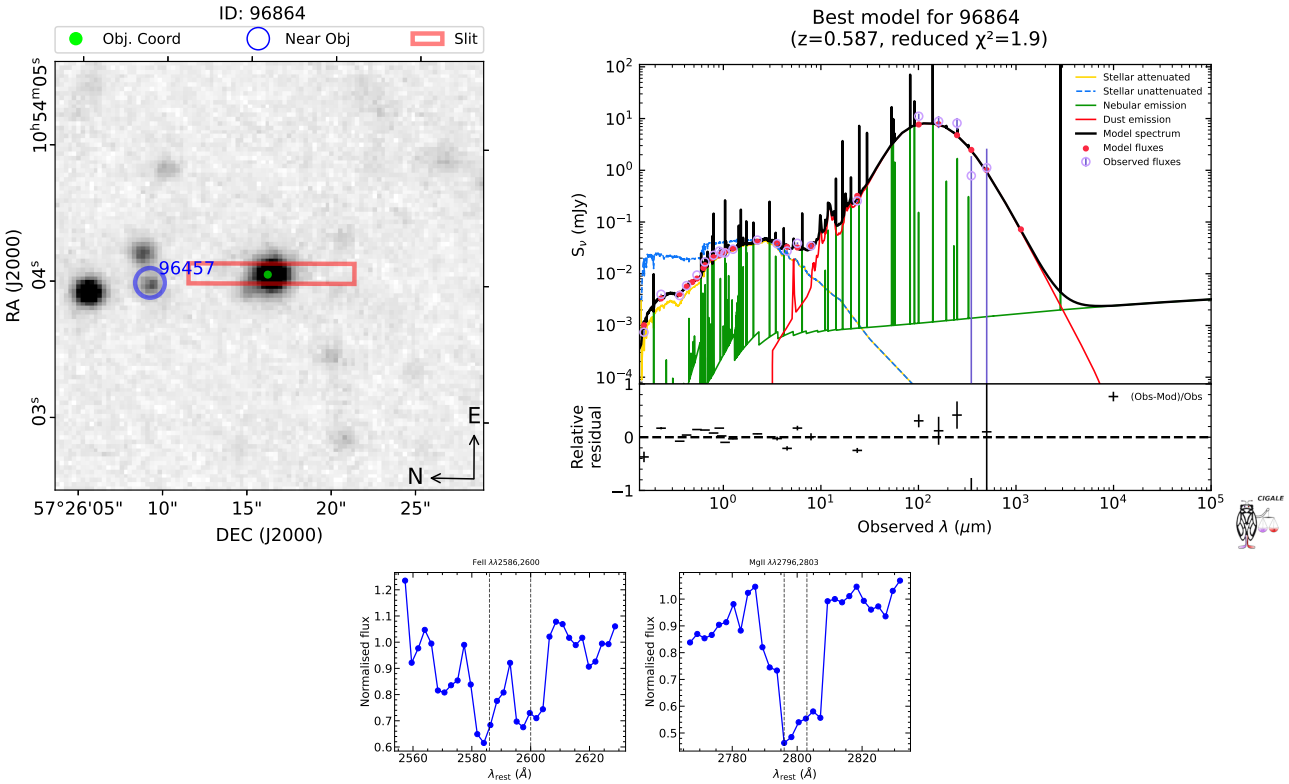

Fig. A.2. Same as Fig. A.1 but for object ID 96864.

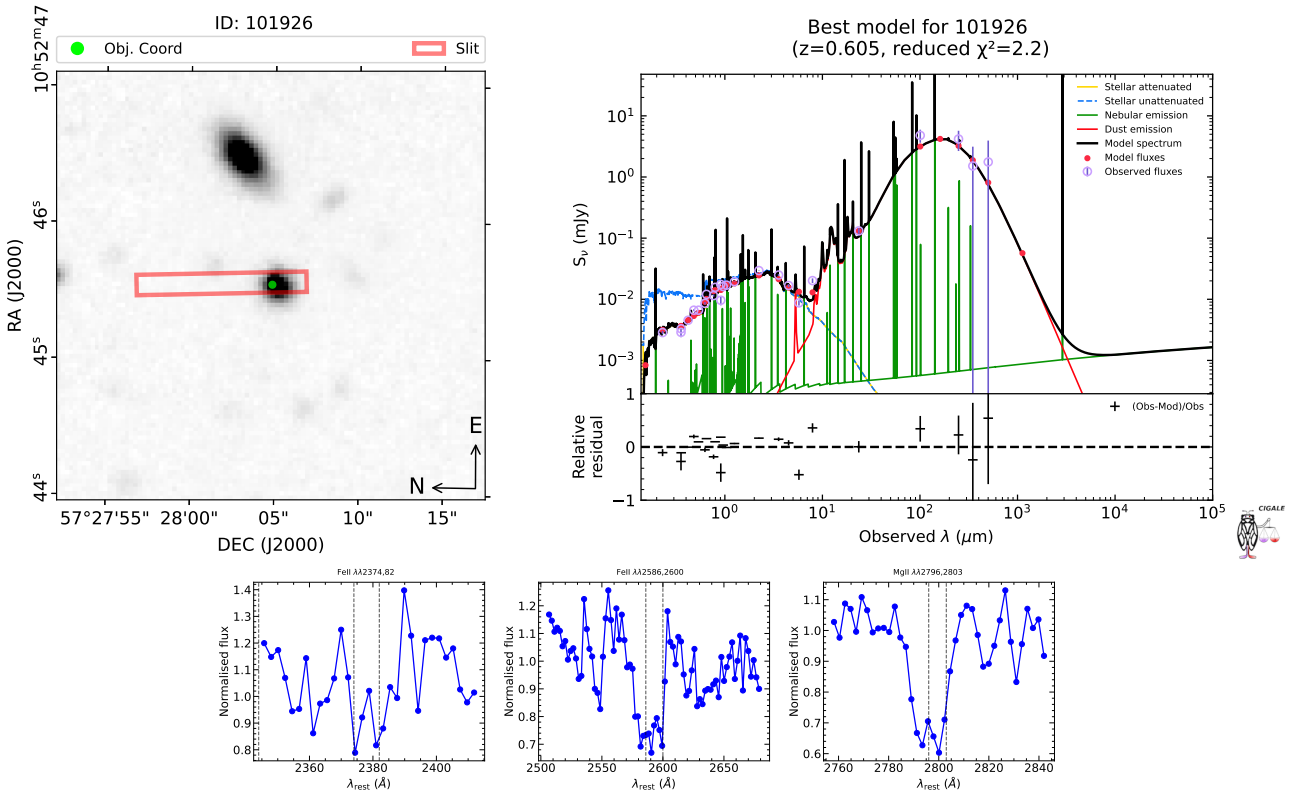

Fig. A.3. Same as Fig. A.1 but for object ID 101926.

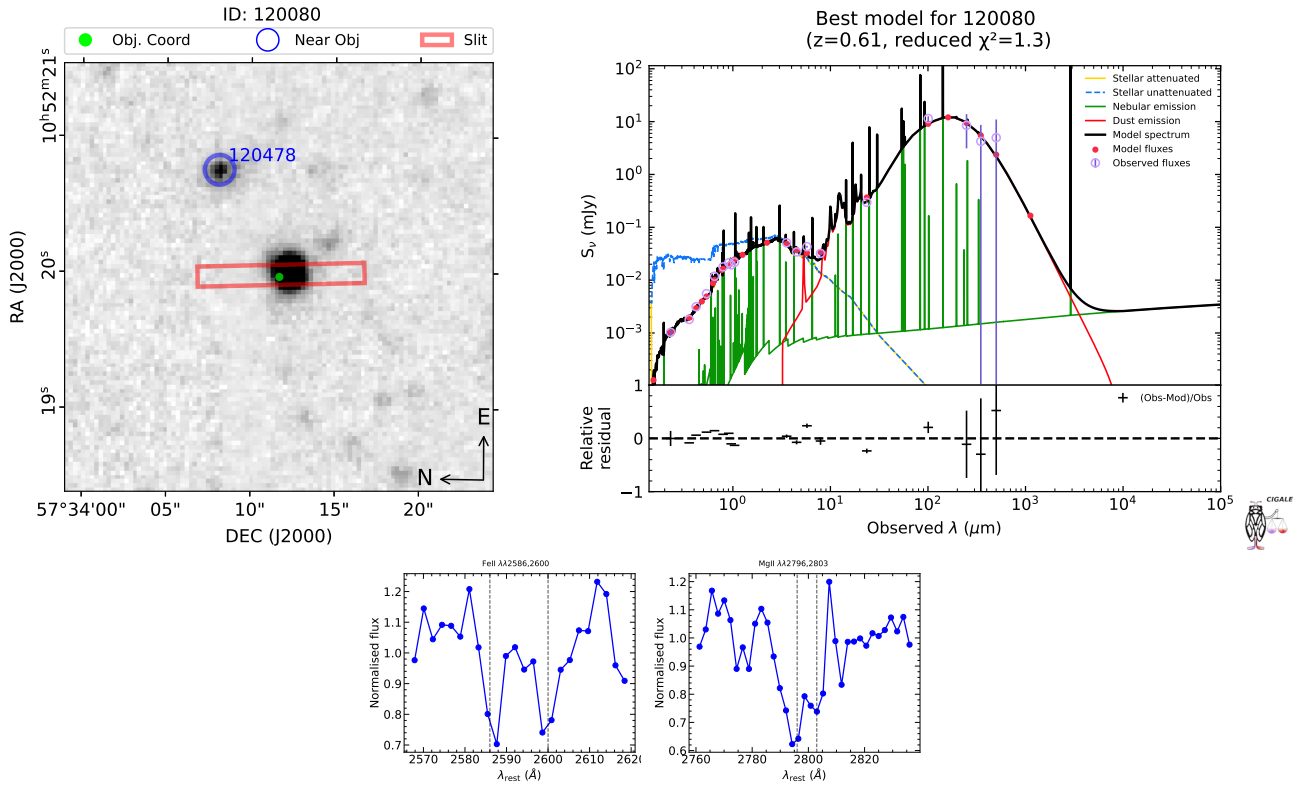

Fig. A.4. Same as Fig. A.1 but for object ID 120080.

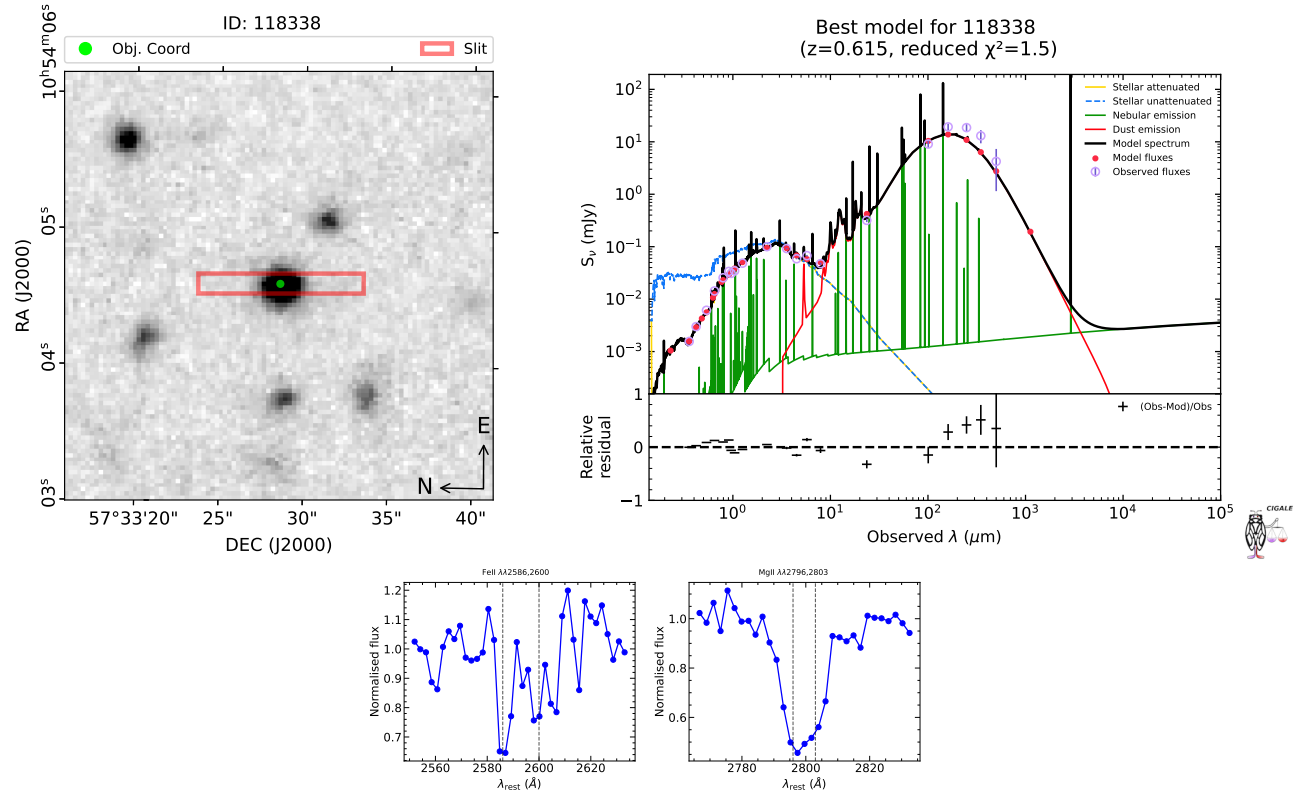

Fig. A.5. Same as Fig. A.1 but for object ID 118338.

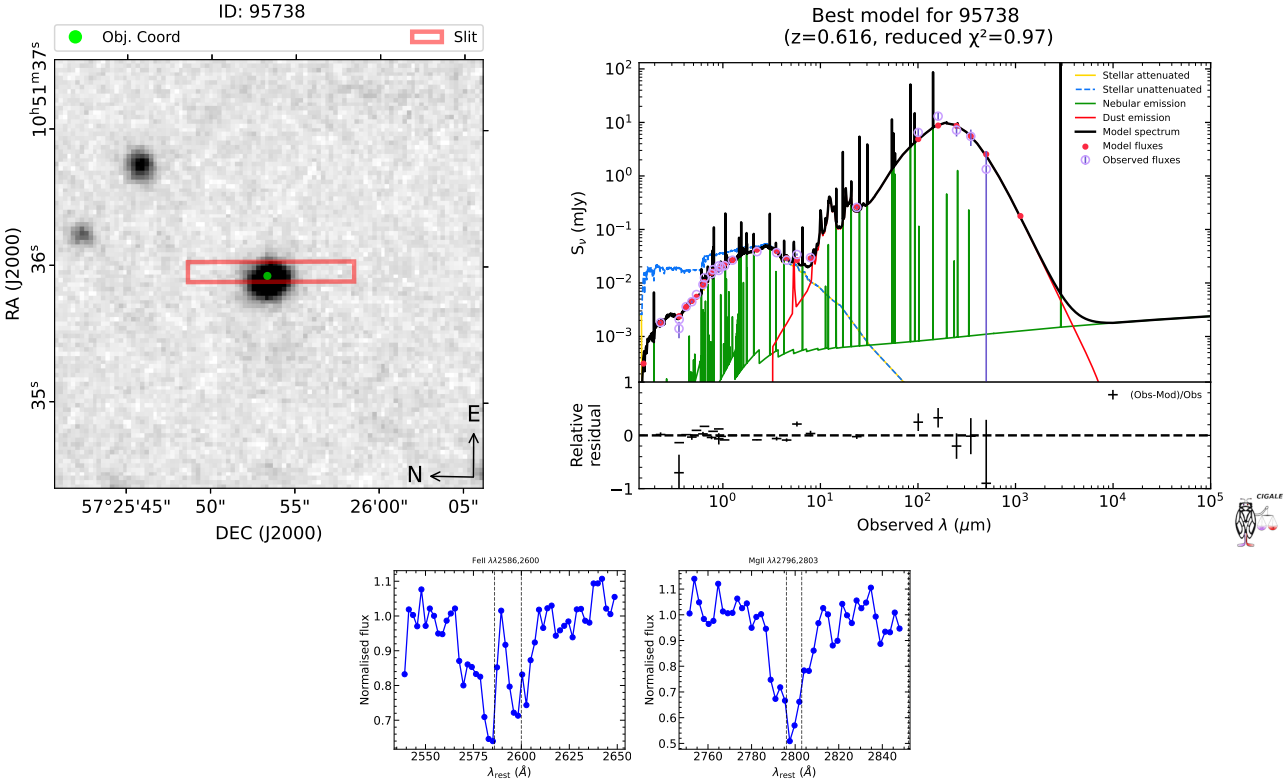

Fig. A.6. Same as Fig. A.1 but for object ID 95738.

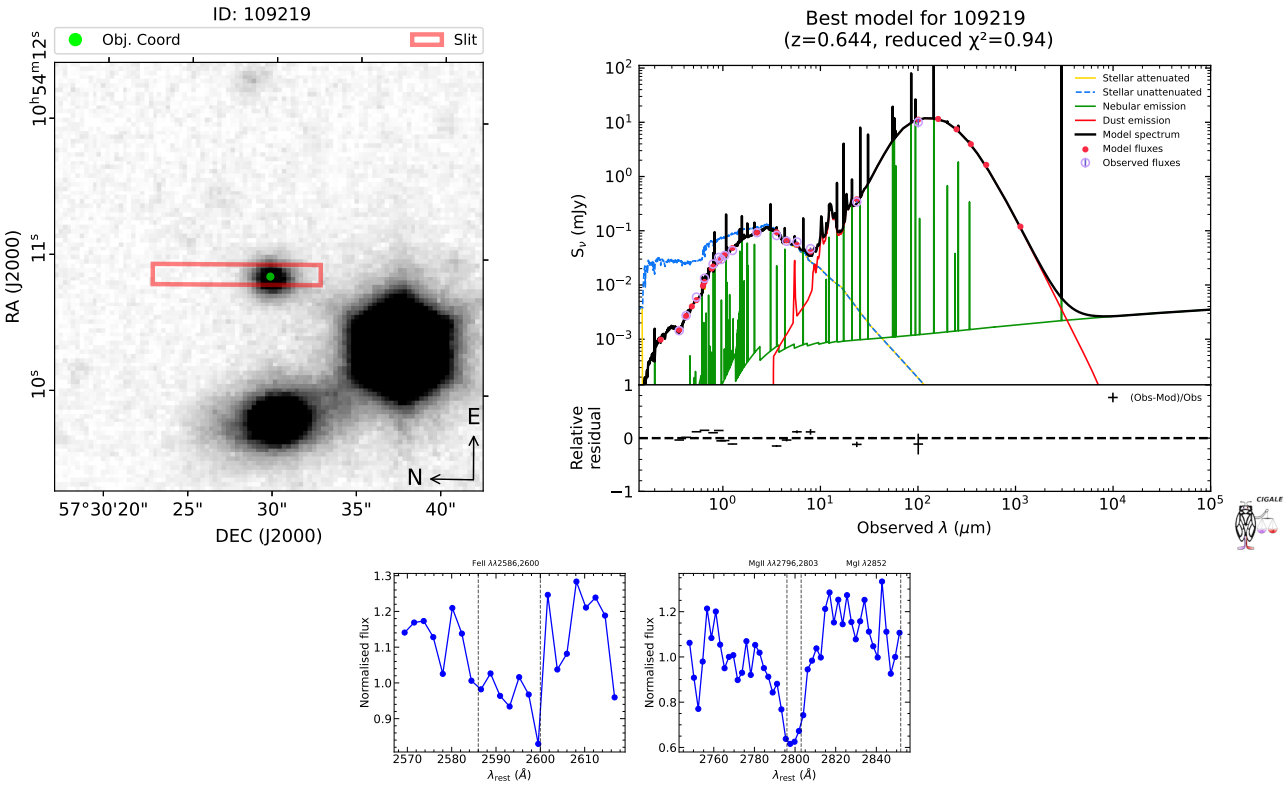

Fig. A.7. Same as Fig. A.1 but for object ID 109219.

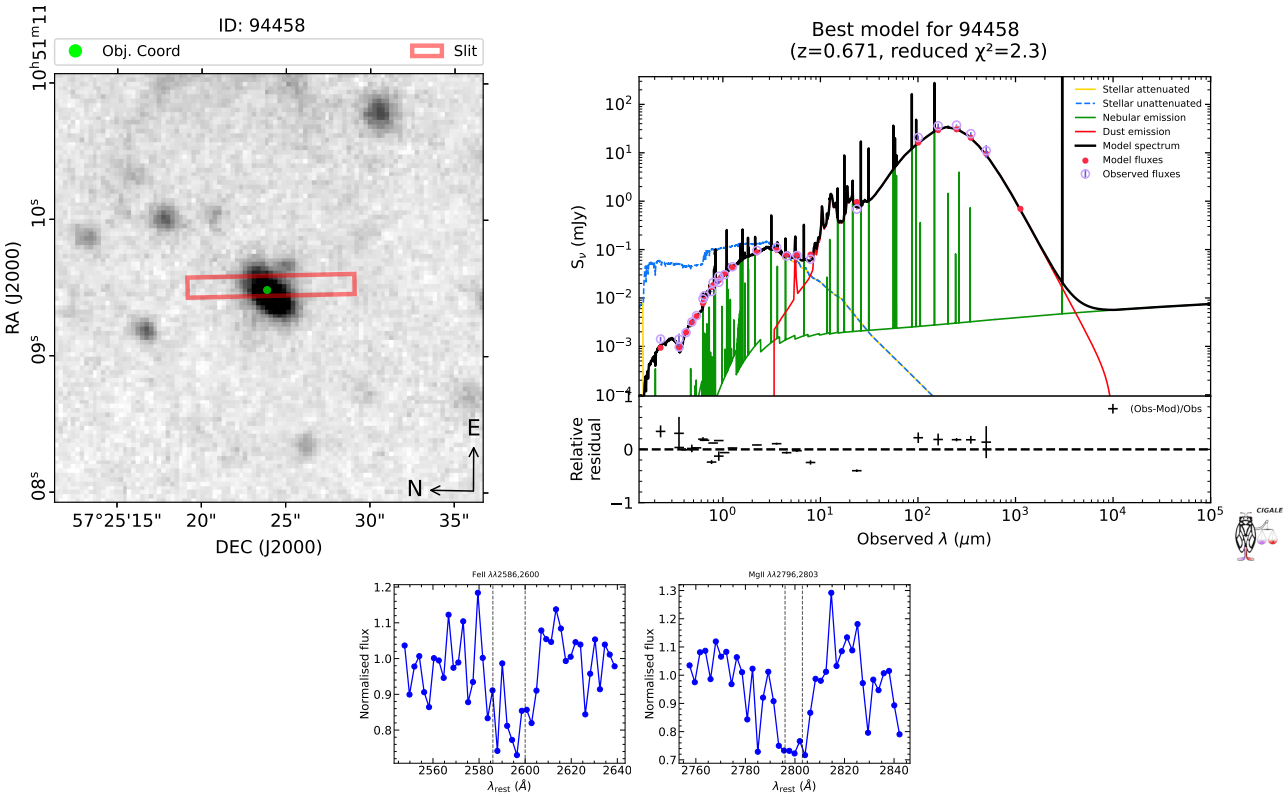

Fig. A.8. Same as Fig. A.1 but for object ID 94458.

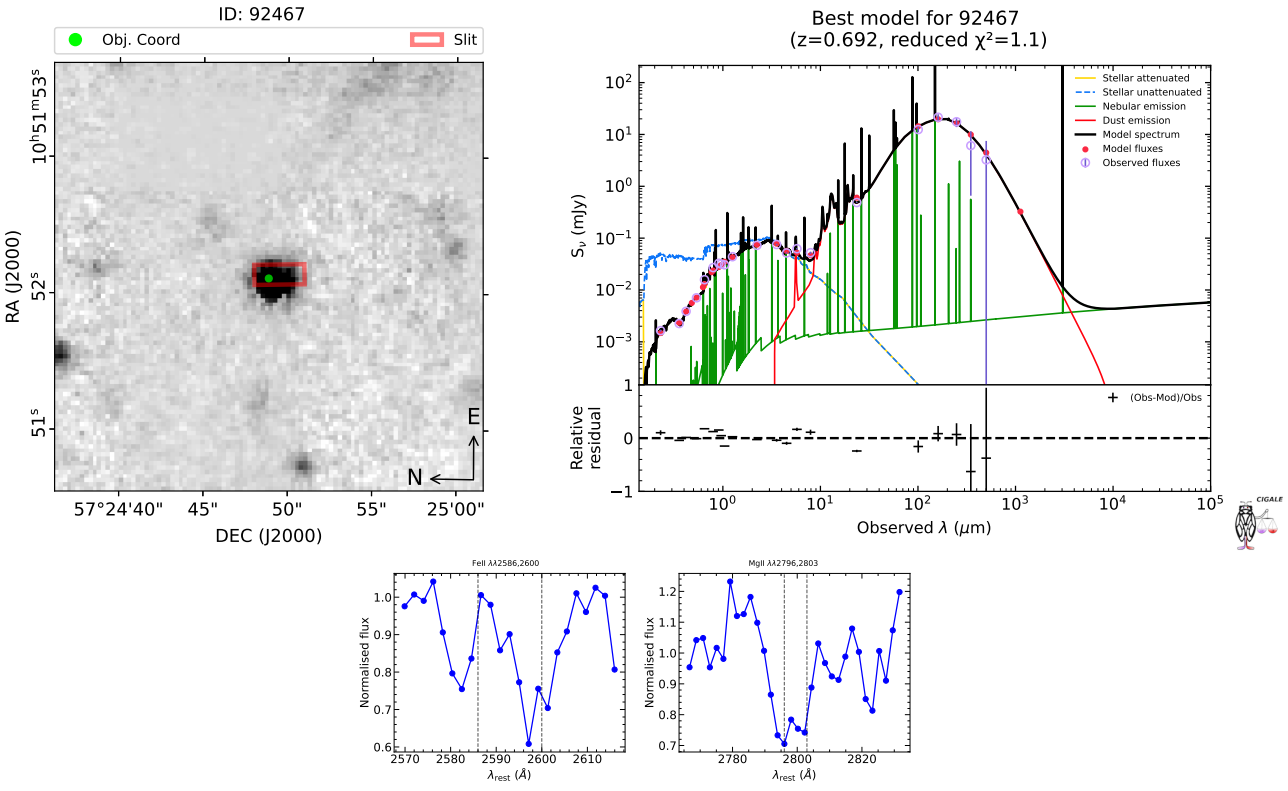

Fig. A.9. Same as Fig. A.1 but for object ID 92467.

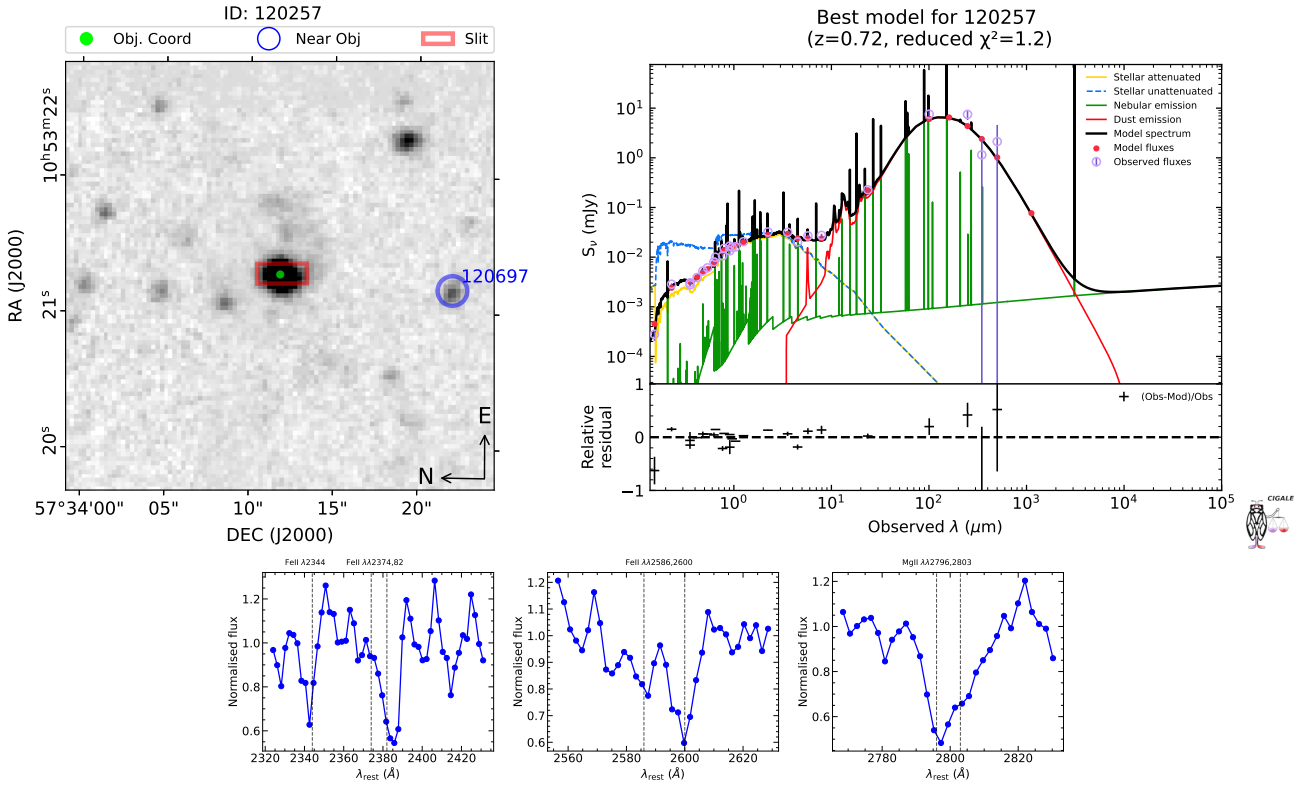

Fig. A.10. Same as Fig. A.1 but for object ID 120257.

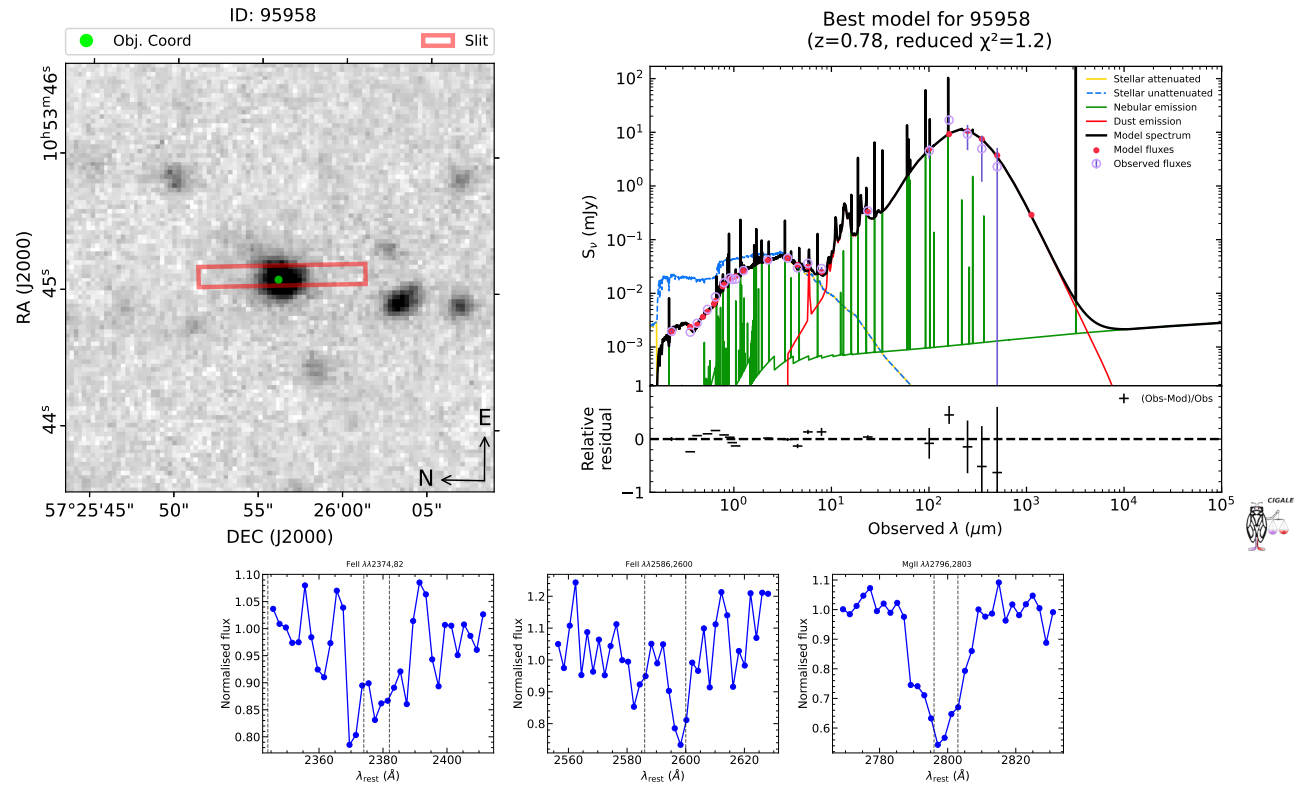

Fig. A.11. Same as Fig. A.1 but for object ID 95958.

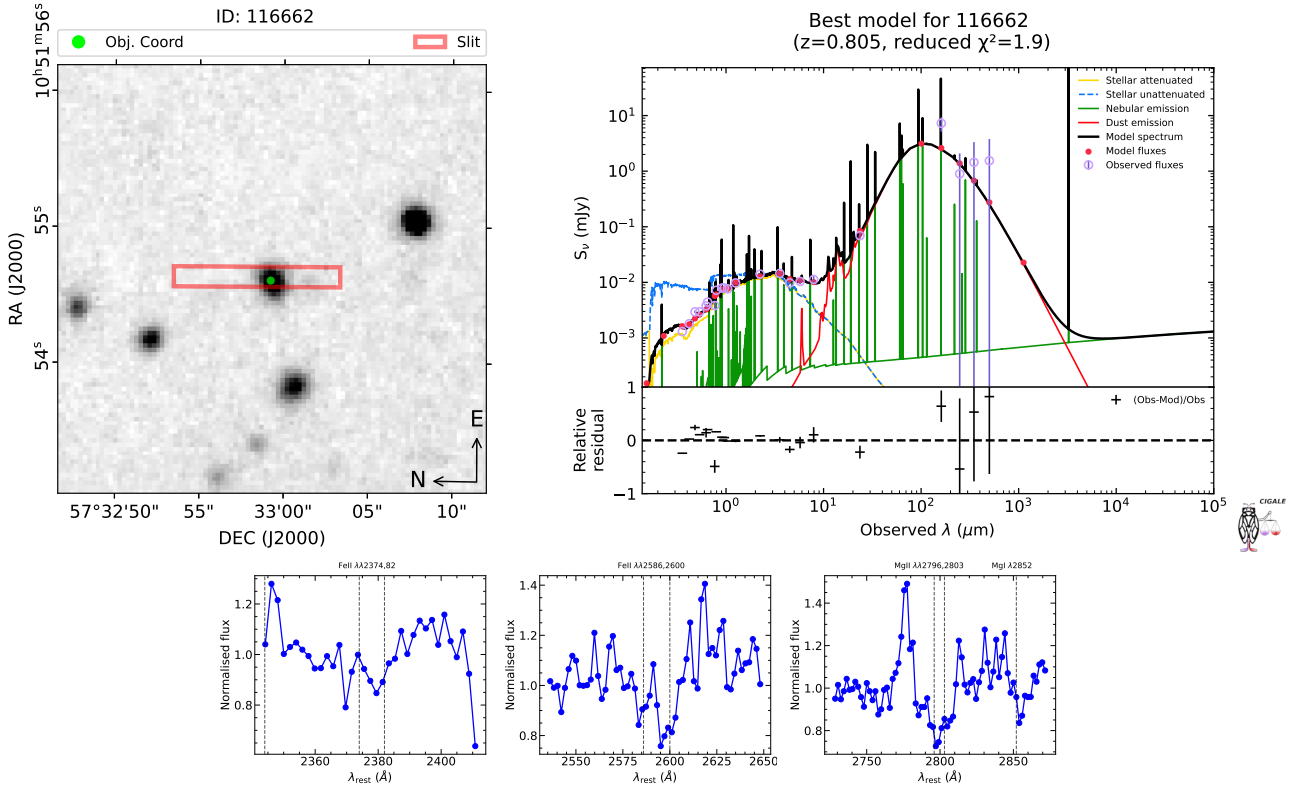

Fig. A.12. Same as Fig. A.1 but for object ID 116662.

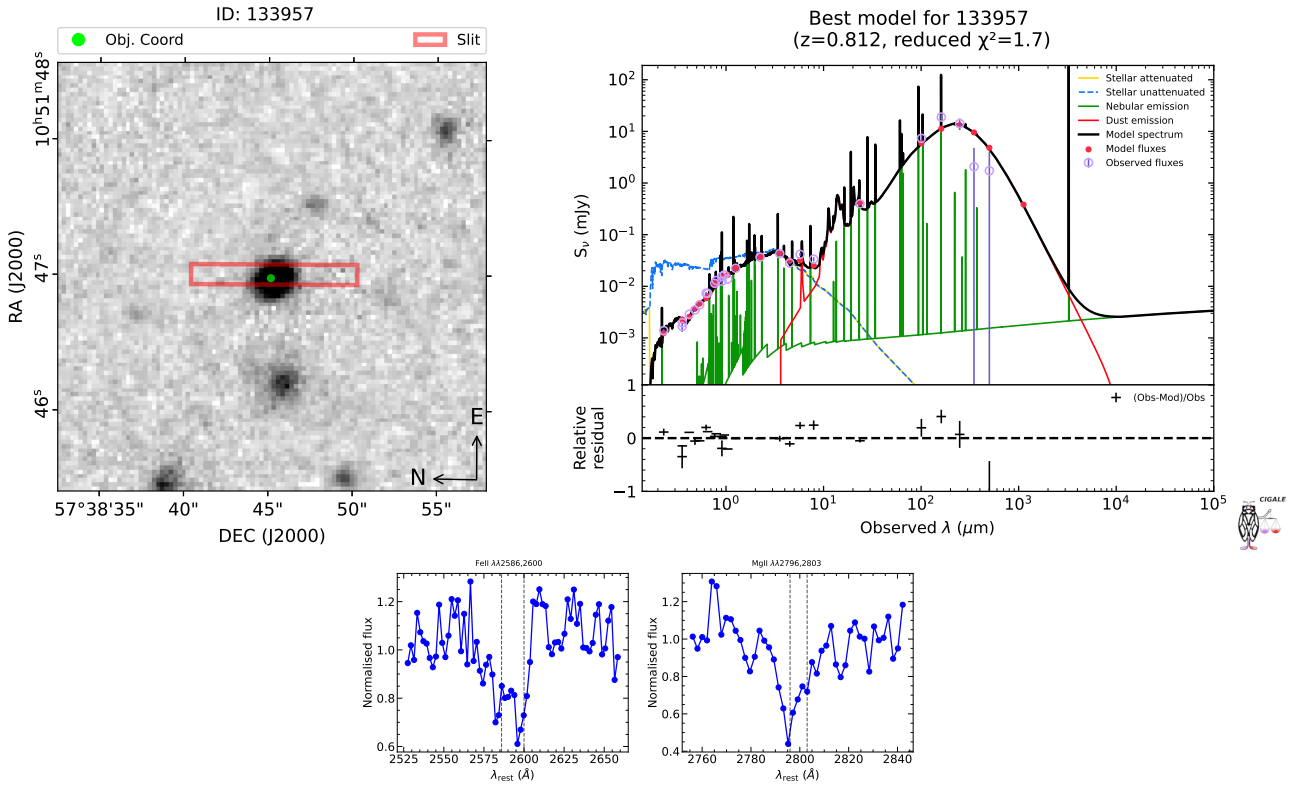

Fig. A.13. Same as Fig. A.1 but for object ID 133957.

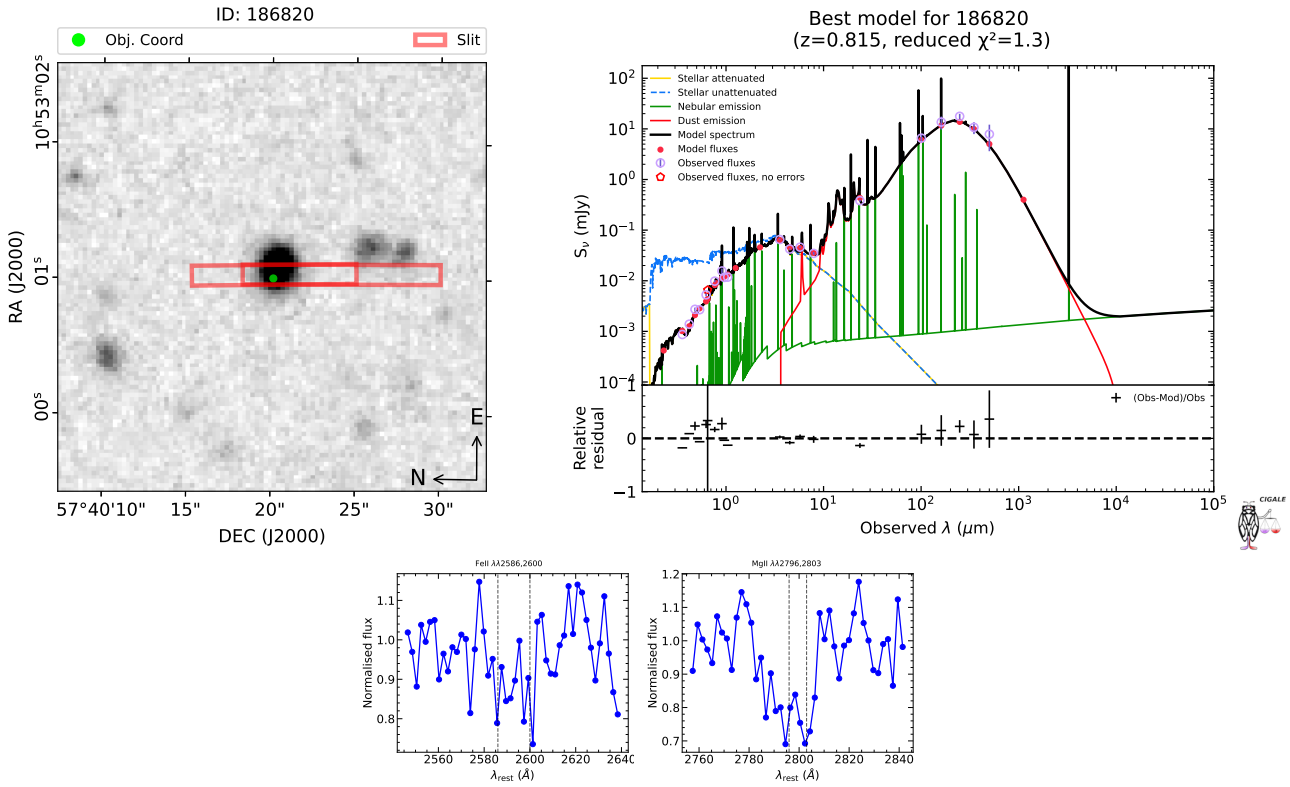

Fig. A.14. Same as Fig. A.1 but for object ID 186820.

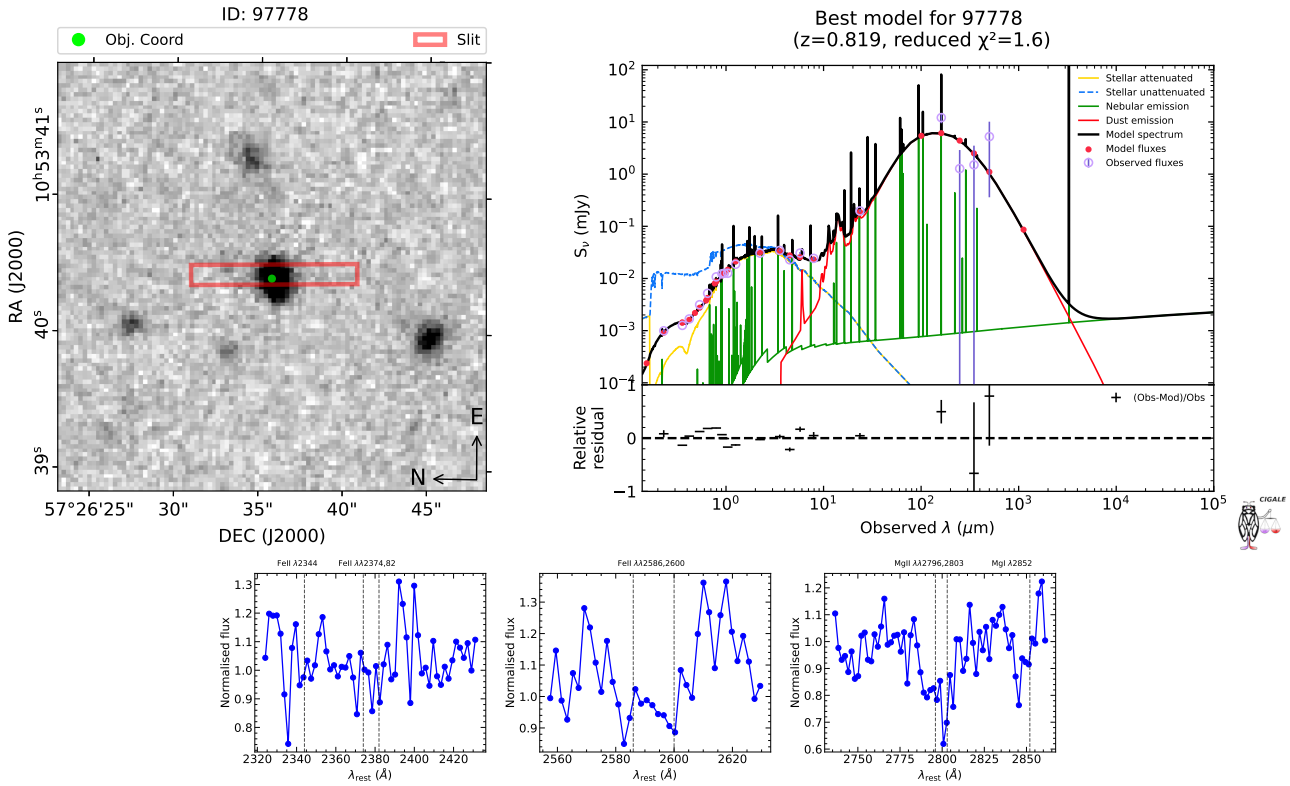

Fig. A.15. Same as Fig. A.1 but for object ID 97778.

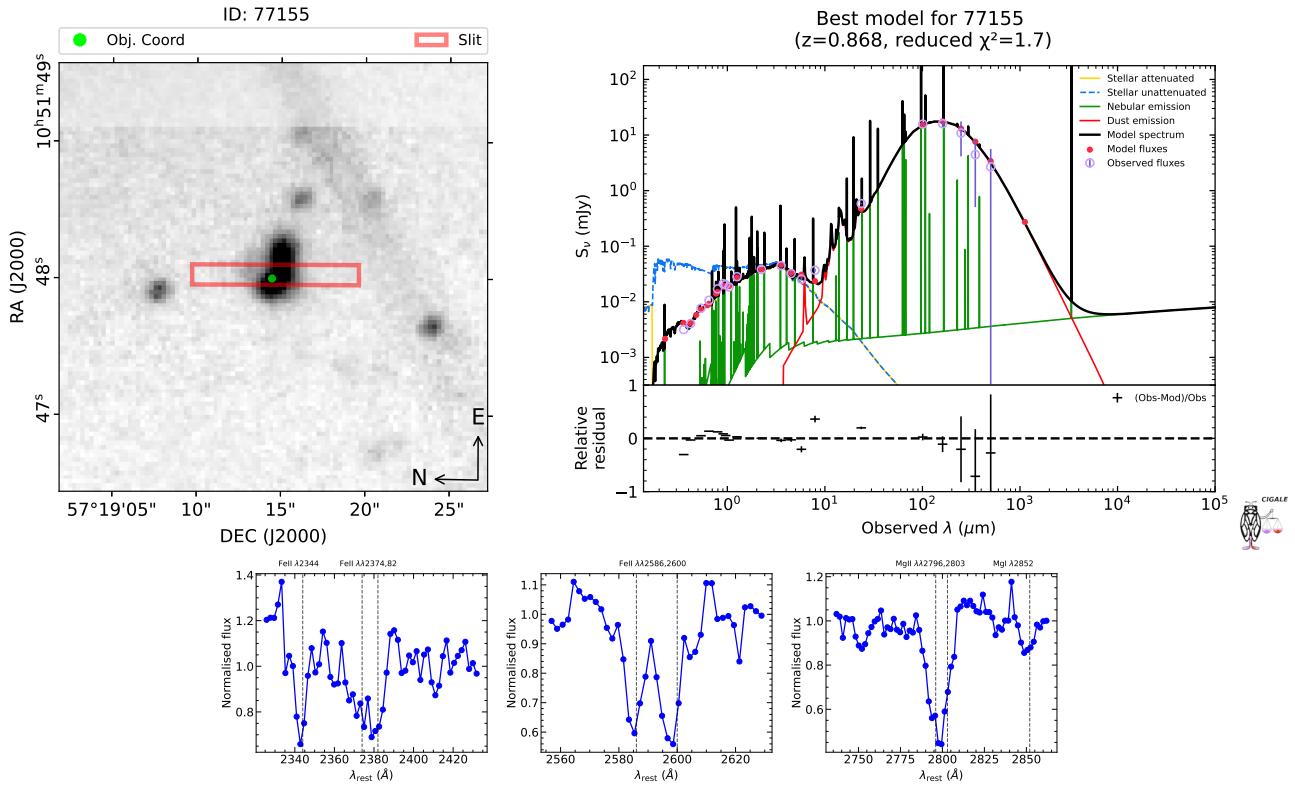

Fig. A.16. Same as Fig. A.1 but for object ID 77155.

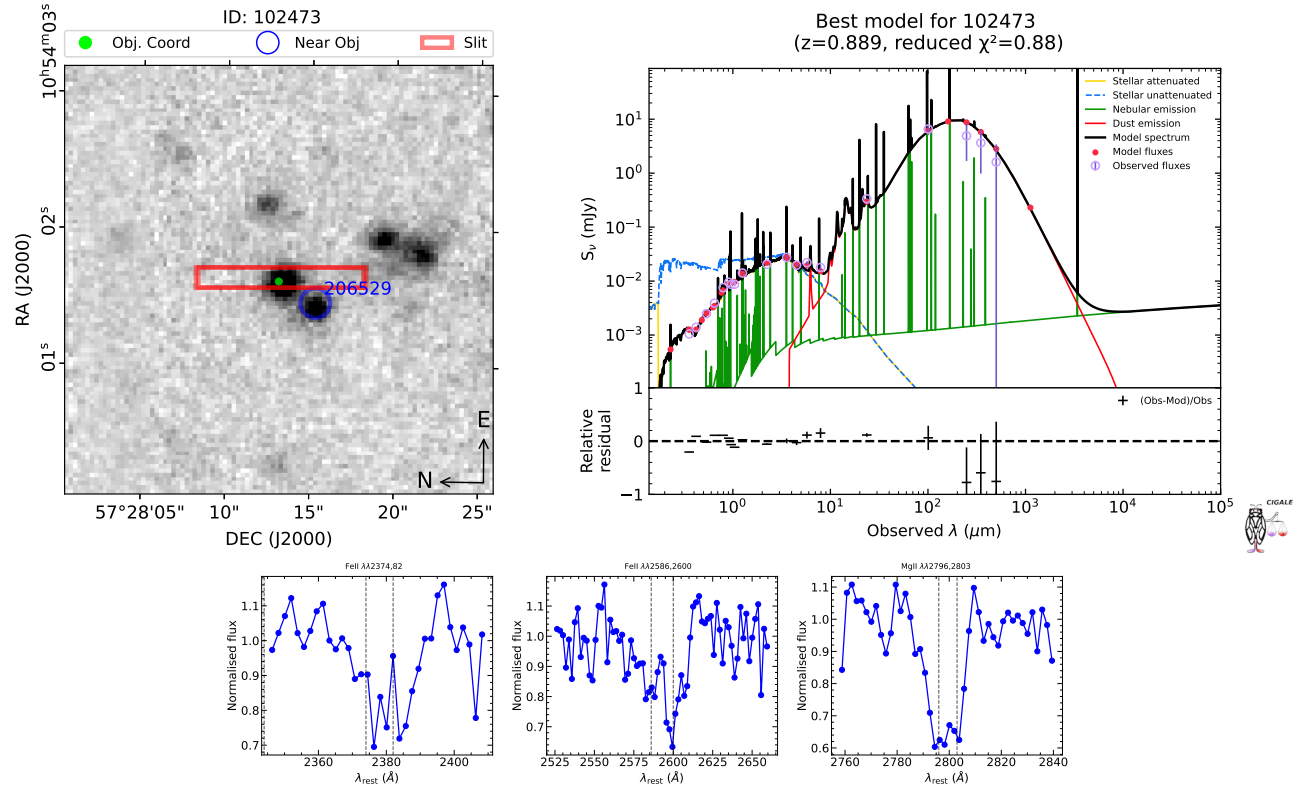

Fig. A.17. Same as Fig. A.1 but for object ID 102473.

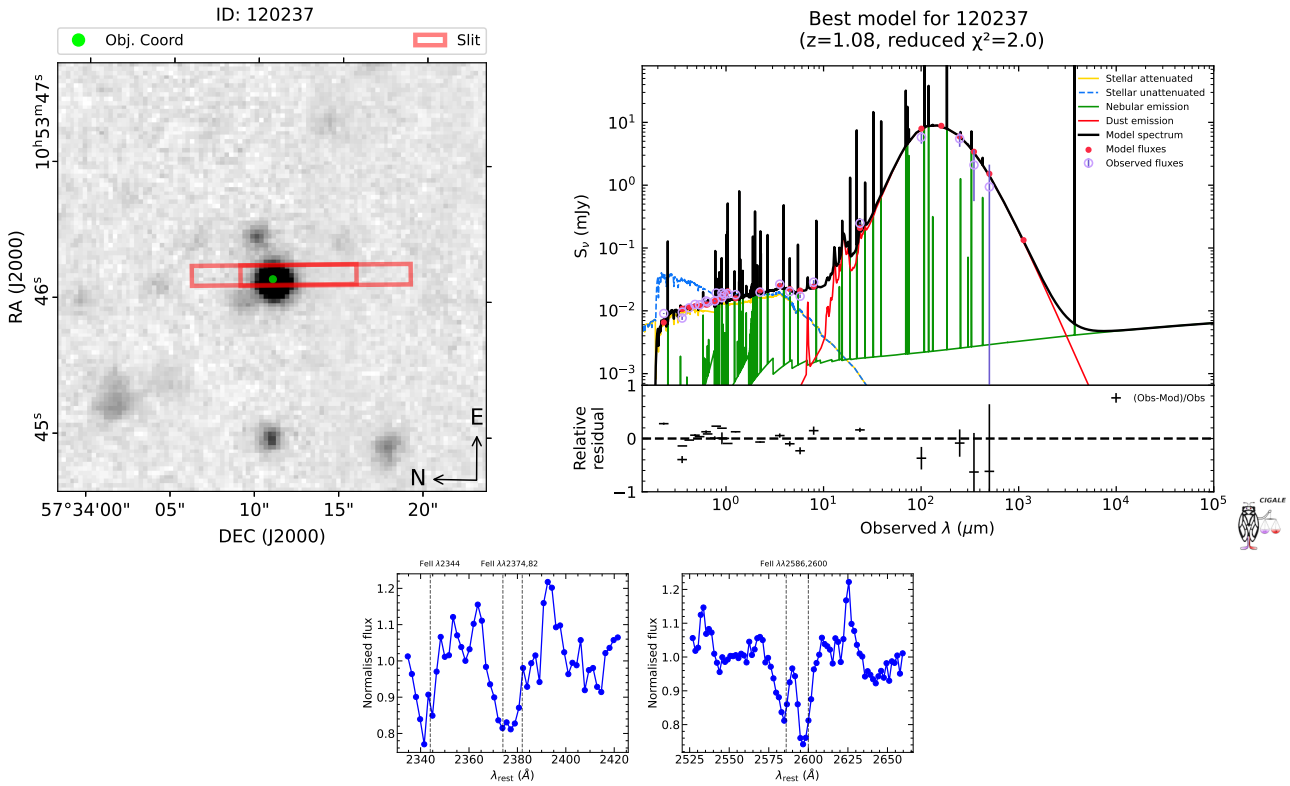

Fig. A.18. Same as Fig. A.1 but for object ID 120237.

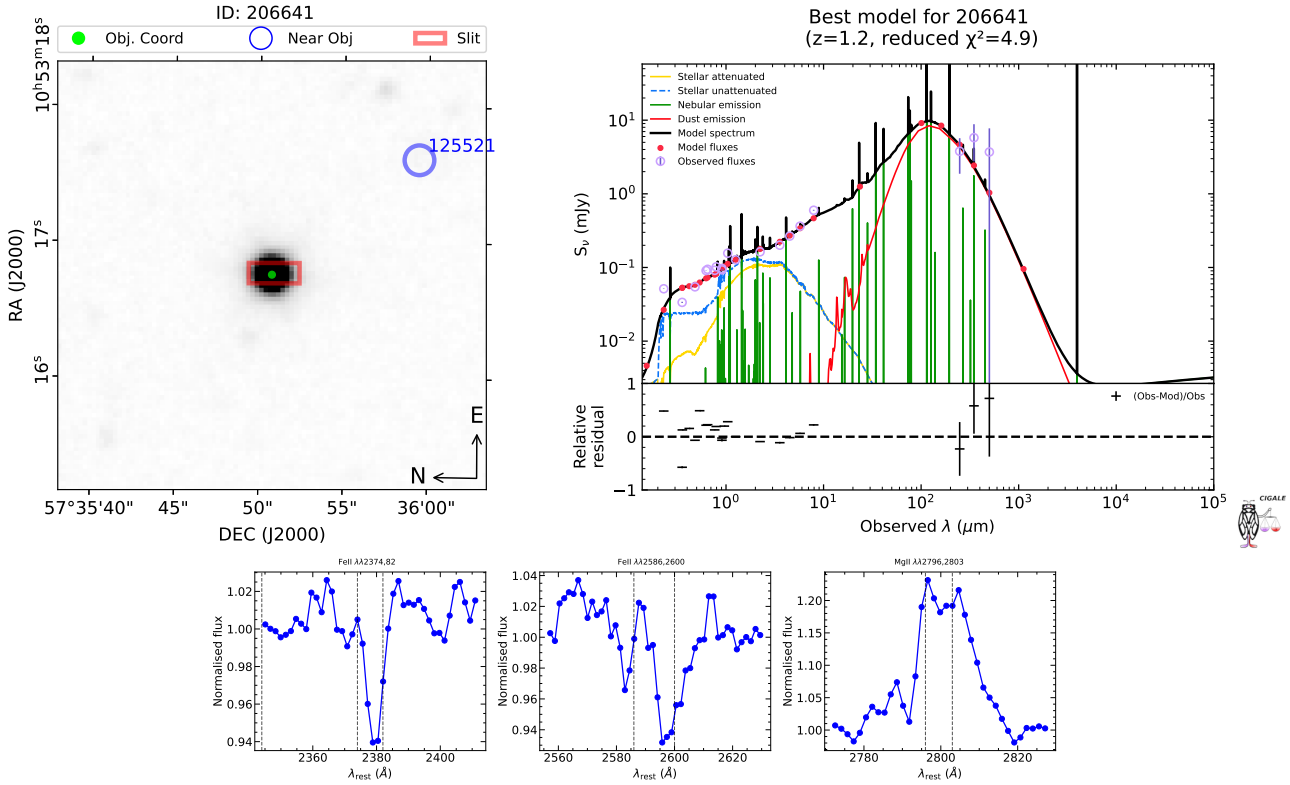

Fig. A.19. Same as Fig. A.1 but for object ID 206641.

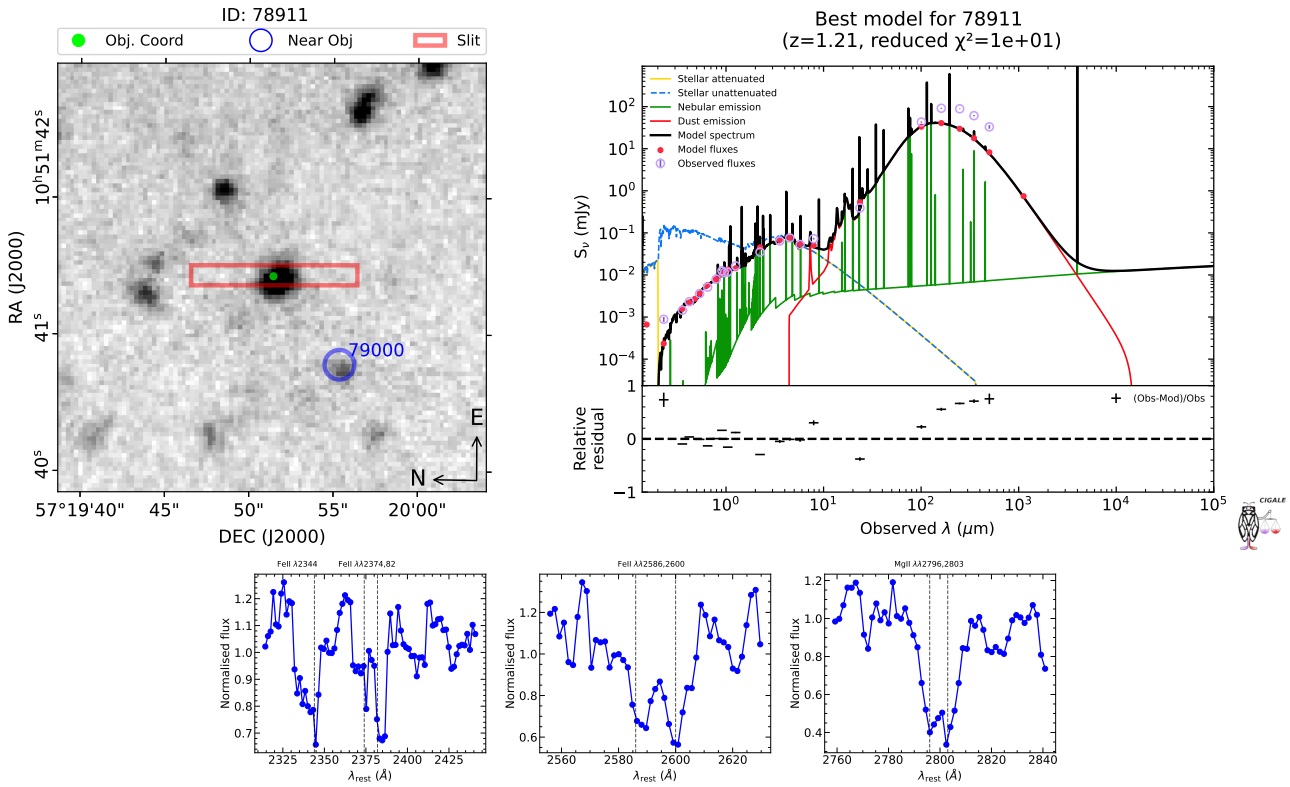

Fig. A.20. Same as Fig. A.1 but for object ID 78911.

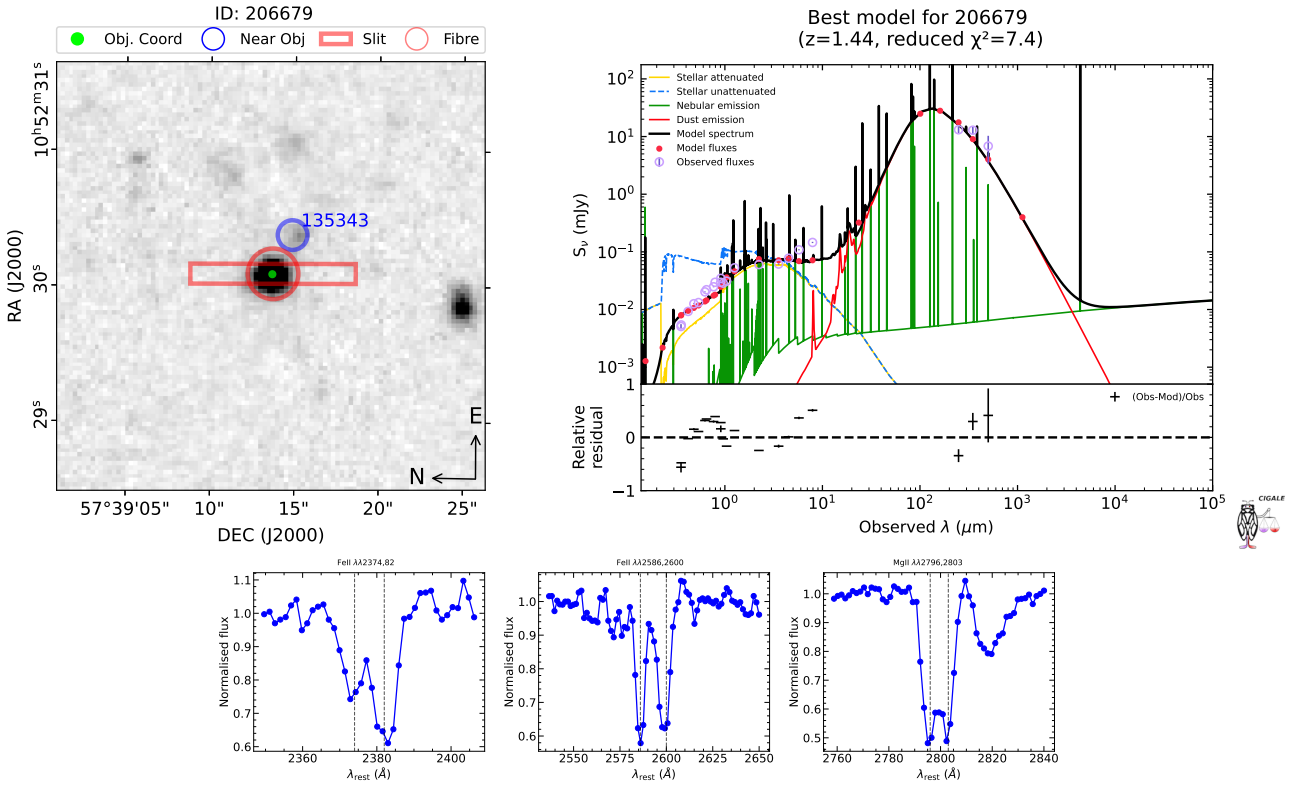

Fig. A.21. Same as Fig. A.1 but for object ID 206679.

5

Summary & Conclusions

All that is gold does not glitter,
Not all those who wander are lost;
The old that is strong does not wither,
Deep roots are not reached by the frost.
From the ashes a fire shall be woken,
A light from the shadows shall spring;
Renewed shall be blade that was broken:
The crownless again shall be king.
Bilbo at the Council of Elrond, The Fellowship of the Ring
J. R. R. Tolkien (1954)

This thesis presents the first findings of the analysis of the data from the Lockman–SpReSO project which is a spectroscopic survey in the optical range dedicated to the follow-up of IR galaxies previously observed with the *Herschel Space Telescope*.

The initial phase of the thesis involved the comprehensive reduction of the survey data. This process entailed the application of exquisite corrections to the raw observations, resulting in the generation of the final spectra of the objects. From these, the spectral line measurements and the spectroscopic redshifts of the objects were derived. Furthermore, a comprehensive compilation of all available information pertaining to the objects was undertaken, with the objective of creating a comprehensive survey catalogue. Finally, using the redshift and the available photometric information, the SED of the objects were fitted to derive the M_* and $L_{\rm TIR}$.

The subsequent phase of the thesis focused on the investigation of the characteristics of the SFGs. To this end, we initially distinguished the SFGs from the AGNs through the application of both photometric and spectroscopic criteria. Subsequently, the spectral lines were corrected for the extinction caused by the interstellar dust in

order to determine the SFR and metallicity of the SFGs. This approach enabled us to examine the relations between their properties. On the one hand, the MS was studied by analysing the M_* in conjunction with the SFR. On the other hand, the MZR of the SFGs was studied, analysing the behaviour of M_* and metallicity together. Finally, the three-dimensional relationship between M_*, SFR and metallicity was analysed.

In the final part of the thesis, the galactic flows present in a small sample of objects in the catalogue were studied. For this purpose, the ultraviolet absorption lines of Mg II and Fe II were analysed. The EW of the lines and the velocities of the flows were analysed with respect to the host galaxy properties such as the M_*, SFR and the sSFR.

To conclude this thesis, a synopsis of the principal results and conclusions derived from the study is presented below.

- At the outset of the thesis, the observations of the survey were completed in their entirety, commencing in 2014 and concluding in 2018. The observations of the central region of the LH field (24×24 arcmin^2) were mainly conducted with the OSIRIS spectrograph attached to the GTC telescope. The sample of objects comprises 956 FIR-selected galaxies and 188 additional objects of interest in the field. A satisfactory reduction of all survey observations was achieved. For this purpose, established routines in *IRAF* and own-designed Python programs were employed. In particular, the subtraction of the sky contribution in the spectra represents a challenging and pivotal aspect of the data reduction process. This was satisfactorily achieved by the use of both an innovative strategy of observations and own-designed Python programs. Taking the final spectra of the objects as a starting point, the following results were obtained:

  - The spectroscopic redshift was determined for 357 objects in the range $0.0290 < z < 4.9671$, using two or more spectral lines available in the spectra. Additionally, for 99 objects for which only one spectral line could be found, an in-depth study was conducted to provide a reliable redshift value. In order to achieve this, all available photometric information, including magnitudes and photometric redshifts, was utilised, resulting in a redshift range of $0.0973 < z < 1.4470$. Of the 456 objects for which we were able to provide a redshift value, less than the 25% had a value in the literature. In addition, the redshift determination allowed us to clarify the nature of some of the complementary objects in the catalogue. For instance, sources that were identified as potential cataclysmic star candidates were observed to exhibit redshifts within the range $0.5263 < z < 1.9387$. This indicates that they are not stars, but rather distant compact objects.

  - The most significant spectral lines within the ultraviolet-optical range were measured. The *LMFIT* routine, implemented in Python, was employed for this purpose. Each line was fitted using a Gaussian and a linear component.
  - The survey database was fully described and constructed. It included all available information on the survey objects in the literature and comprised observations from more than 10 different telescopes and data from more than 30 photometric bands, spanning the electromagnetic spectrum from X-ray to submillimetre wavelengths.
  - The SEDs of the objects were fitted using the CIGALE software, which took advantage of the extensive photometric coverage available for the objects, from FUV to FIR, and the obtained spectroscopic redshift. This allowed us to derive galaxy properties such as M_* and $L_{\rm TIR}$. The M_* of the galaxies is distributed in the range $7.65 < \log(M_*/M_\odot) < 12.07$ with a mean value of $\log(M_*/M_\odot) = 10.28$. Conversely, the $L_{\rm TIR}$ encompasses a range of $8.12 < \log(L_{\rm TIR}/L_\odot) < 13.06$, with 55% of the objects classified as LIRGs, 6% as ULIRGs, and 1% as HLIRGs.

- In order to study the properties of the SFGs, we have based ourselves on the catalogue of FIR-selected objects with the spectroscopic redshift determined in the previous section. To do so, we segregated the sample in order to remove the AGNs and keep only the SFGs. Furthermore, we corrected the extinction of the spectral lines using the E(B-V) derived from the SED fittings with CIGALE. In this manner, a number of different calibrations for the determination of SFR and gas-phase metallicity were studied. The principal findings are presented below:

  - The distinction between SFGs and AGNs was made on the basis of photometric and spectroscopic criteria. Of the 409 FIR-selected objects with determined redshift, 69 were classified as AGNs, representing 17% of the initial sample. This value is slightly higher than that observed in local galaxies, where $\sim$ 11% has been obtained for SDSS and MANGA. However, this result is highly dependent on the selection criterion of the analysed sample. The sample of star-forming galaxies (SFGs) obtained exhibited a spectroscopic redshift range of $0.03 < z < 1.52$, with a mean value of $z \sim 0.6$.
  - The M_* and the SFR were analysed to investigate the MS of the SFGs. In order to gain a more comprehensive understanding, the SFR derived from the flux of the Hα, Hβ, Hγ, and [O II] lines, as well as the SFR derived from the $L_{\rm TIR}$, were also analysed. We observed that objects at low redshift ($z < 0.4$) are well represented by the MS described by

Popesso et al. (2023), exhibiting a mean shift of 0.03 dex. However, objects at higher redshifts tend to populate regions above the MS, which encompasses the regime of starburst galaxies, regardless of the SFR tracer employed and showing a median shift of ~ 0.4. It has been demonstrated that FIR-selected SFGs at $z > 0.4$ exhibit higher SFRs than would be expected for a given M_* and redshift, with shifts of up to 2 dex with respect to the MS.

- The MZR of the FIR-selected SFGs was investigated utilising the metallicity calibrations of Kobulnicky and Kewley (2004) and Tremonti et al. (2004), both of which employed R_{23} as a tracer. This study revealed that the FIR-selected SFGs exhibited lower metallicities than anticipated for their M_* and redshift, both for objects in the OSSY catalogue (low redshfit, ~ 0.1) and for Lockman-SpReSO objects (intermediate redshift, ~ 0.6).
  - A comparison of the metallicities of galaxies in the OSSY catalogue that exhibit IR information in the HELP database with those of non-IR emitting OSSY galaxies revealed that the former exhibited lower metallicities.
  - The MZR for Lockman-SpReSO galaxies, with a mean redshift of 0.6, is more closely aligned with higher redshift models, such as that of Zahid et al. (2014) for galaxies at $z \sim 1.55$, which exhibits a mean dispersion of 0.04 dex for galaxies with $M_* < 10^{10.2}\,M_\odot$. At higher masses, the range of evolution of the MZR is more limited, with the most massive galaxies achieving their current metallicity at redshfit $z \sim 1$. Nevertheless, the observed metallicity for Lockman-SpReSO galaxies is lower than expected.
- The three-dimensional relationship between M_*, SFR and metallicity of FIR-selected SFGs was investigated by applying the FP calibration that is described by Lara-López et al. (2010). The SFR derived from Hβ flux and $L_{\rm TIR}$ was studied together with the metallicity obtained from the calibration of Tremonti et al. (2004) in order to analyse the universality of the FP.
  - The SFR derived from Hβ flux revealed that both the OSSY sample and the FIR-selected SFGs are well represented by the FP, thereby supporting the non-evolution and universality of the FP. This is evidenced by the fact that the FP reproduces the behaviour of objects well, regardless of their redshift or nature. The dispersion observed was 0.2 dex, which is only slightly larger than the mean uncertainty of the M_* (0.1 dex) used as the independent variable in the calibration.

  - ∗ The FP was re-calibrated to be applied with the SFR derived from L_{TIR}, as its definition is based on the SFR derived from Hα, which analyses smaller timescales and different, but related, regions of galaxies. The obtained mean dispersion was 0.17 dex.

- Finally, in the sample of 456 objects with a determined redshift, 21 objects (three of which were classified as AGNs and retrieved from the correlation analysis) were found to have galactic flows in the redshift range $0.5 < z < 1.44$. In works such as those by Rubin et al. (2014) and Prusinski et al. (2021), relationships were found between the EW of the ultraviolet Mg II and Fe II lines and the flow velocity, with properties of the host galaxies such as the M_*, SFR, and sSFR. Therefore, measurements of these available lines were performed to check whether these relations are also valid in FIR-selected samples. Although the emission filling factor in dusty galaxies such as Lockman-SpReSO is not important, we have studied the blue lines of the Mg II $\lambda\lambda$2796, 2803, Fe II $\lambda\lambda$2374, 82, and Fe II $\lambda\lambda$2586, 2600 doublets. The correlations were studied in conjunction with the Lockman-SpReSO, Prusinski and Rubin galaxies, by 10^7 bootstrap simulations using Spearman's rank correlation coefficient.

  - The EW of the Mg II λ2796 line was found to have a strong correlation ($\rho_s = 0.43$) at a significance of 4.5σ with the M_*. With the SFR, the correlation is equally strong ($\rho_s = 0.42$) at a significance of 4.4σ. Although the properties of Lockman-SpReSO galaxies are consistent with those of Rubin or Prusinski, the EWs measured in Lockman-SpReSO objects are larger, mainly due to a bias caused by the resolution of the observations. Consequently, Lockman-SpReSO galaxies permit a more comprehensive investigation of these relationships by populating regions of parameter space that other samples do not. With respect to the line velocity, no correlations with galaxy properties were identified in the analysis of the Mg II λ2796 line.
  - The analysis of the EW of the Fe II λ2586 line revealed a strong correlation between the EW and M_* ($\rho_s = 0.43$) at a significance of 3.3σ. Similarly, SFR exhibited an even stronger correlation ($\rho_s = 0.69$) at a significance of 5.3σ. The velocity of the flow has a strong correlation ($\rho_s = 0.34$) and a high significance of 3.6σ with the SFR, while the correlation with M_* is negligible. This indicates that the Fe II λ2586 line velocity is decoupled from the M_*, but strongly depends on the SFR of the galaxy. That is, the energy with which the material is ejected from the galaxies depends more on the SFR than on the M_*.
  - One of the three objects classified as AGNs was identified as a clear candidate for the recently proposed class of "loitering outflow", a new

category of FeLoBAL quasars. These objects are distinguished by low outflow velocities ($v \lesssim 2000\,\mathrm{km\,s^{-1}}$) and high-column-density winds located at $\log R_\mathrm{d} < 1$ pc.

In conclusion, this thesis has carried out the data reduction of the Lockman-SpReSO project and has also performed the first scientific exploitation of its data. This demonstrates the quality of the project, which is one of the most comprehensive works carried out in the LH field, and shows the importance of the optical study of distant galaxies for understanding galaxy evolution.

Bibliography

Almeida, A., Anderson, S. F., Argudo-Fernández, M., Badenes, C., Barger, K., Barrera-Ballesteros, J. K., Bender, C. F., Benitez, E., Besser, F., Bird, J. C., Bizyaev, D., Blanton, M. R., Bochanski, J., Bovy, J., Brandt, W. N., Brownstein, J. R., Buchner, J., Bulbul, E., Burchett, J. N., Cano Díaz, M., Carlberg, J. K., Casey, A. R., Chandra, V., Cherinka, B., Chiappini, C., Coker, A. A., Comparat, J., Conroy, C., Contardo, G., Cortes, A., Covey, K., Crane, J. D., Cunha, K., Dabbieri, C., Davidson, J. W., Davis, M. C., de Andrade Queiroz, A. B., De Lee, N., Méndez Delgado, J. E., Demasi, S., Di Mille, F., Donor, J., Dow, P., Dwelly, T., Eracleous, M., Eriksen, J., Fan, X., Farr, E., Frederick, S., Fries, L., Frinchaboy, P., Gänsicke, B. T., Ge, J., González Ávila, C., Grabowski, K., Grier, C., Guiglion, G., Gupta, P., Hall, P., Hawkins, K., Hayes, C. R., Hermes, J. J., Hernández-García, L., Hogg, D. W., Holtzman, J. A., Ibarra-Medel, H. J., Ji, A., Jofre, P., Johnson, J. A., Jones, A. M., Kinemuchi, K., Kluge, M., Koekemoer, A., Kollmeier, J. A., Kounkel, M., Krishnarao, D., Krumpe, M., Lacerna, I., Lago, P. J. A., Laporte, C., Liu, C., Liu, A., Liu, X., Lopes, A. R., Macktoobian, M., Majewski, S. R., Malanushenko, V., Maoz, D., Masseron, T., Masters, K. L., Matijevic, G., McBride, A., Medan, I., Merloni, A., Morrison, S., Myers, N., Mészáros, S., Negrete, C. A., Nidever, D. L., Nitschelm, C., Oravetz, D., Oravetz, A., Pan, K., Peng, Y., Pinsonneault, M. H., Pogge, R., Qiu, D., Ramirez, S. V., Rix, H.-W., Fernández Rosso, D., Runnoe, J., Salvato, M., Sanchez, S. F., Santana, F. A., Saydjari, A., Sayres, C., Schlaufman, K. C., Schneider, D. P., Schwope, A., Serna, J., Shen, Y., Sobeck, J., Song, Y.-Y., Souto, D., Spoo, T., Stassun, K. G., Steinmetz, M., Straumit, I., Stringfellow, G., Sánchez-Gallego, J., Taghizadeh-Popp, M., Tayar, J., Thakar, A., Tissera, P. B., Tkachenko, A., Hernandez Toledo, H., Trakhtenbrot, B., Fernández-Trincado, J. G., Troup, N., Trump, J. R., Tuttle, S., Ulloa, N., Vazquez-Mata, J. A., Vera Alfaro, P., Villanova, S., Wachter, S., Weijmans, A.-M., Wheeler, A., Wilson, J., Wojno, L., Wolf, J., Xue, X.-X., Ybarra, J. E., Zari, E., and Zasowski, G. The Eighteenth Data Release of the Sloan Digital Sky Surveys: Targeting and First Spectra from SDSS-V. *ApJS*, 267(2):44, August 2023. doi: 10.3847/1538-4365/acda98.

Astropy Collaboration, Robitaille, T. P., Tollerud, E. J., Greenfield, P., Droettboom, M., Bray, E., Aldcroft, T., Davis, M., Ginsburg, A., Price-Whelan, A. M., Kerzendorf, W. E., Conley, A., Crighton, N., Barbary, K., Muna, D., Ferguson, H., Grollier, F., Parikh, M. M., Nair, P. H., Unther, H. M., Deil, C., Woillez, J., Conseil, S., Kramer, R., Turner, J. E. H., Singer, L., Fox, R., Weaver, B. A., Zabalza, V., Edwards, Z. I., Azalee Bostroem, K., Burke, D. J., Casey, A. R., Crawford, S. M., Dencheva, N., Ely, J., Jenness, T., Labrie, K., Lim, P. L., Pierfederici, F., Pontzen, A., Ptak, A., Refsdal, B., Servillat, M., and Streicher, O. Astropy: A community Python package for astronomy. *A&A*, 558:A33, October 2013. doi: 10.1051/0004-6361/201322068.

Baldwin, J. A., Phillips, M. M., and Terlevich, R. Classification parameters for the emission-line spectra of extragalactic objects. *PASP*, 93:5–19, February 1981. doi: 10.1086/130766.

Beckwith, S. V. W., Stiavelli, M., Koekemoer, A. M., Caldwell, J. A. R., Ferguson, H. C., Hook, R., Lucas, R. A., Bergeron, L. E., Corbin, M., Jogee, S., Panagia, N., Robberto, M., Royle, P., Somerville, R. S., and Sosey, M. The Hubble Ultra Deep Field. *AJ*, 132(5):1729–1755, November 2006. doi: 10.1086/507302.

Bongiovanni, Á., Ramón-Pérez, M., Pérez García, A. M., Cepa, J., Cerviño, M., Nadolny, J., Pérez Martínez, R., Alfaro, E., Castañeda, H. O., de Diego, J. A., Ederoclite, A., Fernández-Lorenzo, M., Gallego, J., González, J. J., González-Serrano, J. I., Lara-López, M. A., Oteo Gómez, I., Padilla Torres, C. P., Pintos-Castro, I., Pović, M., Sánchez-Portal, M., Jones, H., Bland-Hawthorn, J., and Cabrera-Lavers, A. The OTELO survey. I. Description, data reduction, and multi-wavelength catalogue. *A&A*, 631:A9, November 2019. doi: 10.1051/0004-6361/201833294.

Bonnarel, F., Fernique, P., Bienaymé, O., Egret, D., Genova, F., Louys, M., Ochsenbein, F., Wenger, M., and Bartlett, J. G. The ALADIN interactive sky atlas. A reference tool for identification of astronomical sources. *A&AS*, 143:33–40, April 2000. doi: 10.1051/aas:2000331.

Brinchmann, J., Charlot, S., White, S. D. M., Tremonti, C., Kauffmann, G., Heckman, T., and Brinkmann, J. The physical properties of star-forming galaxies in the low-redshift Universe. *MNRAS*, 351(4):1151–1179, July 2004. doi: 10.1111/j.1365-2966.2004.07881.x.

Bruzual, G. and Charlot, S. Stellar population synthesis at the resolution of 2003. *MNRAS*, 344(4):1000–1028, October 2003. doi: 10.1046/j.1365-8711.2003.06897.x.

Calzetti, D., Kinney, A. L., and Storchi-Bergmann, T. Dust Extinction of the Stellar Continua in Starburst Galaxies: The Ultraviolet and Optical Extinction Law. ApJ, 429:582, July 1994. doi: 10.1086/174346.

Calzetti, D., Armus, L., Bohlin, R. C., Kinney, A. L., Koornneef, J., and Storchi-Bergmann, T. The Dust Content and Opacity of Actively Star-forming Galaxies. ApJ, 533(2):682–695, April 2000. doi: 10.1086/308692.

Cannon, A. J. and Pickering, E. C. The Henry Draper catalogue 0h, 1h, 2h, and 3h. *Annals of Harvard College Observatory*, 91:1–290, January 1918.

Cannon, A. J. and Pickering, E. C. The Henry Draper catalogue : 21h, 22h, and 23h. *Annals of Harvard College Observatory*, 99:1, January 1924.

Cedrés, B., Pérez-García, A. M., Pérez-Martínez, R., Cerviño, M., Gallego, J., Bongiovanni, Á., Cepa, J., Navarro Martínez, R., Nadolny, J., Lara-López, M. A., Sánchez-Portal, M., Alfaro, E. J., de Diego, J. A., González-Otero, M., Jesús González, J., Ignacio González-Serrano, J., and Padilla Torres, C. P. The OTELO Survey: The Star Formation Rate Evolution of Low-mass Galaxies. *ApJL*, 915(1): L17, July 2021. doi: 10.3847/2041-8213/ac0a7e.

Cedrés, B., De Daniloff, S. B., Bongiovanni, Á., Sánchez-Portal, M., Cerviño, M., Pérez-Martínez, R., María Pérez-García, A., Cepa, J., Lara-López, M. A., González-Otero, M., Castillo-Fraile, M., González-Serrano, J. I., Negrete, C. A., Padilla-Torres, C. P., Pintos-Castro, I., Povic, M., Alfaro1, E., Beyoro-Amado, Z., Cruz-González, I., de Diego, J. A., Navarro Martínez, R., Mancillas, B., Rodríguez, M. I., and Valtchanov, I. GLACE survey: OSIRIS/GTC tuneable imaging of the galaxy cluster ZwCl 0024.0+1652 II. The mass–metallicity relationship and the effect of the environment. *A&A*, art. arXiv:2403.11629, March 2024. doi: 10.1051/0004-6361/202449143.

Cepa, J., Aguiar, M., Escalera, V. G., Gonzalez-Serrano, I., Joven-Alvarez, E., Peraza, L., Rasilla, J. L., Rodriguez-Ramos, L. F., Gonzalez, J. J., Cobos Duenas, F. J., Sanchez, B., Tejada, C., Bland-Hawthorn, J., Militello, C., and Rosa, F. OSIRIS tunable imager and spectrograph. In Iye, M. and Moorwood, A. F., editors, *Optical and IR Telescope Instrumentation and Detectors*, volume 4008 of *Proc. SPIE*, pages 623–631, August 2000. doi: 10.1117/12.395520.

Cepa, J. *The Emission-Line Universe*. Canary Islands Winter School of Astrophysics. 2008. doi: 10.1017/CBO9780511552038.

Cid Fernandes, R., Stasińska, G., Schlickmann, M. S., Mateus, A., Vale Asari, N., Schoenell, W., and Sodré, L. Alternative diagnostic diagrams and the 'forgotten'

population of weak line galaxies in the SDSS. *MNRAS*, 403(2):1036–1053, April 2010. doi: 10.1111/j.1365-2966.2009.16185.x.

Colless, M., Dalton, G., Maddox, S., Sutherland, W., Norberg, P., Cole, S., Bland-Hawthorn, J., Bridges, T., Cannon, R., Collins, C., Couch, W., Cross, N., Deeley, K., De Propris, R., Driver, S. P., Efstathiou, G., Ellis, R. S., Frenk, C. S., Glazebrook, K., Jackson, C., Lahav, O., Lewis, I., Lumsden, S., Madgwick, D., Peacock, J. A., Peterson, B. A., Price, I., Seaborne, M., and Taylor, K. The 2dF Galaxy Redshift Survey: spectra and redshifts. *MNRAS*, 328(4):1039–1063, December 2001. doi: 10.1046/j.1365-8711.2001.04902.x.

Cresci, G., Mannucci, F., and Curti, M. Fundamental metallicity relation in CALIFA, SDSS-IV MaNGA, and high-z galaxies. *A&A*, 627:A42, July 2019. doi: 10.1051/0004-6361/201834637.

Curti, M., Maiolino, R., Curtis-Lake, E., Chevallard, J., Carniani, S., D'Eugenio, F., Looser, T. J., Scholtz, J., Charlot, S., Cameron, A., Übler, H., Witstok, J., Boyett, K., Laseter, I., Sandles, L., Arribas, S., Bunker, A., Giardino, G., Maseda, M. V., Rawle, T., Rodríguez Del Pino, B., Smit, R., Willott, C. J., Eisenstein, D. J., Hausen, R., Johnson, B., Rieke, M., Robertson, B., Tacchella, S., Williams, C. C., Willmer, C., Baker, W. M., Bhatawdekar, R., Egami, E., Helton, J. M., Ji, Z., Kumari, N., Perna, M., Shivaei, I., and Sun, F. JADES: Insights into the low-mass end of the mass-metallicity-SFR relation at $3 < z < 10$ from deep JWST/NIRSpec spectroscopy. *A&A*, 684:A75, April 2024. doi: 10.1051/0004-6361/202346698.

de Diego, J. A., Nadolny, J., Bongiovanni, Á., Cepa, J., Lara-López, M. A., Gallego, J., Cerviño, M., Sánchez-Portal, M., Ignacio González-Serrano, J., Alfaro, E. J., Pović, M., Pérez García, A. M., Pérez Martínez, R., Padilla Torres, C. P., Cedrés, B., García-Aguilar, D., González, J. J., González-Otero, M., Navarro-Martínez, R., and Pintos-Castro, I. Nonsequential neural network for simultaneous, consistent classification, and photometric redshifts of OTELO galaxies. *A&A*, 655:A56, November 2021. doi: 10.1051/0004-6361/202141360.

de Diego, J. A., Nadolny, J., Bongiovanni, Á., Cepa, J., Pović, M., Pérez García, A. M., Padilla Torres, C. P., Lara-López, M. A., Cerviño, M., Pérez Martínez, R., Alfaro, E. J., Castañeda, H. O., Fernández-Lorenzo, M., Gallego, J., González, J. J., González-Serrano, J. I., Pintos-Castro, I., Sánchez-Portal, M., Cedrés, B., González-Otero, M., Heath Jones, D., and Bland-Hawthorn, J. Galaxy classification: deep learning on the OTELO and COSMOS databases. *A&A*, 638:A134, June 2020. doi: 10.1051/0004-6361/202037697.

de Sitter, W. Einstein's theory of gravitation and its astronomical consequences. Third paper. *MNRAS*, 78:3–28, November 1917. doi: 10.1093/mnras/78.1.3.

Dickey, J. M. and Lockman, F. J. H I in the galaxy. *ARA&A*, 28:215–261, January 1990. doi: 10.1146/annurev.aa.28.090190.001243.

Djorgovski, S. G., Mahabal, A., Drake, A., Graham, M., and Donalek, C. Sky Surveys. In Oswalt, T. D. and Bond, H. E., editors, *Planets, Stars and Stellar Systems. Volume 2: Astronomical Techniques, Software and Data*, page 223. 2013. doi: 10.1007/978-94-007-5618-2_5.

Dopita, M. A., Kewley, L. J., Sutherland, R. S., and Nicholls, D. C. Chemical abundances in high-redshift galaxies: a powerful new emission line diagnostic. *A&SS*, 361:61, February 2016. doi: 10.1007/s10509-016-2657-8.

Dreyer, J. L. E. A New General Catalogue of Nebulæ and Clusters of Stars, being the Catalogue of the late Sir John F. W. Herschel, Bart, revised, corrected, and enlarged. *MmRAS*, 49:1, January 1888.

Edge, D. O., Shakeshaft, J. R., McAdam, W. B., Baldwin, J. E., and Archer, S. A survey of radio sources at a frequency of 159 Mc/s. *MmRAS*, 68:37–60, January 1959.

Einstein, A. and de Sitter, W. On the Relation between the Expansion and the Mean Density of the Universe. *Proceedings of the National Academy of Science*, 18(3): 213–214, March 1932. doi: 10.1073/pnas.18.3.213.

Einstein, A. Kosmologische Betrachtungen zur allgemeinen Relativitätstheorie. *Sitzungsberichte der Königlich Preussischen Akademie der Wissenschaften*, pages 142–152, January 1917.

Ellison, S. L., Patton, D. R., Simard, L., and McConnachie, A. W. Clues to the Origin of the Mass-Metallicity Relation: Dependence on Star Formation Rate and Galaxy Size. *ApJL*, 672(2):L107, January 2008. doi: 10.1086/527296.

Ferland, G. J., Korista, K. T., Verner, D. A., Ferguson, J. W., Kingdon, J. B., and Verner, E. M. CLOUDY 90: Numerical Simulation of Plasmas and Their Spectra. *PASP*, 110(749):761–778, July 1998. doi: 10.1086/316190.

Figueira, M., Pollo, A., Ma lek, K., Buat, V., Boquien, M., Pistis, F., Cassarà, L. P., Vergani, D., Hamed, M., and Salim, S. SFR estimations from z = 0 to z = 0.9. A comparison of SFR calibrators for star-forming galaxies. *A&A*, 667:A29, November 2022. doi: 10.1051/0004-6361/202141701.

Fotopoulou, S., Salvato, M., Hasinger, G., Rovilos, E., Brusa, M., Egami, E., Lutz, D., Burwitz, V., Henry, J. P., Huang, J. H., Rigopoulou, D., and Vaccari, M. Photometry and Photometric Redshift Catalogs for the Lockman Hole Deep Field. *ApJS*, 198(1):1, January 2012. doi: 10.1088/0067-0049/198/1/1.

Garnett, D. R. The Luminosity-Metallicity Relation, Effective Yields, and Metal Loss in Spiral and Irregular Galaxies. ApJ, 581(2):1019–1031, December 2002. doi: 10.1086/344301.

Gavazzi, G. and Scodeggio, M. The mass dependence of the star formation history of disk galaxies. *A&A*, 312:L29–L32, August 1996.

Gonzalez-Otero, M., Padilla-Torres, C. P., Cepa, J., de Jesús González, J., Bongiovanni, Á., Pérez García, A. M., González-Serrano, J. I., Alfaro, E., Avila-Reese, V., Benítez, E., Binette, L., Cerviño, M., Cruz-González, I., de Diego, J. A., Gallego, J., Hernández-Toledo, H., Krongold, Y., Lara-López, M. A., Nadolny, J., Pérez-Martínez, R., Pović, M., Sánchez-Portal, M., Cedrés, B., Dultzin, D., Jiménez-Bailón, E., Navarro Martínez, R., Negrete, C. A., Pintos-Castro, I., and Valenzuela, O. The Lockman-SpReSO project. Description, target selection, observations, and catalogue preparation. *A&A*, 669:A85, January 2023. doi: 10.1051/0004-6361/202244480.

González-Otero, M., Cepa, J., Padilla-Torres, C. P., Lara-López, M. A., Jesús González, J., Bongiovanni, Á., Cedrés, B., Cerviño, M., Cruz-González, I., Elías-Chávez, M., Herrera-Edoqui, M., Ibarra-Medel, H. J., Krongold, Y., Nadolny, J., Negrete, C. A., María Pérez García, A., De Diego, J. A., González-Serrano, J. I., Hernández-Toledo, H., Pérez-Martínez, R., and Sánchez-Portal, M. The Lockman–SpReSO project. Main properties of infrared selected star-forming galaxies. *arXiv e-prints*, art. arXiv:2404.13629, April 2024a. doi: 10.48550/arXiv.2404.13629.

González-Otero, M., Padilla-Torres, C. P., González-Serrano, J. I., Cepa, J., María Pérez García, A., Jesús González, J., Benítez, E., Bongiovanni, Á., Cerviño, M., Cruz-González, I., Gallego, J., Herrera-Endoqui, M., Ibarra-Medel, H. J., Krongold, Y., Lara-López, M. A., Nadolny, J., Alenka Negrete, C., Pérez-Martínez, R., Pović, M., Sánchez-Portal, M., Cedrés, B., de Diego, J. A., Hernández-Toledo, H., and Navarro Martínez, R. The Lockman-SpReSO project. Galactic flows in a sample of far-infrared galaxies. *A&A*, 684:A31, April 2024b. doi: 10.1051/0004-6361/202347826.

Hamel-Bravo, M. J., Fisher, D. B., Berg, D., Björgvinsson, B., Bolatto, A. D., Cameron, A. J., Chisholm, J., Fielding, D. B., Herrera-Camus, R., Kacprzak, G. G., Li, M., Ciraulo, B. M., McLeod, A. F., McPherson, D. K., Nielsen, N. M., Reichardt Chu, B., Vaught, R. J. R., and Sandstrom, K. DUVET: Resolved direct metallicity measurements in the outflow of starburst galaxy NGC 1569. *MNRAS*, April 2024. doi: 10.1093/mnras/stae983.

Harris, C. R., Millman, K. J., van der Walt, S. J., Gommers, R., Virtanen, P., Cournapeau, D., Wieser, E., Taylor, J., Berg, S., Smith, N. J., Kern, R., Picus, M.,

Hoyer, S., van Kerkwijk, M. H., Brett, M., Haldane, A., del Río, J. F., Wiebe, M., Peterson, P., Gérard-Marchant, P., Sheppard, K., Reddy, T., Weckesser, W., Abbasi, H., Gohlke, C., and Oliphant, T. E. Array programming with NumPy. *Nature*, 585 (7825):357–362, September 2020. doi: 10.1038/s41586-020-2649-2.

Herschel, J. F. W. A General Catalogue of Nebulae and Clusters of Stars. *Philosophical Transactions of the Royal Society of London Series I*, 154:1–137, January 1864.

Herschel, W. Catalogue of One Thousand New Nebulae and Clusters of Stars. By William Herschel, LL.D. F. R. S. *Philosophical Transactions of the Royal Society of London Series I*, 76:457–499, January 1786.

Huang, C., Zou, H., Kong, X., Comparat, J., Lin, Z., Gao, Y., Liang, Z., Delubac, T., Raichoor, A., Kneib, J.-P., Schneider, D. P., Zhou, X., Yuan, Q., and Bershady, M. A. The Mass-Metallicity Relation at z $\sim$ 0.8: Redshift Evolution and Parameter Dependency. ApJ, 886(1):31, November 2019. doi: 10.3847/1538-4357/ab4902.

Hubble, E. P. Cepheids in Spiral Nebulae. *Popular Astronomy*, 33:252–255, January 1925a.

Hubble, E. P. NGC 6822, a remote stellar system. ApJ, 62:409–433, December 1925b. doi: 10.1086/142943.

Hubble, E. P. Extragalactic nebulae. ApJ, 64:321–369, December 1926. doi: 10.1086/143018.

Hubble, E. P. *Realm of the Nebulae*. 1936.

Hubble, E. A Relation between Distance and Radial Velocity among Extra-Galactic Nebulae. *Proceedings of the National Academy of Science*, 15(3):168–173, March 1929. doi: 10.1073/pnas.15.3.168.

Hunter, J. D. Matplotlib: A 2d graphics environment. *Computing in Science & Engineering*, 9(3):90–95, 2007. doi: 10.1109/MCSE.2007.55.

Ibrahim, D. and Kobayashi, C. The impact of supernova feedback on the mass-metallicity relations. *MNRAS*, 527(2):3276–3290, January 2024. doi: 10.1093/mnras/stad3313.

Kauffmann, G., Heckman, T. M., Tremonti, C., Brinchmann, J., Charlot, S., White, S. D. M., Ridgway, S. E., Brinkmann, J., Fukugita, M., Hall, P. B., Ivezić, Ž., Richards, G. T., and Schneider, D. P. The host galaxies of active galactic nuclei. *MNRAS*, 346(4):1055–1077, December 2003. doi: 10.1111/j.1365-2966.2003.07154.x.

Kennicutt, J., R. C. The rate of star formation in normal disk galaxies. ApJ, 272: 54–67, September 1983. doi: 10.1086/161261.

Kennicutt, J., Robert C. Star Formation in Galaxies Along the Hubble Sequence. *ARA&A*, 36:189–232, January 1998. doi: 10.1146/annurev.astro.36.1.189.

Kennicutt, J., Robert C., Tamblyn, P., and Congdon, C. E. Past and Future Star Formation in Disk Galaxies. ApJ, 435:22, November 1994. doi: 10.1086/174790.

Kennicutt, R. C. and Evans, N. J. Star Formation in the Milky Way and Nearby Galaxies. *ARA&A*, 50:531–608, September 2012. doi: 10.1146/annurev-astro-081811-125610.

Kewley, L. J., Dopita, M. A., Sutherland, R. S., Heisler, C. A., and Trevena, J. Theoretical Modeling of Starburst Galaxies. ApJ, 556(1):121–140, July 2001. doi: 10.1086/321545.

Kewley, L. J. and Ellison, S. L. Metallicity Calibrations and the Mass-Metallicity Relation for Star-forming Galaxies. ApJ, 681(2):1183–1204, July 2008. doi: 10.1086/587500.

Kewley, L. J., Maier, C., Yabe, K., Ohta, K., Akiyama, M., Dopita, M. A., and Yuan, T. The Cosmic BPT Diagram: Confronting Theory with Observations. *ApJL*, 774 (1):L10, September 2013. doi: 10.1088/2041-8205/774/1/L10.

Kobulnicky, H. A. and Kewley, L. J. Metallicities of 0.3¡z¡1.0 Galaxies in the GOODS-North Field. ApJ, 617(1):240–261, December 2004. doi: 10.1086/425299.

Kondapally, R., Best, P. N., Hardcastle, M. J., Nisbet, D., Bonato, M., Sabater, J., Duncan, K. J., McCheyne, I., Cochrane, R. K., Bowler, R. A. A., Williams, W. L., Shimwell, T. W., Tasse, C., Croston, J. H., Goyal, A., Jamrozy, M., Jarvis, M. J., Mahatma, V. H., Röttgering, H. J. A., Smith, D. J. B., Wo lowska, A., Bondi, M., Brienza, M., Brown, M. J. I., Brüggen, M., Chambers, K., Garrett, M. A., Gürkan, G., Huber, M., Kunert-Bajraszewska, M., Magnier, E., Mingo, B., Mostert, R., Nikiel-Wroczyński, B., O'Sullivan, S. P., Paladino, R., Ploeckinger, T., Prandoni, I., Rosenthal, M. J., Schwarz, D. J., Shulevski, A., Wagenveld, J. D., and Wang, L. The LOFAR Two-meter Sky Survey: Deep Fields Data Release 1. III. Host-galaxy identifications and value added catalogues. *A&A*, 648:A3, April 2021. doi: 10.1051/0004-6361/202038813.

Lamareille, F. Spectral classification of emission-line galaxies from the Sloan Digital Sky Survey. I. An improved classification for high-redshift galaxies. *A&A*, 509: A53, January 2010. doi: 10.1051/0004-6361/200913168.

Lamareille, F., Mouhcine, M., Contini, T., Lewis, I., and Maddox, S. The luminosity-metallicity relation in the local Universe from the 2dF Galaxy Redshift Survey. *MNRAS*, 350(2):396–406, May 2004. doi: 10.1111/j.1365-2966.2004.07697.x.

Lara-López, M. A., Cepa, J., Bongiovanni, A., Pérez García, A. M., Ederoclite, A., Castañeda, H., Fernández Lorenzo, M., Pović, M., and Sánchez-Portal, M. A fundamental plane for field star-forming galaxies. *A&A*, 521:L53, October 2010. doi: 10.1051/0004-6361/201014803.

Lee, H., Skillman, E. D., Cannon, J. M., Jackson, D. C., Gehrz, R. D., Polomski, E. F., and Woodward, C. E. On Extending the Mass-Metallicity Relation of Galaxies by 2.5 Decades in Stellar Mass. ApJ, 647(2):970–983, August 2006. doi: 10.1086/505573.

Lemaître, G. Un Univers homogène de masse constante et de rayon croissant rendant compte de la vitesse radiale des nébuleuses extra-galactiques. *Annales de la Société Scientifique de Bruxelles*, 47:49–59, January 1927.

Lequeux, J., Peimbert, M., Rayo, J. F., Serrano, A., and Torres-Peimbert, S. Chemical Composition and Evolution of Irregular and Blue Compact Galaxies. *A&A*, 80: 155, December 1979.

Lockman, F. J., Jahoda, K., and McCammon, D. The Structure of Galactic H i in Directions of Low Total Column Density. ApJ, 302:432, March 1986. doi: 10.1086/164002.

Lutz, D., Poglitsch, A., Altieri, B., Andreani, P., Aussel, H., Berta, S., Bongiovanni, A., Brisbin, D., Cava, A., Cepa, J., Cimatti, A., Daddi, E., Dominguez-Sanchez, H., Elbaz, D., Förster Schreiber, N. M., Genzel, R., Grazian, A., Gruppioni, C., Harwit, M., Le Floc'h, E., Magdis, G., Magnelli, B., Maiolino, R., Nordon, R., Pérez García, A. M., Popesso, P., Pozzi, F., Riguccini, L., Rodighiero, G., Saintonge, A., Sanchez Portal, M., Santini, P., Shao, L., Sturm, E., Tacconi, L. J., Valtchanov, I., Wetzstein, M., and Wieprecht, E. PACS Evolutionary Probe (PEP) - A Herschel key program. *A&A*, 532:A90, August 2011. doi: 10.1051/0004-6361/201117107.

Mannucci, F., Cresci, G., Maiolino, R., Marconi, A., and Gnerucci, A. A fundamental relation between mass, star formation rate and metallicity in local and high-redshift galaxies. *MNRAS*, 408(4):2115–2127, November 2010. doi: 10.1111/j.1365-2966.2010.17291.x.

Matsuoka, K., Nagao, T., Maiolino, R., Marconi, A., and Taniguchi, Y. Chemical evolution of high-redshift radio galaxies. *A&A*, 503(3):721–730, September 2009. doi: 10.1051/0004-6361/200811478.

Matsuoka, K., Nagao, T., Marconi, A., Maiolino, R., Mannucci, F., Cresci, G., Terao, K., and Ikeda, H. The mass-metallicity relation of high-z type-2 active galactic nuclei. *A&A*, 616:L4, August 2018. doi: 10.1051/0004-6361/201833418.

Messier, C. Catalogue des Nébuleuses et des Amas d'Étoiles (Catalog of Nebulae and Star Clusters). Connoissance des Temps ou des Mouvements Célestes, for 1784, p. 227-267, January 1781.

Navarro Martínez, R., Pérez-García, A. M., Pérez-Martínez, R., Cerviño, M., Gallego, J., Bongiovanni, Á., Barrufet, L., Nadolny, J., Cedrés, B., Cepa, J., Alfaro, E., Castañeda, H. O., de Diego, J. A., González-Otero, M., Jesús González, J., González-Serrano, J. I., Lara-López, M. A., Padilla Torres, C. P., and Sánchez-Portal, M. The OTELO survey. Revealing a population of low-luminosity active star-forming galaxies at z $\sim$ 0.9. *A&A*, 653:A24, September 2021. doi: 10.1051/0004-6361/202140353.

Newville, M., Stensitzki, T., Allen, D. B., and Ingargiola, A. LMFIT: Non-Linear Least-Square Minimization and Curve-Fitting for Python, September 2014.

Osterbrock, D. E. *Astrophysics of gaseous nebulae and active galactic nuclei*. 1989.

Pettini, M. and Pagel, B. E. J. [OIII]/[NII] as an abundance indicator at high redshift. *MNRAS*, 348(3):L59–L63, March 2004. doi: 10.1111/j.1365-2966.2004.07591.x.

Pickering, E. C. The Draper Catalogue of stellar spectra photographed with the 8-inch Bache telescope as a part of the Henry Draper memorial. *Annals of Harvard College Observatory*, 27:1–388, January 1890.

Pilyugin, L. S. and Grebel, E. K. New calibrations for abundance determinations in H II regions. *MNRAS*, 457(4):3678–3692, April 2016. doi: 10.1093/mnras/stw238.

Pilyugin, L. S., Vílchez, J. M., and Contini, T. Oxygen and nitrogen abundances in nearby galaxies. Correlations between oxygen abundance and macroscopic properties. *A&A*, 425:849–869, October 2004. doi: 10.1051/0004-6361:20034522.

Pilyugin, L. S., Cedrés, B., Zinchenko, I. A., Pérez Garcia, A. M., Lara-López, M. A., Nadolny, J., Nefedyev, Y. A., González-Otero, M., Vílchez, J. M., Duarte Puertas, S., and Navarro Martinez, R. MaNGA galaxies with off-centered spots of enhanced gas velocity dispersion. *A&A*, 653:A11, September 2021. doi: 10.1051/0004-6361/202141012.

Pistis, F., Pollo, A., Scodeggio, M., Figueira, M., Durkalec, A., Ma lek, K., Iovino, A., Vergani, D., and Salim, S. The fundamental metallicity relation from SDSS (z $\sim$ 0) to VIPERS (z $\sim$ 0.7). Data selection or evolution. *A&A*, 663:A162, July 2022. doi: 10.1051/0004-6361/202142430.

Popesso, P., Concas, A., Cresci, G., Belli, S., Rodighiero, G., Inami, H., Dickinson, M., Ilbert, O., Pannella, M., and Elbaz, D. The main sequence of star-forming galaxies across cosmic times. *MNRAS*, 519(1):1526–1544, February 2023. doi: 10.1093/mnras/stac3214.

Prusinski, N. Z., Erb, D. K., and Martin, C. L. Connecting Galactic Outflows and Star Formation: Inferences from Hα Maps and Absorption-line Spectroscopy at 1 $\lesssim$ z $\lesssim$ 1.5. *AJ*, 161(5):212, May 2021. doi: 10.3847/1538-3881/abe85b.

Rubin, K. H. R., Prochaska, J. X., Koo, D. C., Phillips, A. C., Martin, C. L., and Winstrom, L. O. Evidence for Ubiquitous Collimated Galactic-scale Outflows along the Star-forming Sequence at z ~0.5. ApJ, 794(2):156, October 2014. doi: 10.1088/0004-637X/794/2/156.

Ryle, M., Smith, F. G., and Elsmore, B. A preliminary survey of the radio stars in the Northern Hemisphere. *MNRAS*, 110:508, January 1950. doi: 10.1093/mnras/110.6.508.

Sanders, R. L., Shapley, A. E., Jones, T., Reddy, N. A., Kriek, M., Siana, B., Coil, A. L., Mobasher, B., Shivaei, I., Davé, R., Azadi, M., Price, S. H., Leung, G., Freeman, W. R., Fetherolf, T., de Groot, L., Zick, T., and Barro, G. The MOSDEF Survey: The Evolution of the Mass-Metallicity Relation from z = 0 to z 3.3. ApJ, 914(1):19, June 2021. doi: 10.3847/1538-4357/abf4c1.

Skrutskie, M. F., Cutri, R. M., Stiening, R., Weinberg, M. D., Schneider, S., Carpenter, J. M., Beichman, C., Capps, R., Chester, T., Elias, J., Huchra, J., Liebert, J., Lonsdale, C., Monet, D. G., Price, S., Seitzer, P., Jarrett, T., Kirkpatrick, J. D., Gizis, J. E., Howard, E., Evans, T., Fowler, J., Fullmer, L., Hurt, R., Light, R., Kopan, E. L., Marsh, K. A., McCallon, H. L., Tam, R., Van Dyk, S., and Wheelock, S. The Two Micron All Sky Survey (2MASS). *AJ*, 131(2):1163–1183, February 2006. doi: 10.1086/498708.

Smith, R. W. Beyond the Galaxy: the development of extragalactic astronomy 1885 - 1965 Part 1. *Journal for the History of Astronomy*, 39(134):91–119, February 2008. doi: 10.1177/002182860803900106.

Smith, R. W. Beyond the Galaxy: The Development of Extragalactic Astronomy 1885-1965: Part 2. *Journal for the History of Astronomy*, 40:71–107, January 2009. doi: 10.1177/002182860904000106.

Smithsonian Astrophysical Observatory. SAOImage DS9: A utility for displaying astronomical images in the X11 window environment. Astrophysics Source Code Library, record ascl:0003.002, March 2000.

Speagle, J. S., Steinhardt, C. L., Capak, P. L., and Silverman, J. D. A Highly Consistent Framework for the Evolution of the Star-Forming "Main Sequence" from z ~0-6. *ApJS*, 214(2):15, October 2014. doi: 10.1088/0067-0049/214/2/15.

Spitoni, E., Calura, F., Mignoli, M., Gilli, R., Silva Aguirre, V., and Gallazzi, A. Connection between galactic downsizing and the most fundamental galactic scaling relations. *A&A*, 642:A113, October 2020. doi: 10.1051/0004-6361/202037879.

Stasińska, G., Cid Fernandes, R., Mateus, A., Sodré, L., and Asari, N. V. Semi-empirical analysis of Sloan Digital Sky Survey galaxies - III. How to distinguish AGN hosts. *MNRAS*, 371(2):972–982, September 2006. doi: 10.1111/j.1365-2966.2006.10732.x.

Stromberg, G. Analysis of radial velocities of globular clusters and non-galactic nebulae. ApJ, 61:353–362, June 1925. doi: 10.1086/142897.

Taylor, M. TOPCAT: Tool for OPerations on Catalogues And Tables. Astrophysics Source Code Library, record ascl:1101.010, January 2011.

The pandas development Team. pandas-dev/pandas: Pandas, April 2024.

Thomas, A. D., Kewley, L. J., Dopita, M. A., Groves, B. A., Hopkins, A. M., and Sutherland, R. S. The Mass-Metallicity Relation of Local Active Galaxies. ApJ, 874(1):100, March 2019. doi: 10.3847/1538-4357/ab08a1.

Tody, D. The IRAF Data Reduction and Analysis System. In Crawford, D. L., editor, *Instrumentation in astronomy VI*, volume 627 of *Society of Photo-Optical Instrumentation Engineers (SPIE) Conference Series*, page 733, January 1986. doi: 10.1117/12.968154.

Tremonti, C. A., Heckman, T. M., Kauffmann, G., Brinchmann, J., Charlot, S., White, S. D. M., Seibert, M., Peng, E. W., Schlegel, D. J., Uomoto, A., Fukugita, M., and Brinkmann, J. The Origin of the Mass-Metallicity Relation: Insights from 53,000 Star-forming Galaxies in the Sloan Digital Sky Survey. ApJ, 613(2):898–913, October 2004. doi: 10.1086/423264.

Veilleux, S. and Osterbrock, D. E. Spectral Classification of Emission-Line Galaxies. *ApJS*, 63:295, February 1987. doi: 10.1086/191166.

Virtanen, P., Gommers, R., Oliphant, T. E., Haberland, M., Reddy, T., Cournapeau, D., Burovski, E., Peterson, P., Weckesser, W., Bright, J., van der Walt, S. J., Brett, M., Wilson, J., Millman, K. J., Mayorov, N., Nelson, A. R. J., Jones, E., Kern, R., Larson, E., Carey, C. J., Polat, İ., Feng, Y., Moore, E. W., VanderPlas, J., Laxalde, D., Perktold, J., Cimrman, R., Henriksen, I., Quintero, E. A., Harris,

C. R., Archibald, A. M., Ribeiro, A. H., Pedregosa, F., van Mulbregt, P., and SciPy 1.0 Contributors. SciPy 1.0: Fundamental Algorithms for Scientific Computing in Python. *Nature Methods*, 17:261–272, 2020. doi: 10.1038/s41592-019-0686-2.

Waskom, M., Botvinnik, O., O'Kane, D., Hobson, P., Lukauskas, S., Gemperline, D. C., Augspurger, T., Halchenko, Y., Cole, J. B., Warmenhoven, J., de Ruiter, J., Pye, C., Hoyer, S., Vanderplas, J., Villalba, S., Kunter, G., Quintero, E., Bachant, P., Martin, M., Meyer, K., Miles, A., Ram, Y., Yarkoni, T., Williams, M. L., Evans, C., Fitzgerald, C., Brian, Fonnesbeck, C., Lee, A., and Qalieh, A. mwaskom/seaborn: v0.8.1 (september 2017), September 2017.

Wright, E. L. A Cosmology Calculator for the World Wide Web. *PASP*, 118(850): 1711–1715, December 2006. doi: 10.1086/510102.

York, D. G., Adelman, J., Anderson, J., John E., Anderson, S. F., Annis, J., Bahcall, N. A., Bakken, J. A., Barkhouser, R., Bastian, S., Berman, E., Boroski, W. N., Bracker, S., Briegel, C., Briggs, J. W., Brinkmann, J., Brunner, R., Burles, S., Carey, L., Carr, M. A., Castander, F. J., Chen, B., Colestock, P. L., Connolly, A. J., Crocker, J. H., Csabai, I., Czarapata, P. C., Davis, J. E., Doi, M., Dombeck, T., Eisenstein, D., Ellman, N., Elms, B. R., Evans, M. L., Fan, X., Federwitz, G. R., Fiscelli, L., Friedman, S., Frieman, J. A., Fukugita, M., Gillespie, B., Gunn, J. E., Gurbani, V. K., de Haas, E., Haldeman, M., Harris, F. H., Hayes, J., Heckman, T. M., Hennessy, G. S., Hindsley, R. B., Holm, S., Holmgren, D. J., Huang, C.-h., Hull, C., Husby, D., Ichikawa, S.-I., Ichikawa, T., Ivezić, Ž., Kent, S., Kim, R. S. J., Kinney, E., Klaene, M., Kleinman, A. N., Kleinman, S., Knapp, G. R., Korienek, J., Kron, R. G., Kunszt, P. Z., Lamb, D. Q., Lee, B., Leger, R. F., Limmongkol, S., Lindenmeyer, C., Long, D. C., Loomis, C., Loveday, J., Lucinio, R., Lupton, R. H., MacKinnon, B., Mannery, E. J., Mantsch, P. M., Margon, B., McGehee, P., McKay, T. A., Meiksin, A., Merelli, A., Monet, D. G., Munn, J. A., Narayanan, V. K., Nash, T., Neilsen, E., Neswold, R., Newberg, H. J., Nichol, R. C., Nicinski, T., Nonino, M., Okada, N., Okamura, S., Ostriker, J. P., Owen, R., Pauls, A. G., Peoples, J., Peterson, R. L., Petravick, D., Pier, J. R., Pope, A., Pordes, R., Prosapio, A., Rechenmacher, R., Quinn, T. R., Richards, G. T., Richmond, M. W., Rivetta, C. H., Rockosi, C. M., Ruthmansdorfer, K., Sandford, D., Schlegel, D. J., Schneider, D. P., Sekiguchi, M., Sergey, G., Shimasaku, K., Siegmund, W. A., Smee, S., Smith, J. A., Snedden, S., Stone, R., Stoughton, C., Strauss, M. A., Stubbs, C., SubbaRao, M., Szalay, A. S., Szapudi, I., Szokoly, G. P., Thakar, A. R., Tremonti, C., Tucker, D. L., Uomoto, A., Vanden Berk, D., Vogeley, M. S., Waddell, P., Wang, S.-i., Watanabe, M., Weinberg, D. H., Yanny, B., Yasuda, N., and SDSS Collaboration. The Sloan Digital Sky Survey: Technical Summary. *AJ*, 120(3): 1579–1587, September 2000. doi: 10.1086/301513.

Zahid, H. J., Kashino, D., Silverman, J. D., Kewley, L. J., Daddi, E., Renzini, A., Rodighiero, G., Nagao, T., Arimoto, N., Sanders, D. B., Kartaltepe, J., Lilly, S. J., Maier, C., Geller, M. J., Capak, P., Carollo, C. M., Chu, J., Hasinger, G., Ilbert, O., Kajisawa, M., Koekemoer, A. M., Kovacs, K., Le Fèvre, O., Masters, D., McCracken, H. J., Onodera, M., Scoville, N., Strazzullo, V., Sugiyama, N., Taniguchi, Y., and COSMOS Team. The FMOS-COSMOS Survey of Star-forming Galaxies at z ~1.6. II. The Mass-Metallicity Relation and the Dependence on Star Formation Rate and Dust Extinction. ApJ, 792(1):75, September 2014. doi: 10.1088/0004-637X/792/1/75.

List of Acronyms

AGN ..... Active Galactic Nuclei
CCD ..... Charge-Couple Device
ETG ..... Early Type Galaxy
T_e ..... Electron Temperature
EW ..... Equivalent Width
FIR ..... Far-Infrared
FMR ..... Fundamental Metallicity Relation
FP ..... Fundamental Plane
GLACE ..... GaLAxy Cluster Evolution survey
GTC ..... Gran Telescopio de Canarias
GTR ..... General Theory of Relativity
HLIRG ..... Hyper-Luminosity Infrared Galaxy
IR ..... Infrared
ISM ..... Interstellar medium
JWST ..... *James Webb Space Telescope*
LBT ..... Large Binocular Telescope
LH ..... Lockman Hole
LIRG ..... Luminosity Infrared Galaxy
Lockman–SpReSO ..... Lockman Spectroscopic Survey using OSIRIS
LOFAR ..... LOw-Frequency ARray
MOS ..... Multi-Object Spectroscopy
MS ..... Main Sequence
MZR ..... Mass–metallicity relation
NGC ..... *New General Catalogue*
NIR ..... Near-Infrared
NUV ..... Near-Ultraviolet
OSIRIS ..... Optical System for Imaging and low-Intermediate-Resolution Integrated Spectroscopy
OTELO ..... OSIRIS Tunable Emission Line Object survey

PACS ..... Photodetector Array Camera and Spectrometer
PEP ..... *Herchel*/PACS Evolutionary Probe
POSS-I ..... *Palomar Observatory Sky Survey I*
POSS-II ..... *Palomar Observatory Sky Survey II*
SDSS ..... *Sloan Digital Sky Survey*
sSFR ..... Specific Star Formation Rate
SFG ..... Star-Forming Galaxy
SFR ..... Star Formation Rate
S/N ..... Signal to Noise
M_* ..... Stellar Mass
L_{TIR} ..... Total Infrared Luminosity
UKIRT ..... United Kingdom Infrared Telescope
ULIRG ..... Ultra-Luminosity Infrared Galaxy
UV ..... Ultraviolet
VLA ..... Very Large Array
WHT ..... William Herschel Telescope
WIYN .. Wisconsin, Indiana, Yale, and National optical astronomy observatory
2dFGRS ..... *Two-degree Field Galaxy Redshift Survey*
2MASS ..... *Two Micron All-Sky Survey*